

# **The Thermodynamic Behaviour and Miscibility of Discotic Liquid Crystals**

**Tingjun Zhong**

**PhD Thesis**

**University of York**

**Chemistry**

**September 2015**

## **Abstract**

This thesis is concerned with the self-organization of molecules that have disc-like shapes. The disc-like molecules may have relatively rigid structures as in polyaromatic systems, or they may have amphiphilic structures with polyaromatics at their cores, and soft outer shells made up of aliphatic chains. This research seeks to explore molecular compatibility and the ensuing structures formed by such disc-like systems through the study of phase diagrams. Thus, the thermodynamic behaviour and miscibilities of discotic liquid crystal materials were investigated by the formation of Gibbs phase diagrams and calculations using the Schröder-van Laar equation for liquid crystals that have structural common features.

Polyaromatics were reviewed and investigated as they are hard discs, and are as the central cores of the molecules that form discotic liquid crystals. Existing discotic materials, such as triphenylene hexa-esters, phenyl hexa-esters, phenyl hexa-alkynes, and rod-like compounds such as benzoate esters were studied and analysed using polarized optical microscopy (POM), differential scanning calorimetry (DSC), and X-ray diffraction where appropriate, for the preparations of mixture studies.

Mixture series made by triphenylene derivatives with each other, and with rod-like molecules or star-shape molecules were prepared and examined in order to investigate the potential co-miscibilities for both discotic nematic phase and hexagonal columnar phases. Mixture series made by triphenylene derivatives with polyaromatics were also prepared, and examined by POM and DSC to explore the virtual N-I phase transition temperatures for polyaromatics. These studies appear to show that nematic discotic materials are liquid crystals, whereas columnar materials exhibit 2D crystalline soft solid phases. In addition, a novel new phase was found to form in the isotropic liquid of mixtures of polyaromatic materials, suggesting the possibility of the cubatic nematic phase being present.

# Contents

<b>Abstract</b> .....	2
Contents .....	3
List of Figures .....	8
List of Tables .....	23
Acknowledgements.....	29
Declaration.....	30
<b>Chapter 1: Introduction</b> .....	31
1.1 Liquid Crystals.....	32
1.1.1 General Definitions of Liquid Crystals.....	32
1.1.2 The Theory of Liquid Crystals.....	33
1.1.2.1 Onsager Theory for Liquid Crystals .....	34
1.1.2.2 The Maier and Saupe Theory for the Nematic Phase .....	35
1.2 Thermotropic Liquid Crystals.....	36
1.3 Liquid Crystal Phases of Disc-like Materials .....	39
1.3.1 General Structure for Discotic Liquid Crystals .....	39
1.3.2 Phases formed by Discotic Liquid Crystals .....	41
1.3.2.1 Discotic Nematic Phase .....	42
1.3.2.2 Cubatic Nematic Phase .....	45
1.3.2.3 Columnar Phases.....	46
1.3.3 Important Applications for Discotic Liquid Crystal Mesogens.....	49
1.3.3.1 Wide Angle Views Films for Displays .....	50
1.4 Carbonaceous Liquid Crystals .....	53
1.5 Liquid Crystal Mixtures and Formulations.....	54
1.5.1 Gibbs Phase Diagrams .....	54

1.5.2 Schröder-van Laar Equation .....	57
1.5.3 Mixture Systems of Liquid Crystals .....	57
1.6 Techniques in the Study of Liquid Crystals.....	58
1.6.1 Polarized Optical Microscopy (POM) .....	59
1.6.2 Differential Scanning Calorimetry (DSC) .....	61
1.6.3 X-ray Diffraction (XRD) .....	63
1.6.4 Density functional theory (DFT) .....	68
<b>Chapter 2: Aims</b> .....	69
2.1 General Aims .....	70
2.2 Target Systems for Study.....	72
2.2.1 Polyaromatics.....	72
2.2.2 Mixture Studies.....	73
<b>Chapter 3: Experimental</b> .....	75
3.1 Materials, Reagents and Solvents .....	76
3.1.1 Experimental of Existing Materials for Mixture Studies.....	76
3.2 General Techniques .....	86
3.2.1 Polarized Optical Microscopy (POM) .....	86
3.2.2 Differential Scanning Calorimetry (DSC) .....	86
3.2.3 X-ray Diffraction (XRD) .....	87
3.2.4 Preparation of Mixture systems .....	87
3.2.5 Calculations of Schröder-van Laar Equation.....	87
3.2.6 Computing Modelling.....	87
<b>Chapter 4: Polyaromatics</b> .....	89
4.1 Introduction.....	90
4.2 Determination of the Clearing Points for Selected Polyaromatics .....	92
4.3 Extrapolation of the Values of Virtual N-I for Selected Polyaromatics .....	96

4.4 Mixing Polyaromatics to Generate Carbonaceous Liquid Crystals.....	96
4.4.1 Mixture Studies of Different Hard Discs and Hard Rods.....	97
4.5 Summary.....	102
<b>Chapter 5: The Miscibility of Nematogenic Disc-like Materials</b> .....	103
5.1 Introduction.....	104
5.2 The Co-miscibility of Nematogenic Materials formed by Disc-like Molecules .....	104
5.2.1 Co-miscibility of nematogens of disc-like triphenylene derivatives .....	105
5.2.1.1 Mixture studies of Compounds 4 and 11 .....	105
5.2.2 Co-miscibility of nematogens of discotic triphenylene derivatives with rod-like tetra-benzoate molecules .....	114
5.2.2.1 Studies for Binary Mixtures between Compounds 4 and 38 .....	119
5.2.2.2 Studies for Binary Mixtures between Compounds 11 and 51 .....	128
5.2.2.3 Studies for Binary Mixtures between Compounds 27 and 56 .....	132
5.2.3 Co-miscibility of disc-like triphenylene mesogens with phenyl hexa- alkynes .....	140
5.2.3.1 Mixture Studies between Compounds 16 and 64 .....	142
5.2.3.2 Mixture Studies between Compounds 18 and 64 .....	150
5.2.3.3 Mixture Studies between Compounds 26 and 64 .....	158
5.2.3.4 Mixture Studies between Compounds 27 and 64 .....	165
5.2.3.5 Mixture Studies between Compounds 22 and 64 .....	171
5.2.3.6 Mixture Studies between Compounds 14 and 64 .....	176
5.2.3.7 Mixture Studies between Compounds 19 and 64 .....	184
5.2.3.8 Mixture Studies between Compounds 20 and 64 .....	192

5.2.3.9 Mixture Studies of Compounds 13, 15 and 17 with 64 .....	200
5.3 Summary .....	220
<b>Chapter 6: Phase Diagrams of Columnar Disc-like Materials .....</b>	<b>221</b>
6.1 Introduction.....	222
6.2 Structures of Columnar Liquid Crystals .....	222
6.3 Phase Behaviour of Binary Columnar Systems .....	223
6.3.1 Mixture Studies of Compounds 21 with 32 .....	223
6.4 Phase Behaviour of Mixed Nematic and Columnar Systems .....	234
6.4.1 Phase Behaviour of Nematic and Columnar Triphenylene Derivatives .....	234
6.4.1.1 Mixture Studies between Compounds 21 and 24 .....	234
6.4.2 Phase Behaviour of Tetra-benzoate Esters and Columnar Triphenylene Hexa-esters.....	245
6.4.2.1 Mixture Studies between Compounds 32 and 52 .....	246
6.4.2.2 Mixture Studies between Compounds 21 and 40 .....	251
6.4.2.3 Mixture Studies between Compounds 29 and 41 .....	258
6.4.3 Phase Behaviour of Nematogenic Phenyl Hexa-alkynes and Columnar Triphenylene Hexa-esters .....	266
6.4.3.1 Mixture Studies of Compounds 24 and 64 .....	267
6.4.3.2 Mixture Studies of Compounds 21 and 64 .....	274
6.4.3.3 Mixture Studies of Compounds 23 and 64 .....	283
6.5 Recalculations of the Schröder-van Laar Equation for Mixtures Containing Columnar Mesogens .....	291
6.6 Discussion .....	294
6.7 Summary .....	296
<b>Chapter 7: Mixing Polyaromatics with Conventional Discotic Liquid Crystals .....</b>	<b>297</b>

7.1 Introduction.....	298
7.2 Mixture Studies between Triphenylene and Triphenylene Derivatives.....	298
7.2.1 Mixture Studies of Triphenylene and Compound 14.....	298
7.2.2 Mixture Studies of Triphenylene and Compound 23.....	303
7.2.3 Discussion.....	308
7.3 Miscibility Results of Other Polyaromatics with Triphenylene Derivatives .....	309
7.4 Summary.....	310
<b>Chapter 8: Conclusion.....</b>	<b>311</b>
8.1 Conclusion for Polyaromatics and Cubatic Phases.....	312
8.2 Conclusion for Miscibility Investigation for Discotic Liquid Crystals .....	315
8.2.1 Co-miscibility of Nematic of Disc-like Mesogens .....	316
8.2.2 Phase Behaviour of Columnar Discotic Mesogens.....	319
Appendix 1: The Chemical Structures of the Compounds for Misibility Studies in the Thesis .....	322
<b>References.....</b>	<b>334</b>

## List of Figures

Figure 1.1 The different states of matter and the molecule ordering for those....	33
Figure 1.2 The molecular ordering in the melting process for calamitic liquid crystals. ....	37
Figure 1.3 The mesophases formed by calamitic systems made of rod-like molecules. ....	38
Figure 1.4 The structure of benzene-hexa-n-alkanoates. ....	39
Figure 1.5 The General structure for the discoidal liquid crystal molecules. ....	40
Figure 1.6 Formation of the columnar phase form 1D columns by the self-assembling and self-organizing discotic molecules. ....	40
Figure 1.7 An example of the structure of a typical derivative of triphenylene. .	41
Figure 1.8 Different types of the phases formed by disk-like materials and their structures. ....	42
Figure 1.9 The local structure of the discotic nematic phase with a preferred director. ....	43
Figure 1.10 The local structure of nematic phase formed by calamitic liquid crystals (rod-like molecules). ....	43
Figure 1.11 (a) The typical shlieren structures of the discotic nematic phase (x100) showing two and four brush defects and (b) The typical x-ray diffraction pattern showing discotic nematic phase. ....	44
Figure 1.12 The helical macrostructure of the chiral nematic discotic phase. ....	44
Figure 1.13 The side view of a cut sphere and the hard-cut spheres with thickness L and diameter D. ....	45
Figure 1.14 The structure of the cubatic nematic phase for hard-cut spheres ....	46
Figure 1.15 The structures of columnar phases formed by discotic molecules and the plan view of the two-dimensional lattices of the columns: (a) Hexagonal columnar phase (disordered and ordered); (b) (d) (e) Rectangular columnar phase (disordered) with P21/a, p2/a, C2/a space	

symmetry; (c) Oblique columnar phase (disordered) with P1 symmetry.....	48
Figure 1.16 The columnar phases with axis symmetry: (a) Hexagonal columnar phase with C6 axis; (b) Tilted hexagonal columnar phase with C2 axis; (c) Rectangular columnar phase with C2 axis. ....	49
Figure 1.17 The effect by different angle of view for a Fuji WV optical compensating film on a liquid crystal display. ....	51
Figure 1.18 The fixed birefringence of a calamitic liquid crystal display. ....	52
Figure 1.19 Polarized light micrograph (crossed polarizers) (150 X) of extracted pitch carbonized to 450 °C at approximately 0.4 °C /min. ....	53
Figure 1.20 The pressure-temperature phase of water. ....	55
Figure 1.21 The typical liquid-solid phase diagram for a two-component nematogenic system showing the temperature as a function of composition.....	56
Figure 1.22 The chemical structure and phase transitions of 5CB. ....	58
Figure 1.23 A micrograph (x100) showing the 4-brush defects in the nematic phase of a discogen. ....	59
Figure 1.24 Micrographs (x100) showing optical textures of columnar hexagonal phases formed by various discotic liquid crystal materials ....	61
Figure 1.25 The X-ray diffraction from a set of parallel crystal planes separated by distance d. ....	64
Figure 1.26 The X-ray diffraction suffering a net change by an angle of $2\theta$ during scattering.....	65
Figure 1.27 The X-ray pattern illustrated the different phases obtained by compound 4.....	66
Figure 1.28 The X-ray pattern illustrated the different phases obtained by compound 32.....	67
Figure 2.1 The chemical structures of polyaromatics.....	70
Figure 2.2 Potential phases formed by mixtures of hard disc-like molecules. ....	71

Figure 2.3 Mixtures of disc-like molecules that have soft structure and an amphiphilic structure. ....	72
Figure 2.4 Typical chemical structures of amphiphiles selected for investigation. ....	74
Figure 4.1 The liquid crystal phase behaviour of sexiphenyl and (I) and quinquephenyl (II). ....	90
Figure 4.2 Effect of molecular bending on the clearing point for di-oxadiazoles and di-thiophenes. ....	91
Figure 4.3 The DSC thermograms as a function of temperature (°C) for p-sexiphenyl. ....	94
Figure 4.4 The DSC thermograms as a function of temperature (°C) for triphenylene, pyrene, perylene, truxene and coronene. ....	95
Figure 4.5 The DSC thermograms as a function of temperature (°C) for mixtures TZ-3M, TZ-4M and TZ-5M. ....	98
Figure 4.6 The micrograph TZ-4M (x100) showing the dark texture of the mixture at approximately 200 °C. ....	100
Figure 4.7 The DSC peak for the unidentified phase for TZ-4M showing the intermediate mesophase transition to the isotropic liquid on heating. ....	101
Figure 4.8 Self-organization of triphenylene and truxene. ....	102
Figure 5.1 The chemical structures and phase transitions of compound 4 and 11. ....	106
Figure 5.2 The energy structure for compounds 4 and 11, at the mixed ONIOM(B3LYP/6-31G(d):PM6) level of theory. ....	107
Figure 5.3 The Gibbs phase diagram for the binary mixture series TZ-M001 of 4 and 11. ....	111
Figure 5.4 The Gibbs phase diagram showing the biphasic region between heating and cooling for nematic to isotropic transition of mixtures of 4 and 11. ....	113

Figure 5.5 The diagram showing the enthalpies (kJ/mol) of the nematic to isotropic liquid transition in heating process of mixtures of 4 and 11.....	114
Figure 5.6 The diagram showing the structures of compound 37, 38, 46 and 58. .....	115
Figure 5.7 The micrographs (x100) obtained for: (a) 38, heating, 101.3 °C, N; (b) 37, cooling, 87.3 °C, N; (c) 37, cooling, 74.1 °C, SmC; (d) 46, cooling, 119.6 °C, N; (e) 58, cooling, 58.0 °C, N; (f) TZ-M005-E, cooling, 100 °C, N; (g) TZ-M007-E, cooling, 83.4 °C, N; (h) TZ-M008-E, heating, 186.3 °C, N; (i) TZ-M008-E, cooling, 67.5 °C, SmC.....	116
Figure 5.8 The structures of compound 1, 4, 10, 11, 27, 38, 51 and 56. ....	118
Figure 5.9 The chemical structures and phase transitions of compounds 4 and 38.. .....	120
Figure 5.10 The energy minimised structures for compounds 4 and 38, using the mixed ONIOM(B3LYP/6-31G(d):PM6) level of theory.....	121
Figure 5.11 The Gibbs phase diagram for the binary mixture series TZ-M012 of 4 and 38.....	126
Figure 5.12 The Gibbs phase diagram showing the biphasic region determined by DSC between heating and cooling for nematic to isotropic transition of mixtures of compounds 4 and 38.....	127
Figure 5.13 The diagram showing the enthalpies (kJ/mol) of the nematic to isotropic liquid transition in heating process of mixtures of 4 and 38. .....	127
Figure 5.14 The chemical structures and phase transitions of compounds 11 and 51, and the space filling structures of compounds 11 and 51 determined in gas phase at 0 K using the MM2 force field as implemented in ChemDraw 3D. ....	128
Figure 5.15 The energy minimised structures for compounds 11 and 51, at the ONIOM(B3LYP/6-31G(d):PM6) Level of theory.....	129
Figure 5.16 The Gibbs phase diagram for the binary mixture series TZ-M019 of 11 and 51.....	131

Figure 5.17 The chemical structures and phase transitions of compounds 27 and 56.....	132
Figure 5.18 The space filling structures of compounds 27 and 56 determined in gas phase at 0 K using the MM2 force field as implemented in ChemDraw 3D.....	133
Figure 5.19 The energy structures for compounds 27 and 56, at the ONIOM(B3LYP/6-31G(d):PM6) Level of theory.....	134
Figure 5.20 The Gibbs phase diagram for the binary mixture series TZ-M021 of 27 and 56.....	138
Figure 5.21 The Gibbs phase diagram showing the biphasic region determined by DSC between heating and cooling for nematic to isotropic transition of mixtures of compounds 27 and 56.....	139
Figure 5.22 The diagram showing the enthalpies (kJ/mol) for the nematic to isotropic liquid transition in cooling process of mixtures of 27 and 56. ....	140
Figure 5.23 The structure of compound 64, and the respective photomicrograph for nematic texture at 178.0 °C.....	141
Figure 5.24 The energy minimised structures for compound 64, at the mixed ONIOM(B3LYP/6-31G(d):PM6) Level of theory.....	142
Figure 5.25 The chemical structures and phase transitions (°C) for compounds 16 and 64.....	143
Figure 5.26 The space filling structures of compounds 16 and 64 determined in gas phase at 0 K using the MM2 force field as implemented in ChemDraw 3D.....	144
Figure 5.27 The energy structure for compound 16, at the mixed ONIOM(B3LYP/6-31G(d):PM6) Level of theory.....	144
Figure 5.28 The Gibbs phase diagram obtained from the binary mixture series TZ-M022. ....	148
Figure 5.29 The Gibbs phase diagram showing the biphasic region between heating and cooling for transition of mixtures of 16 and 64.....	149

Figure 5.30 The enthalpies (kJ/mol) for nematic to isotropic liquid transition in both heating and cooling process of the mixtures of 16 and 64.....	149
Figure 5.31 The DSC tracing result for the mixture TZ-M022-1 both on heating and cooling of the first cycle.....	150
Figure 5.32 The chemical structures and phase transitions of compound 18 and 64. ....	151
Figure 5.33 The space filling structures of compounds 18 and 64 determined in gas phase at 0 K using the MM2 force field as implemented in ChemDraw 3D.....	151
Figure 5.34 The energy structure for compound 18, at the mixed ONIOM(B3LYP/6-31G(d):PM6) level of theory.....	152
Figure 5.35 The Gibbs phase diagram for the binary mixture series TZ-M023-1-5 of 18 and 64. ....	155
Figure 5.36 The Gibbs phase diagram showing the biphasic region between heating and cooling for transition of mixtures of 18 and 64.....	156
Figure 5.37 The diagram showing the enthalpies (kJ/mol) of transitions on heating as a function of the mol concentration of compound 18 in a mixture with compound 64.....	157
Figure 5.38 The DSC curve for the mixture TZ-M023-3 (59.9 mol% of compound 16) both on heating and cooling in the first cycle.....	158
Figure 5.39 The chemical structures and phase transitions of compound 26 and 64. ....	159
Figure 5.40 The space filling structures of compounds 26 and 64 determined in gas phase at 0 K using the MM2 force field as implemented in ChemDraw 3D.....	159
Figure 5.41 The energy structure for compound 26, at the mixed ONIOM(B3LYP/6-31G(d):PM6) level of theory.....	160
Figure 5.42 The Gibbs phase diagram for binary mixture series TZ-M024 of 26 and 64.....	164

Figure 5.43 The chemical structures and phase transitions of compound 27 and 64. .....	165
Figure 5.44 The Gibbs phase diagram for the binary mixture series TZ-M030 of 27 and 64.....	168
Figure 5.45 The Gibbs phase diagram showing the biphasic region between heating and cooling for transitions for mixtures of 27 and 64. ....	169
Figure 5.46 The diagram showing the function of enthalpies (kJ/mol) of each phase transition in heating session with the mol concentration of compound 27 in a mixture with compound 64. ....	170
Figure 5.47 The chemical structures and phase transition temperatures (°C) for compounds 22 and 64. ....	172
Figure 5.48 The space filling structures of compounds 22 and 64 determined in gas phase at 0 K using the MM2 force field as implemented in ChemDraw 3D.....	172
Figure 5.49 The energy structure for compound 22, at the mixed ONIOM(B3LYP/6-31G(d):PM6) level of theory.....	173
Figure 5.50 The Gibbs phase diagram for the binary mixture series TZ-M031 of 22 and 64.....	175
Figure 5.51 The chemical structures and phase transitions (°C) for compounds 14 and 64.....	177
Figure 5.52 The space filling structures of compounds 14 and 64 determined in gas phase at 0 K using the MM2 force field as implemented in ChemDraw 3D.....	177
Figure 5.53 The energy structure for compound 14, at the mixed ONIOM(B3LYP/6-31G(d):PM6) level of theory.....	178
Figure 5.54 The Gibbs phase diagram for the binary mixture series TZ-M032 of 14 and 64.....	181
Figure 5.55 The Gibbs phase diagram showing the biphasic region between heating and cooling for transition of mixtures of 14 and 64.....	182

Figure 5.56 The diagram showing the function of enthalpies (kJ/mol) of N-I phase transition in heating session with the mol concentration of compound 14 in a mixture with compound 64. ....	183
Figure 5.57 The chemical structures and phase transitions of compounds 19 and 64.....	184
Figure 5.58 The space filling structures of compounds 19 and 64 determined in gas phase at 0 K using the MM2 force field as implemented in ChemDraw 3D.....	185
Figure 5.59 The energy structure for compound 19, at the mixed ONIOM(B3LYP/6-31G(d):PM6) level of theory.....	186
Figure 5.60 The Gibbs phase diagram for the binary mixture series TZ-M033 of 19 and 64. ....	188
Figure 5.61 The Gibbs phase diagram showing the biphasic region between heating and cooling for transition of mixtures of 19 and 24.....	190
Figure 5.62 The DSC curve of the mixture TZ-M033-1 showing no peaks for the N-I phase transition.....	191
Figure 5.63 The diagram showing the function of enthalpies (kJ/mol) of phase transitions in heating session with the mol concentration of compound 19 in a mixture with compound 64. ....	191
Figure 5.64 The packing together two types of molecules that have disc-like structures of differing diameters .....	192
Figure 5.65 The chemical structures and phase transitions of compounds 20 and 64.....	193
Figure 5.66 The space filling structures of compounds 20 and 64 determined in gas phase at 0 K using the MM2 force field as implemented in ChemDraw 3D.....	194
Figure 5.67 The energy structure for compound 20, at the mixed ONIOM(B3LYP/6-31G(d):PM6) level of theory.....	194
Figure 5.68 The Gibbs phase diagram for the binary mixture series TZ-M034 of 20 and 64. ....	197

Figure 5.69 The Gibbs phase diagram showing the biphasic region between heating and cooling for transition of mixtures of 20 and 64.....	199
Figure 5.70 The diagram showing the function of enthalpies (kJ/mol) of phase transitions in heating session with the mol concentration of compound 20 in a mixture with compound 64. ....	200
Figure 5.71 The chemical structures and phase transition temperatures (°C) for compounds 13, 15, 17 and 64. ....	201
Figure 5.72 The space filling structures of compounds 13 to 17 and 64 determined in gas phase at 0 K using the MM2 force field as implemented in ChemDraw 3D. ....	202
Figure 5.73 The energy structures for compounds 13 and 15, at the mixed ONIOM(B3LYP/6-31G(d):PM6) level of theory.....	203
Figure 5.74 The energy structure for compounds 17 and 64, at the mixed ONIOM(B3LYP/6-31G(d):PM6) level of theory.....	204
Figure 5.75 The Gibbs phase diagram for the binary mixture series TZ-M035-1-5 of 13 and 64. ....	207
Figure 5.76 The Gibbs phase diagram showing the biphasic region between heating and cooling for transition of mixtures of 13 and 64.....	208
Figure 5.77 The diagram showing the function of enthalpies of phase transitions in heating session with the mol% concentration of compound 13 in a mixture with compound 64. ....	209
Figure 5.78 The Gibbs phase diagram for the binary mixture series TZ-M036 of 15 and 64. ....	213
Figure 5.79 The Gibbs phase diagram showing the biphasic region between heating and cooling (°C) for transition of mixtures of 15 and 64..	214
Figure 5.80 The diagram showing the function of enthalpies (kJ/mol) of phase transitions on heating with the mol% concentration of compound 15 in a mixture with compound 64. ....	214
Figure 5.81 The Gibbs phase diagram for the binary mixture series TZ-M037 of 17 and 64. ....	218

Figure 5.82 The Gibbs phase diagram showing the biphasic region between heating and cooling cycles for phase transitions for mixtures of 17 and 64.....	219
Figure 5.83 The diagram showing the function of enthalpies (kJ/mol) of phase transitions in heating process with the mol% concentration of compound 17 in a mixture with compound 64. ....	219
Figure 6.1 The structures of the disordered and ordered columnar mesophases. ....	223
Figure 6.2 The chemical structures and phase transitions of compounds 21 and 32. ....	225
Figure 6.3 The space filling structures of compounds 21 and 32 determined in gas phase at 0 K using the MM2 force field as implemented in ChemDraw 3D.....	225
Figure 6.4 The energy structure for compound 21 at the mixed ONIOM(B3LYP/6-31G(d):PM6) level of theory. ....	226
Figure 6.5 The Gibbs phase diagram for the binary mixture series TZ-M003 of 21 and 32. ....	230
Figure 6.6 The microscopy showing the phase texture for the concentration of 56.1 mol% of compound 21 in the mixture with compound 32. ....	231
Figure 6.7 Classical phase diagram for a binary mixture showing ideal behaviour. ....	232
Figure 6.8 The Gibbs phase diagram showing the biphasic region between heating and cooling for hexagonal columnar to isotropic liquid transition of mixtures of 21 and 32. ....	232
Figure 6.9 Diagram showing the enthalpies (kJ/mol) for the columnar phase to isotropic liquid transitions on heating cycles for binary mixtures between compounds 21 and 32 as a function of the concentration of 21 (mol%). ....	233
Figure 6.10 The chemical structures and phase transitions of compounds 21 and 24.....	235

Figure 6.11 The space filling structures of compounds 21 and 24 determined in gas phase at 0 K using the MM2 force field as implemented in ChemDraw 3D.....	235
Figure 6.12 The energy structures for compounds 21 and 24, at the mixed ONIOM(B3LYP/6-31G(d):PM6) level of theory.....	237
Figure 6.13 The Gibbs phase diagram for the binary mixture series TZ-M040-1-8 of 21 and 24. ....	240
Figure 6.14 The representative optical textures for the co-existence phase region. ....	241
Figure 6.15 The Gibbs phase diagram showing the biphasic region between heating and cooling for transition of mixtures of 21 and 24.....	243
Figure 6.16 The diagram showing the function of enthalpies (kJ/mol) of each phase transition in heating cycle with the mol% concentration of compound 21 in a mixture with compound 24. ....	244
Figure 6.17 The chemical structures and phase transition temperatures (°C) for compounds 32 and 52. ....	247
Figure 6.18 The space filling structures of compounds 32 and 52 determined in gas phase at 0 K using the MM2 force field as implemented in ChemDraw 3D.....	248
Figure 6.19 The minimised energy structure for compound 52, at the mixed ONIOM(B3LYP/6-31G(d):PM6) level of theory.....	248
Figure 6.20 The Gibbs phase diagram for the binary mixture series TZ-M016 of 32 and 52.....	250
Figure 6.21 The chemical structures and phase transitions of compounds 21 and 40. ....	252
Figure 6.22 The space filling structures of compounds 21 and 40 determined in gas phase at 0 K using the MM2 force field as implemented in ChemDraw 3D.....	252
Figure 6.23 The energy structures for compounds 21 and 40, at the mixed ONIOM(B3LYP/6-31G(d):PM6) level of theory.....	253

Figure 6.24 The Gibbs phase diagram for the binary mixture series TZ-M018 and photo micrographs (x100 magnification) of the series of mixture TZ-M018.....	255
Figure 6.25 The Gibbs phase diagram showing the biphasic region between heating and cooling for hexagonal columnar phase to isotropic transition temperatures (°C) for mixtures of compounds 21 and 40. ....	257
Figure 6.26 The diagram showing the enthalpies (kJ/mol) for the hexagonal columnar phase to isotropic liquid transition in heating process of mixtures TZ-M018 with a function of mol percentage of compound 21.....	258
Figure 6.27 The chemical structures and phase transition temperatures (°C) for compounds 29 and 41. ....	259
Figure 6.28 The space filling structures of compounds 29 and 41 determined in gas phase at 0 K using the MM2 force field as implemented in ChemDraw 3D.....	260
Figure 6.29 The energy structures for compounds 29 and 41, at the mixed ONIOM(B3LYP/6-31G(d):PM6) level of theory.....	261
Figure 6.30 The Gibbs phase diagram for binary mixture series TZ-M020 and photo micrographs (x100 magnification) of the series of mixture TZ-M020.....	264
Figure 6.31 The Gibbs phase diagram showing the biphasic region between heating and cooling for transitions of mixtures TZ-M020 with a function of mol percentage of compound 29. ....	265
Figure 6.32 The diagram showing the enthalpies (kJ/mol) of the hexagonal columnar phase to isotropic liquid transition in cooling process of mixtures of 29 and 41 with a function of mol percentage of compound 29.....	266
Figure 6.33 The chemical structures and phase transitions of compounds 24 and 64.....	268

Figure 6.34 The space filling structures of compounds 24 and 64 determined in gas phase at 0 K using the MM2 force field as implemented in ChemDraw 3D.....	268
Figure 6.35 The energy structure for compound 24, at the mixed ONIOM(B3LYP/6-31G(d):PM6) level of theory.....	269
Figure 6.36 The Gibbs phase diagram obtained from the binary mixture series TZ-M027.....	271
Figure 6.37 The Gibbs phase diagram showing the biphasic region between heating and cooling for phase transitions of mixtures of the series TZ-M027.....	273
Figure 6.38 The diagram showing the function of enthalpies (kJ/mol) of mixtures exhibiting nematic to isotropic liquid transitions on heating cycles with respect to the mol concentration of compound 24 in a mixture with compound 64.....	274
Figure 6.39 The chemical structures and phase transitions for compounds 21 and 64.....	275
Figure 6.40 The space filling structures of compounds 21 and 64 determined in gas phase at 0 K using the MM2 force field as implemented in ChemDraw 3D.....	275
Figure 6.41 The minimised energy structures for compounds 21, at the mixed ONIOM(B3LYP/6-31G(d):PM6) level of theory.....	276
Figure 6.42 The Gibbs phase diagram for the binary mixture series TZ-M028 and the photo micrographs (x100 magnification) of the series of mixture TZ-M028.....	280
Figure 6.43 The micrographs (x100 magnification) of the series of mixture TZ-M028 showing representative optical separated phases textures...	281
Figure 6.44 The Gibbs phase diagram showing the biphasic region between heating and cooling for nematic to isotropic liquid and hexagonal columnar to isotropic liquid transitions of mixtures of 21 and 64.....	282

Figure 6.45 The diagram showing the function of enthalpies (kJ/mol) of phase transitions in heating cycles with the mol concentration of compound 21 in a mixture with compound 64. ....	283
Figure 6.46 The chemical structures and phase transitions (°C) for compounds 23 and 64.....	284
Figure 6.47 The space filling structures of compounds 23 and 64 determined in gas phase at 0 K using the MM2 force field as implemented in ChemDraw 3D.....	285
Figure 6.48 The energy structure for compounds 23, at the mixed ONIOM(B3LYP/6-31G(d):PM6) level of theory.....	286
Figure 6.49 The Gibbs phase diagram for the binary mixture series TZ-M029. ....	289
Figure 6.50 The Gibbs phase diagram showing the biphasic region between heating and cooling for phase transitions (°C) of mixtures (mol%) of 23 and 64.....	290
Figure 6.51 The diagram showing the function of enthalpies (kJ/mol) of each phase transition in heating or cooling session with the mol concentration of compound 23 in a mixture with compound 64. ....	291
Figure 6.52 Hexagonal arrangements of triphenylene derivatives that form the basic structure of columnar liquid crystals. ....	294
Figure 6.53 A disordered hexagonal columnar phase made by molecules differing diameters, which are laterally and vertically disorganised along the column axes.. ....	296
Figure 7.1 The chemical structures and phase transitions (°C) for triphenylene and compound 14.....	299
Figure 7.2 The space filling structures of triphenylene, and compound 14 determined in gas phase at 0 K using the MM2 force field as implemented in ChemDraw 3D. ....	299
Figure 7.3 The energy structure for compound 14, at the mixed ONIOM(B3LYP/6-31G(d):PM6) level of theory. ....	300

Figure 7.4 The phase diagram for the binary mixture series TZ-M046 of Triphenylene and 14. ....	302
Figure 7.5 The chemical structure and phase transition temperatures for compound 23.....	303
Figure 7.6 The space filling structures of triphenylene, and compound 23 determined in gas phase at 0 K using the MM2 force field as implemented in ChemDraw 3D. ....	304
Figure 7.7 The energy structure for compound 23, at the mixed ONIOM(B3LYP/6-31G(d):PM6) level of theory. ....	304
Figure 7.8 The phase diagram for the binary mixture series TZ-M047 of Triphenylene and 23. ....	307
Figure 7.9 Comparison of the phase diagrams and the determination of the virtual N-I transition temperature (°C) for triphenylene. ....	308
Figure 8.1 An impression of the shapes of the polyaromatic materials triphenylene and coronene in gas phase at 0K as determined by modelling using the MM2 force field as implemented in ChemDraw 3D, and their local self-organizations. ....	314
Figure 8.2 An impression of the twisted shape of truxene in gas phase at 0K as determined by modelling using the MM2 force field as implemented in ChemDraw 3D, and its local self-organization.....	315

## List of Tables

Table 3.1 The structures, phase transition temperatures (°C) and mesophases of the triphenylene benzoate hexa-esters. ....	77
Table 3.2 The structures, phase transition temperatures (°C) and mesophases of the triphenylene derivatives. ....	80
Table 3.3 The structures, phase transition temperatures (°C) and mesophases of the benzoate hexa-esters. ....	80
Table 3.4 The structures, phase transition temperatures (°C) and mesophases of the tetra-benzoate esters. ....	81
Table 3.5 The structures, phase transition temperatures (°C) and mesophases of the tetra-benzoate esters. ....	82
Table 3.6 The structures, phase transition temperatures (°C) and mesophases of the benzoate esters. ....	82
Table 3.7 The structures, phase transition temperatures (°C) and mesophases of the tetra-benzoate esters. ....	83
Table 3.8 The structures, phase transition temperatures (°C) and mesophases of the benzoate esters. ....	84
Table 3.9 The structures, phase transition temperatures (°C) and mesophases of the phenyl hexa-alkynes. ....	84
Table 3.10 The enthalpies of the melting process for the samples 1-64. ....	85
Table 4.1 The chemical structures and melting points (°C) for a variety of polyaromatics. ....	93
Table 4.2 Mixture compositions (mol %) and predicted eutectic point with examined melting point (°C) for the different components mixtures. .	97
Table 4.3 Mixture compositions (mol %) and predicted eutectic point (°C) for the binary mixtures (SVL means Schröder-van Laar). ....	99
Table 5.1 Mixture compositions (mol%) and transition temperatures (°C) for binary mixtures of 4 and 11 determined by POM. ....	109

Table 5.2 Mixture compositions (mol%) and nematic to isotropic transition temperatures (°C) and enthalpies (J/g) both on heating and cooling for binary mixtures of 4 and 11. ....	110
Table 5.3 Binary mixture composition (mol%), predicted eutectic melting points (°C) and phase transition temperatures (°C) for tetra-benzoate esters. ....	115
Table 5.4 Binary mixture compositions (mol%), predicted eutectic melting points (°C) and phase transition temperatures (°C) for nematic triphenylene hexa-esters (1, 4, 10, 11, and 27) and tetra-benzoate esters (38, 51, and 56). ....	117
Table 5.5 Compositions and transition temperatures (°C) for binary mixtures of 4 and 38 by POM. ....	123
Table 5.6 Mixture compositions (mol%) and nematic to isotropic transition temperatures (°C) and enthalpies (J/g) both on heating and cooling for binary mixtures of 4 and 38. ....	123
Table 5.7 Mixture compositions (mol%) and transition temperatures (°C) for binary mixtures of 11 and 51. ....	130
Table 5.8 Compositions (mol%) and transition temperatures (°C) for binary mixtures of compounds 27 and 56. ....	135
Table 5.9 Mixture compositions (mol%) and nematic to isotropic transition temperatures (°C) and enthalpies (J/g) both on heating and cooling for binary mixtures of 56 and 27. ....	136
Table 5.10 Compositions (mol%) and transition temperatures (°C) for binary mixtures of 16 and 64 determined by POM. ....	145
Table 5.11 Mixture compositions (mol%) and transition temperatures (°C) and enthalpies (J/g) both on heating and cooling for binary mixtures of 16 and 64. ....	146
Table 5.12 Compositions (mol%) and transition temperatures (°C) for binary mixtures of 18 and 64 determined by POM. ....	153

Table 5.13 Mixture compositions (mol%) and transition temperatures (°C) and enthalpies (J/g) both on heating and cooling for binary mixtures of 18 and 64.....	154
Table 5.14 Compositions (mol%) and transition temperatures (°C) for binary mixtures of 26 and 64 determined by POM.....	161
Table 5.15 Mixture compositions (mol%) and transition temperatures (°C) and enthalpies both on heating and cooling for binary mixtures of 26 and 64. ....	162
Table 5.16 Compositions (mol%) and transition temperatures (°C) for binary mixtures of 27 and 64 determined by POM.....	166
Table 5.17 Mixture compositions (mol%) and transition temperatures (°C) and enthalpies (J/g) both in heating and cooling sessions for binary mixtures of 27 and 64. ....	167
Table 5.18 Compositions (mol%) and transition temperatures (°C) for binary mixtures of 22 and 64 determined by POM.....	174
Table 5.19 Compositions (mol%) and transition temperatures (°C) for binary mixtures of 14 and 64 determined by POM.....	179
Table 5.20 Compositions (mol%) and transition temperatures (°C) and enthalpies (J/g) both on heating and cooling for binary mixtures of 14 and 64..	180
Table 5.21 Compositions (mol%) and transition temperatures (°C) for binary mixtures of 19 and 64 determined by POM.....	187
Table 5.22 Mixture compositions (mol%) and transition temperatures (°C) and enthalpies (J/g) both on heating and cooling for binary mixtures of 19 and 64.....	189
Table 5.23 Compositions (mol%) and transition temperatures (°C) for binary mixtures of 20 and 64 determined by POM.....	195
Table 5.24 Mixture compositions (mol%) and transition temperatures (°C) and enthalpies (J/g) both on heating and cooling for binary mixtures of 20 and 64 by DSC. ....	196

Table 5.25 Compositions (mol%) and transition temperatures (°C) for binary mixtures of 13 and 64 determined by POM.....	205
Table 5.26 Mixture compositions (mol%) and transition temperatures (°C) and enthalpies (J/g) both on heating and cooling for binary mixtures of 13 and 64.....	206
Table 5.27 Compositions (mol%) and transition temperatures (°C) for binary mixtures of 15 and 64 determined by POM.....	210
Table 5.28 Mixture compositions (mol%) and transition temperatures (°C) and enthalpies (J/g) both on heating and cooling for binary mixtures of 15 and 64.....	211
Table 5.29 Compositions (mol%) and transition temperatures (°C) for binary mixtures of 17 and 64 determined by POM.....	215
Table 5.30 Mixture compositions (mol%) and transition temperatures (°C) and enthalpies (J/g) both on heating and cooling for binary mixtures of 17 and 64.....	216
Table 6.1 Mixture compositions (mol%) and transition temperatures (°C) for binary mixtures of compounds 21 and 32.....	227
Table 6.2 Mixture compositions (mol%) and phase transition temperatures (°C) and enthalpies (J/g) both in heating and cooling session for binary mixtures of 21 and 32. ....	228
Table 6.3 Compositions (mol%) and transition temperatures (°C) determined by POM for binary mixtures of compounds 21 and 24. ....	238
Table 6.4 Mixture compositions (mol%) and transition temperatures (°C) and enthalpies (J/g) both in heating and cooling cycles for binary mixtures of 21 and 24. ....	239
Table 6.5 The components and concentrations (mol%), the phase classifications and transition temperatures (°C) of the eutectic mixtures by columnar triphenylene hexa-esters and tetra-benzoate esters. ....	246
Table 6.6 Mixture compositions (mol%) and transition temperatures (°C) for binary mixtures of compounds 32 and 52.....	249

Table 6.7 Compositions (mol %) and transition temperatures (°C) for binary mixtures of 21 and 40 determined by POM.....	254
Table 6.8 Mixture compositions (mol%) and nematic to isotropic liquid and hexagonal columnar to isotropic liquid transition temperatures (°C) and enthalpies (J/g) both in heating and cooling cycles for binary mixtures of 21 and 40. ....	256
Table 6.9 Mixture compositions (mol%) and transition temperatures (°C) for binary mixtures of 29 and 41. ....	262
Table 6.10 Mixture compositions (mol%) and nematic to isotropic liquid and hexagonal columnar to isotropic liquid transition temperatures (°C) and enthalpies (J/g) both in heating and cooling cycles for binary mixtures of 29 and 41. ....	263
Table 6.11 Compositions (mol%) and transition temperatures (°C) for binary mixtures of compounds 24 and 64 determined by POM. ....	270
Table 6.12 Mixture compositions (mol%) and transition temperatures (°C) and enthalpies (J/g) both on heating and cooling cycles for binary mixtures of compounds 24 and 64. ....	272
Table 6.13 Compositions (mol%) and transition temperatures (°C) for binary mixtures of compounds 21 and 64 determined by POM. ....	277
Table 6.14 Mixture compositions (mol%) and transition temperatures (°C) and enthalpies (J/g) in heating and cooling cycles for binary mixtures of compounds 21 and 64. ....	278
Table 6.15 Compositions (mol%) and transition temperatures (°C) for binary mixtures of compounds 23 and 64 determined by POM. ....	287
Table 6.16 Mixture compositions (mol%) and transition temperatures (°C) and enthalpies (J/g) in heating and cooling cycles for binary mixtures of 23 and 64.....	288
Table 6.17 Calculation results by Schröder-van Laar equation using melting temperatures and related enthalpies. ....	292

Table 6.18 Calculation results by Schröder-van Laar equation using Colh-Iso temperatures and related enthalpies.....	292
Table 6.19 The eutectic results of the mixture TZ-M016.....	293
Table 6.20 The eutectic results of the mixture TZ-M018.....	293
Table 7.1 Mixture compositions (mol %) and transition temperatures (°C) for binary mixtures of triphenylene and compound 14. ....	301
Table 7.2 Mixture compositions (mol %) and transition temperatures (°C) for binary mixtures of triphenylene and compound 23. ....	305
Table 7.3 The miscibility results for the mixtures obtained by different polyaromatics with different nematic and columnar triphenylene derivatives.....	310
Table 8.1 The mixture series and results for the binary mixtures of triphenylene hexa-esters with each other.....	317
Table 8.2 The mixture series and results for the binary mixtures of triphenylene hexa-esters and rod-like tetra-benzoate molecules. ....	317
Table 8.3 The mixture series and results for the binary mixtures of triphenylene hexa-esters and star-shaped phenyl hexa-alkynes.....	318
Table 8.4 The series of mixtures and results for the columnar phases of triphenylene hexa-esters with each other.....	319
Table 8.5 The mixture series and results for mixing of materials exhibiting columnar and possibly nematic phases.....	320

## **Acknowledgements**

I would like to give my genuine acknowledgement to my supervisor John Goodby FRS, for giving me the opportunity in studying my PhD in University of York, and the guidance and support though the four years in my PhD.

I also would like to thank Dr Stephen Cowling to share his great knowledge of the use of the instruments to me and the guidance and help in the physical analysis and also the written work.

I would like to thank all the colleagues in our Advanced Materials Group for the help and discussion, especially Dr Richard Mandle, Dr Edward Davis and Dr Katrina Bakker for their help, guidance and discussion.

I also would like to thank Dr Tony Wild for his generosity in enabling my Wild Fund Scholarship to support my PhD in these years, and my friends and family for continuing moral and financial support.

## Declaration

I, Tingjun Zhong, declare that this thesis is a presentation of original work and I am the sole author. This work has not previously been presented for an award at this, or any other, University and it has not been submitted for publications anywhere else. All sources are acknowledged as References, with the exceptions below:

- Published paper: J.W. Goodby, R.J. Mandle, E.J. Davis, Tingjun Zhong and S.J. Cowling, *Liq. Cryst.*, 2015, **42**, 593-622, DOI: 10.1080/02678292.2015.1030348.
- British Liquid Crystal Society Conference in Cambridge, in 2013; Poster presentation: The Thermodynamic and Thermo-optical Properties of Discotic Liquid Crystals.
- 9<sup>th</sup> International Union of Pure and Applied Chemists (IUPAC) NMS-IX Conference in Shanghai, China, in 2013; Invited oral presentation: The Thermodynamic and Thermo-optical Properties of Discotic Liquid Crystals.
- Bruker Poster Competition in Department of Chemistry, University of York, in 2014; Poster Title: The Thermodynamic and Thermo-optical Properties of Discotic Liquid Crystals.
- British Liquid Crystal Society Conference in Durham, in 2014; Poster presentation: The Thermodynamic and Thermo-optical Properties of Discotic Liquid Crystals.
- 25<sup>th</sup> International Liquid Crystal Conference in Dublin, in 2014; Poster presentation: The Thermodynamic and Thermo-optical Properties of Discotic Liquid Crystals.
- 10<sup>th</sup> International Union of Pure and Applied Chemists (IUPAC) NMS-X Conference in Zhengzhou, China, in 2014; Invited lecture: The Thermodynamic Properties of Discoidal Materials.
- The computer modelling and simulations shown in Chapter 5, Chapter 6 and Chapter 7 were performed with the help by Professor John Goodby FRS and Dr Richard Mandle during their time in University of York.

## **Chapter 1: Introduction**

# **Chapter 1: Introduction**

In this chapter will incorporate background on the following sections:

1. Liquid crystals,
2. Thermotropic Liquid Crystals,
3. Liquid Crystal Phases of Disc-like Materials,
4. Liquid Crystal Mixtures and Formulations, and
5. Techniques in the Study of Liquid Crystals.

## **1.1 Liquid Crystals**

### **1.1.1 General Definitions of Liquid Crystals**

Generally, liquid crystals are materials which have properties between those of conventional liquids and those of solid crystals, they have phases that do not possess long-range positional ordering, but do have long-range orientational order, which is a phase occurring over a defined range of temperature or pressure or concentration within the mesomorphic state.[1] For conventional liquids, the molecules translate and rotate freely, and therefore possess no positional or orientational ordering. Conversely, for crystalline solids, the constituent molecules are in defined sites of a three-dimensional lattice, and therefore there is a high degree of both orientational and positional ordering, with the molecules only vibrating on their lattice sites. The molecular ordering for different types of states of matter is shown in Figure 1.1.

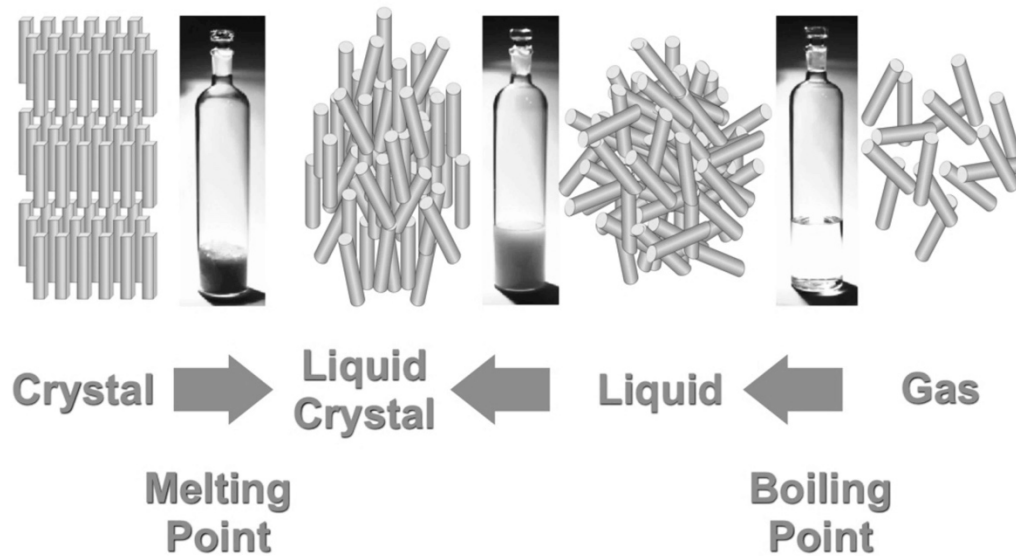


**Figure 1.1** The different states of matter and the molecule ordering for those.

The types of liquid crystals can be roughly divided into two topics generally; thermotropic liquid crystals and lyotropic liquid crystals. Thermotropic liquid crystals are mesophases that are dependent on temperature thermal, either by heating the crystalline solid or by cooling the isotropic liquid. Conversely, lyotropic liquid crystals are formed by materials that possess amphiphilic properties, and in the presence of solvents form mesophases.[2] In addition, based on different optical properties, there are many types of liquid crystal phases, such as nematics, smectics, cholesterics and discotics. The class of materials and phase types will be discussed more in detail in sections 1.2, 1.3.1 and 1.3.2.

### 1.1.2 The Theory of Liquid Crystals

From the early models by Onsager and the theory of Maier and Saupe, the theoretical treatments of liquid crystals, have proved to be a challenge.[3-5] Recently various researchers have worked on such problems involving the development of a continuum theory, a statistical mechanical approaches of the mean field theory, the role of repulsive, and attractive forces in phase formation.[6]

### 1.1.2.1 Onsager Theory for Liquid Crystals

The Onsager theory is known for its prediction of the critical transition density for small aspect ratio hard rods. A number of liquid crystals theories are based on the Onsager theory[7-8] because it is the first theory to demonstrate that orientational order can arise from molecular shape anisotropy, and also due to its subsequent influence in diverse areas of physics and applied mathematics.[9]

Onsager treated liquid crystal molecules as interacting hard rods, where the free energy could be expanded as “*virial*” coefficients, in terms of the orientational distribution function. He showed that the ordering in the nematic phase could be stabilized by the hard-core repulsion effects between rigid rod-like molecules without the presence of any forces of attraction. The steric repulsion between rigid particles is a limiting case of a strong short-range repulsion interaction, which does not allow molecules to penetrate each other’s space.[1] The corresponding model interaction  $V_s$  can be written as:

$$V_s(1,2) = \Omega(\gamma_{12} - \xi_{12}) \quad (\text{Equation 1.1})$$

Where  $\Omega(\chi)$  is a step function, if  $\gamma_{12} < \xi_{12}$ , thus  $\Omega(\gamma_{12} - \xi_{12}) = \infty$  and the molecules penetrate each other's space; otherwise  $\Omega(\gamma_{12} - \xi_{12}) = 0$ . Here  $\gamma_{12}$  is the distance between the centers of defined molecules 1 and 2, and  $\xi_{12}$  is the minimum distance of approach between the centers of defined molecules 1 and 2 for a given orientation. The function  $\xi_{12}$  is determined by the molecular shapes and depends on the orientations of the two molecules relative to one another. For hard spheres  $\xi_{12} = D$  where  $D$  is the diameter of the sphere. For two prolate molecules,  $\xi_{12}$  varies between the diameter  $D$  and the length  $L$ .

### 1.1.2.2 The Maier and Saupe Theory for the Nematic Phase

In the previous subsection, hard-core repulsion effects between anisotropic molecules were discussed. For thermotropic liquid crystal systems, which will be discussed in section 1.2, pp 6-8, the transition occurs at a particular temperature, and therefore must involve some attractive interactions. A corresponding molecular theory, based on anisotropic dispersion interactions, was proposed by Maier and Saupe.[3-5] This molecular theory of the nematic-isotropic phase transition was developed *via* a mean-field approximation. In the mean-field approximation one neglects correlations between different molecules, and thus it is obviously a relatively unrealistic approximation. However, it enables the reader to obtain very simple and useful expressions for the free energy of the system. It appears to be sufficient for a qualitative description of the N-I transition as well.[1]

The dispersion (or Van der Waals) interaction forces appear in the second-order perturbation theory. The initial interaction potential is an electrostatic one. If the molecules are sufficiently far apart, the dispersion interaction energy can be obtained from a second-order perturbation theory. It often used in molecular theories of liquid crystals to draw qualitative conclusions, and has been used in the Maier-Saupe theory.[1]

Using the Maier and Saupe theory, it can describe the nematic order parameter and the free energy of the nematic phase in a first order nematic to isotropic liquid transition, when one neglects the asymmetry of the molecule shape ( $\xi_{12}=D$ , as mentioned in previous section). An important feature of this theory is based on its simplicity and universality, which is not dependent on intermolecular forces or the molecular structure, but based on the temperature variation of the order parameter. Thus its value at the transition point is also predicted to be universal.

## 1.2 Thermotropic Liquid Crystals

The definition of a crystalline solid is that it has long-range order of the positions of the molecules in three dimensions. The thermal motions of the molecules within the lattice increase and after all the vibrations become so intense when the fully-ordered crystal is heated, thus in this way it leads to that the regular arrangement of molecules is broken down with the loss of long-range orientational and positional order to give the disorganized isotropic liquid. The temperature at which this process occurs is called as *melting point*. For some materials, they have one or more intermediate phases as the temperature is increased. These intermediate states are called *mesophases*. Some of these mesophases are liquid crystalline and the materials are said to be thermotropic liquid crystals.

Usually, thermotropic liquid crystals mainly have either rod-shape molecular structures[10-11] or disc-shape molecules[12], and many other cases of this type can be produced by using mixtures of compounds, *i.e.* E7[13], which do not need to be individually capable of forming liquid crystal phases or mesophases.[2] The mesophases formed by rod-like shape molecules are sometimes referred to as *calamitic* liquid crystals, which includes nematic or smectic liquid crystal phases.[7] Figure 1.2 shows the molecular ordering in the melting process for calamitic liquid crystals, and Figure 1.3 shows the structures of the mesophases of calamitic liquid crystals.

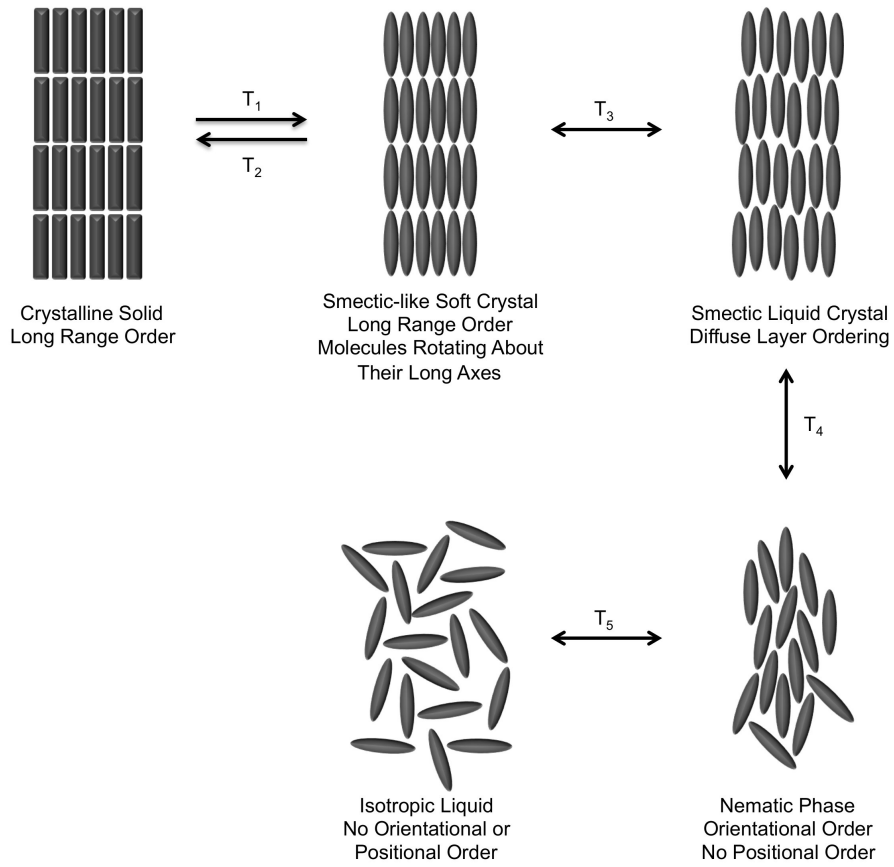


**Figure 1.2** The molecular ordering in the melting process for calamitic liquid crystals.[14]

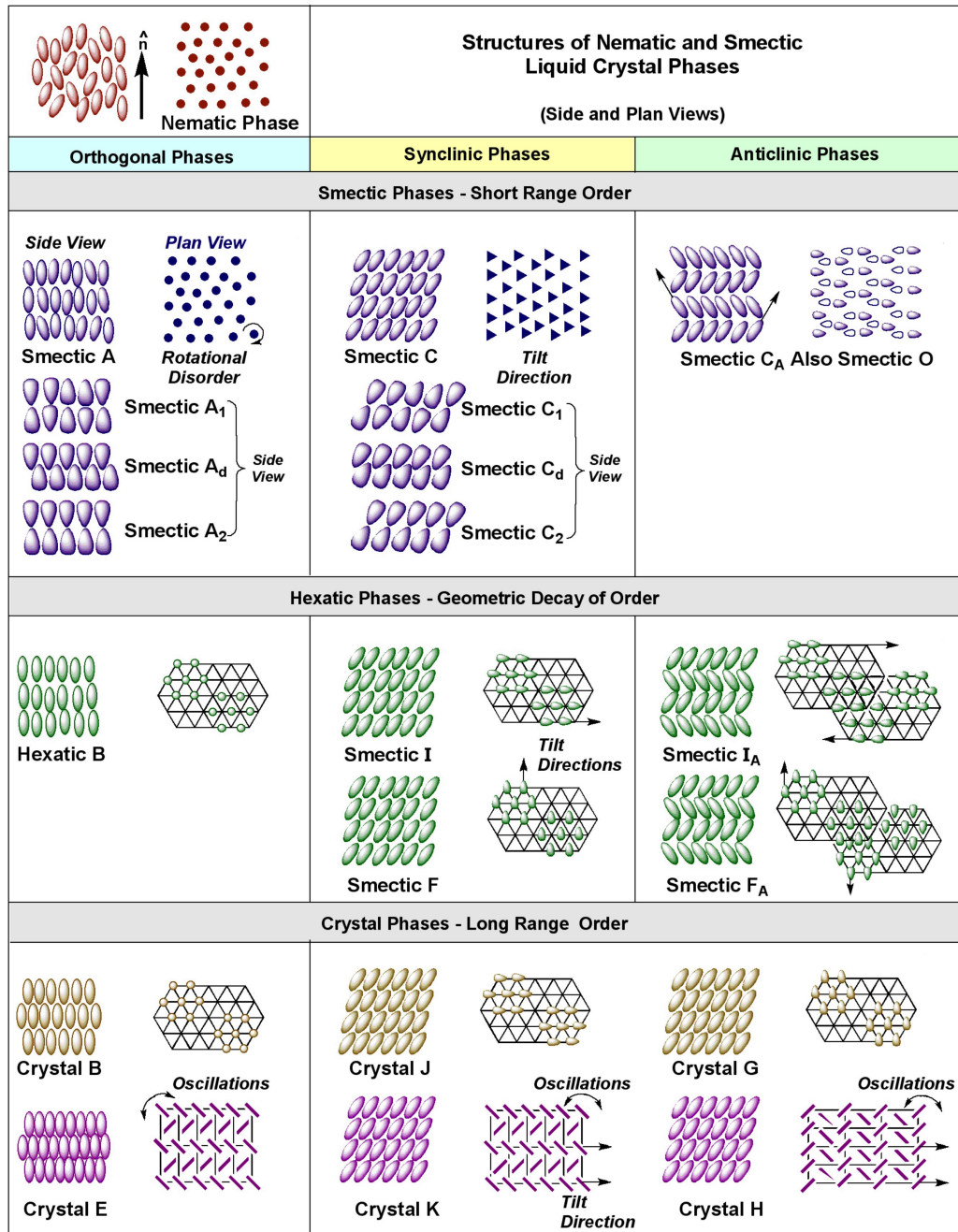


**Figure 1.3** The mesophases formed by calamitic systems made of rod-like molecules.[14]

For the discotic liquid crystals and the mesophases of discotic mesogens, they will be discussed in next following section 1.3 more in detail.

## 1.3 Liquid Crystal Phases of Disc-like Materials

In 1977 liquid crystals composed of disc-like molecules were first synthesized and their phases identified.[12] The compounds they investigated were benzene-hexa-*n*-alkanoates (shown in Figure 1.4), and all of the compounds investigated were found to exhibit mesophases, except BHn-pentanoate and BHn-decanoate which were non-mesomorphic.

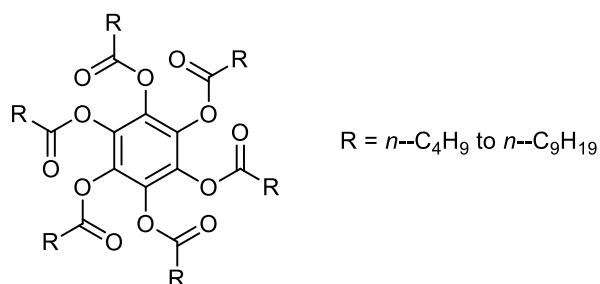


**Figure 1.4** The structure of benzene-hexa-*n*-alkanoates.

Now that a reasonable understanding of discoid materials and the various types of mesophases they exhibit exist,[15-23] many researchers have investigated their structures and properties *via* computer modelling and simulations.[24-25]

### 1.3.1 General Structure for Discotic Liquid Crystals

The molecules forming discotic liquid crystals are generally composed of a central disc-like core (such as benzene, triphenylene, truxene) and around the central core 3 to 12 saturated peripheral chains of three or more carbon atoms are substituted.[26] Recently researchers have been investigating changes in the number, size, and nature of the lateral chains, in addition to the central core unit. These discotic materials often have rotational symmetry properties. The general structure for discotic mesogens is shown in Figure 1.5.

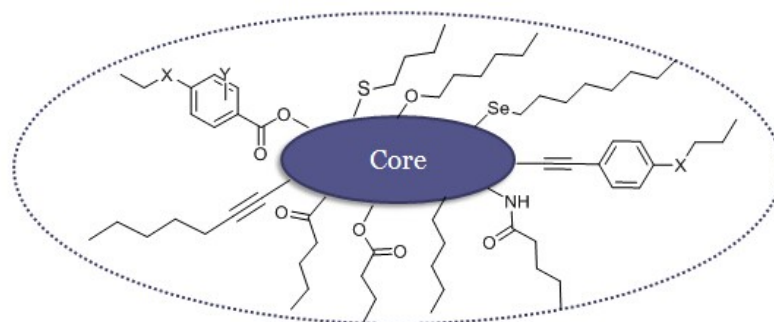


**Figure 1.5** The General structure for the discotic liquid crystal molecules.

Discotic molecules can organize spontaneously in a form of 1D columns, which have self-assembling and self-organization properties[27], which can repair the structural defects inside self-assembling structures *via* the self-healing properties. For example, the Figure 1.6 shows the formation of columnar phases from the one self-assembly of discotic molecules.[26]

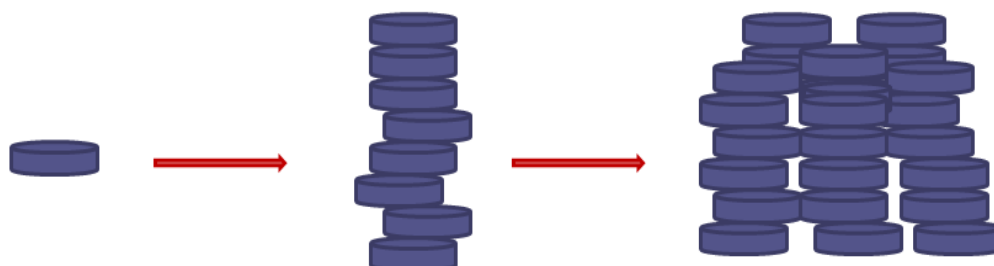


**Figure 1.6** Formation of the columnar phase form 1D columns by the self-assembling and self-organizing discotic molecules.

Discotic thermotropic liquid crystals are usually  $\pi$ -conjugated materials, and have unique combined properties of relative fluidity, processability, and self-healing, combined with the orientational ordering of crystals, which can give properties such as anisotropic conductivity and optical anisotropy.[28] In this discotic liquid crystal structure, the orientational order arises from the anisotropy of molecules that flat aromatic centre core is surrounded by aliphatic chains at the periphery. Compounds with different abilities to self-organize and conduct charge

carriers can be obtained by tuning the shape and the size of the conjugated core, and the type of the attached peripheral chains.[27]

In this thesis, discotic materials based on triphenylene is widely used in the studies made. An example of a triphenylene based mesogen with peripheral aliphatic chains as substituents is shown in Figure 1.7.

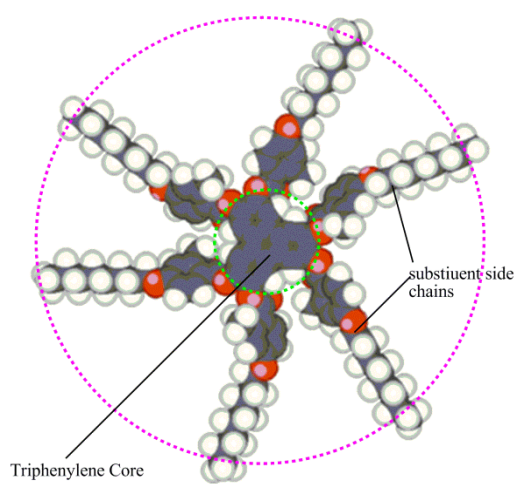


**Figure 1.7** Structure of a typical derivative of triphenylene.

### 1.3.2 Phases formed by Discotic Liquid Crystals

The most common discotic liquid crystal phases are discotic nematic phase ( $N_D$ ), hexagonal columnar phase ( $Col_h$ ), and hexagonal rectangular phase ( $Col_r$ ), formed by disc-like molecules which are characterized by the degree of positional order. The molecule ordering for various types of the phases formed by disk-like materials is shown in Figure 1.8, and each individual phase will be discussed more in detail in the following subsections.

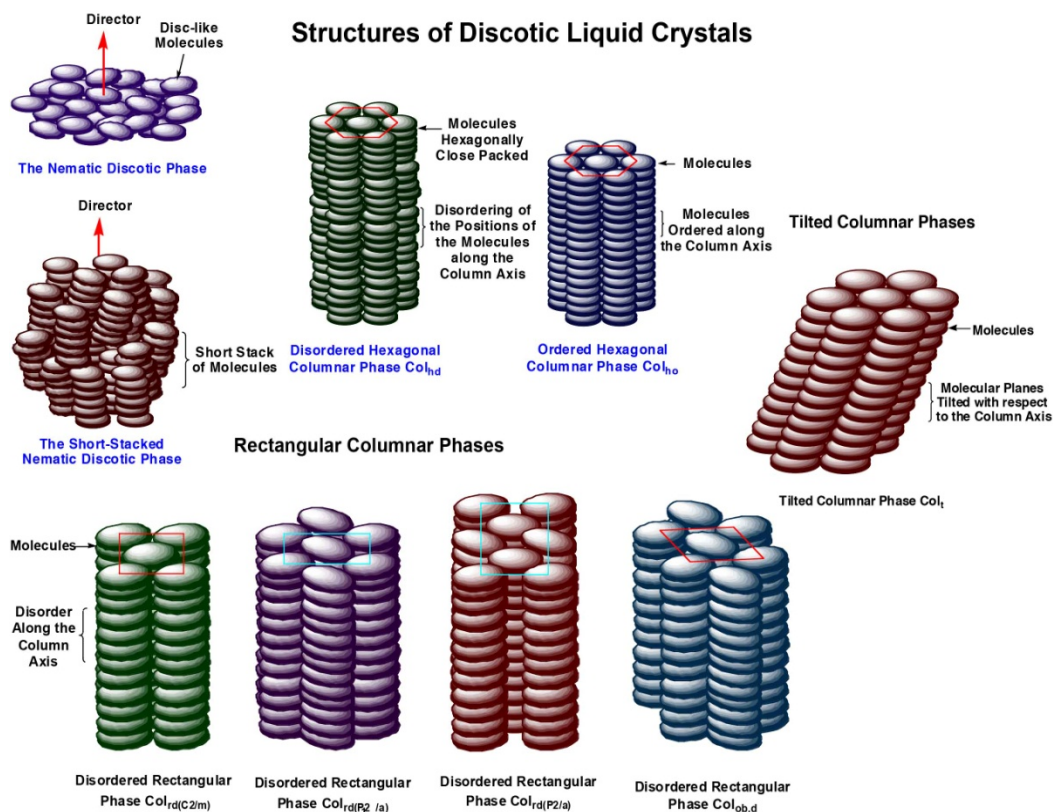


**Figure 1.8** Different types of the phases formed by disk-like materials and their structures. (The graph was provided by Professor John Goodby FRS in University of York.)

### 1.3.2.1 Discotic Nematic Phase

The discotic nematic phase ( $N_D$ ) composed of disk-like shape molecules is the least ordered, but the more rotationally restricted mesophase compared with the other nematic phases *i.e.* formed by rod-like molecules[26,29]. The discotic phases are anisotropic fluids possessing full translational and rotational freedom around the centre of the disks, with a single order parameter associated with the tendency of the discs to align parallel, and consequently the short molecular axes tend to point along a preferred common director  $\mathbf{n}$  as shown in Figure 1.9, the analog with the calamitic nematic phase shown in Figure 1.10 respectively.

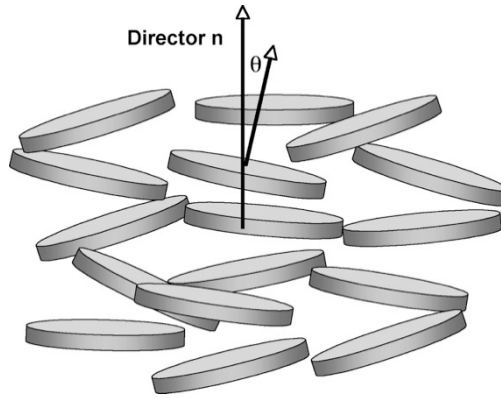


**Figure 1.9** The local structure of the discotic nematic phase with a preferred director.

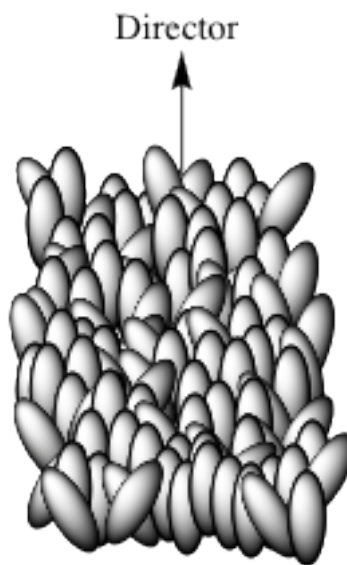


**Figure 1.10** The local structure of nematic phase formed by calamitic liquid crystals (rod-like molecules).

As seen in Figure 1.9, the discotic nematic phase has the same symmetry as that of nematic phase formed by calamitic liquid crystals (rod-like molecules, shown in Figure 1.10). In addition, all discotic nematic phases are fluid and exhibit typical *schlieren* textures with two and four brush defects and marbled textures similar to those of rod-like molecules, which are shown in Figure 1.11, as well as the x-ray diffraction pattern. However, the difference in the two nematic phases is not clear, but might have connections with molecular associations as for rod-like reentrant behavior.[2]

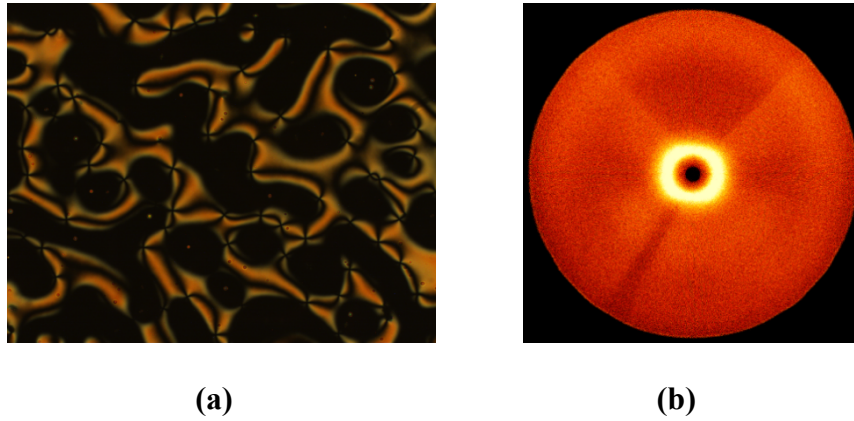


**Figure 1.11** (a) The typical *shlieren* structures of the discotic nematic phase (x100) showing two and four brush defects and (b) The typical x-ray diffraction pattern showing discotic nematic phase.

The discotic nematic phase when composed of chiral material, as with calamitic phases, exhibits a helical macrostructuring as shown in Figure 1.12.

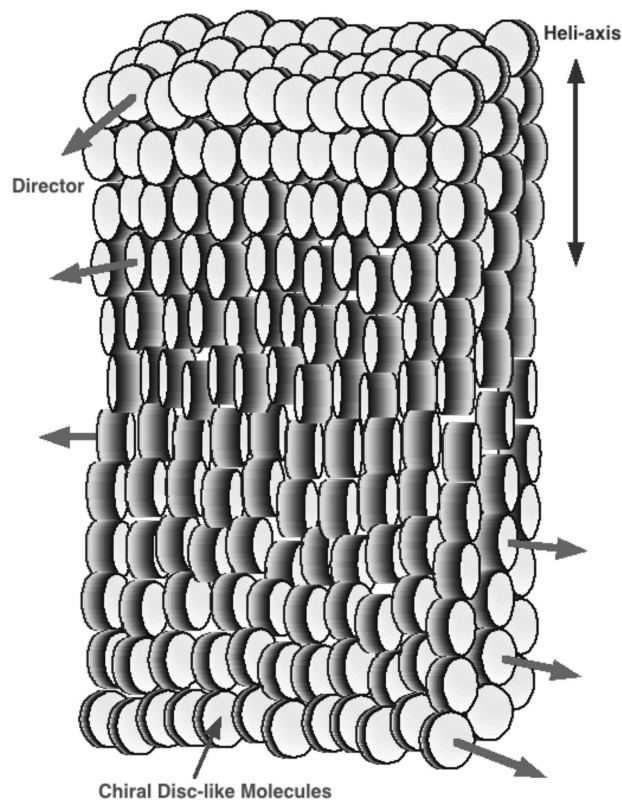


**Figure 1.12** The helical macrostructuring of the chiral nematic discotic phase. (The graph was provided by Professor John Goodby FRS in University of York.)

Obviously in this phase, because of the size of the molecules and their disc-like shapes, the helical pitch length can be relatively long, and therefore the phase is less likely to exhibit selective reflection of visible light. However, in some cases where there are numerous stereogenic centres in the molecular structure the possibility of colour reflection becomes more likely.

### 1.3.2.2 Cubatic Nematic Phase

The cubatic nematic phase is a long-range orientationally ordered phase without any positional order of the particles, which is a theoretically postulated phase and has yet to be fully confirmed by experiment.[30] The theoretical postulation of a cubatic nematic phase uses a high-order virial theory and Monte Carlo simulation based on a system of the organized hard-cut spheres, where the cut-sphere particles are disks of thickness  $L$  formed by symmetrically truncating the end caps of a sphere of diameter  $D$  (shown in Figure 1.13).

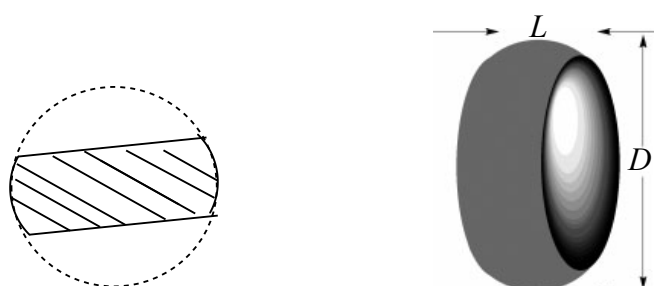


**Figure 1.13** The side view of a cut sphere and the hard-cut spheres with thickness  $L$  and diameter  $D$ .

In the system of hard-cut spheres, the phase behavior is dependent on the length-to-width ratio ( $L/D$ ) of the molecular structure. Based on the theory and simulations, it predicted a stable nematic phase and columnar phase occurs when the aspect ratio  $L/D = 0.1$ , but when the aspect ratio  $L/D = 0.3$ , it found only the presence of a stable fluid and solid. In addition, it predicts a stable cubatic phase for the ratio  $L/D=0.15-0.3$ . [6] In the results, the virial series aggregated rapidly for the equation of state of the isotropic liquid and nematic phases. Conversely, the convergence was slower for the cubatic phase, but it still gives a good agreement

with the computer simulations at high order. Also, it was found that truncation of the virial theory at low order did not predict the formation of a cubatic nematic phase, thus a high-order expansion is required to predict the formation of a stable cubatic phase for  $L/D \geq 0.15$ , for the many-body interactions are required for stability of the cubatic nematic phase.[31]

The proposed structure for the cubatic nematic phase formed by hard-cut spheres is shown in Figure 1.14. In the process of its formation, molecules with truncated spherical shapes are allowed to self-organize and they form short stacks at first, but in further the stacks were expected to form columns. As the rotation of the short stacks and reorientation is difficult, the intermediary phase is stabilized and called cubatic nematic phase. It has been found that the cubatic phase is metastable with respect to an isotropic to columnar phase coexistence for all three model platelets, and the cubatic phase can be regarded as a transient phase in the isotropic to columnar phase transformation.[32]

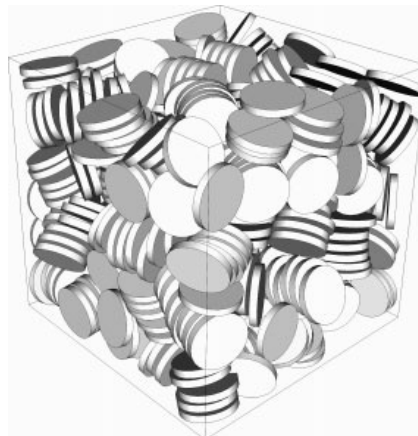


**Figure 1.14** The structure of the cubatic nematic phase for hard-cut spheres.[6]

### 1.3.2.3 Columnar Phases

Disk-like molecules often self-assemble with one another with a tendency to stack face-to-face in columns and then self-organize to columnar phases. The plan view for the two-dimensional lattices of the columns is shown in Figure 1.15. These

columns can pack in different ways so that they can arrange in different ways, such as hexagonal columnar, rectangular columnar and oblique columnar (shown in Figure 1.16).

For the hexagonal columnar phase, the molecules have fluid properties but might have different correlation lengths, thus they can be called ordered or disordered hexagonal columnar phases. This kind of arrangement possesses  $D_{6h}$  symmetry, because it possesses a sixfold rotational ( $C_6$ ) axis perpendicular to the long axis of the columns, one mirror plane perpendicular to this axis, six mirror planes in the plane of the  $C_6$  axis, six  $C_2$  axes perpendicular to the  $C_6$  axis, a center of inversion, and two axes of improper rotation ( $S_3$  and  $S_6$ ).[33] On the other hand, for the rectangular motifs packing, they exhibit  $D_{2h}$  point symmetry, because they possess three mutually orthogonal  $C_2$  axes, three mutually orthogonal mirror planes, and a center of inversion.[34]

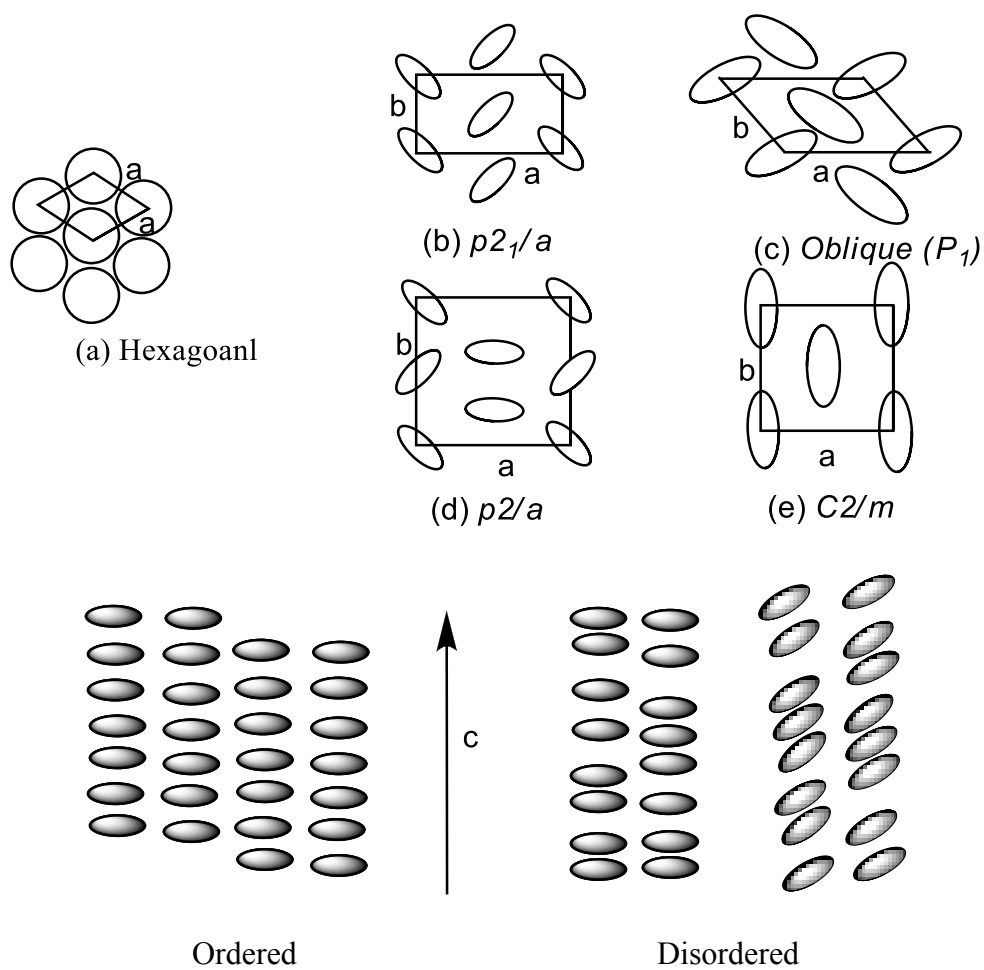


**Figure 1.15** The structures of columnar phases formed by discotic molecules and the plan view of the two-dimensional lattices of the columns: **(a)** Hexagonal columnar phase (disordered and ordered); **(b)** **(d)** **(e)** Rectangular columnar phase (disordered) with  $P2_1/a$ ,  $p2/a$ ,  $C2/a$  space symmetry; **(c)** Oblique columnar phase (disordered) with  $P1$  symmetry.

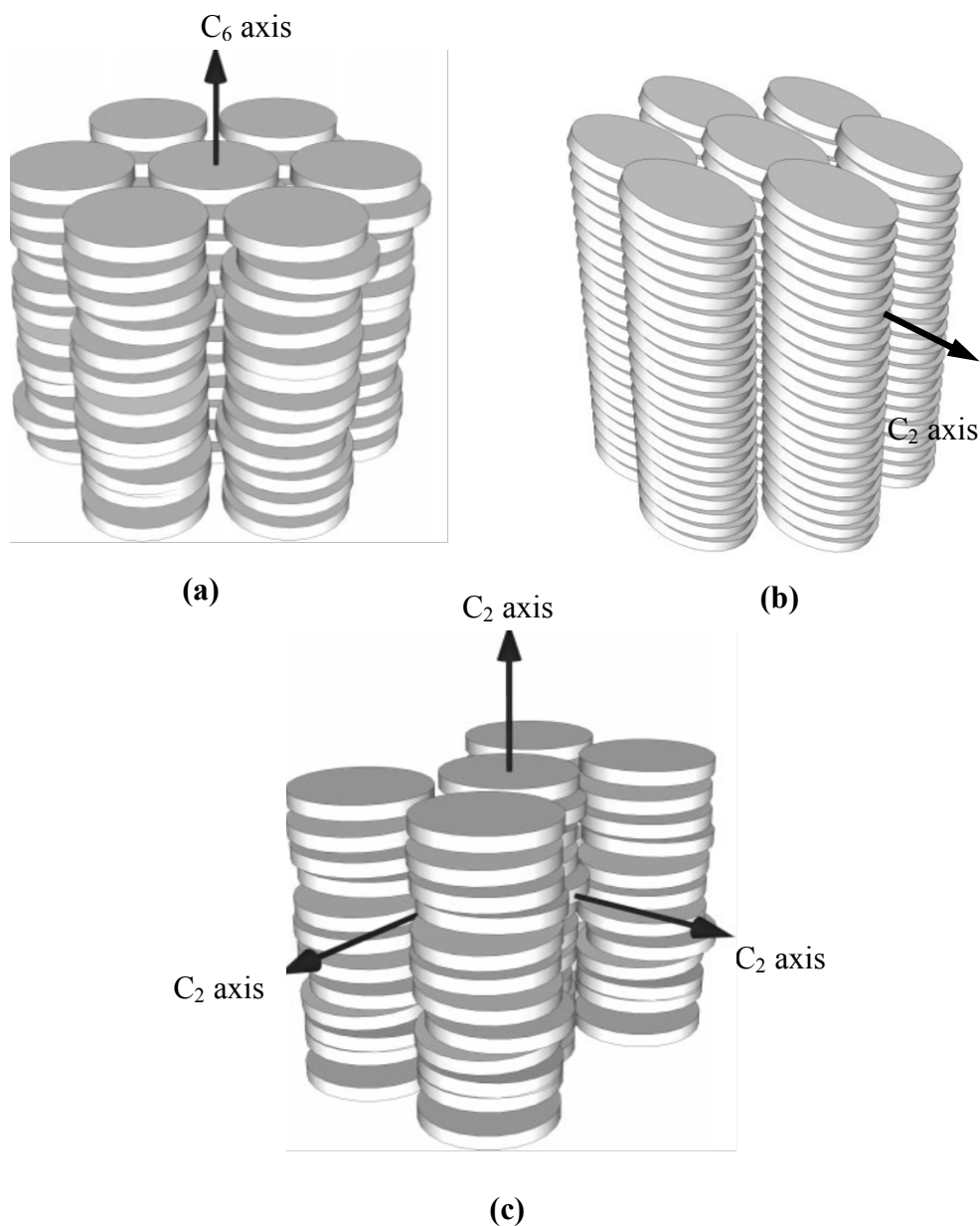


**Figure 1.16** The columnar phases with axis symmetry: **(a)** Hexagonal columnar phase with  $C_6$  axis; **(b)** Tilted hexagonal columnar phase with  $C_2$  axis; **(c)** Rectangular columnar phase with  $C_2$  axis.[35]

### 1.3.3 Important Applications for Discotic Liquid Crystal Mesogens

The properties of discotic liquid crystals have been used in many fields[36], for example, in potential applications of semi-conducting discotic liquid crystals, which is due to charge migration along the columns is much easier than charge

migration column-to-column in columnar phases. Then each column functions as a self-assembled molecular wire and the stack of aromatic cores act like the wire and the annulus of alkyl chains acts like a plastic insulation. These applications include organic field-effect transistors (OFETs)[37], organic light-emitting displays (OLEDs)[38-39], photovoltaic devices (PVDs)[40-41] and light-harvesting systems[42], electronic noses[43], and organic semi-conductors[44]. However, the significant applications for the discotic liquid crystals are as single-layer lubricants for hard-disk drives in computers such as elasto-hydrodynamic lubrication contacts and extreme pressure lubrication contacts[36], and in negative birefringent films for wide viewing angles in displays, which will be discussed more in detail in next subsection.

### **1.3.3.1 Wide Angle Views Films for Displays**

In the 1970's, liquid crystal displays had a constant problem, called the 'angle of view'. The problem was that a good image with true colours could be seen only when sitting directly in front of the screen, otherwise when viewed off-centre there was a loss of image quality and a distortion of the colour balance, see Figure 1.17[45]. In the Figure, the left side of the screen in each case is covered with the WV film but on the right side of the screen is uncovered. The centre image is viewed 'straight on' and other images on edge and corners are viewed tilted from the screen.



**Figure 1.17** The effect by different angle of view for a Fuji WV optical compensating film on a liquid crystal display.[45]

This ‘angle of view’ problem is not merely an inconvenience for most liquid crystal display applications, but for a clear display from all viewing angles is necessary and important. Due to the optically birefringent properties of oriented liquid crystals, the problem, that the loss of image quality when viewed off-centre, is inherent to the uncompensated liquid crystal displays. However, the sign of the optical birefringence for calamitic liquid crystals is positive but that for discotic liquid crystals is negative, if adding a layer of discotic liquid crystals, the birefringence of a calamitic display can effectively be cancelled, as shown in Figure 1.18.

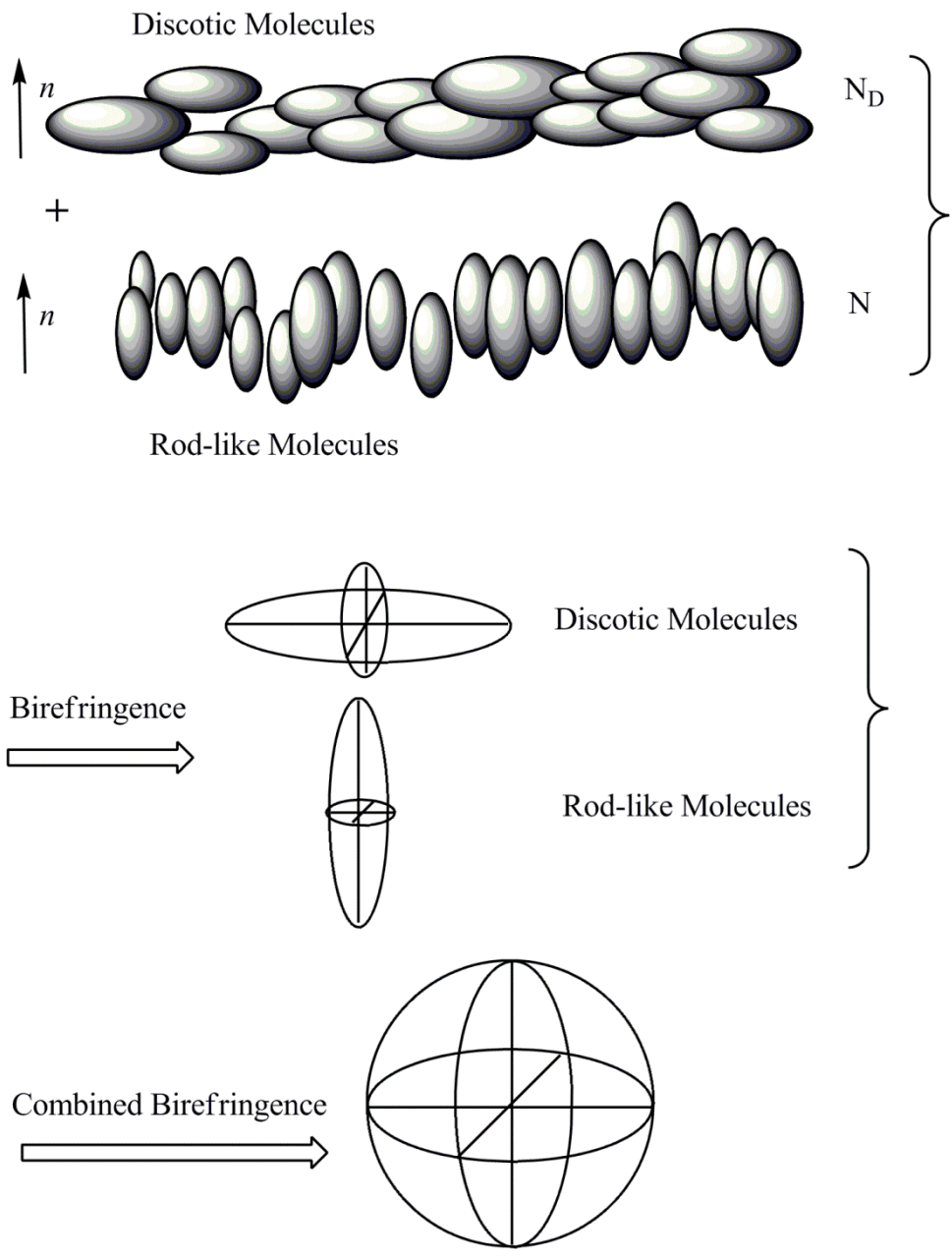


**Figure 1.18** The fixed birefringence of a calamitic liquid crystal display. When the directors  $n$  are aligned, the optical birefringence of the nematic phase of calamitic liquid crystals can be cancelled by a film made by discotic liquid crystals.

However, the problem of compensating the optical birefringence of real displays is a little more complex than that which is shown in Figure 1.18. After many years of research in the 1990s[45-48], the first commercial compensation films of this type were created by the Fuji Photo Film Company[48], which have captured the worldwide market.

Hence, although discotic molecules for discotic liquid crystals are generally too large and the phases are too viscous with poor switching times, and generally are not good candidates for the active ‘switchable’ components of displays, one of the most important applications of discotic liquid crystals is the solution for the problem of ‘angle of view’ to the display industry.

## 1.4 Carbonaceous Liquid Crystals

In the 1960s, J.L. White’s group demonstrated the significance of a mesophase transformation which occurred for structural changes in graphitizable organic materials during pyrolysis at temperatures around 450 °C.[49] They postulated that the mesophase was a two-phase, liquid-state, and the structural transition involved the sheet molecules being aligned in a parallel array to form a liquid crystal. The polarized optical microscopy showing the *schlieren* texture of nematic phase with 2-brush and 4-brush is given in Figure 1.19.



**Figure 1.19** Polarized light micrograph (crossed polarizers) (150 X) of extracted pitch carbonized to 450 °C at approximately 0.4 °C /min.[49]

In addition, several groups[50-53] have researched this mesophase transformation taking place in graphitizable organic materials during carbonization between 350 °C and 500 °C.

Initially, the formation of graphitizing low-temperature carbons by solidification from a liquid phase proceeds *via* the separation of a mesophase having properties similar to those of liquid crystals.[29] Recently, those mesophases were called the *carbonaceous mesophase*. It is an optically anisotropic phase formed by the reactions of thermal cracking and aromatic polymerisation, which orient more or less parallel during the carbonisation of certain graphite organic materials.

## 1.5 Liquid Crystal Mixtures and Formulations

Generally, miscibility is a powerful tool in the study of liquid crystals and for the confirmation of mesophase types. In calamitic systems made by rod-like molecules, miscibility and the use of Gibbs phase diagrams is commonplace. It has led to the formation of eutectic mixtures for wide temperature operating ranges for materials in displays.

Liquid crystal mixtures are created to lower the melting point of liquid crystal phases, to increase the liquid crystal temperature range, or to improve upon the physical properties. Classically, binary and more complex liquid crystal mixtures were prepared using the Schröder-van Laar equation to lower the melting point of liquid crystal materials through the formation of eutectic mixtures, and to increase the liquid crystal phase range for wider operating windows for display applications.

### 1.5.1 Gibbs Phase Diagrams

A phase can be defined as a physically distinct and chemically homogeneous portion of a system possessing a particular chemical composition and structure.[54]

The Gibbs phase rule is expressed as:

$$F = C - P + 2 \quad \text{(Equation 1.7)}$$

Where  $F$  is the number of degrees of freedom, which means the number of independently variable factors,  $C$  is the number of components, and  $P$  is number of phases in equilibrium.

For a one-component system, the simplest is water in liquid state or vapor state, which is single phase system. It is well known for a pressure-temperature (P-T) diagram, two phases exist along each of the three phase boundaries. At low pressure (0.006 atm) and temperature (0.01°C) all the three phases coexist at a point called *triple point* (shown in Figure 1.20).[55] A binary phase is a two component system and a multiple phase means a multiple component system, which are most commonly used for liquid crystal mixture design.

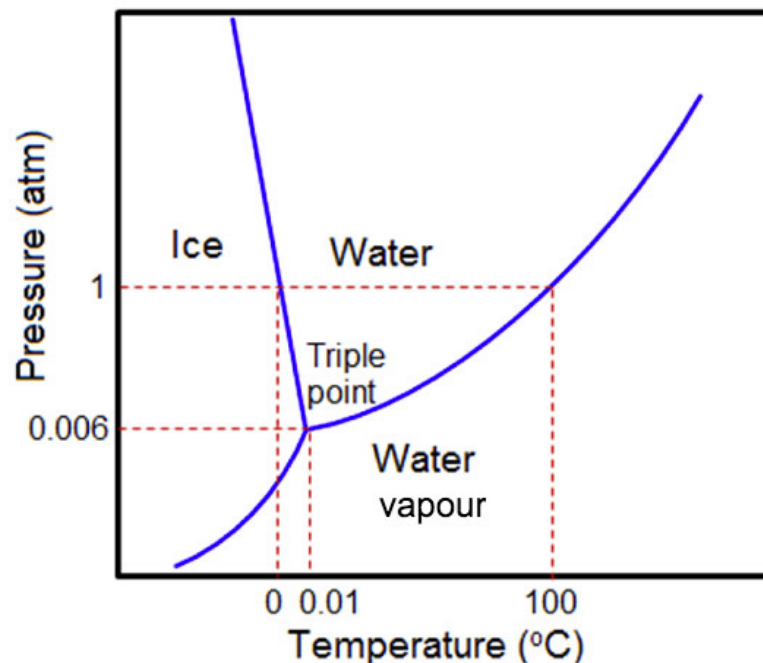


**Figure 1.20** The pressure-temperature phase of water.[55]

In physical chemistry, mixed systems are well known and phase diagrams are commonplace in order to investigate the features of a mixed system. In Figure 1.21, the liquid-solid phase diagram for two-component mixtures for nematogenic liquid crystals shows the relationship between temperature and composition, where the

lowest temperature at the convergent point in the isopleth is called *eutectic* composition.

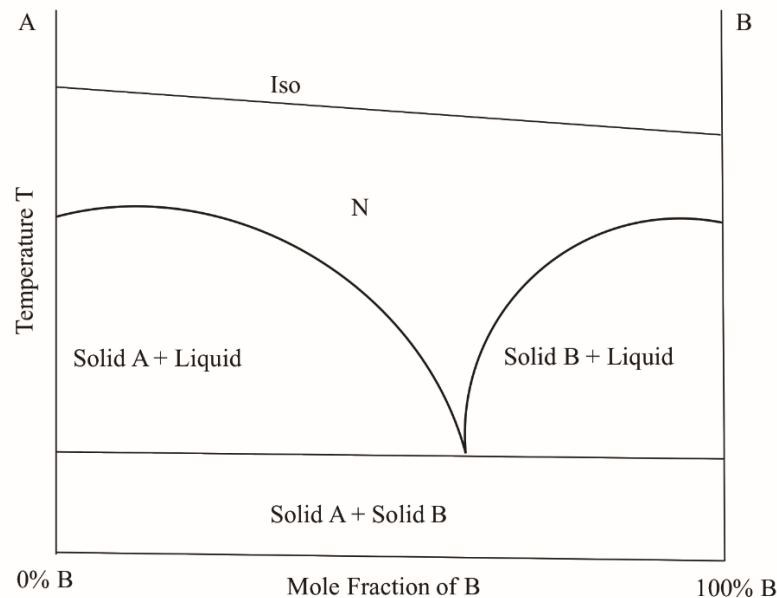


**Figure 1.21** The typical liquid-solid phase diagram for a two-component nematogenic system showing the temperature as a function of composition.

Normally the depression curve on the left related to the melting point depression curve of material A when the concentration of material B in a binary mixture is increased, there is an analogous process for the depression curve on the right. On the other hand, it can also be interpreted as the solubility curve for component A in the liquid solution. As the temperature decreases, the solubility of component A decreases as well. The melting process of a mixture when it is heated up can be regarded as a change in solubility as well, and therefore it is spread over a range of temperature from the eutectic temperature up to the solubility curve. In addition, this spread of temperature decreases as the composition approaches the eutectic composition, where the melting is instantaneous, with no spread in temperature, *i.e.*, the eutectic point has no degrees of freedom.[56]

### 1.5.2 Schröder-van Laar Equation

The Schröder-van Laar equation[57-58] for the ideal behaviour can be written as:

$$\ln(X_i) = \frac{\Delta H_i}{R} \left\{ \frac{1}{T_i} - \frac{1}{T} \right\} \quad (\text{Equation 1.8})$$

where  $X_i$  is the mole fraction at temperature  $T$  in an ideal solution referring to the solubility of component  $i$ ,  $\Delta H_i$  is the latent heat of melting enthalpy, and the melting point  $T_i$  of pure component  $i$ .

For the mixture with eutectic composition, Equation 1.8 can be used to predict all the components simultaneously, and

$$\sum_{i=1}^N X_i = 1 \quad (\text{Equation 1.9})$$

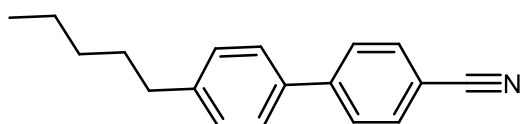
The results predicted by Equation 1.8 only depend on the properties of that particular component; however, it is independent of the other components present in the solution. This is known as *ideal behaviour*. However, the departures from ideality always can be seen in liquid crystals mixtures, even in simple binary mixtures.

When preparing the mixtures for liquid crystal systems, the Schröder-van Laar equation is commonly used to predict the eutectic mixture, which has the lowest melting point, by using the enthalpies of the melting process, the melting point, and the clearing point of the each of the mixture systems.

### 1.5.3 Mixture Systems of Liquid Crystals

Liquid crystal materials used in the display industry are usually multi-component eutectic mixtures.[59] For calamitic liquid crystal systems, miscibility and the formation of Gibbs phase diagrams is common place and for these systems the behaviour is generally predictable and well understood. The mixtures based on calamitic liquid crystals made of rod-like molecules often contain cyanobiphenyl

liquid crystals (nCB series)[60-66], such as 4-cyano-4'-pentylbiphenyl (**5CB**), shown in Figure 1.22. In addition, many investigations of calamitic liquid crystal systems contain E7[66-69], which is a eutectic mixture, offering a wide range of operating temperatures for applications in display devices[70]. On the other hand, computer modelling and simulations[59, 71-72] have also been investigated in recent years.



**5CB** K 18 N 35 °C Iso Liq

**Figure 1.22** The chemical structure and phase transitions of **5CB**.

However, for the miscibility of discotic molecules, there is still less knowledge and seldom in results are published. In 1979, Billard's group investigated the miscibility of the BHA series compounds (structure shown in Figure 1.4, section 1.3, pp 9), but they did not find miscibility in a mesophase for two component systems of two different discotic series, and the existence of different mesophase types in three or more series was not observed.[73] However, at the time there were no molecular dynamics or computer simulation studies about mixtures based on disc-like liquid crystals.[74-76]

## 1.6 Techniques in the Study of Liquid Crystals

There are various liquid crystal phases exhibited by many, many varieties of materials, thus the mesophases are characterised and classified according to the molecular ordering of the structures of the phases. However, there is not big difference among some mesophases with respect to structures. It does mean that these kind of minimal differences in structure require analytical techniques for the precise classification of liquid crystals.

The techniques relevant to a wide range of scientific areas are the major methods used to characterise and identify liquid crystalline phases, which are important for working in any discipline of the wider field of liquid crystals. The techniques include Polarized Optical Microscopy (POM), Differential Scanning Calorimetry (DSC), X-ray Diffraction, and computer modelling methods (Density functional theory (DFT)). These will be discussed in the following subsections.

### 1.6.1 Polarized Optical Microscopy (POM)

The polarised optical microscopy (POM) is an important diagnostic tool used in the analysis of liquid crystals. It is used to classify types of liquid crystals and other mesophases *via* the identification of the optical textures generated and to evaluate the physical properties of those phases when they are in some particular temperature range or sample preparation. For liquid crystals, when the molecules are allowed to self-organise usually some defects are produced in the process. When they are observed by polarized optical microscopy the defects produce classical optical textures (patterns), which allow for characterisation and identification of mesophases by the trained eye. For example, Figure 1.23 shows the defects formed in the nematic phase with 4-brush by a discogen. As shown in the *schlieren* texture illustrated in the micrograph, the dark lines run throughout the sample and join together as brushes around a defect site (usually a singularity).

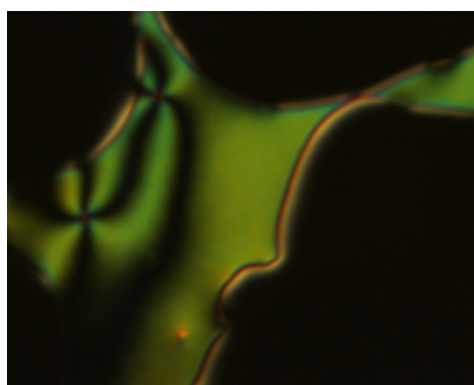
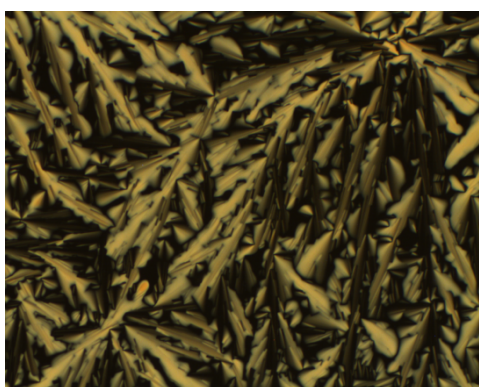


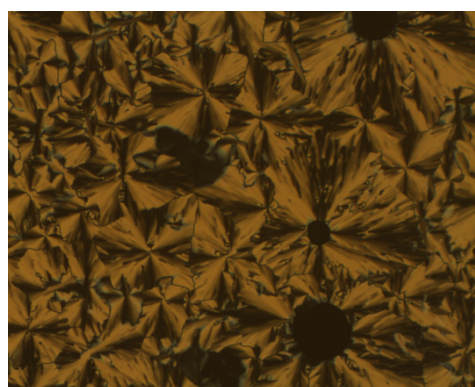
**Figure 1.23** A micrograph (x100) showing the 4-brush defects in the nematic phase of a discogen.

Generally, liquid crystals are prepared as a sandwich between a microscope slide and a coverslip. In this preparation for calamitic, rod-like liquid crystals, the molecules can take orientation either parallel to the glass plane or perpendicular to the plane of the slide. When they are in the parallel orientation, it is called as *homogeneous* orientation, conversely, when they are in the perpendicular orientation, it is called as *homeotropic* orientation.

However, for discotic liquid crystals, the orientations for those columnar phases are not so distinct as those for calamitic phases. For example, the most common hexagonal columnar phase, where the molecules are organised in columns and the columns are close packed hexagonally. For this phase the defects are commonly observed as spine-like defects (shown in Figure 1.24), occurring between two homeotropic domains[77].

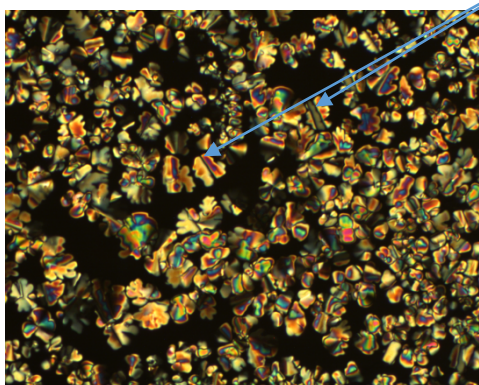


Compound 2, Col<sub>h</sub>

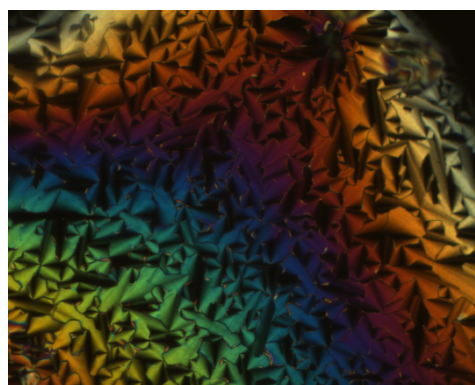


Compound 2, Col<sub>h</sub>

Spine-like defects



Compound 21, Col<sub>h</sub>



Compound 32, Col<sub>h</sub>

**Figure 1.24** Micrographs (x100) showing typical optical textures of columnar hexagonal phases formed by various discotic liquid crystal materials.

### 1.6.2 Differential Scanning Calorimetry (DSC)

Differential Scanning Calorimetry (DSC) is a significant tool in the analysis of liquid crystals *via* detecting the enthalpy change associated with each phase transition, which indicates the presence of a phase transition in a material. Actually, using this technique, it only can investigate the level of enthalpy change that is involved during the phase transition, but it cannot give the precise identity of a mesophase. However, the level of enthalpy change does provide some indication of the types of phases present, for instance through determining the order of the phase transition, for example, SmA to SmC is usually a second-order phase

transition. Thus this method is often used in conjunction with polarised optical microscopy to determine those mesophases.

Naturally, when a material melts, it requires energy to change the state from a solid to a liquid, thus it is endothermic from the surroundings. Conversely, when it crystallizes, it will release the energy to the surroundings and it is exothermic. As the DSC instrument measures the energy absorbed or released by a sample when it heated or cooled, it can detect different phase transitions. For example, the melting transition from a solid to a liquid is a relatively energetic transition due to the collapse in the lattice, which is reflected by the relatively high enthalpy change in the DSC. This means the magnitude of the enthalpy change is related to the degree of change in the molecular ordering at the phase transition.

The DSC instrument is precalibrated with a sample of known enthalpy of transition and this enables the enthalpy of transition to be recorded for the material being examined relative to a standard (usually indium).[78] The sample (usually 1 to 2 mg) to be investigated is weighed into a small aluminium pan and sealed by crimping with an aluminium top. Then the sample pan is placed into a holder in a large aluminium block to ensure good temperature control and in the dry nitrogen atmosphere. Also the sample can be cooled using liquid nitrogen, and the working temperature range can be from -180 to 600 °C if needed. The latest DSC equipment can also detect remarkably small enthalpy values.

Generally, there are two types of phase transition; discontinuous (called first order) and continuous (called second order). The thermodynamics of the phase transition explains the difference between these two types of phases. The Gibbs free energy ( $G$ ) is defined as:

$$G = H - TS \quad \text{(Equation 1.10)}$$

Where  $H$  is the enthalpy,  $T$  is the absolute temperature and  $S$  is entropy. The pressure is constant.

The first derivative of  $G$  with respect to  $T$  gives the negative of the entropy, it can be written as:

$$\left(\frac{dG}{dT}\right)_p = -S \quad (\text{Equation 1.11})$$

The second derivative is related to the heat capacity at constant pressure, it can be written as:

$$\left(\frac{d^2G}{dT^2}\right)_p = -\frac{C_p}{T} \quad (\text{Equation 1.12})$$

As a consequence, if the entropy at a phase transition shows a discontinuity, then it is a first order phase transition, otherwise in some cases, where there is no change in entropy and enthalpy, there is a discontinuity in the second derivative and a second order phase transition results. For example, most liquid crystal to liquid crystal phase transitions are first order phase transitions but with the exception such as smectic C phase to smectic A phase transition as noted earlier.

The DSC may reveal the presence of a phase transition at a particular temperature which is missed by polarised optical microscopy, on the other hand microscopy may indicate the presence of a phase transition when the enthalpy change is tiny and cannot be detected in the DSC. Therefore, these two techniques are always used in combination.

### **1.6.3 X-ray Diffraction (XRD)**

As most liquid crystal phases have a small number of diffraction peaks, and as it is difficult to obtain well-oriented defect-free single domain samples, the standard structural analysis techniques such as X-ray crystallography are hard to apply in the structural analysis of liquid crystals.[79] Consequently, X-ray diffraction (XRD) is usually applied to the determination of their structural properties, and to obtain static and dynamic information of their structures, orientational and

positional order parameter (OPs), and order fluctuations (*i.e.* PO correlations). Many researchers have investigated the basic theory and description of XRD pertaining to liquid crystals systems. [80-85]

The well-known Bragg's law forms the basic theory of XRD as an experimental technique for structure determination, which indicates that constructive interference, between the X-rays reflected by adjacent planes which are separated by a distance  $d$  in a crystal, will occur when the path differences are integers.[79] It is an integral multiple of the X-ray wavelength,  $\lambda$ , between them,  $2d\sin\theta$ , which can be written as:

$$2d \sin \theta = n\lambda \quad (\text{Equation 1.13})$$

Where,  $\theta$  is the angle of incidence of the X-rays, which is illustrated schematically in Figure 1.25, with  $n$  is an integer.

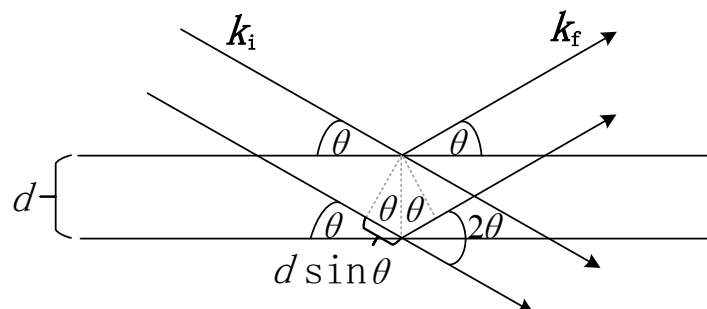


**Figure 1.25** The X-ray diffraction from a set of parallel crystal planes separated by distance  $d$ .

The Bragg's law can also be expressed in terms of the scattering vector  $\vec{q}$ , which can be written as:

$$|\vec{q}| = |\vec{k}_i - \vec{k}_f| = \frac{(4\pi \sin \theta)}{\lambda} \quad (\text{Equation 1.14})$$

Where  $k_i$  and  $k_f$  are the incident and scattered X-ray wave vectors respectively as shown in Figure 1.26. The magnitudes of  $k_i = k_f = 2\pi/\lambda$  are related to the scattering, which is elastic. The scattered intensity  $I(\vec{q})$  is zero except when

Bragg's law is satisfied. The direction of propagation of X-rays suffers a net change by an angle of  $2\theta$  during scattering.

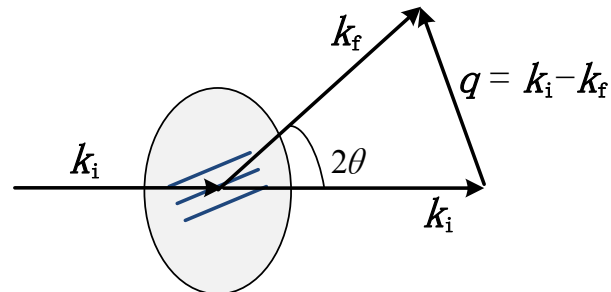
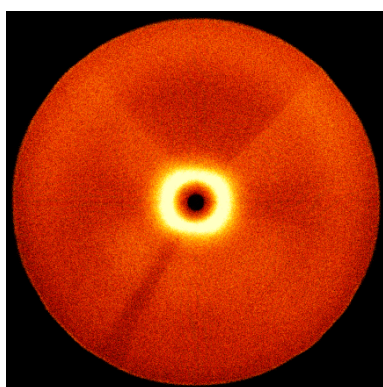


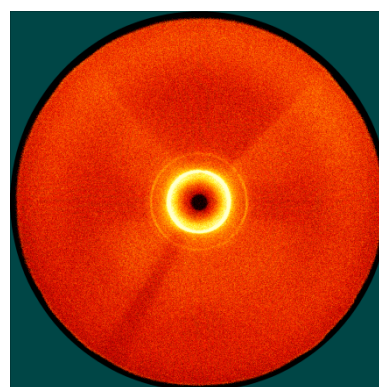
**Figure 1.26** The X-ray diffraction suffering a net change by an angle of  $2\theta$  during scattering.

The X-ray diffraction experiments from liquid crystals require special sample handling and conditioning techniques, which is somewhat difficult to perform and less-straight forward to analyze, because liquid crystals often exhibit weak and broad peaks that are smaller in number than the reflections from typical crystalline solids. In order to obtain diffraction patterns for qualitative analysis, unaligned liquid-crystalline samples can be used, which is equivalent to a powder sample.[79] Therefore, only circular rings in the diffraction pattern are obtained in the results.

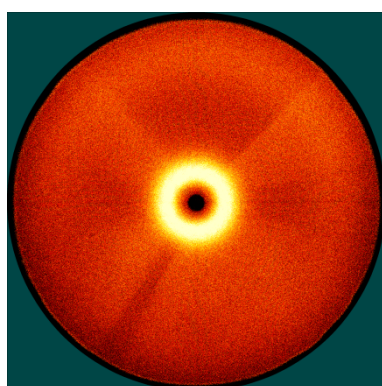
In these powder diffraction experiments, the diffraction angle and the width of the rings are obtained to distinguish different mesophases (*i.e.* shown in Figure 1.27 and Figure 1.28).



Compound 4, N



Compound 4, K



Compound 4, Iso Liq

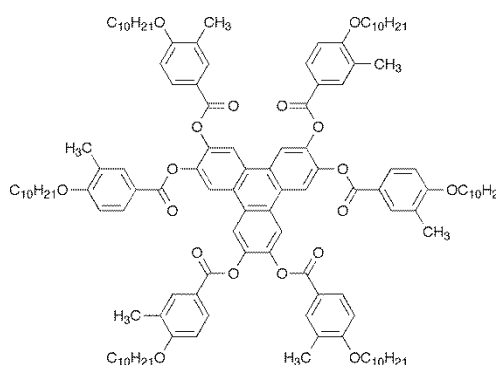
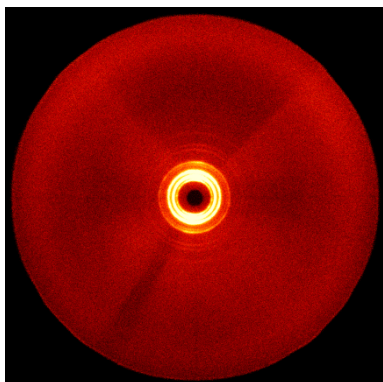


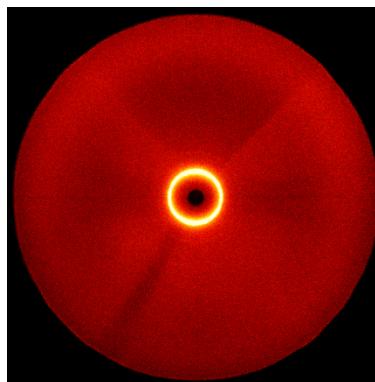
**Figure 1.27** The X-ray pattern illustrated the different phases obtained by compound 4.

As shown in Figure 1.27, the nematic phase is randomly oriented of the symmetry axis thus from the X-ray pattern for nematic phase, it reveals that two diffuse rings, one in the small-angle and the other in the wide-angle region, and it is somewhat similar as shown in the X-ray pattern for isotropic liquid. Whereas in Figure 1.28, it indicates that X-ray pattern for hexagonal columnar phase where the diffuse ring in the central is sharper compared with the nematic ring. In this figure, the crystal phase shows a number of sharp rings, which are due to reflections from a lattice. The liquid just shows a diffuse pattern indicating that the molecules are disordered. The intermediary hexagonal phase shows a number of diffuse rings that are related to the hexagonal ordering of the columns. The relationships between the d spacings

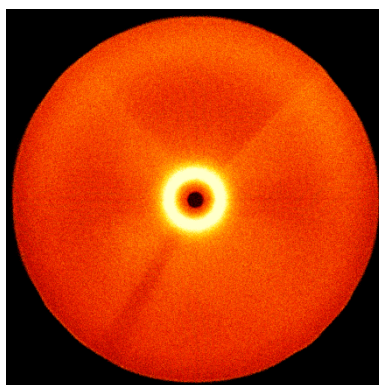
of the rings in this phase are specific for the hexagonal structure, and their diffuse nature indicates that the columns are not packed together in a fully crystalline way.



Compound **32**, K



Compound **32**, Col<sub>h</sub>



Compound **32**, Iso Liq

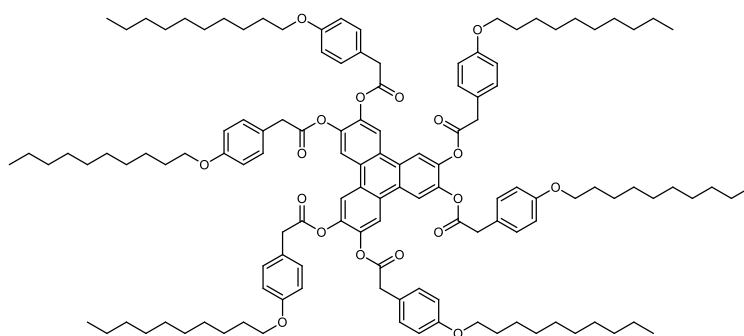


**Figure 1.28** The X-ray pattern illustrated the different phases obtained by compound **32**.

#### 1.6.4 Density functional theory (DFT)

Typically, density functional theory (DFT) is a computing modelling method used to investigate the electronic structure of the molecules. In many-body electronic structure calculations the nuclei of molecules are fixed generating a static external potential  $V$ , in which electrons move, and a stationary electronic state that is described by a wave function fulfilling the many-body Schrödinger equation which has an influence on the electron-electron terms of interaction.

However, the density functional theory provides a way to avoid a single-body problem that is without the electron-electron interaction terms of the many-body problem. In this theory, the key variable is the particle density,  $n(\vec{r})$ , which can be calculated by Kohn-Sham equation for an auxiliary non-interacting system, and the problem of solving the Kohn-Sham equation has to be done in a self-consistent (*i.e.* iterative) way. Then from these one calculates a new density and it starts again, additionally, this procedure is then repeated until convergence is reached.[86]

## **Chapter 2: Aims**

## Chapter 2: Aims

### 2.1 General Aims

The aims of the project are to examine the thermodynamic properties and miscibility of discotic liquid crystals that have structural features in common with hard discs, and also to use the self-organizing and self-assembling capabilities of the liquid crystals to organize small fragments of disc-like molecules such as triphenylene and coronene. The project was broken down into three distinct parts - the first part was to investigate the binary mixing properties of polyaromatics such as triphenylene, perylene, coronene, and truxene, see Figure 2.1, and to explore their self-assembly, see Figure 2.2, and the potential for determination of the virtual N-I phase transition temperatures for polyaromatics; and use these systems to produce carbonaceous liquid crystals.

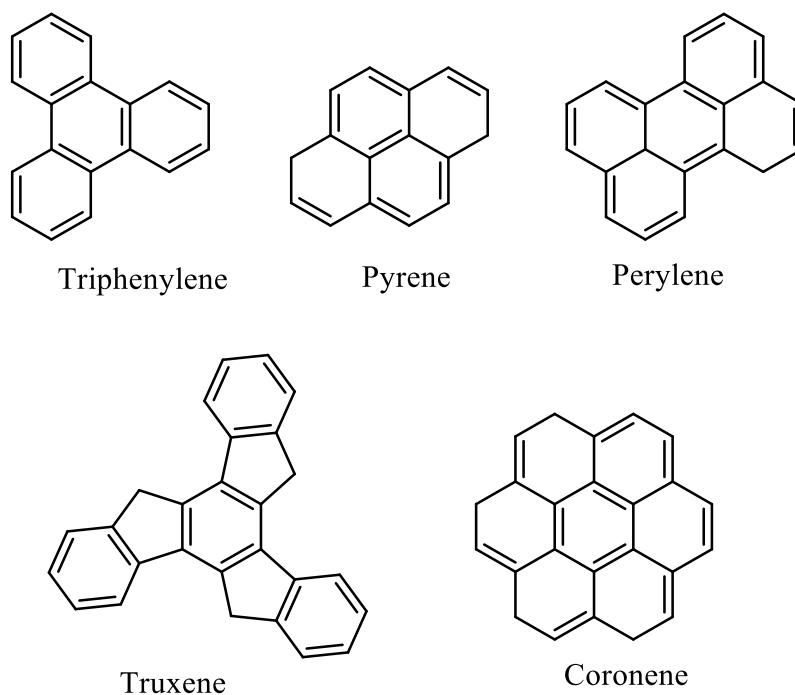


**Figure 2.1** The chemical structures of polyaromatics.

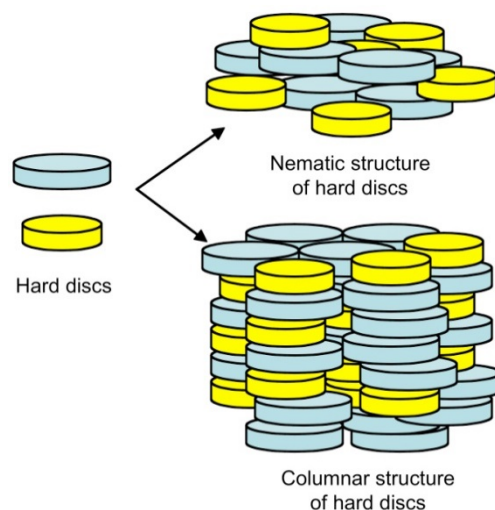


**Figure 2.2** Potential phases formed by mixtures of hard disc-like molecules.

The second part of the project focuses on the investigation of the miscibility of nematic disc-like amphiphiles where amphiphiles in this thesis means disc-like systems composed of rigid-aromatic cores (polarisable) and segregation flexible aliphatic periphery (non-polarisable) of differing structures with each other, and this will include mixing materials with the same or different mesomorphism, as shown in Figure 2.3. Blue and yellow molecules are different amphiphiles that may be different in core types or chain-lengths.

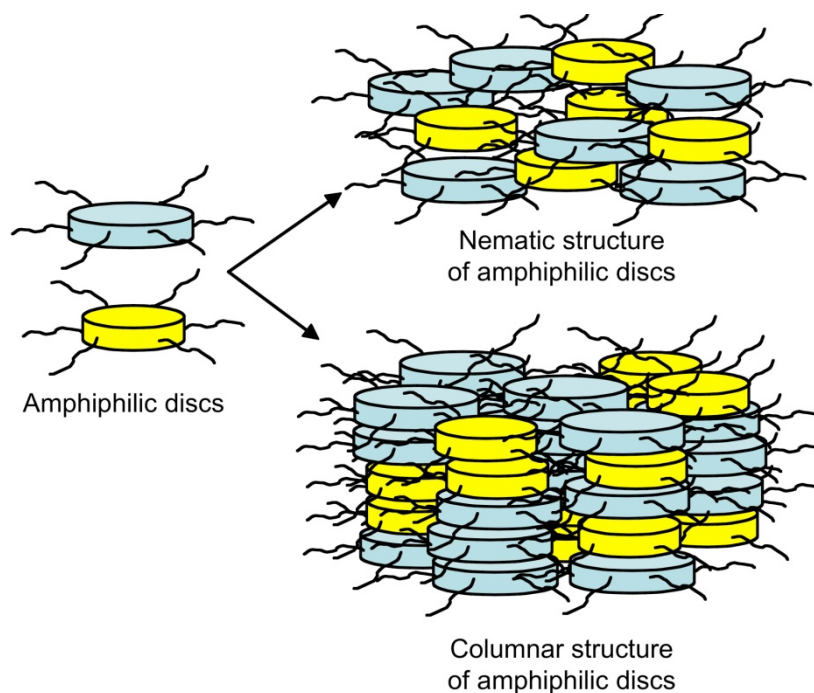


**Figure 2.3** Mixtures of disc-like molecules that have soft structure and an amphiphilic structure.

The final stage of the project involves the investigation of the miscibility of columnar discotic liquid crystals with each other or with different mesophases in differing structures. The portion of the co-miscibility work targets on the development of structure-property correlations and the investigation of eutectic mixtures based on Gibbs phase diagrams. Both of these parts of the project have not been attempted previously and therefore represent novel studies. These studies will use polarised optical microscopy and calorimetry techniques to investigate the mixtures.

## 2.2 Target Systems for Study

### 2.2.1 Polyaromatics

As simple discotic materials such as triphenylene, truxene, coronene are non-mesogenic, unlike simple rod-like molecules such as *p*-sexiphenyl,[87] and the mesophase transformation taking place in polyaromatics during carbonization at

high temperatures between 350-450 °C has been found in 1960s-1970s.[49-50, 53] Thus for the investigation for polyaromatics, the attempt is based on examination of polyaromatics, to determine the clearing points for selected polyaromatics, and to explore N-I phase transition temperatures for the polyaromatics as a function of disc size, as well as to achieve a carbonaceous liquid crystal phase by mixing the polyaromatics at lower temperatures than the high temperatures between 350-450 °C. In this section, differential scanning calorimetry (DSC) is to be used for the determination of the clearing points, and polarized optical microscopy will also be used for the investigation of mixtures by different polyaromatics. In addition, the binary Gibbs phase diagram of discotic liquid crystals and polyaromatics is an attempt to investigate for exploration an N-I phase transition temperature for non-mesogenic polyaromatics, therefore the miscibility studies of discotic liquid crystals and polyaromatics are essential for these studies. It should be noted that little research on the co-miscibility between disc-like materials has been reported for discotic mesophases.[88]

### **2.2.2 Mixture Studies**

As mentioned in the previous section, there are very few intensive investigations on the miscibility behaviour and thermodynamics of discotic liquid crystals, whereas for the co-miscibility of calamitic systems made of rod-like molecules the process and investigations are relatively well understood by using the construction of Gibbs phase diagrams and the determination of eutectic behaviour of Schröder-van Laar Equation. Thus in this section, these methods are also used for the examination for discoidal liquid crystals. As the most common phases for discotic liquid crystals are the nematic and columnar phases, the co-miscibility investigations were split into two based on nematics and columnars. For the disc-like nematic mesogens, miscibility studies and binary phase diagrams will be developed in order to examine how well fluid-like mesophases will mix. On the other hand, the mixing of materials that exhibit columnar phases will be examined in order to investigate how such systems with potentially 2D crystal structures might mix together or phase segregate. These studies will ultimately provide insights into the nature of crystallinity versus true liquid-crystallinity. In this part,

the mixtures of triphenylene derivatives (disc-like), benzoate esters (rod-like), and phenyl alkynes (disc-like) with different or similar mesophases are selected for investigation, see Figure 2.4, and the resulting phase diagrams will be created and discussed.

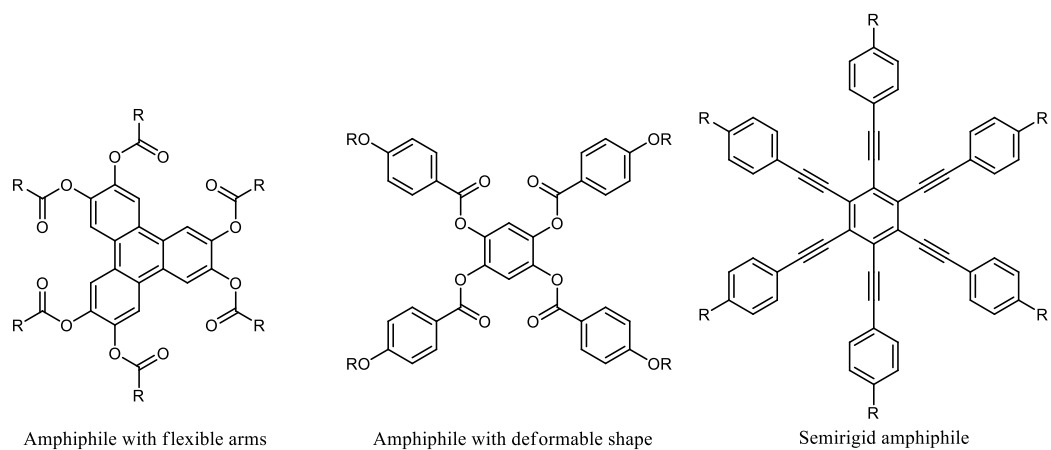


**Figure 2.4** Typical chemical structures of amphiphiles selected for investigation.

## **Chapter 3: Experimental**

## Chapter 3: Experimental

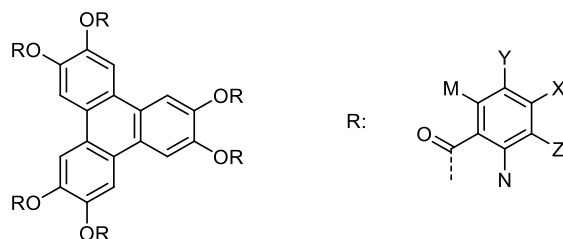
### 3.1 Materials, Reagents and Solvents

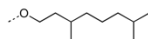
All the starting materials were bought from Sigma-Aldrich, TCI-UK, Fischer and other scientific brands; they were used without any further purification. All the discotic compounds were obtained from the Advanced Materials Groups of the Universities of York and Hull for BDH Chemicals, and used without purification. All the solvents were obtained from Fischer and used without purification.

#### 3.1.1 Experimental of Existing Materials for Mixture Studies

A wide range of existing materials were available for mixture studies and they were examined by polarized optical microscopy and differential scanning calorimetry, based on the Liqcryst 4.6 database. The structures, phase transition temperatures, and mesophases of the triphenylene derivatives **1-34** are shown in Table 3.1 and Table 3.2. Table 3.3 shows the structures, phase transition temperatures, and mesophases of the phenyl hexa-esters. Table 3.4-3.8 shows the structures, phase transition temperatures, and mesophases of the benzoate esters. Table 3.9 shows the structures, phase transition temperatures and mesophases of the phenyl hexa-alkynes. The enthalpies of the melting process for all the materials **1-64** are shown in Table 3.10. The errors of the temperatures are  $\pm 0.1$  °C.

**Table 3.1** The structures, phase transition temperatures (°C) and mesophases of the triphenylene benzoate hexa-esters.



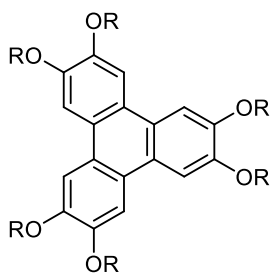
Sample Number	Structure					Transition temperatures/ °C
	X	Y	Z	M	N	
<b>3</b> [90]	OC <sub>7</sub> H <sub>15</sub>	H	H	H	H	K 163.0 N 174.0 Iso
<b>24</b> [90]	OC <sub>8</sub> H <sub>17</sub>	H	H	H	H	K 147.5 Col <sub>h</sub> 165.8 N 238.1 Iso
<b>8</b> [89]	OC <sub>10</sub> H <sub>21</sub>	H	H	H	H	K 191.0 N 212.0 Iso 214.0
<b>21</b>		H	H	H	H	K 128.2 Col <sub>h</sub> 208.4 Iso
<b>23</b> [90]	OC <sub>6</sub> H <sub>13</sub>	CH <sub>3</sub>	H	H	H	K 217.9 (Col <sub>h</sub> 167.0) N 230.0 Iso
<b>25</b> [90]	OC <sub>8</sub> H <sub>17</sub>	CH <sub>3</sub>	H	H	H	K 150.0 N 218.6 Iso
<b>4, 9</b> [89]	OC <sub>10</sub> H <sub>21</sub>	CH <sub>3</sub>	H	H	H	K 123.0 N 192.0 Iso
<b>13</b> [89]	OC <sub>10</sub> H <sub>21</sub>	Et	H	H	H	K 134.0 N 206.3 Iso

<b>15</b> [89]	OC <sub>10</sub> H <sub>21</sub>	tBu	H	H	H	K 194.0 N 225.0 Iso
<b>14</b> [89]	OC <sub>10</sub> H <sub>21</sub>	iPr	H	H	H	K 160.0 N 204.6 Iso
<b>30</b>	OC <sub>10</sub> H <sub>21</sub>	CF <sub>3</sub>	H	H	H	Not melted at 280.0 °C
<b>29</b>	OC <sub>10</sub> H <sub>21</sub>	F	H	H	H	K 200.7 Col <sub>h</sub> 222.9 Iso
<b>31</b>	OC <sub>10</sub> H <sub>21</sub>	Cl	H	H	H	Decomposed
<b>19</b> [90]	OC <sub>12</sub> H <sub>25</sub>	CH <sub>3</sub>	H	H	H	K 126.0 N 166.9 Iso
<b>5</b> [90]	OC <sub>6</sub> H <sub>13</sub>	CH <sub>3</sub>	CH <sub>3</sub>	H	H	Decomposed
<b>6</b> [91]	OC <sub>8</sub> H <sub>17</sub>	CH <sub>3</sub>	CH <sub>3</sub>	H	H	K 155.0 N 169.9 Iso
<b>7</b> [89]	OCH(CH <sub>3</sub> ) C <sub>6</sub> H <sub>13</sub>	CH <sub>3</sub>	CH <sub>3</sub>	H	H	K 151.0 N 184.3 Iso
<b>22</b> [91]	OC <sub>6</sub> H <sub>13</sub>	H	H	CH <sub>3</sub>	H	K 170.8 N 225.0 Iso
<b>26</b> [91]	OC <sub>8</sub> H <sub>17</sub>	H	H	CH <sub>3</sub>	H	K 126.0 N 198.0 Iso
<b>1, 12</b> [89]	OC <sub>10</sub> H <sub>21</sub>	H	H	CH <sub>3</sub>	H	K 107.5 N 164.0 Iso
<b>10</b> [89]	OC <sub>10</sub> H <sub>21</sub>	H	H	Et	H	K 117.0 N 131.8 Iso

<b>11</b> [89]	OC <sub>10</sub> H <sub>21</sub>	H	H	iPr	H	K 92.0 (N 73.2) Iso
<b>27</b>	OC <sub>10</sub> H <sub>21</sub>	H	H	F	H	K 158.8 N 184.4 Iso
<b>20</b> [91]	OC <sub>12</sub> H <sub>25</sub>	H	H	CH <sub>3</sub>	H	K 104.9 N 132.0 Iso
<b>16</b> [91]	OC <sub>6</sub> H <sub>13</sub>	H	H	CH <sub>3</sub>	CH <sub>3</sub>	K 170.0 N 195.9 Iso
<b>17</b> [91]	OC <sub>8</sub> H <sub>17</sub>	H	H	CH <sub>3</sub>	CH <sub>3</sub>	K 152.1 N 169.6 Iso
<b>28</b>	OC <sub>10</sub> H <sub>21</sub>	H	H	F	F	K 137.1 Iso
<b>18</b> [91]	OC <sub>12</sub> H <sub>25</sub>	H	H	CH <sub>3</sub>	CH <sub>3</sub>	K 87.1 N 98.7 Iso

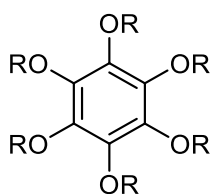
All the results shown in Table 3.1 were examined and analysed by POM and DSC before use. The results for the referenced materials are broadly in an agreement with those materials results in the reference[88]. For compounds not having their transition temperatures reported in the literature, the results shown are a result of the research provided by this thesis.

**Table 3.2** The structures, phase transition temperatures (°C) and mesophases of the triphenylene derivatives.



Sample Number	R	Transition temperatures/ °C
2 [90]		K 78.0 Col <sub>h</sub> 104.9 Iso
32		K 113.0 Col <sub>h</sub> 180.4 Iso
33		K 75.0 Iso

**Table 3.3** The structures, phase transition temperatures (°C) and mesophases of the benzoate hexa-esters.

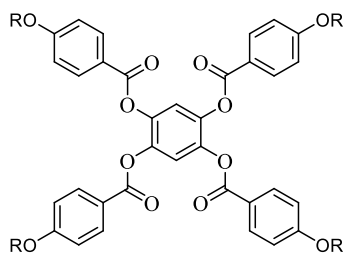


Sample Number	R	Transition temperatures/ °C
35[12]	COC <sub>5</sub> H <sub>11</sub>	K 94.4 Iso
36[12]	COC <sub>7</sub> H <sub>15</sub>	k 81.3 Col <sub>r</sub> 84.0 Iso

All the results shown in Tables 3.2 and 3.3 were investigated and analysed by POM and DSC before use. Because the compounds in Tables 3.2 do not have their transition temperatures reported in the literature, the results shown are a result of

the research provided by this thesis. The results of compound of compound **35** do not have a liquid phase and do not agree in the reference, thus it do not been used for the mixture studies.

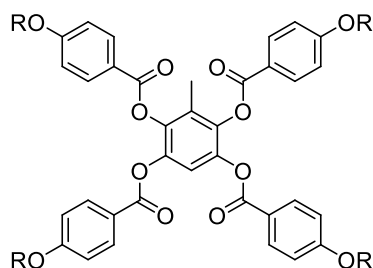
**Table 3.4** The structures, phase transition temperatures (°C) and mesophases of the tetra-benzoate esters.



Sample Number	R	Transition temperatures/ °C
<b>46</b> [92]	C <sub>4</sub> H <sub>9</sub>	K 122.0 N 126.0 Iso
<b>58</b> [92]	C <sub>6</sub> H <sub>13</sub>	K 132.8 (107.5 N) Iso
<b>56</b> [92]	C <sub>8</sub> H <sub>17</sub>	K 109.2 (105.0 N) Iso
<b>60</b> [92]	C <sub>9</sub> H <sub>19</sub>	K (101.2 N) 102.6 Iso
<b>38</b> [92]	C <sub>10</sub> H <sub>21</sub>	K 91.4 N 103.0 Iso
<b>59</b> [92]	C <sub>11</sub> H <sub>23</sub>	K (79.9 SmC) 98.4 N 101.5 Iso
<b>52</b> [92]	C <sub>12</sub> H <sub>25</sub>	K (88.6 SmC) 99.8 N 102.1 Iso
<b>61</b> [92]	C <sub>13</sub> H <sub>27</sub>	K (93.3 SmC) 95.5 N 100.0 Iso
<b>54</b> [92]	C <sub>14</sub> H <sub>29</sub>	K 97.8 SmC 98.3 N 100.0 Iso
<b>57</b> [92]	C <sub>15</sub> H <sub>31</sub>	K 96.3 SmC 100.1 Iso
<b>53</b> [92]	C <sub>16</sub> H <sub>33</sub>	K 97.9 SmC 102.5 Iso
<b>45</b> [92]	C <sub>18</sub> H <sub>37</sub>	K 98.2 N 102.1 Iso

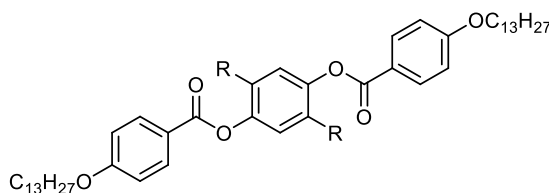
All the results shown in Table 3.4 were examined and analysed by POM and DSC before use. The results for the referenced materials are broadly in an agreement with those materials results in the reference paper[89].

**Table 3.5** The structures, phase transition temperatures ( $^{\circ}\text{C}$ ) and mesophases of the tetra-benzoate esters.



Sample Number	R	Transition temperatures/ $^{\circ}\text{C}$
47	$\text{C}_7\text{H}_{15}$	K 126.5 Iso
48	$\text{C}_{10}\text{H}_{21}$	K (98.0 N) 105.2 Iso
51	$\text{C}_{13}\text{H}_{27}$	K (93.8 N) 102.6 Iso

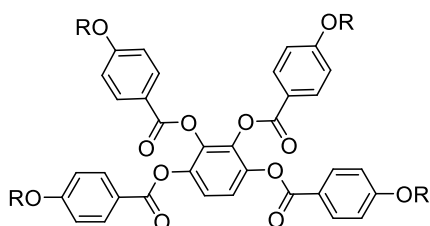
**Table 3.6** The structures, phase transition temperatures ( $^{\circ}\text{C}$ ) and mesophases of the benzoate esters.



Sample Number	R	Transition Temperature/ $^{\circ}\text{C}$
42[93]		K (101.8 SmC) 106.0 Iso
55		K 105.6 Iso

All the results shown in Tables 3.5 and 3.6 were investigated and analysed by POM and DSC before use and they are a result of the research provided by this thesis (except compound **42**, whose result is broadly agreed with the reference), for the compounds do not having their transition temperatures reported in the literature.

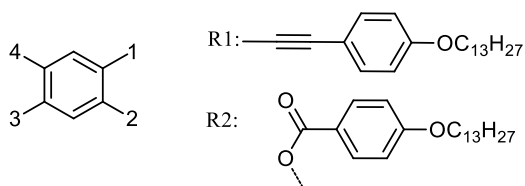
**Table 3.7** The structures, phase transition temperatures (°C) and mesophases of the tetra-benzoate esters.



Sample Number	R	Transition temperatures/ °C
<b>49</b>	C <sub>7</sub> H <sub>15</sub>	K 66.7 Iso
<b>50</b>	C <sub>10</sub> H <sub>21</sub>	K 55.0 Iso

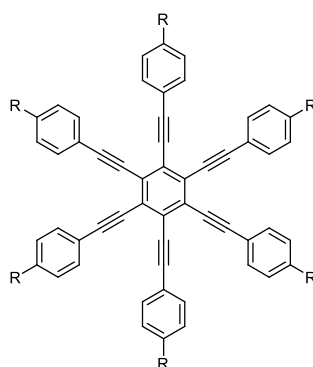
In Tables 3.7, all the results were investigated and analysed by POM and DSC before use and they are a result of the research provided by this thesis, because of the compounds not having their transition temperatures reported in the literature.

**Table 3.8** The structures, phase transition temperatures (°C) and mesophases of the benzoate esters.



Sample Number	Structure				Transition temperatures /°C
	1	2	3	4	
37[93]	R1	R1	R2	R2	K (74.1 SmC) 74.9 N 88.9 Iso
39[93]	R1	R1	R1	R1	K 96.0 Iso
40[93]	R2	R1	R1	R2	K (102.6 N) 104.5 Iso
41[93]	R1	R2	R1	R2	K (97.0 N) 108.0 Iso
43[93]	R1	R2	R2	R2	K 84.0 SmC 90.0 N 100.1 Iso
44[93]	R1	R1	R1	R2	K (66.1 SmC) 72.3 N 86.8 Iso

**Table 3.9** The structures, phase transition temperatures (°C) and mesophases of the phenyl hexa-alkynes.



Sample Number	R	Transition temperatures/ °C
62[94]	C <sub>3</sub> H <sub>7</sub>	Decomposed 160.0
63[94]	C <sub>8</sub> H <sub>17</sub>	K 80.3 N 101.4 Iso
64[94]	C <sub>5</sub> H <sub>11</sub>	K 166.0 N 183.8 Iso

In Table 3.8 and 3.9, all the results are investigated and analysed by POM and DSC, and The results of the research provided by this thesis are broadly agreed with the reference.

**Table 3.10** The enthalpies of the melting process for the samples **1-64**.

Sample Number	Enthalpies of melting process kJ/mol	Sample Number	Enthalpies of melting process kJ/mol
<b>1</b>	41.70	<b>33</b>	-
<b>2</b>	17.83	<b>34</b>	53.58
<b>3</b>	75.00	<b>35</b>	29.65
<b>4</b>	35.12	<b>36</b>	26.11
<b>5</b>	-	<b>37</b>	52.69
<b>6</b>	26.22	<b>38</b>	67.99
<b>7</b>	43.58	<b>39</b>	76.55
<b>8</b>	72.25	<b>40</b>	88.79
<b>9</b>	33.10	<b>41</b>	85.03
<b>10</b>	46.03	<b>42</b>	69.87
<b>11</b>	19.53	<b>43</b>	58.82
<b>12</b>	44.95	<b>44</b>	66.57
<b>13</b>	55.07	<b>45</b>	47.46
<b>14</b>	29.80	<b>46</b>	51.19
<b>15</b>	54.78	<b>47</b>	60.02
<b>16</b>	33.23	<b>48</b>	50.02
<b>17</b>	40.07	<b>49</b>	20.96
<b>18</b>	33.44	<b>50</b>	25.32
<b>19</b>	42.78	<b>51</b>	79.07
<b>20</b>	30.20	<b>52</b>	87.17
<b>21</b>	24.90	<b>53</b>	67.12
<b>22</b>	58.58	<b>54</b>	93.21
<b>23</b>	37.58	<b>55</b>	93.46

<b>24</b>	24.39	<b>56</b>	68.65
<b>25</b>	29.02	<b>57</b>	39.58
<b>26</b>	41.35	<b>58</b>	62.64
<b>27</b>	28.22	<b>59</b>	80.61
<b>28</b>	49.28	<b>60</b>	66.94
<b>29</b>	14.36	<b>61</b>	69.87
<b>30</b>	-	<b>62</b>	-
<b>31</b>	-	<b>63</b>	75.91
<b>32</b>	21.18	<b>64</b>	34.84

In Table 3.10, all the results shown were calculated based on the DSC results and used in the simulations of eutectic mixture by the calculations of Schröder-van Laar Equation.

## 3.2 General Techniques

### 3.2.1 Polarized Optical Microscopy (POM)

Polarized optical microscopy was performed on a Zeiss Axioskop 40 Pol microscope with a Mettler TP82HT hotstage in conjunction with a Mettler FP90 central controller. All the micrographs were captured with aid of an InfinityX-21 MP digital camera. The error of the temperature of the hotstage is  $\pm 0.1$  °C.

### 3.2.2 Differential Scanning Calorimetry (DSC)

Differential Scanning Calorimetry was performed on a Mettler DSC822<sup>e</sup> fitted with an autosampler operating with Mettler Star<sup>e</sup> software and calibrated before use each opening time using an indium standard sample (onset =  $156.55 \pm 0.2$  °C,  $\Delta H = 28.45 \pm 0.40$  J g<sup>-1</sup>°C)[95] under an atmosphere of dry nitrogen.

### 3.2.3 X-ray Diffraction (XRD)

X-ray diffraction experiments were performed on a Bruker D8 Diffractometer fitted with DHS900 sample stage with Diffraction WIZARD software. All the X-ray Diffraction patterns were captured in the calibration distance of 149.8 mm.

### 3.2.4 Preparation of Mixture systems

The liquid crystal mixtures were prepared by desired quantities of components for the formation, the construction of the Gibbs phase diagram and the calculation results from the Schröder-van Laar Equation for the eutectic based on **Table 3.1-3.10**. All the components were added together and dissolved in DCM, and the resulted solution was agitated in an ultrasonic bath for 30 minutes. The solvent was then removed by 40 °C overnight. The resulted mixtures (mol %) were then analysed by polarized optical microscopy, differential scanning calorimetry, and x-ray diffraction where appropriate. The error of the sample weight is  $\pm 0.01$ mg.

### 3.2.5 Calculations of Schröder-van Laar Equation

The calculations were performed by computer fitted with SVL3 software using the melting points, the enthalpies derived from melting cycles and the clearing points to the isotropic liquid. The results from the Schröder-van Laar equation gave the eutectic point with the material concentrations and the clearing point (°C) of the eutectic mixture.

### 3.2.6 Computing Modelling

All the modelling was performed using the MM2 force field in ChemDraw 3D to obtain minimized space filling structures in gas phase at 0 K. Alternatively, the ONIOM method in Gaussian G09 d.01 was used as follows. The aromatic core was modeled using the Becke 3-parameter Lee-Yang-Parr hybrid functional (B3LYP) with the 6-31G basis set (Gaussian type) with additional polarisation on

non hydrogen atoms (d), as implemented in Gaussian G09 d.01. The outer aliphatic 'chains' were modeled using the parameterization model 6 (PM6) methods as implemented in Gaussian G09 d.01. This method is described in the text as ONIOM(B3LYP/6-31G(d):PM6).

Geometry optimisations were requested using the OPT keyword and confirmed as minima when the FREQ keyword returned zero imaginary frequencies. Calculations were performed at a temperature of 298 K. Calculations were performed on the YARCC machine at the University of York.

## **Chapter 4: Polyaromatics**

## Chapter 4: Polyaromatics

### 4.1 Introduction

Modern day thermotropic liquid crystals tend to be amphiphiles that are composed of differing molecular segments, for example, rigid or flexible, polar or non-polar, aromatic or aliphatic *etc*, however Onsager theory suggests that at least for calamitic phases made up of rod-like molecules the molecular aspect ratio is important. Linear polyaromatics such as biphenyls, terphenyls *etc* however are not mesogenic because their aspect ratios are too small. For the higher homologues the aspect ratios for quinquephenyl and sexiphenyl support nematic phase formation, see structures **I** and **II** in Figure 4.1.[96] The well-known material sexiphenyl has a clearing point above 500 °C and also shows a N to SmA transition at 464 °C.[97] The interesting point about sexiphenyl is that it does not have an amphiphilic structure; therefore the dominant molecular interactions are principally through  $\pi$ - $\pi$  stacking. Consequently, its only structural feature relevant to the formation of liquid crystals is its aspect ratio (molecular length to breadth), and when it melts the solid collapses because of the increasing molecular rotations and fluctuations. Reducing the aspect ratio by removing one of the phenyl rings gives quinquephenyl and a reduction of the clearing point by 85 °C to 415 °C.

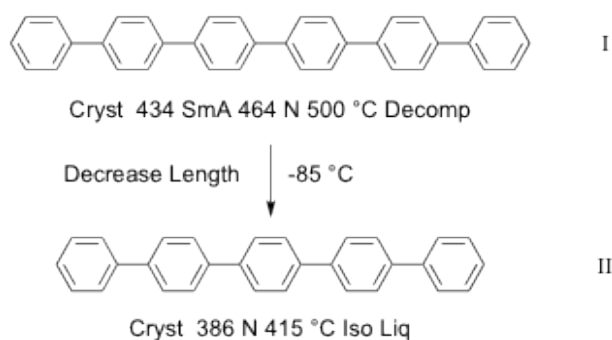


**Figure 4.1** The liquid crystal phase behaviour of sexiphenyl (I) and quinquephenyl (II).

Similar results have been obtained in heterocyclic systems where the incorporation of 5-membered ring systems can result in reductions in clearing temperatures. For

example, Figure 4.2 shows two oxadiazole based materials and one thiophene material.[98] The di-oxadiazole material III has effectively the same number of aromatic ring units as sexiphenyl, but the N to I phase transition temperature is only 312 °C, which is substantially lower due to the reduced aspect ratio. Increasing the number of phenyl rings in the system increases the aspect ratio and the N to I increases. The clearing point values of the di-oxadiazole IV and the di-thiophene material V are very similar thereby demonstrating that the detailed chemical structure for non-amphiphiles is not so important in mesophase stability in comparison to hard body interactions.

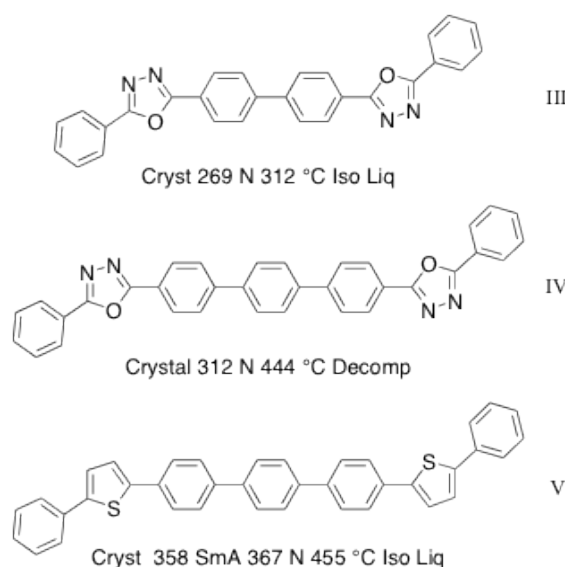


**Figure 4.2** Effect of molecular bending on the clearing point for di-oxadiazoles and di-thiophenes.

If we turn now to disc-like systems and consider the mesomorphic properties of hard discs we find there are very few studies on the phase behaviour of materials with disc-like structures such as triphenylene, truxene, coronene etc. However, nematic phases have been found in the heavy ends of oil when heated to high temperatures. These phases were called *carbonaceous* mesophases, and photomicrographs of their textures confirm that they are nematic (Chapter 1 Introduction, Section 1.4, pp 22-23). Most of the material in mixtures of the heavy ends of oil were found to be polyaromatics; therefore, in a thesis based on disc-like liquid crystals, it appeared important that the tendency of polyaromatics to form liquid crystal phases should be explored. In the following sections the melting

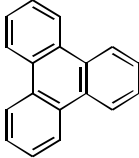
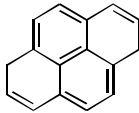
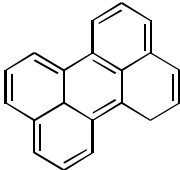
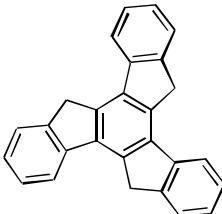
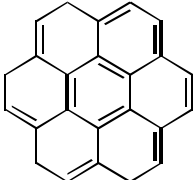
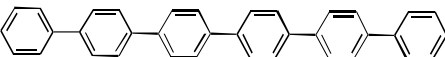
behaviour of selected polyaromatics was examined, and their properties when mixed (as in carbonaceous mesophases) were studied. This chapter is split into the three sections listed below:

1. Determination of the clearing points of selected polyaromatics;
2. Extrapolation of the values of virtual N-I for selected polyaromatics;
3. Mixing different polyaromatics to generate carbonaceous liquid crystals.

## **4.2 Determination of the Clearing Points for Selected Polyaromatics**

The polyaromatics selected for this study are given in Table 4.1, along with their chemical structures and melting points (*p*-sexiphenyl is added for comparison).

**Table 4.1** The chemical structures and melting points (°C) for a variety of polyaromatics.

ID	Chemical structure	Melting point/ °C
<b>Triphenylene</b>		197.32 ( $\Delta H = 90.31$ J/g)
<b>Pyrene</b>		150.21 ( $\Delta H = 62.00$ J/g)
<b>Perylene</b>		274.85 ( $\Delta H = 126.02$ J/g)
<b>Truxene</b>		384.67 ( $\Delta H = 106.95$ J/g)
<b>Coronene</b>		432.86 ( $\Delta H = 73.06$ J/g)
<b><i>p</i>-sexiphenyl</b>		439.86 ( $\Delta H = 60.66$ J/g)

The materials in Table 4.1 were investigated firstly by differential scanning calorimetry (DSC), and the results for which are split into two charts. Firstly the DSC thermograms for calamitic *p*-sexiphenyl are shown in Figure 4.3, whereas those for the disc-like systems triphenylene, pyrene, perylene, truxene, and coronene are shown in Figure 4.4. The thermograms for *p*-sexiphenyl show two crystal forms on heating, followed by a smectic A to nematic phase transition at approximately 472 °C. The material was not heated above 490 °C because it started to decompose which would affect the thermal cycling of the DSC. The melting point taken from the first heating cycle for *p*-sexiphenyl was found to be 439.86 °C

with an enthalpy of  $\Delta H = 60.66 \text{ J g}^{-1}$ . Cycling of the heating and cooling processes shows that the material did not appreciably decompose, and the transition events were reversible, except for supercooling of the lower temperature crystal phase.

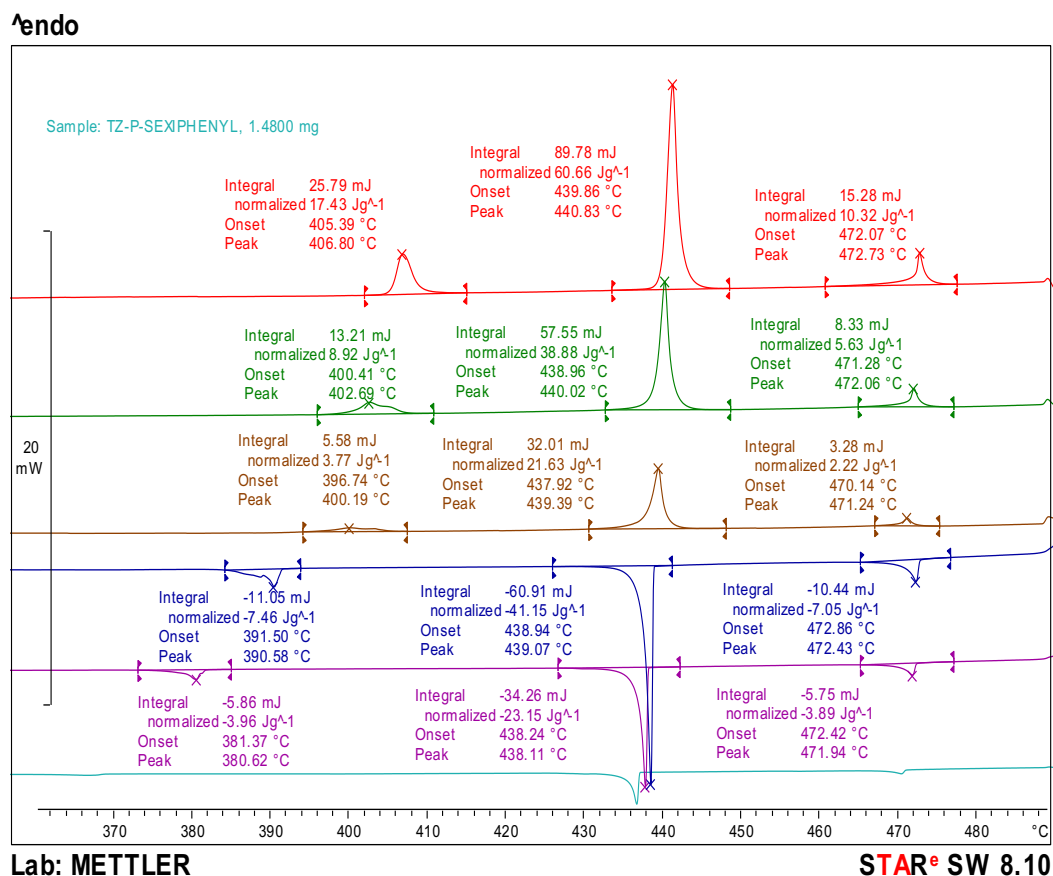


**Figure 4.3** The DSC thermograms as a function of temperature (°C) for *p*-sexiphenyl.

The results of the DSC studies for the disc-like systems are shown together in Figure 4.4. The first point to note from the data is that, pyrene and perylene show one crystal phase on heating but two on cooling, and there is substantial supercooling of the recrystallization temperature. However, no mesophases were formed, which is in keeping with rod-like systems, for which the melting points and relative enthalpies are similar. Truxene and coronene exhibit high melting points (384.67 and 432.86 °C respectively) and upon melting the DSC thermograms show some decomposition, thus on cooling an enthalpy was not observed in either of the thermograms. However, their melting temperatures and

associated enthalpies are not so dissimilar to those of *p*-sexiphenyl, in contrast, no mesophases were observed for truxene and coronene. This may be an indicator that the  $\pi$ - $\pi$  face-to-face interactions may be too strong, even at high temperatures, to allow the molecular discs to flow past one another in a nematic phase. This indicates that hard discs may be less likely to form mesophases, and that the intermolecular interactions are more important than for rod-like systems, which may be related to the fact that intermolecular twisting of adjacent phenyl rings in materials such as *p*-sexiphenyl prevent to some degree  $\pi$ - $\pi$  interactions, thus allowing mesophases to form.

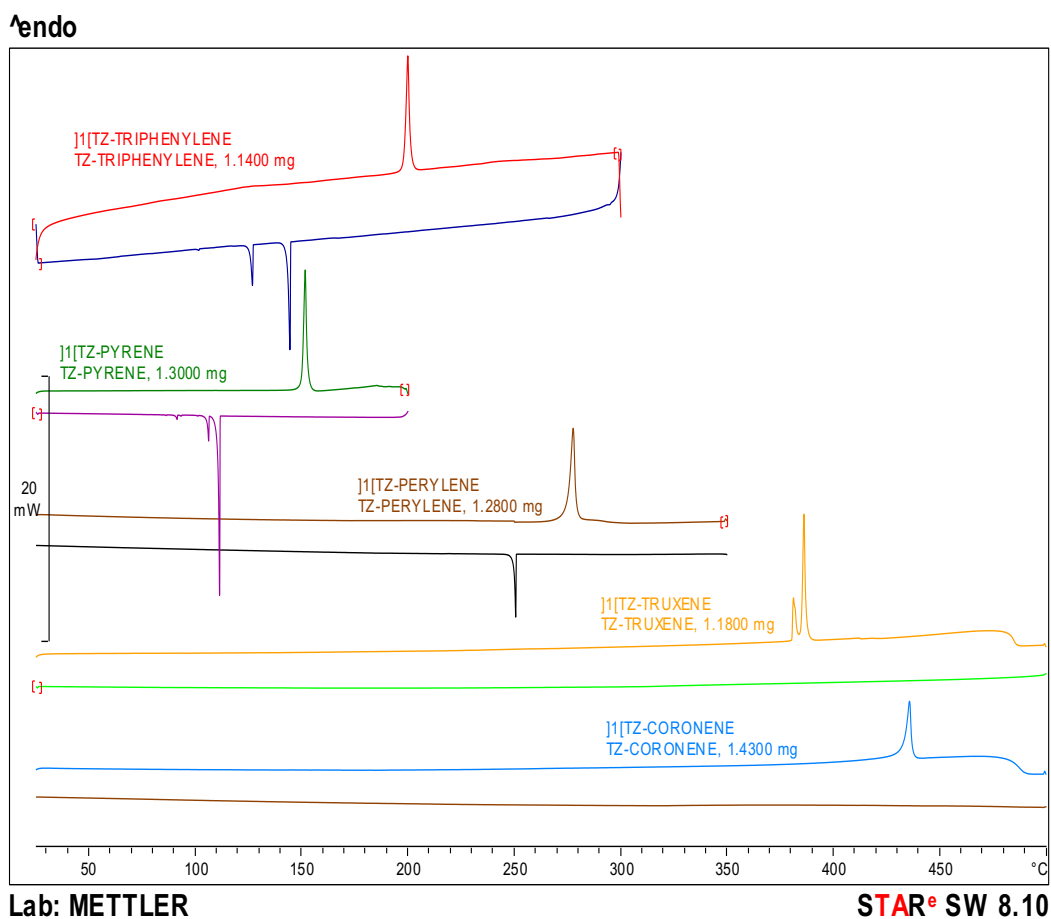


**Figure 4.4** The DSC thermograms as a function of temperature ( $^{\circ}\text{C}$ ) for triphenylene, pyrene, perylene, truxene and coronene.

### **4.3 Extrapolation of the Values of Virtual N-I for Selected Polyaromatics**

In 1979, A. Béguin *et al* attempted to investigate discotic mesophase potentiality.[88] They did this by creating two binary phase diagrams in order to determine the virtual discotic liquid crystal to liquid transition for a compound exhibiting no discotic phases (stable or monotropic). In these studies, they mixed amphiphilic discotic liquid crystal materials with triphenylene and pyrene to determine the virtual phase transitions for these polyaromatics. However, as noted in the previous section the intermolecular interactions could be strong and as such the polyaromatics could effectively hide in the local structure by packing between the molecules of the discotic liquid crystal. Thus the investigations the virtual N-I phase transition by extrapolation in binary phase diagrams between hard and soft disc systems are given in more detail in Chapter 7, where the phase diagrams are analyzed after a sequence of chapters that discuss miscibility and segregation in extensive detail. In the following therefore the study of the self-organization of hard disc systems is continued through mixture studies using the Schröder-van Laar simulations of eutectic behaviour in order to investigation potential mesophase behaviour.

### **4.4 Mixing Polyaromatics to Generate Carbonaceous Liquid Crystals**

Simple discoidal materials such as triphenylene, truxene, coronene are non-mesogenic, unlike simple rod-like molecules such as *p*-sexiphenyl[87]. In 1970s, several groups demonstrated the mesophase transformation taking place in polyaromatics during carbonization at high temperatures between 350-450 °C.[49-50, 53] Thus in the following section, we considered achieving carbonaceous liquid crystal phases using polyaromatics at lower temperatures.

#### 4.4.1 Mixture Studies of Different Hard Discs and Hard Rods

As polyaromatics are big and with no side-chain aliphatic units, in order to prepare mixtures using differing polyaromatics, the Schröder-van Laar equation was used to simulate and hence prepare the eutectic mixtures for selected polyaromatics. The results for the eutectic mixtures from the simulations for three-component, four-component, and five-component systems are shown in Table 4.2, as well as the melting points determined by polarized optical microscopy (POM) experiments. The results from the DSC experiments are given in Figure 4.5.

**Table 4.2** Mixture compositions (mol %) and predicted eutectic point with examined melting point (°C) for the different components mixtures.

ID	TZ-3M	TZ-4M	TZ-5M
Triphenylene/ mol %	70.0	67.4	64.1
Perylene/ mol %	19.3	18.4	17.2
Coronene/ mol %	10.7	10.3	10.1
Truxene/ mol %	-	3.7	3.4
<i>p</i> -sexiphenyl/ mol %	-	-	5.2
Calculated eutectic point/ °C	170.0	167.5	164.1
Actual melting point/ °C	172.7	175.8	173.9

The eutectic mixtures **TZ-3M**, **TZ-4M** and **TZ-5M** was the first prepared and investigated, the thermograms for which are shown in Figure 4.5 and exhibit typical melting behaviour for crystal systems. They all melted from the solid to the liquid state *via* rather large enthalpies ( $\Delta H = 110.20, 32.37, 65.46 \text{ J g}^{-1}$  respectively), and recrystallizations in the cooling cycle were accompanied by substantial supercooling. Microscopy (POM) also confirmed that no enantiotropic or monotropic phases were present.

In order to create the three-component eutectic mixture **TZ-3M**, the eutectic mixtures for the binary mixtures were determined for each pair of the components of the three materials, and the results for which are shown in Table 4.3. These indicate that the simulation SVL-1 (triphenylene and perylene) and simulation SVL-2 (triphenylene and coronene) have similar eutectic points to **TZ-3M**, but that the simulation SVL-3 mixture is much higher due to the addition of coronene because of its larger disc-like structure revealing a higher melting point as shown in Table 4.1.

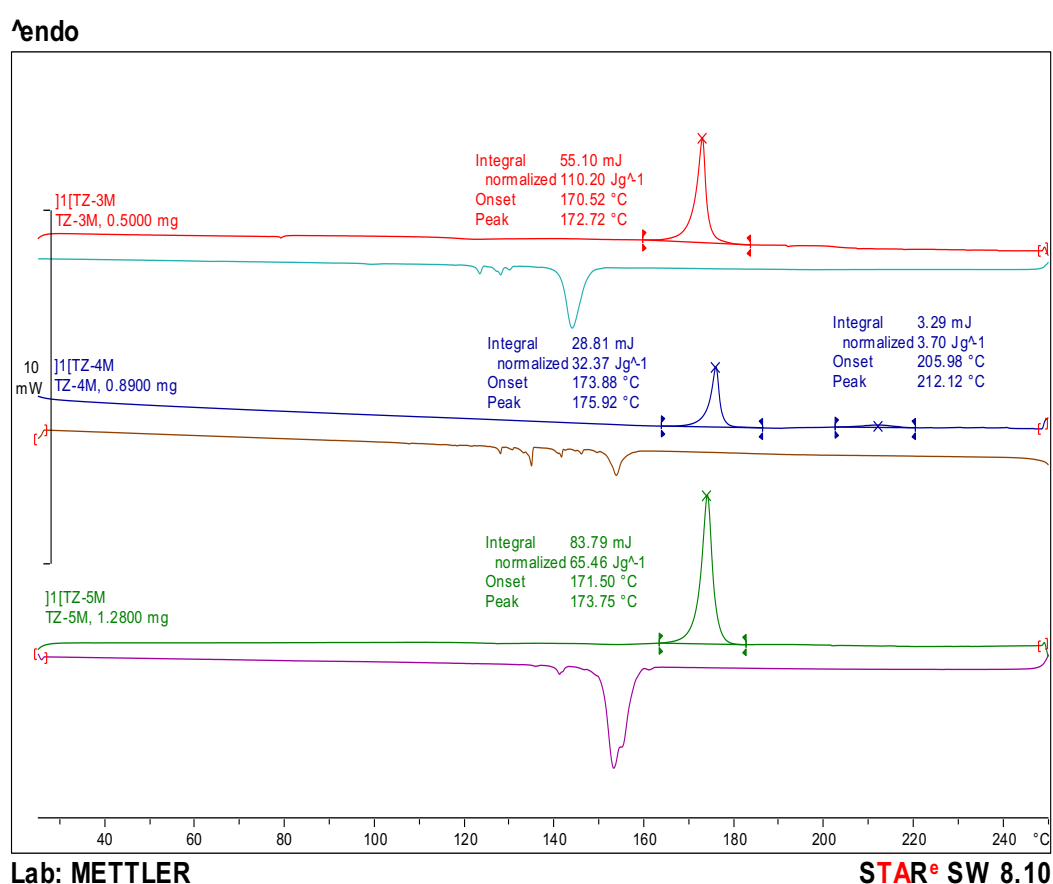


**Figure 4.5** The DSC thermograms as a function of temperature (°C) for mixtures **TZ-3M**, **TZ-4M** and **TZ-5M**.

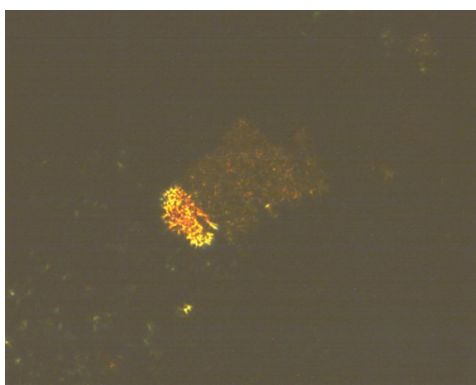
**Table 4.3** Mixture compositions (mol %) and predicted eutectic point (°C) for the binary mixtures (SVL means Schröder-van Laar).

Title	Triphenylene / mol %	Perylene / mol %	Coronene / mol %	Eutectic point/ °C
Simulation SVL-1	78.6	22.4	-	177.7
Simulation SVL-2	86.6	-	13.4	186.0
Simulation SVL-3	-	72.7	27.3	250.7

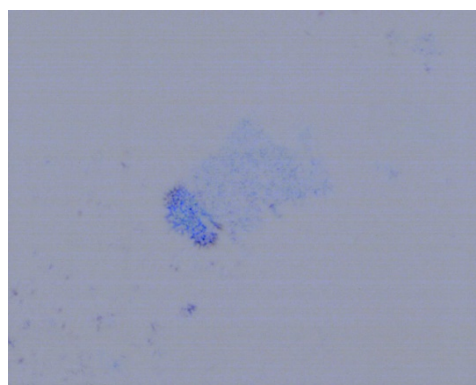
Interestingly, the **TZ-3M** mixture possessed three hard, disc-like materials (triphenylene, perylene and coronene), whereas **TZ-5M** possessed in addition one hard, rod-like material in sexiphenyl. However, neither mixture exhibited liquid crystal phases, but if we turn now to **TZ-4M** mixture in comparison to **TZ-3M** it has truxene added to it. Truxene is slightly different to the other hard disc materials in that it has some aliphatic characteristics associated with three CH<sub>2</sub> groups in the inner part of the core. These will have the ability to prevent to some degree of the face-to-face interactions. Thus, for **TZ-4M**, a dark texture is observed by POM at around 200 °C between solid state and liquid state, thereby indicating that the mixture may exhibit a mesophase (see Figure 4.6). Its almost extinct texture indicates that it is close to being optically isotropic and is probably amorphous in nature.



(a)



(b)



(c)

**Figure 4.6** The micrograph **TZ-4M** (x100) showing the dark texture of the mixture at approximately 200 °C, which occur between the solid and liquid states: **(a)** original photomicrograph; **(b)** over exposed photomicrograph; **(c)** inverted photomicrograph.

Examination of the DSC thermal cycling for **TZ-4M** shows that there is a very small enthalpy in the temperature region in which the mesophase was detected by POM. The enthalpy is weak and broad, but nevertheless detectable (shown in Figure 4.7).

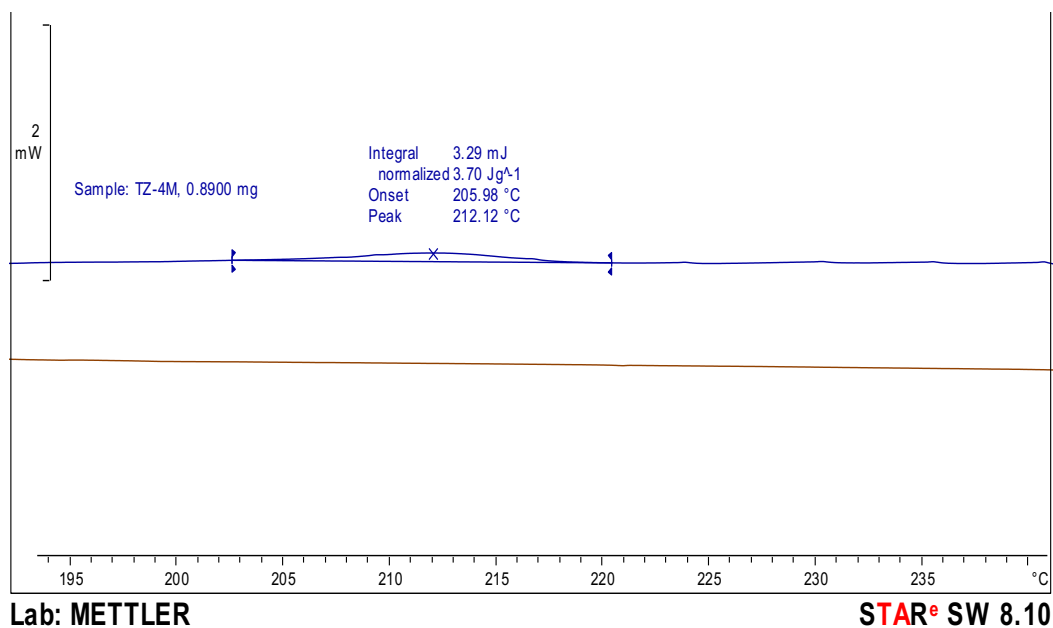


**Figure 4.7** The DSC peak for the unidentified phase for **TZ-4M** showing the intermediate mesophase transition to the isotropic liquid on heating.

Thus these results indicate that a novel phase appears to have been found, its nature and structure however, have remained elusive, and the only theoretical model that fits with the experimental studies is that of a cubatic phase, see the Introduction Section 1.3.2.2. The cubatic phase structure and the simulations of hard discs fit with a slight disordering of the packing of the discs which would be caused by the experimental introduction of truxene into the mixture as shown in schematically in Figure 4.8. Further studies however are required in order to elucidate this experiment.

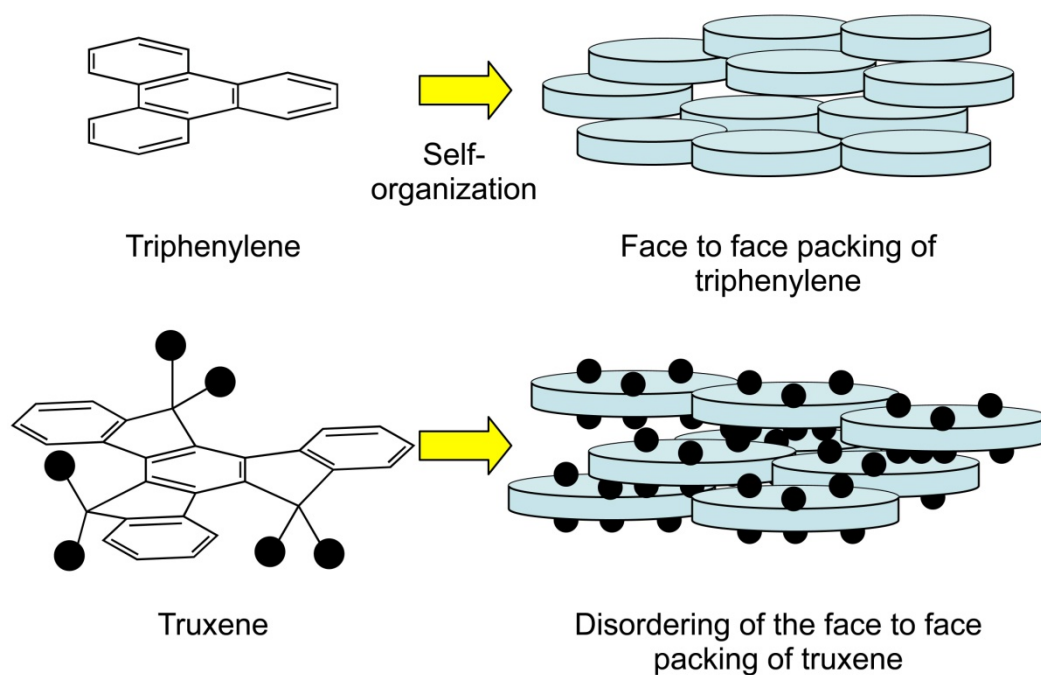


**Figure 4.8** Self-organization of triphenylene and truxene.

## 4.5 Summary

In this chapter, polyaromatics were investigated and their clearing points were determined by DSC. The multiple-component mixtures of polyaromatics were prepared and analysed by POM and DSC, and the aim is to achieve carbonaceous liquid crystal phases formed at lower temperatures, however, only one cubatic nematic phase might have been achieved by a four-component eutectic mixture of triphenylene, perylene, coronene and truxene.

## **Chapter 5: The Miscibility of Nematogenic Disc-like Materials**

## **Chapter 5: The Miscibility of Nematogenic Disc-like Materials**

### **5.1 Introduction**

Classically, binary and more complex liquid crystal mixtures have been prepared in order to lower the melting points of liquid crystal formulations *via* the formation of eutectic mixtures. This increases the temperature ranges of liquid crystal phases to give wider operating windows for display applications. In calamitic systems composed of rod-like molecules, miscibility and the formation of Gibbs phase diagrams is commonplace, and for these systems the behaviour is generally predictable and relatively well understood. However, despite the depth of study of calamitic systems, for discotic liquid crystals, the miscibility of different classes of materials has, as yet, not been made extensively. Thus, at this point, we decided to investigate the liquid crystal phase behaviour of mixtures formed by materials with disc-like structures, such as triphenylene hexa-esters[89] and phenyl hexa-alkynes[98-99]. Miscibility studies and binary phase diagrams for primarily disc-like nematogenic materials were made in order to examine mixing as a function of molecular architecture. This chapter will be split into the following sections:

1. Co-miscibility of nematogens of disc-like triphenylene derivatives.
2. Co-miscibility of nematogens of discotic triphenylene derivatives with rod-like tetra-benzoate molecules.
3. Co-miscibility of disc-like triphenylene mesogens with phenyl hexa-alkynes.

### **5.2 The Co-miscibility of Nematogenic Materials formed by Disc-like Molecules**

Since the first discovery of discotic liquid crystals by Chandrasekhar *et al* in 1977,[100-101] disc-like materials have found uses in a limited range of applications, such as in negative birefringence films for wide viewing angles found in displays and as lubricants for hard-disk drives found in computers.[36, 102]

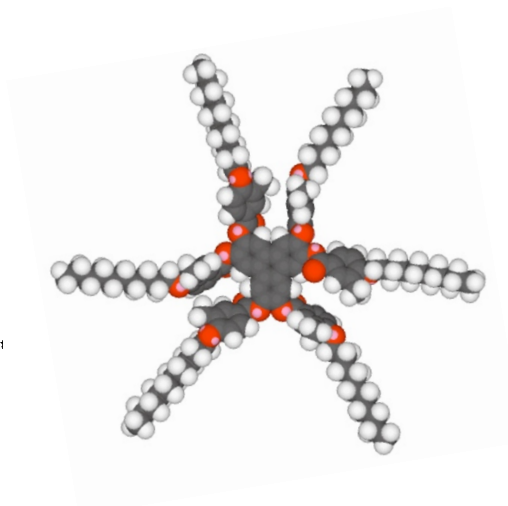
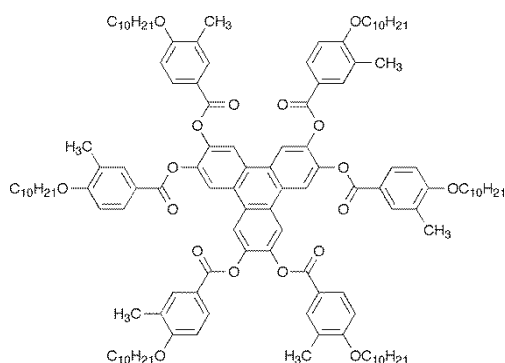
These applications materials with a triphenylene-core unit are often utilized. Thus, this section focuses on disc-like materials that are substituted with four or more flexible peripheral units (usually aliphatic chains) and exhibit nematic phases. Additionally, these materials may also display columnar mesophases.

### **5.2.1 Co-miscibility of nematogens of disc-like triphenylene derivatives**

Liquid crystalline derivatives of triphenylene have been discussed in chapter 3, and as these materials were also available in sufficient quantities studies binary mixtures were performed. It was expected, even predicted, that materials exhibiting liquid-like nematic phases would show co-miscibility with similar systems, although there are very few examples of such studies being performed, and even fewer for co-miscibility experiments on columnar phases.

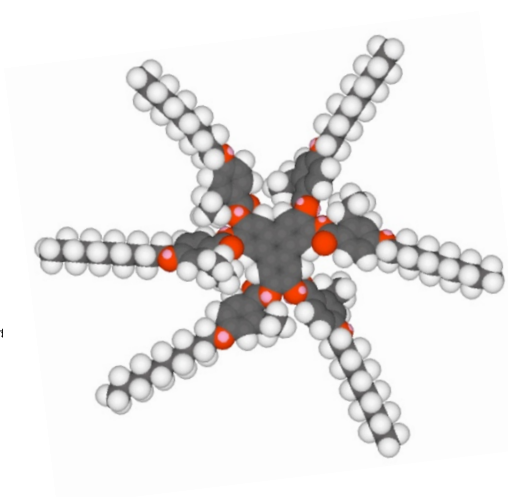
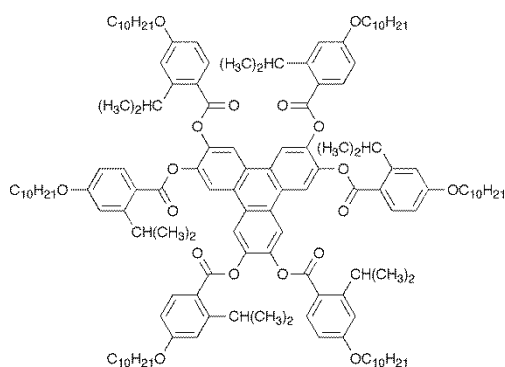
#### **5.2.1.1 Mixture studies of Compounds 4 and 11**

The structures and phase transitions of compounds **4** and **11** are shown in Figure 5.1. Both materials exhibit nematic phases, but neither seem to show columnar phases. The two materials were selected for investigation because they have similar chemical structures, with triphenylene core units and peripheral decyl chains, but differing between the methyl branching and isopropyl branching chains in the phenyl groups for compound **4** and **11** respectively. The lateral aliphatic substituent in the peripheral phenyl rings causes out-of-plane twists of the peripheral phenyl rings with respect to the triphenylene core unit. This twisting probably pushes the molecular discs apart, thereby suppressing the formation of columnar phases, and favouring the formation of nematic phases. These structural features are evident in computer simulations; for example, the minimised structures in gas phase at absolute zero for **4** and **11** are shown together in Figure 5.1 using the MM2 force field as implemented in ChemDraw 3D, and in Figure 5.2 using simulations based on DFT theory.



4

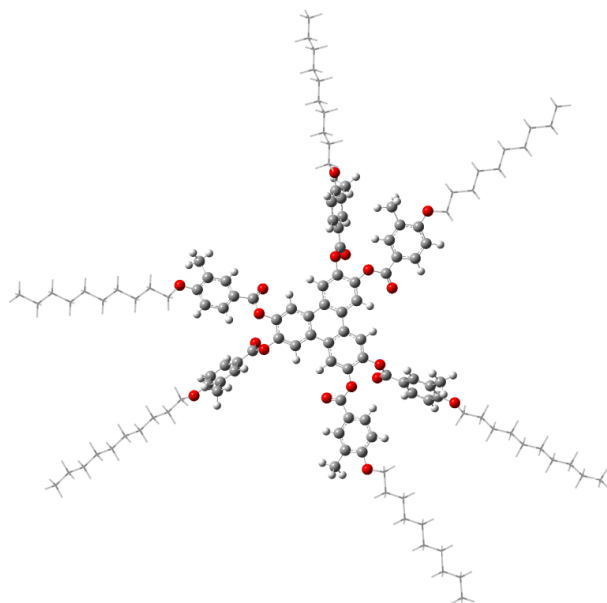
K 105.3 N 193.9 °C Iso Liq



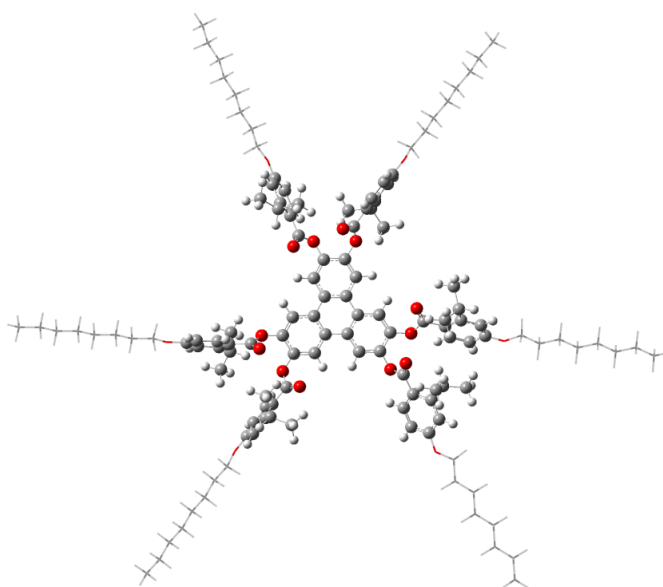
11

K 91.7 (N 73.2) °C Iso Liq

**Figure 5.1** The chemical structures and phase transitions of compound **4** and **11**. The space filling structures of compounds **4** and **11** determined in gas phase at 0 K using the MM2 force field as implemented in ChemDraw 3D.



4



11

**Figure 5.2** The energy structure for compounds **4** and **11**, at the mixed ONIOM(B3LYP/6-31G(d):PM6) level of theory. Geometry minimised using the ONIOM method as implemented in Gaussian G09 revision D.01, with the B3LYP/6-31G(d) method used for the 'core' and the PM6 semi-empirical method used for the aliphatic chains.

From geometry minimised using the mixed ONIOM(B3LYP/6-31G(d):PM6) level of theory, the disc diameters for compounds **4** and **11** were found to be broadly similar with the diameter of compound **4** was determined to be 46.00 Å and the diameter of compound **11** 42.04 Å. Moreover, peripheral aromatic rings are twisted out-of-plane for compound **4** and compound **11**. The ChemDraw3D structures are used to show the volume of the molecules and the space they fill, whereas the DFT simulations can show the internal molecular architecture of the materials as well. Additionally, DFT works from the wavefunction upwards, whereas MM2 works from torsional potentials about bonds downwards. It is interesting that both types of simulation produce similar minimised structures, thus it is expected that the compounds will maintain a twisted structure into the self-organizing mesophase structure, albeit that the twisting will be in constant dynamical flux.

As compounds **4** and **11** have similar molecular architectures it was expected that the materials would be compatible in binary phase diagrams. Thus, a series of mixtures (TZ-M001-1-5) of **4** and **11** were prepared and their phase behaviour was firstly examined by polarized optical microscopy (POM) and secondly by differential scanning calorimetry (DSC). The mixture compositions and transition temperatures determined by POM are given in Table 5.1, whereas those determined from DSC are shown together in Table 5.2. For the DSC results the peak maxima were recorded rather than the tangents drawn at the maximum changes in the heat flow, because heating and cooling values were inverted with respect to one another (heating values lower than cooling values) due to the broadness of the peaks for the various mixtures. Conversely the peak shapes for the pure components are sharper, and reversibilities of the phase transition temperatures are much narrower. Furthermore, the clearing point enthalpy of compound **4** is twice the size of the enthalpy for compound **11**. This is probably because compound **11** possesses lateral isopropyl groups, which induce greater twisting of the peripheral phenyl rings that increase disordering in the system.

The composition of the mixture (**TZ-M001-E**) predicted to exhibit the eutectic for the binary components was calculated from the melting enthalpies of compound **4** and **11** using Schröder-van Laar equation. The phase behaviour of the theoretical eutectic mixture was determined by POM and DSC, the results are shown in both Tables.

The binary phase diagram for the results shown in Table 5.1 and 5.2 are shown respectively in Figure 5.3. In addition, photomicrographs of the defect textures at various points are incorporated into the phase diagram in Figure 5.3. The error for the temperature in POM is  $\pm 0.1$  °C. The error for the temperature in DSC is  $\pm 0.2$  °C and the error for enthalpies in DSC is  $\pm 0.40$  J/g. The error for the weight of the balance is  $\pm 0.01$  mg.

**Table 5.1** Mixture compositions (mol%) and transition temperatures (°C) for binary mixtures of **4** and **11** determined by POM.

ID	<b>4</b> / mol%	K	/°C	N	/°C	Iso Liq
<b>11</b>	0	.	91.7	.	(73.2)	.
<b>TZ-M001-1</b>	9.5	.	79.4	.	94.9	.
<b>TZ-M001-E</b>	32.3	.	55.1	.	146.1	.
<b>TZ-M001-3</b>	46.8	.	67.7	.	152.7	.
<b>TZ-M001-4</b>	67.3	.	105.3	.	182.7	.
<b>TZ-M001-5</b>	88	.	122.5	.	192.1	.
<b>4</b>	100	.	105.3	.	193.9	.

**Table 5.2** Mixture compositions (mol%) and nematic to isotropic transition temperatures (°C) and enthalpies (J/g) both on heating and cooling for binary mixtures of **4** and **11**.

ID	4/ mol%	N-Iso Liq	
		Heating/ °C	Cooling/ °C
<b>11</b>	0	74.35	74.05
		$\Delta H = 0.10$	$\Delta H = -0.10$
<b>TZ-M001-1</b>	9.5	96.10	95.75
		$\Delta H = 0.10$	$\Delta H = -0.10$
<b>TZ-M001-E</b>	32.3	147.28	146.63
		$\Delta H = 0.14$	$\Delta H = -0.13$
<b>TZ-M001-3</b>	46.8	154.37	153.94
		$\Delta H = 0.19$	$\Delta H = -0.19$
<b>TZ-M001-4</b>	67.3	183.44	183.00
		$\Delta H = 0.19$	$\Delta H = -0.29$
<b>TZ-M001-5</b>	88	192.82	192.47
		$\Delta H = 0.32$	$\Delta H = -0.55$
<b>4</b>	100	194.44	194.42
		$\Delta H = 0.24$	$\Delta H = -0.20$

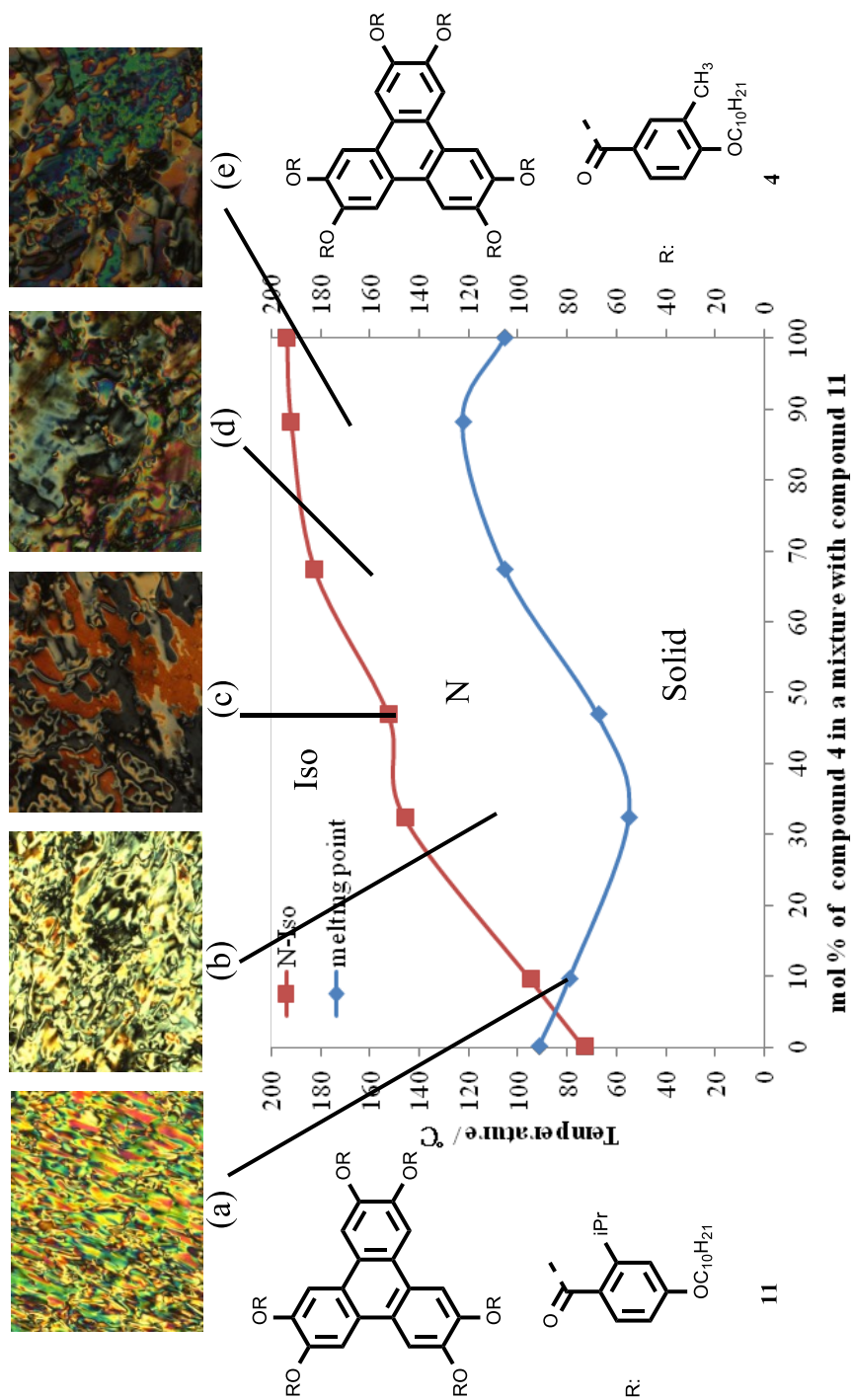


**Figure 5.3** The Gibbs phase diagram for the binary mixture series TZ-M001 of **4** and **11**. Photomicrographs (x 100 magnification) showing representative optical textures for the series of TZ-M001: **(a)** 9.5%, cooling, 79.7 °C, N; **(b)** 32.3%, cooling, 112.6 °C, N; **(c)** 46.8%, cooling, 140 °C, N; **(d)** 67.3%, cooling, 146 °C, N; **(e)** 88.0%, cooling, 171.4 °C, N.

The binary phase diagram for compounds **4** and **11**, shown in Figure 5.3, is effectively as predicted. The nematic phases of the two compounds are miscible across the entire mixture range, with the nematic to liquid phase transition temperature curve showing a slight increase in stability as a function of concentration of **4** indicating that the mixed system exhibits a greater stability of the nematic discotic phase. Thus, both compounds possess the same nematic phase, *i.e.*, a discotic nematic phase with probably a negative birefringence. The melting points for the various mixtures show a minimum value of approximately 30 mol% of compound **4** in the mixture, which is similar to the predicted theoretical result for the eutectic mixture (the experimental result for the **TZ-M001-E** mixture was around 35 mol% of **4**). The photomicrographs shown in Figure 5.3 are all typical of the *schlieren* and *planar* textures of the nematic phase, with both 2- and 4-brush singularities present indicating that the nematic phase was not biaxial. Overall the phase diagram seems to possess properties similar to those exhibited by diagrams formed by rod-like molecules.

In order to examine the reversibility of the phase transitions, and to investigate the degree of the range of the biphasic properties in the phase diagram a plot of the nematic to liquid peak transition temperatures determined by DSC was made, as shown in Figure 5.4. The temperatures for the heating and cooling cycles for the various mixtures virtually overlay one another, indicating a minimal extent for the biphasic region. This indicates that the two materials mix almost ideally as expected from the evaluation of their relative molecular structures. Furthermore, the solid to liquid crystal phase transition accurately shows by DSC a depression associated with eutectic behaviour that is in agreement with the Schröder-van Laar equation prediction. Thus the system behaves like that produced from the mixing of two liquids.

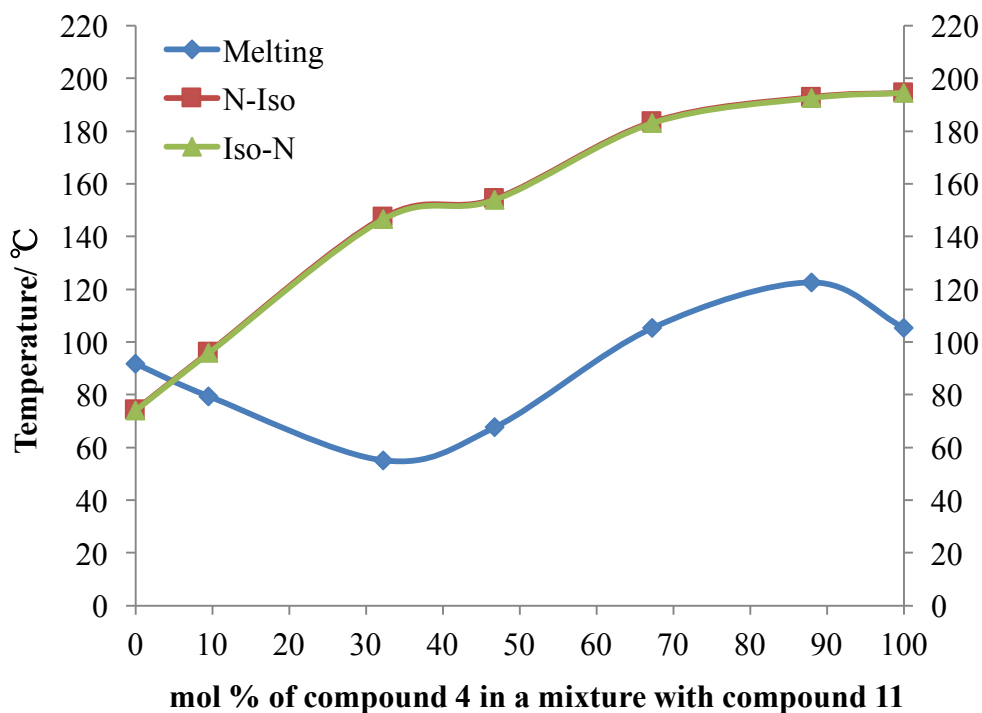


**Figure 5.4** The Gibbs phase diagram showing the biphasic region between heating and cooling for nematic to isotropic transition of mixtures of **4** and **11**.

In order to examine the relative stabilities of the nematic phases formed by binary mixtures and those of the pure components, a plot of the enthalpies of the clearing points as a function of temperature was created as shown in Figure 5.5. This figure does indeed show that the greater the percentage of compound **11** in the mixture, the more stable the nematic phase becomes, so much so that even a 90 mol% concentration of **11** with 10 mol% of **4** is more stable than the pure compound. In other words, the addition of compound **4** to compound **11** reduces the disordering caused by the twisting of the peripheral rings caused by the isopropyl groups of compound **11** and thereby the nematic phase becomes stabilised with the greater ordering raising the enthalpy value.

All of these studies suggest that the nematic discotic triphenylene mixture studied show similar behaviour to rod-like systems.

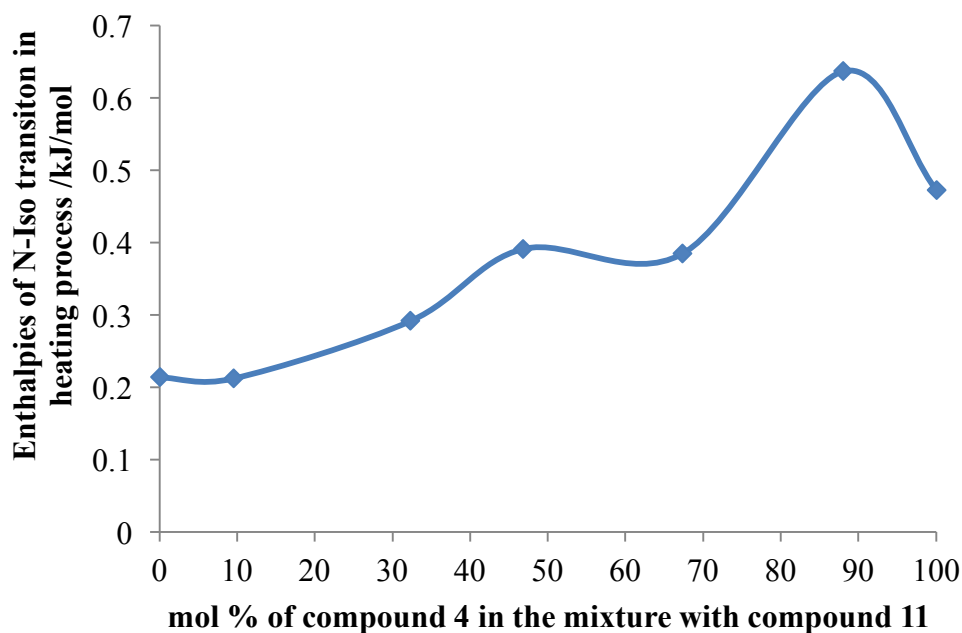


**Figure 5.5** The diagram showing the enthalpies (kJ/mol) of the nematic to isotropic liquid transition in heating process of mixtures of **4** and **11**.

### 5.2.2 Co-miscibility of nematogens of discotic triphenylene derivatives with rod-like tetra-benzoate molecules

In order to examine whether it was possible to mix mesogenic materials with disc-like molecular architectures with materials that have board-like core systems, a number of mixture studies between triphenylene hexa-ester compounds with tetra-benzoate esters were investigated. In each study, the compounds selected for investigation exhibited nematic phases.

Initially, a small selection of tetra-substituted esters, **38**, **46**, **58** and **37** (binary-substituted ester), that differed in their terminal chain lengths (structures shown in Figure 5.6) were mixed according to binary compositions of their eutectic formulations determined from the Schröder-van Laar equation. These mixtures gave the widest temperature ranges for study of mesomorphic behaviour, thus they allowed for the investigation of potential mesomorphic, and in particular smectogenic, properties of the materials. The results for the transition temperatures

and phase sequences are given in Table 5.3. Remarkably the actual and predicted values for the eutectic compositions were in good agreement. Photomicrographs of the optical textures of the phases exhibited by the mixtures are shown in Figure 5.7.

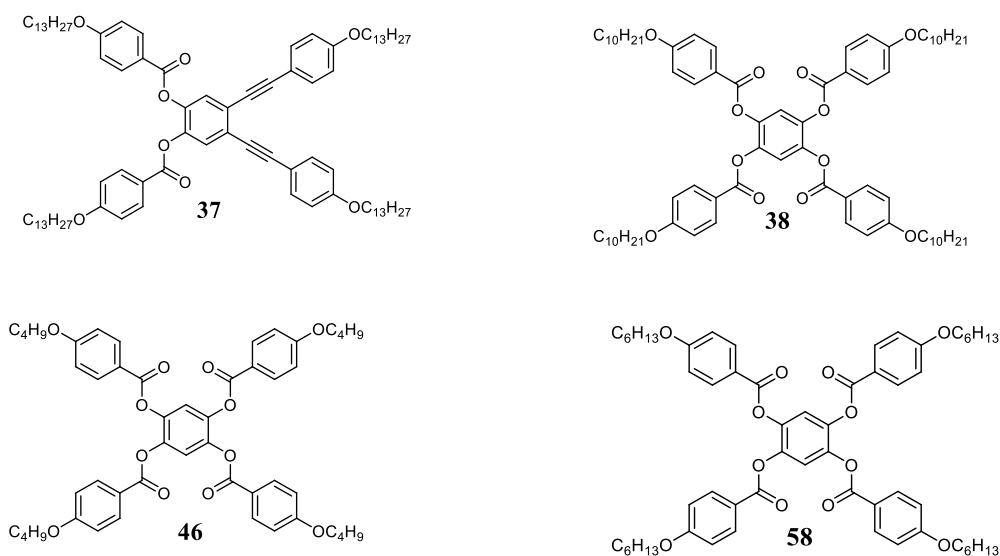


**Figure 5.6** The diagram showing the structures of compound **37**, **38**, **46** and **58**.

**Table 5.3** Binary mixture composition (mol%), predicted eutectic melting points (°C) and phase transition temperatures (°C) for tetra-benzoate esters.

Title	A/ mol%	B	Predicted mp / °C	Transition temperatures/ °C
<b>TZ-M005-E</b>	<b>38/ 77.1</b>	<b>46</b>	90.6	K 90.6 N 102.1 Iso
<b>TZ-M007-E</b>	<b>37/ 93.1</b>	<b>58</b>	75.3	K 75.3 N 88.5 Iso
<b>TZ-M008-E</b>	<b>37/ 76.0</b>	<b>38</b>	71.0	K 71.0 N 91.0 (SmC 67.9) Iso

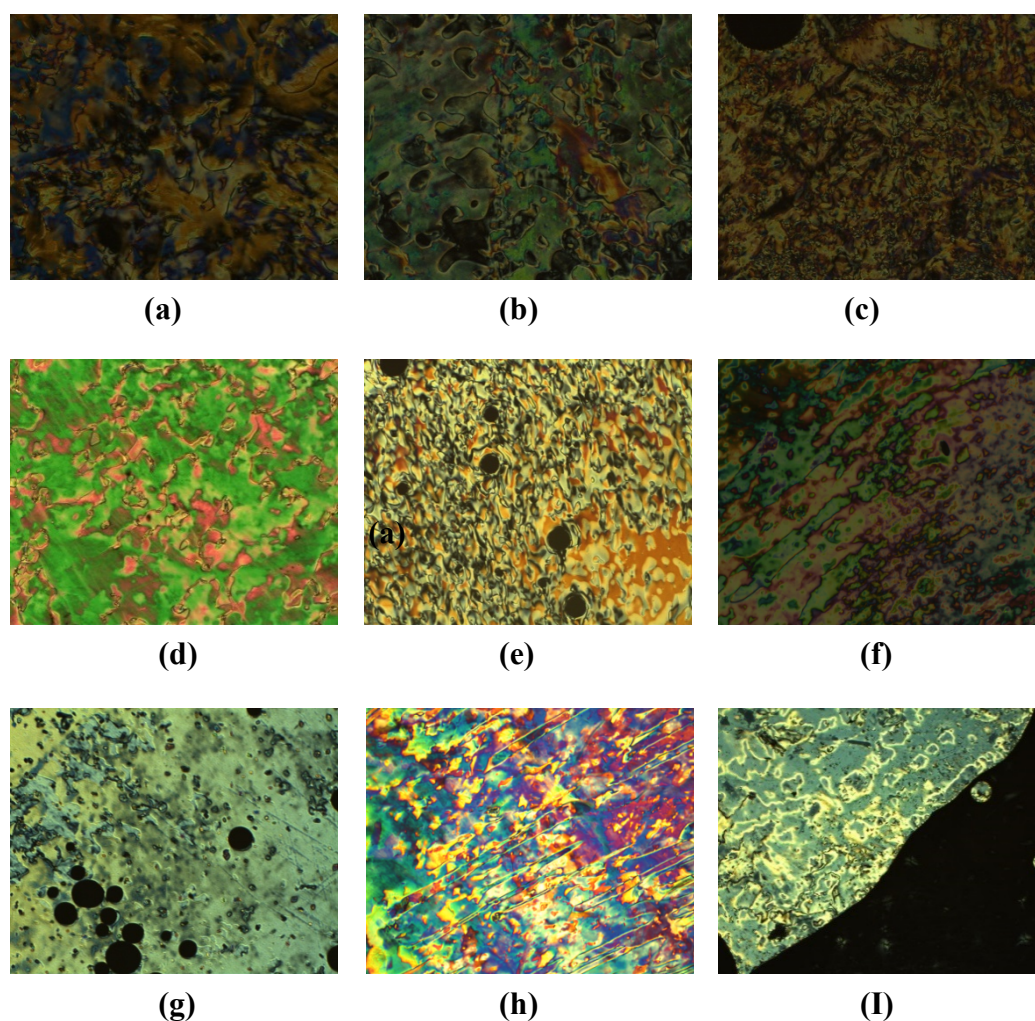


**Figure 5.7** The micrographs (x100) obtained for: (a) **38**, heating, 101.3 °C, N; (b) **37**, cooling, 87.3 °C, N; (c) **37**, cooling, 74.1 °C, SmC; (d) **46**, cooling, 119.6 °C, N; (e) **58**, cooling, 58.0 °C, N; (f) **TZ-M005-E**, cooling, 100 °C, N; (g) **TZ-M007-E**, cooling, 83.4 °C, N; (h) **TZ-M008-E**, heating, 186.3 °C, N; (i) **TZ-M008-E**, cooling, 67.5 °C, SmC.

The results from Table 5.3 show that the mixtures were capable of exhibiting smectic as well as nematic phases. This indicates that the tetra-benzoate esters behave more like rod-like systems than either board or disc-like materials. Thus they are more likely to form layers in preference to columns.

Nevertheless, mixing tetra-substituted esters with hexa-substituted materials (structures shown in Figure 5.8) has the potential for investigating the possibility of biaxial nematic phases being formed. Therefore, eutectic compositions were determined using the Schröder-van Laar equation for triphenylene hexa-esters that exhibit either nematic phase or columnar phases with tetra-benzoate esters that are non-mesogenic. The values for the transition temperatures are reported in Table 5.4.

**Table 5.4** Binary mixture compositions (mol%), predicted eutectic melting points (°C) and phase transition temperatures (°C) for nematic triphenylene hexa-esters (**1**, **4**, **10**, **11**, and **27**) and tetra-benzoate esters (**38**, **51**, and **56**).

Title	A/ mol%	B	Predicted mp / °C	Transition Temperature/ °C
<b>TZ-M006-E</b>	<b>1/ 42.0</b>	<b>38</b>	84.1	K 90.1 Iso
<b>TZ-M011-E</b>	<b>10/ 31.5</b>	<b>38</b>	86.8	K 86.0 Iso
<b>TZ-M013-E</b>	<b>4/ 61.0</b>	<b>51</b>	89.4	K 95.5 Iso
<b>TZ-M012-E</b>	<b>4/ 48.4</b>	<b>38</b>	82.3	K 90.5 Iso
<b>TZ-M019-E</b>	<b>11/ 80.7</b>	<b>51</b>	80.0	K 63.6 Iso
<b>TZ-M021-E</b>	<b>27/ 31.6</b>	<b>56</b>	103.6	K 106.3 Iso

Given this background on the various materials in this part of the study, we now turn to the actual binary phase diagrams between tetra- and hexa-substituted materials.

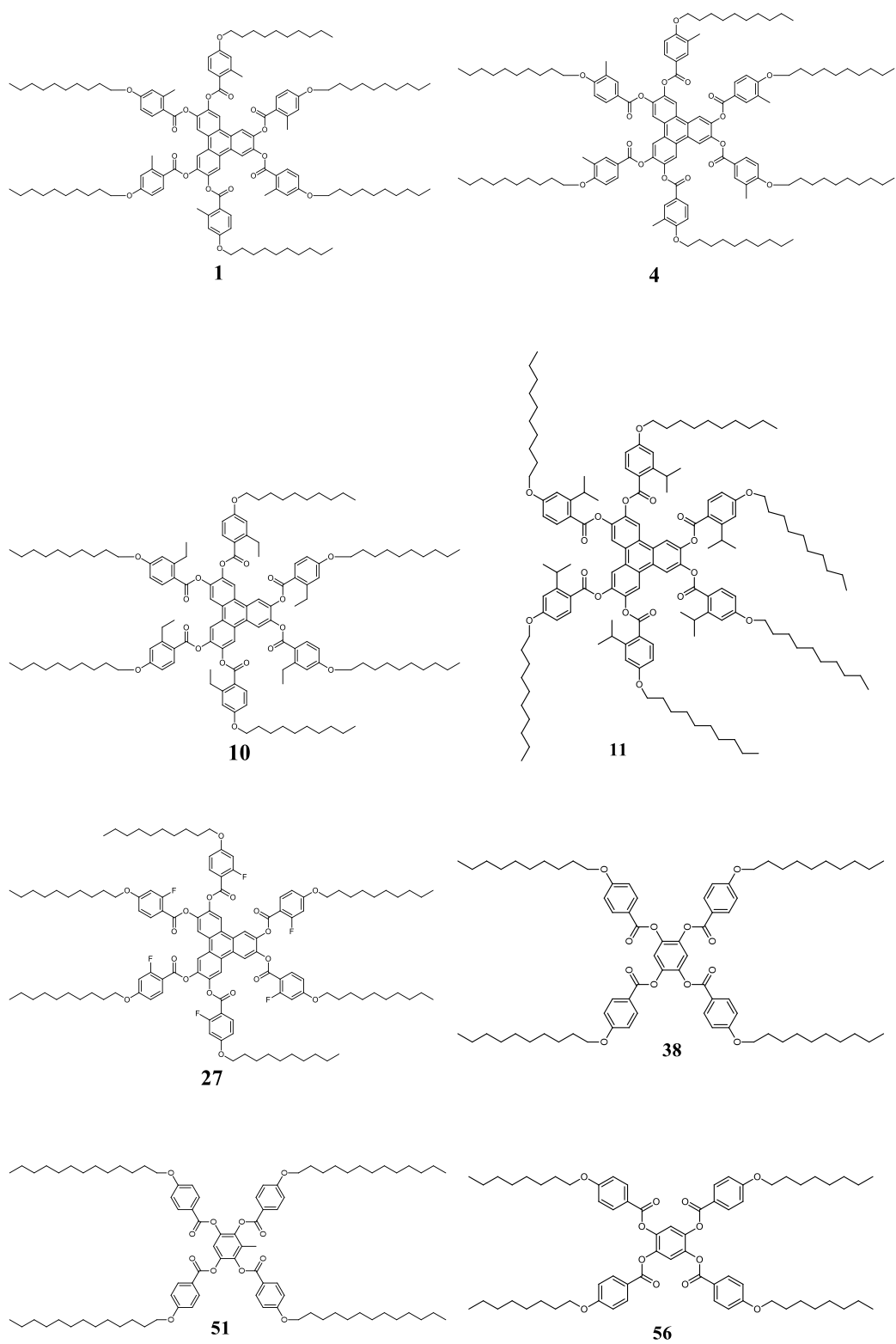
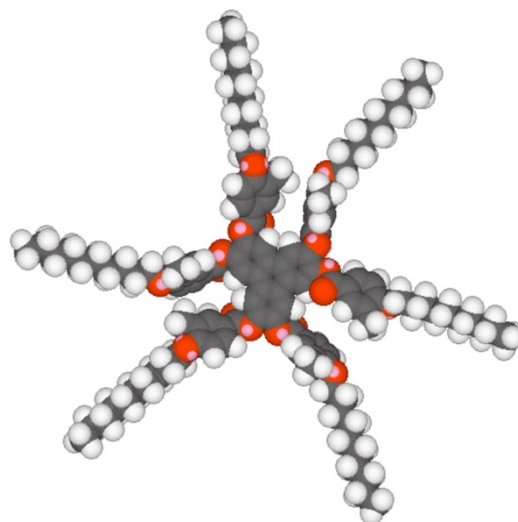
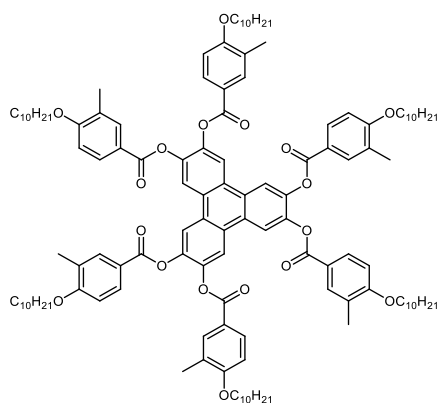


**Figure 5.8** The structures of compound **1**, **4**, **10**, **11**, **27**, **38**, **51** and **56**.

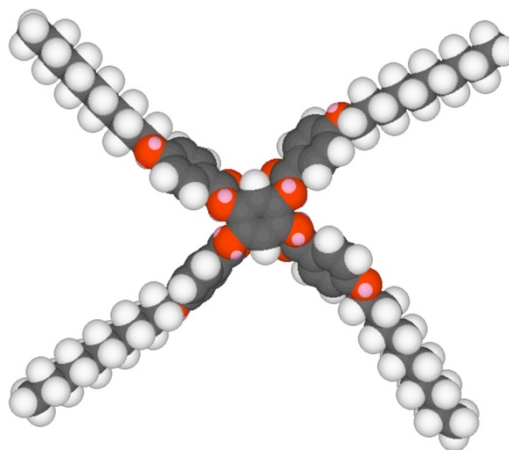
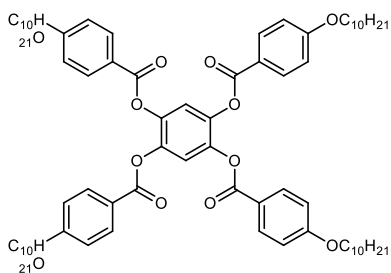
### 5.2.2.1 Studies for Binary Mixtures between Compounds 4 and 38

The binary phase diagram between compounds **4** and **38**, shown in Figure 5.11, was selected for investigation because the two compounds have similar peripheral decyl chains, but differ in the methyl branching in the phenyl group for compound **4** which is absent for compound **38**. The overall molecular topologies were investigated by various computational methods in order to examine if there was any molecular shape compatibility between the two materials. The minimised structures in gas phase at absolute zero for compounds **4** and **38** are shown together in Figure 5.9 using the MM2 force field as implemented in ChemDraw 3D, and in Figure 5.10 using simulations based on DFT theory.



**4**

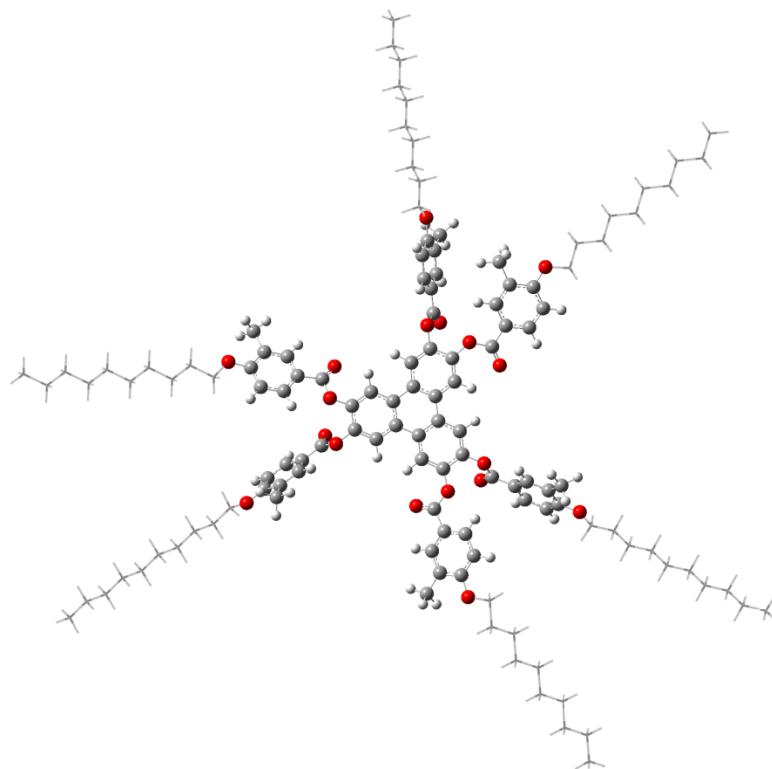
K 105.3 N 193.9 °C Iso Liq



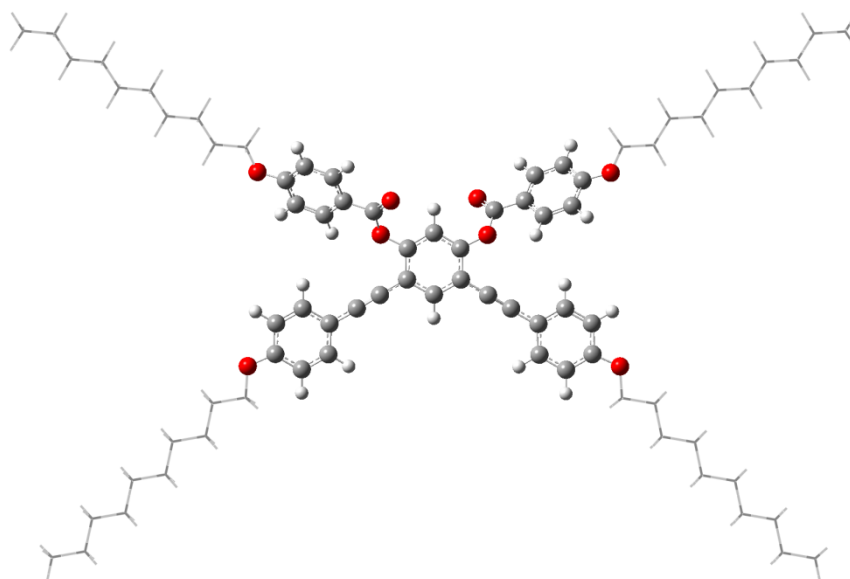
**38**

K 92.9 N 102.8 °C Iso Liq

**Figure 5.9** The chemical structures and phase transitions of compounds **4** and **38**. The space filling structures of compounds **4** and **38** determined in gas phase at 0 K using the MM2 force field as implemented in ChemDraw 3D.



4



38

**Figure 5.10** The energy minimised structures for compounds **4** and **38**, using the mixed ONIOM(B3LYP/6-31G(d):PM6) level of theory.

In the simulated structures, the peripheral aromatic rings of compound **4** are twisted out of the plane of the central triphenylene core, whereas the peripheral aromatic rings of compound **38** are in the same plane as the central benzene core unit. The length of compound **4** is 46.00 Å and that of compound **38** is 43.31 Å, *i.e.*, they are similar in size. The major issue with respect to their packing compatibilities is that compound **38** has poor space filling with respect to the peripheral groups, and which may choose to lie parallel to one another to minimise the free volume. In this arrangement the two materials will not pack well together to fill space efficiently.

Triphenylene liquid crystal **4** and tetra-benzoate ester **38** were found to exhibit a nematic phase. A series of mixtures **TZ-M012** were prepared, and their phase behaviour was examined by POM and DSC. The transition temperatures for the mixtures determined by POM are given in Table 5.5, whereas those determined from DSC are shown together in Table 5.6. The photomicrographs of the mesophases exhibited for the mixtures are shown together in Figure 5.11.

The composition of mixture (**TZ-M012-E**), which was predicted to exhibit the eutectic point for the binary components, was calculated by Schröder-van Laar equation, and its phase behaviour was determined by POM and DSC; the results being shown in both Tables.

**Table 5.5** Compositions and transition temperatures (°C) for binary mixtures of **4** and **38** by POM.

ID	4/ mol%	K	/°C	N	/°C	Iso Liq
<b>38</b>	0	.	92.9	.	102.8	.
<b>TZ-M012-1</b>	25	.	91.9	-	-	.
<b>TZ-M012-E</b>	48.4	.	90.5	-	-	.
<b>TZ-M012-2</b>	75.1	.	120.4	.	151.3	.
<b>4</b>	100	.	105.3	.	193.9	.

**Table 5.6** Mixture compositions (mol%) and nematic to isotropic transition temperatures (°C) and enthalpies (J/g) both on heating and cooling for binary mixtures of **4** and **38**.

ID	4/ mol%	N-Iso Liq	
		Heating/ °C	Cooling/ °C
<b>38</b>	0	103.12	102.83
		$\Delta H = 1.36$	$\Delta H = -1.57$
<b>TZ-M012-1</b>	25	-	-
		-	-
<b>TZ-M012-E</b>	48.4	-	-
		-	-
<b>TZ-M012-2</b>	75.1	164.65	163.78
		$\Delta H = 0.18$	$\Delta H = -1.08$
<b>4</b>	100	194.44	194.42
		$\Delta H = 0.24$	$\Delta H = -0.20$

The Gibbs phase diagram shown in Figure 5.11 revealed that the nematic phase was not miscible across the whole concentration change, and surprisingly the melting curve did not show obvious eutectic behaviour as predicted from the Schröder van-Laar equation (**TZ-M012-E**). Moreover, there was non-mesogenic

behaviour at the eutectic point of 48.4 mol% of **4**, and no phase could be observed at the point of 25 mol% of **4**, but at the point of 75.1 mol% of compound **4**, it was mesogenic. Thus, overall the mixtures of mesogens with disc-like and board-like molecular architectures are non-mesogenic, which indicates that the two materials are incompatible above the melting point, whereas for the solid state the two appear to show appreciable mixing, but without a well-defined eutectic point. Moreover, the photomicrographs shown in the figure show that solid formed from the liquid at low concentrations of compound **4** are needle like, and at higher concentrations the needles are much smaller in size thereby filling the field of view.

In order to investigate the phase behaviour further, and to obtain accurate values for the transition temperatures on heating and cooling for the mixtures in the phase diagram, calorimetric studies were performed for each individual mixture, the results for which are shown in Table 5.6 along with the enthalpies for the transitions.

It is clear that the binary phase diagram for the transition temperatures determined by calorimetry, as shown in Figure 5.12, are broadly in agreement with the phase diagram obtained by microscopy. Additionally, the temperatures show there is little difference between heating and cooling cycles, and again there are no N-I phase transitions observed below 75.1 mol% of compound **4**. However, at 75.1 mol% the melting point is at its highest point, indicating that the mixed solid is most stable at this point.

If we examine the values of the enthalpies of the phase transitions as a function of concentration, as shown in Figure 5.13, it can be seen that the enthalpies for the N-I phase transitions between compound **4** and compound **38** show a big difference. Additionally, the enthalpies for the mixtures, which exhibit nematic phase, are similar to those obtained for compound **4** rather than those for compound **38**. The value of the enthalpy for the N- I of compound **38** is seven times larger than that for compound **4** indicating that the nematic phase of

compound **38** is relatively well ordered in comparison to that of the nematic phase of compound **4** which is more liquid like.

In order to prove the miscibility properties of the tetra-benzoate esters and triphenylene hexa-esters, more mixture series were investigated in this section.

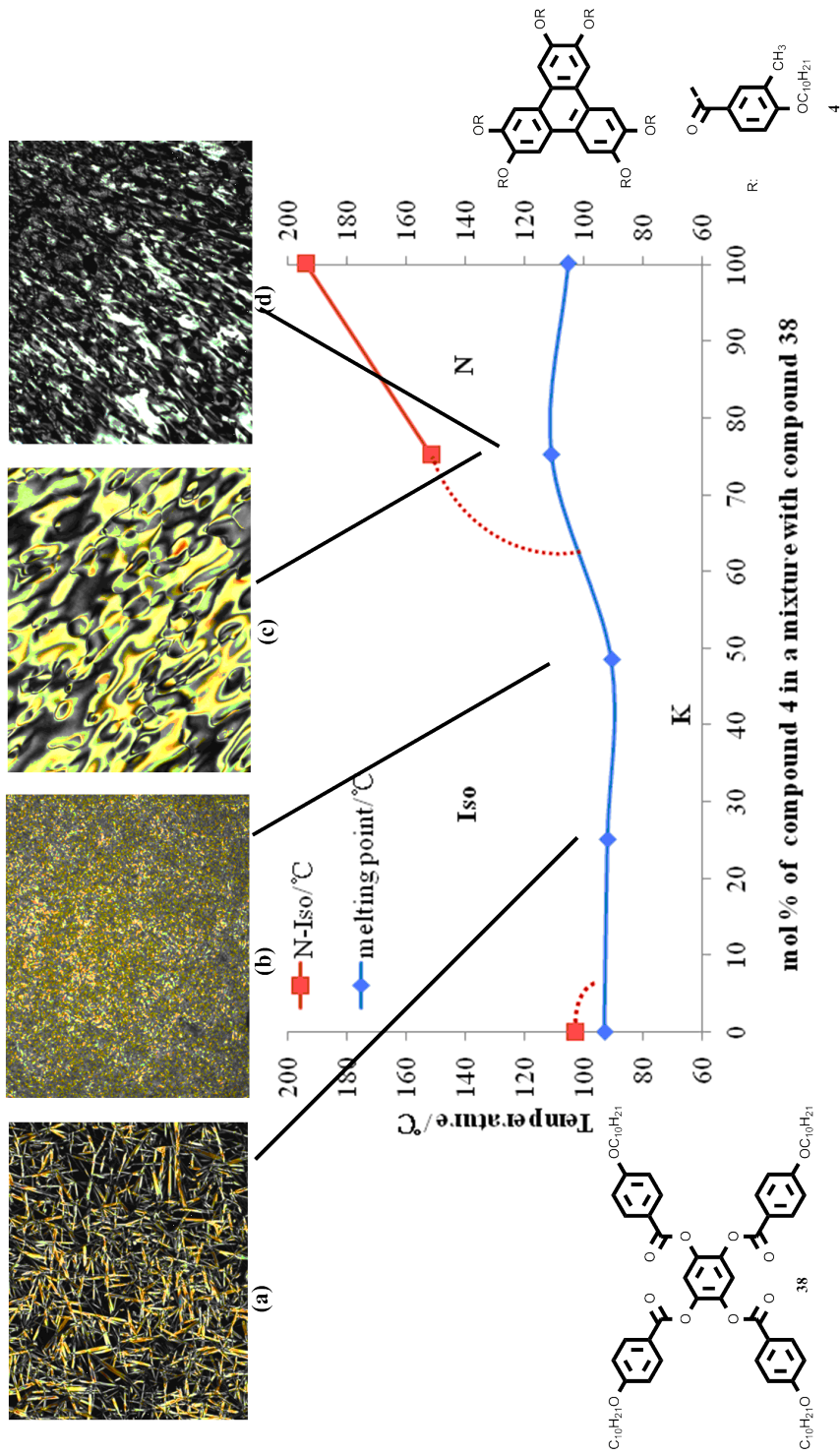


**Figure 5.11** The Gibbs phase diagram for the binary mixture series TZ-M012 of 4 and 38. Photomicrographs (x 100 magnification) showing representative optical textures for TZ-M012: **(a)** 25%, cooling, 100.6 °C, recrystallization; **(b)** 48.4%, cooling, 108.0 °C, recrystallization; **(c)** 75.1%, cooling, 116.9 °C, N; **(d)** 75.1%, heating, 125.6 °C, N.

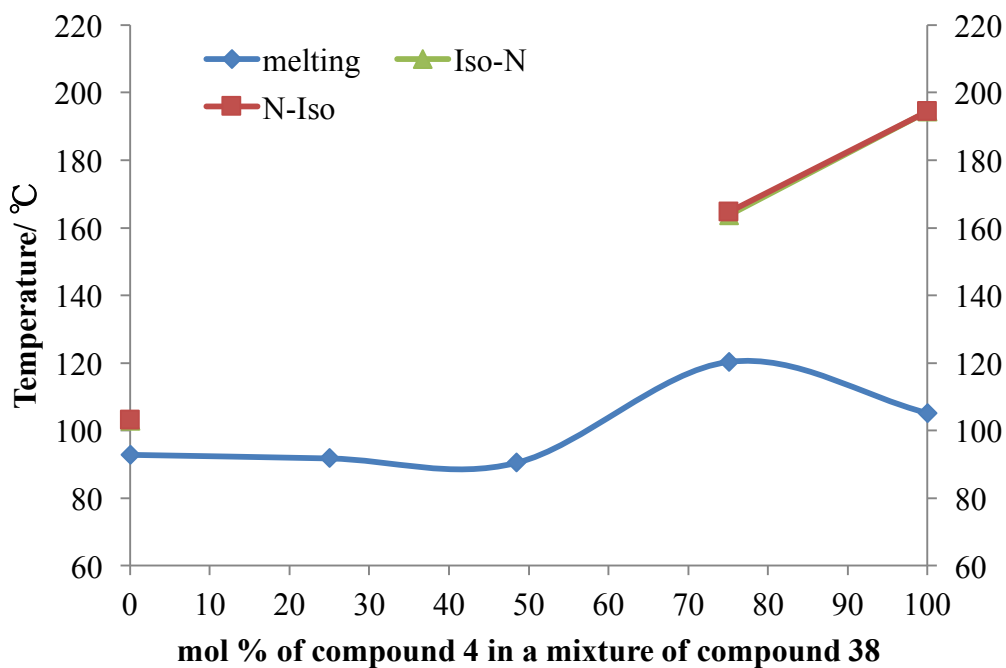


**Figure 5.12** The Gibbs phase diagram showing the biphasic region determined by DSC between heating and cooling for nematic to isotropic transition of mixtures of compounds **4** and **38**.

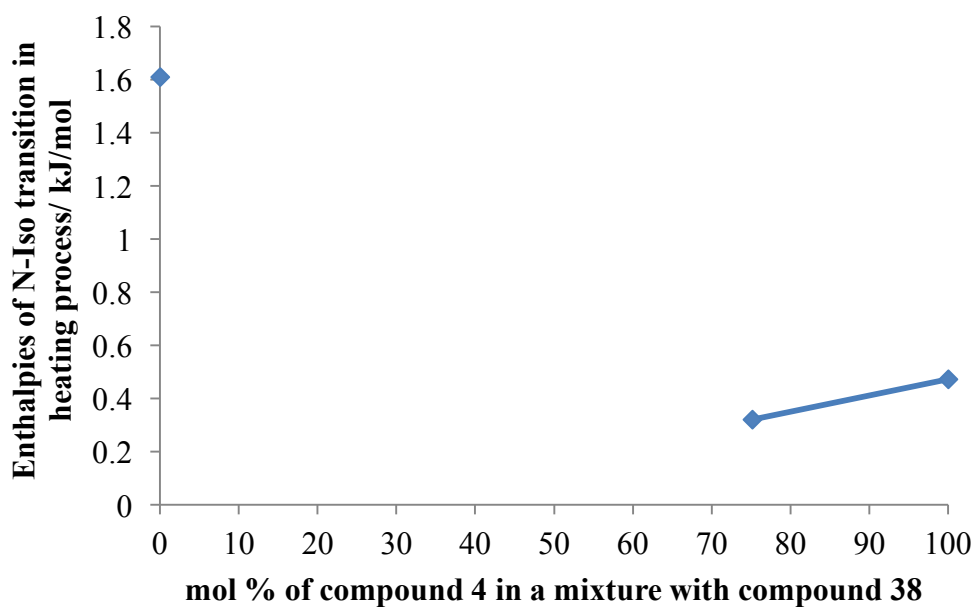


**Figure 5.13** The diagram showing the enthalpies (kJ/mol) of the nematic to isotropic liquid transition in heating process of mixtures of **4** and **38**.

### 5.2.2.2 Studies for Binary Mixtures between Compounds 11 and 51

The binary phase diagram between compounds **11** and **51**, shown in Figure 5.16, was selected for investigation because the diameter of compound **11** was found to be 42.04 Å whereas the diagonal length of compound **51** was determined to be 50.38 Å, and there was an expectation that the longer chains of the tetra-substituted compound **51** might fill the space with interactions of compound **11**. The transition temperatures and chemical structures of the two materials are shown in Figure 5.14, the energy minimised ChemDraw3D space filling structures in gas phase at 0K in Figure 5.14, and simulations based on DFT theory in Figure 5.15.

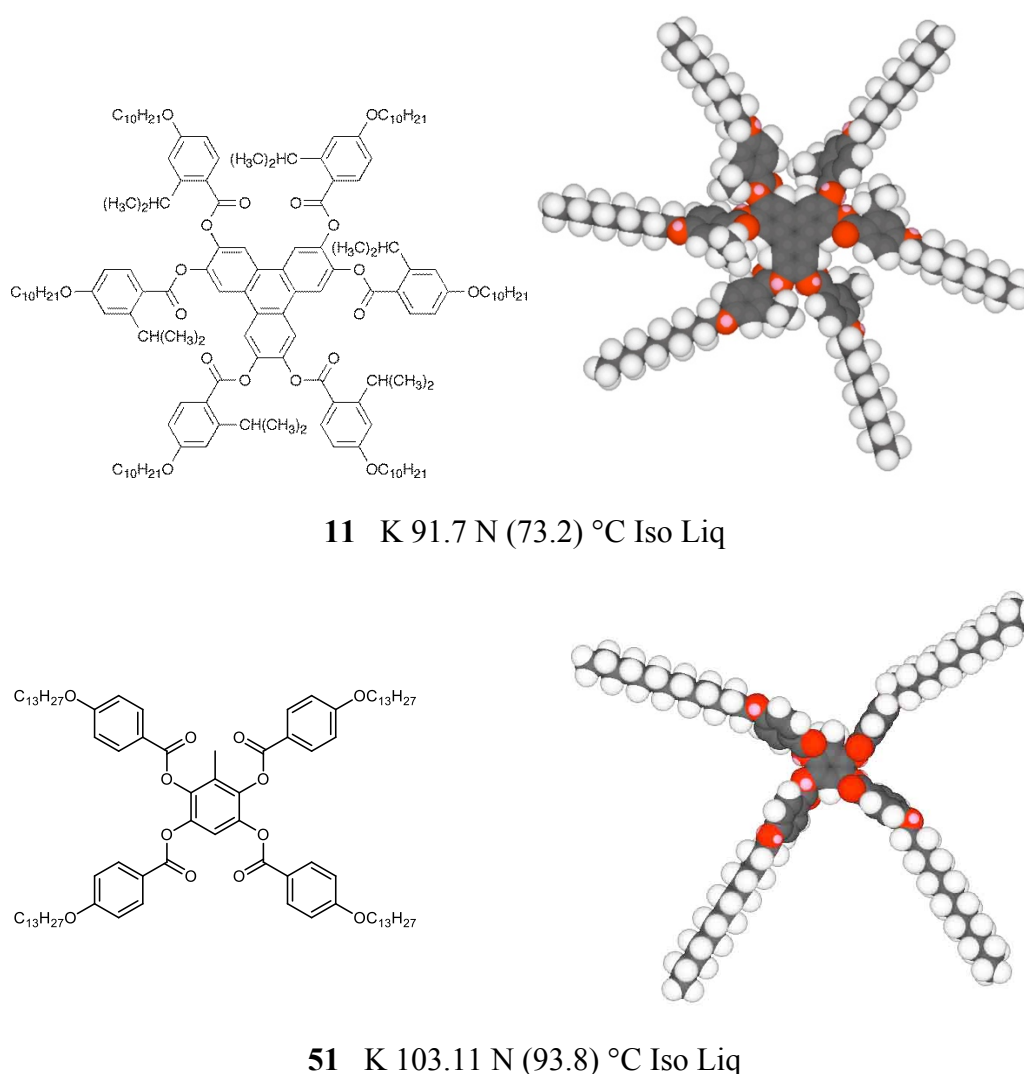
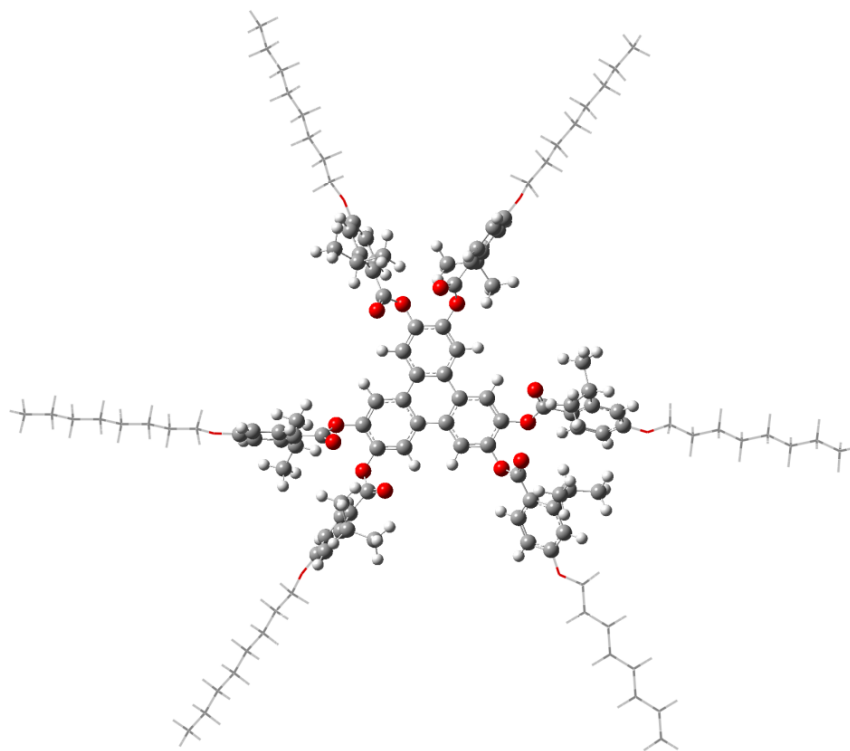
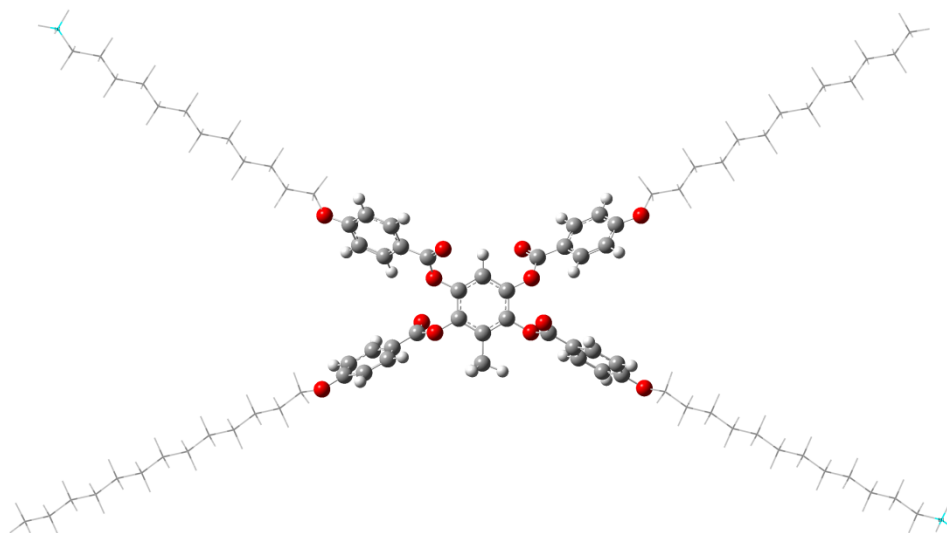


**Figure 5.14** The chemical structures and phase transitions of compounds **11** and **51**, and the space filling structures of compounds **11** and **51** determined in gas phase at 0 K using the MM2 force field as implemented in ChemDraw 3D.



11



51

**Figure 5.15** The energy minimised structures for compounds **11** and **51**, at the ONIOM(B3LYP/6-31G(d):PM6) Level of theory.

Triphenylene liquid crystal **11** and tetra-benzoate ester **51** were both found to exhibit nematic phases. In a similar manner to the previous studies, a series of mixtures (**TZ-M019-1-5**) were prepared and their phase behaviour was examined by POM and then by DSC. The transition temperatures for the various mixtures determined by POM are given in Table 5.7.

The composition of the mixture (**TZ-M019-E**), which was predicted to exhibit the eutectic point for the binary components, was calculated by Schröder van-Laar equation. The transition temperatures for the experimental eutectic mixture were determined by POM and DSC; the results for which are included in Table 5.7. The binary phase diagram for mixtures of compound **11** and **51** with photomicrographs of the phase types is shown in Figure 5.16.

**Table 5.7** Mixture compositions (mol%) and transition temperatures (°C) for binary mixtures of **11** and **51**.

ID	<b>11</b> / mol%	K	/°C	N	/°C	Iso Liq
<b>51</b>	0	.	103.0	.	(93.8)	.
<b>TZ-M019-1</b>	20	.	96.1	-	-	.
<b>TZ-M019-2</b>	40	.	96.8	-	-	.
<b>TZ-M019-3</b>	60	.	93.9	-	-	.
<b>TZ-M019-E</b>	80.7	.	83.8	-	-	.
<b>TZ-M019-4</b>	90	.	89.3	-	-	.
<b>TZ-M019-5</b>	95	.	82.3	-	-	.
<b>11</b>	100	.	91.7	.	(73.2)	.

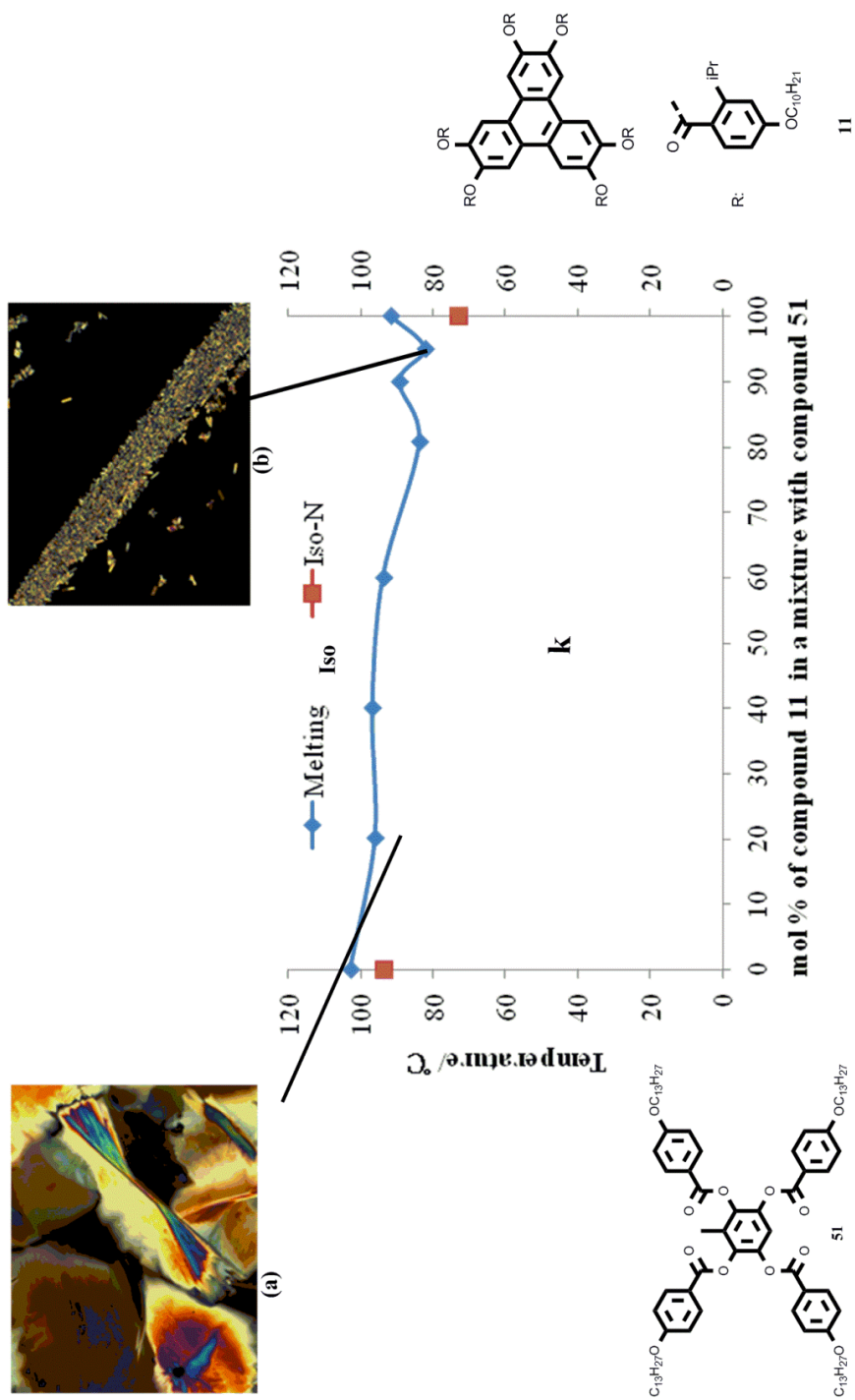


**Figure 5.16** The Gibbs phase diagram for the binary mixture series TZ-M019 of 11 and 51. Photomicrographs (x 100 magnification) showing representative optical textures for TZ-M019: (a) 20%, cooling, 92.3 °C, recrystallization; (b) 95%, heating, 81.8 °C, melting.

The phase diagram in Figure 5.16 shows that the nematic phases are immiscible and that no biaxial nematic phase is observed, thus, the only observations made are for melting processes without any mesophases. This study is supported by the DSC investigations, which showed that the nematic phase was suppressed completely across the diagram. For the melting point curve, it did not appear to have an obvious eutectic point as predicted from the Schröder-van Laar equation.

### 5.2.2.3 Studies for Binary Mixtures between Compounds 27 and 56

Co-miscibility between compounds **27** and **56** was selected for investigation because, with all of the tetra- and hexa-substituted showing immiscibility, it was decided that the inclusion of fluoro substituents in **27** would increase the face-to-face  $\pi$ - $\pi$  interactions with the tetra-substituted system **56**. By increasing the strength of the interactions it was predicted that mesomorphic behaviour would be more likely to be observed. Thus, the binary phase diagram between compound **27** and **56**, as shown in Figure 5.17, was generated. The phase transition temperatures for both materials, the minimised energy structures in gas phase at absolute zero using the MM2 force field as implemented in ChemDraw 3D, and simulations based on DFT theory, are shown respectively in Figures 5.17 to Figure 5.19.

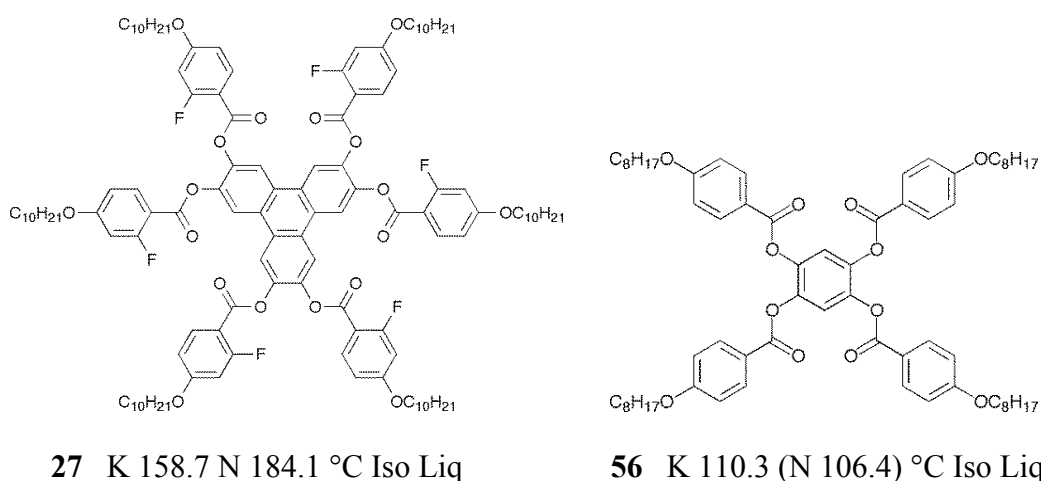
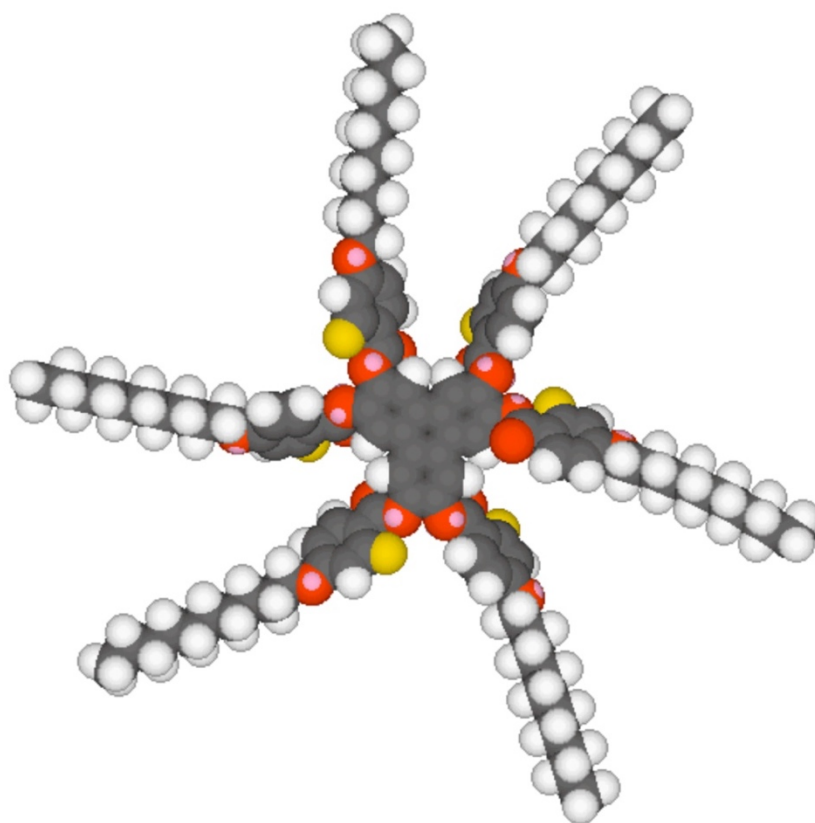
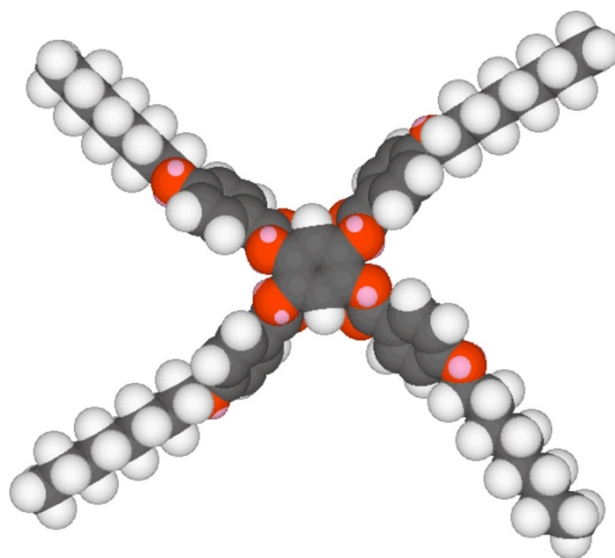


**Figure 5.17** The chemical structures and phase transitions of compounds **27** and **56**.

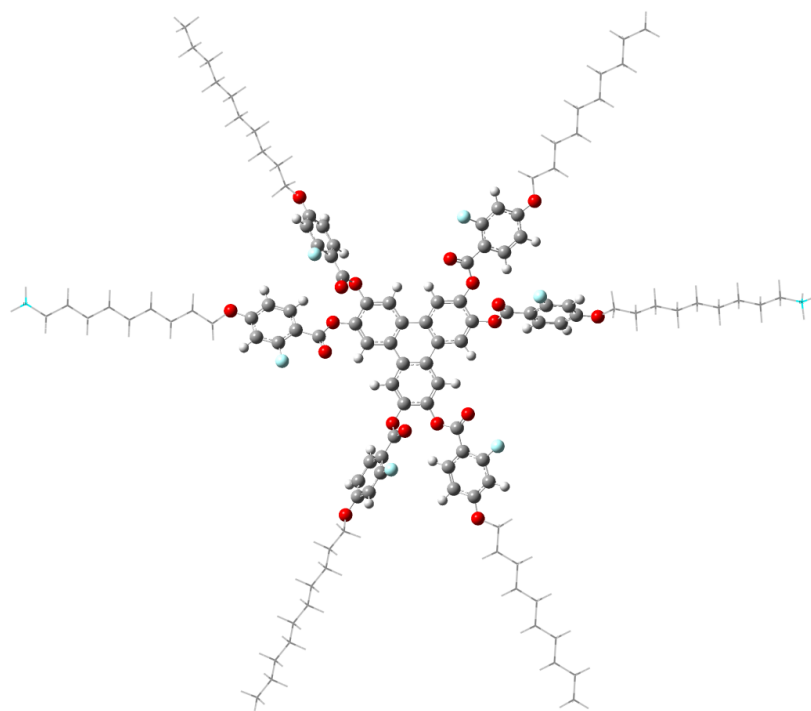


27

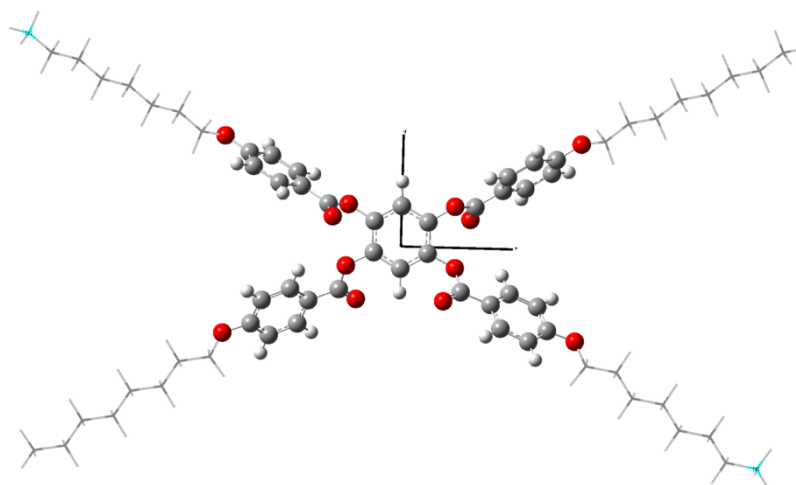


56

**Figure 5.18** The space filling structures of compounds **27** and **56** determined in gas phase at 0 K using the MM2 force field as implemented in ChemDraw 3D.



27



56

**Figure 5.19** The energy structures for compounds **27** and **56**, at the ONIOM(B3LYP/6-31G(d):PM6) Level of theory.

In the simulation results, the diameter of compound **27** was found to be 47.20 Å, whereas the diagonal length for compound **56** was measured to be 38.89 Å. This

relationship between the lengths means that the tetra-substituted material can fit between the triphenylene units in face-to-face orientations, even though the materials all show twisted structures in the computer simulations. These relative relationships will allow for electrostatic interactions to occur over shorter face-to-face distances.

A series of mixtures (**TZ-M021-1-5**) was prepared in different mol ratios of the two components, and their behaviour was examined by POM and then by DSC. The transition temperatures for the various mixtures determined by POM are given in Table 5.8, and those determined by DSC are shown in Table 5.9. The predicted composition of the eutectic mixture **TZ-M021-E** was determined by the calculations from the Schröder-van Laar equation. The experimental results for the predicted eutectic mixture were determined by POM and DSC and are included in Table 5.8 and Table 5.9.

**Table 5.8** Compositions (mol%) and transition temperatures (°C) for binary mixtures of compounds **27** and **56**.

ID	<b>27</b> / mol%	K	/ °C	N	/ °C	Iso Liq
<b>56</b>	0	.	110.3	.	106.4	.
<b>TZ-M021-1</b>	9.9	.	103.0	-	-	.
<b>TZ-M021-2</b>	20	.	101.5	-	-	.
<b>TZ-M021-E</b>	31.6	.	82.0	.	126.4	.
<b>TZ-M021-3</b>	50	.	100.2	.	145.0	.
<b>TZ-M021-4</b>	63.4	.	89.6	.	156.0	.
<b>TZ-M021-5</b>	81.2	.	135.1	.	168.6	.
<b>27</b>	100	.	158.7	.	184.1	.

**Table 5.9** Mixture compositions (mol%) and nematic to isotropic transition temperatures (°C) and enthalpies (J/g) both on heating and cooling for binary mixtures of **56** and **27**.

ID	27/ mol%	N-Iso/ °C	
		Heating	Cooling
<b>56</b>	0	-	106.36
		-	$\Delta H = -1.31$
<b>TZ-M021-1</b>	9.9	-	-
		-	-
<b>TZ-M021-2</b>	20	-	-
		-	-
<b>TZ-M021-E</b>	31.6	-	-
		-	-
<b>TZ-M021-3</b>	50	129.50	110.51
		$\Delta H = 3.17$	$\Delta H = -5.08$
<b>TZ-M021-4</b>	63.4	-	-
		-	-
<b>TZ-M021-5</b>	81.2	-	-
		-	-
<b>27</b>	100	184.43	184.37
		$\Delta H = 0.39$	$\Delta H = -0.34$

The binary phase diagram for the results given in Table 5.8 is shown with the photomicrographs of the defect textures at various concentrations in Figure 5.20. Firstly, the nematic to isotropic liquid phase changes and transition temperatures are shown with a red dotted line because of the uncertainty of observation of the phase transitions in the microscopy due to the weakness of the light transmission. For example, the nematic phase of mixtures 31.6 mol% of **27** and 50% mol of **27** were only observed when they were heated up, and the nematic phase of mixtures 63.4% of **27** and 81.2% of **27** had short temperature ranges when cooled down. Nevertheless, although the photomicrographs appear dark there is a clear indication of the presence of a nematic phase. For the 9.9 and 20 mol% of

compound **27** in the binary mixtures there was no indication that a nematic phase was present. Thus it seems that the nematic phase disappears on passing right to left across the phase diagram and is no longer present at a value of the concentration of **27** just above the 20 mol% point. This indicates that the nematic phases of the two compounds are not miscible. However, an appreciable degree of co-miscibility was achieved indicating that the nematic phase was relatively stable across the phase diagram, unlike the other mixtures discussed earlier between tetra- and hexa-substituted materials, which typically showed nearly total immiscibility. This indicates that the combination of fluoro-substituted materials with non-fluorinated systems appear to form strong and stable interactions which favour the formation of discotic nematic mesophases.[103] At low concentrations of compound **27** no mesophases were observed, but it is likely that if a biaxial phase were to be formed it would be in this concentration range as the calamitic nematic phase crosses over to form a discotic nematic as the percentage of **27** is increased.

Furthermore, the concentration value for the predicted eutectic was 31.6 mol% of compound **27**. This value corresponds to one of two depressions in the melting curve of the phase diagram, thereby indicating that this point is probably a eutectic. The other minimum is approximately 63.4 mol% of compound **26**. Thus between 31.6 and 63.4 mol% the maximum in the melting point suggests that there are strong A-B intermolecular associations between the two components, unlike at lower or higher concentration ranges where the interactions are dominated by one of the components. Again this is an indicator of areas in which to search for the elusive biaxial nematic phase.

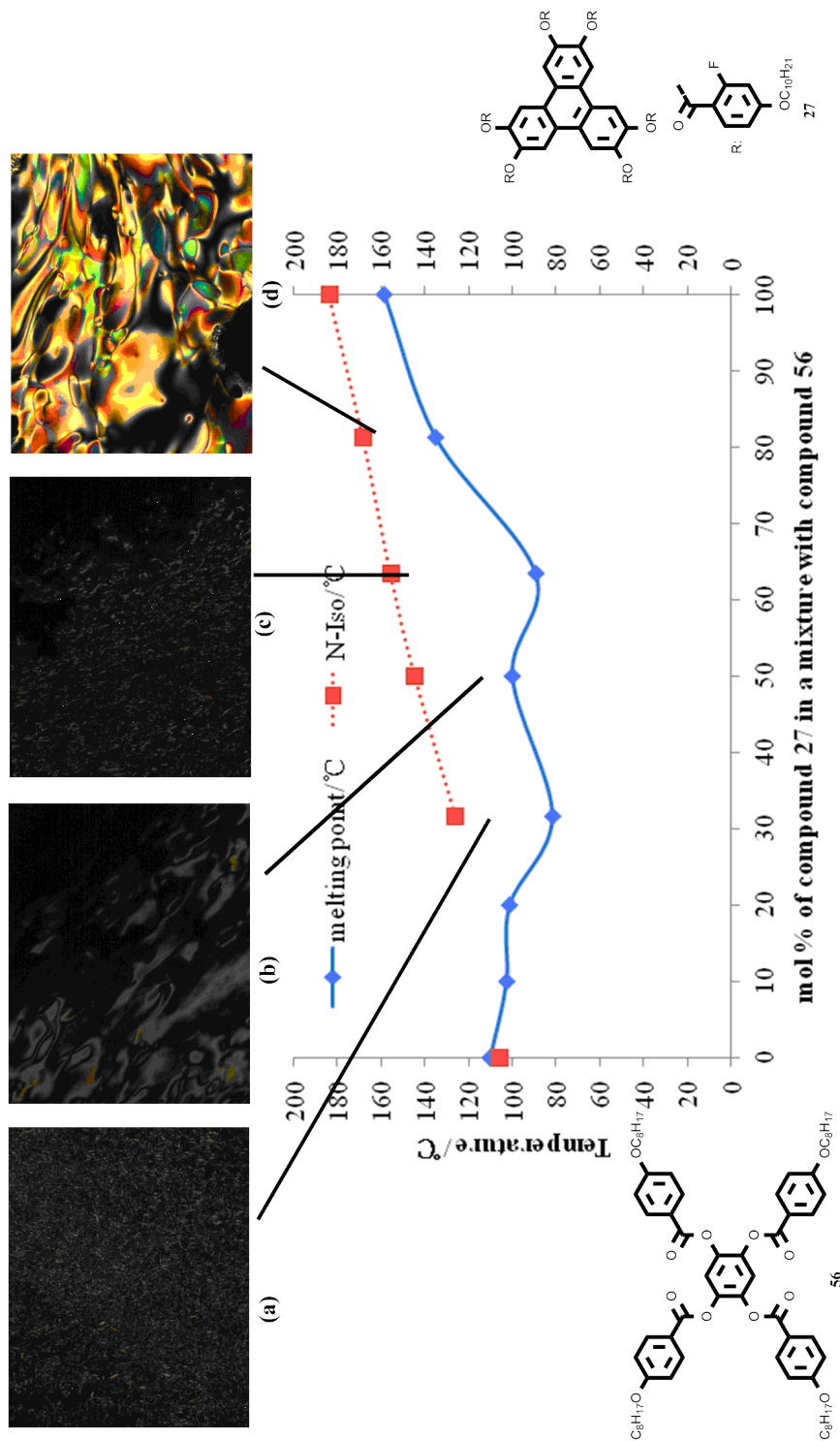


**Figure 5.20** The Gibbs phase diagram for the binary mixture series **TZ-M021** of **27** and **56**. Photomicrographs (x 100 magnification) showing representative optical textures for **TZ-M021**: **(a)** 31.6% heating, 113.6 °C, N; **(b)** 50%, heating, 113.8 °C, N; **(c)** 63.4%, heating, 150 °C, N; **(d)** 81.2%, heating, 156.8 °C, N.

In order to investigate the phase behaviour further, and to obtain accurate values for the transition temperatures on heating and cooling for the mixtures in the phase diagram, calorimetric studies were performed for each individual mixture, the results for which are shown in Table 5.9 along with the enthalpies for the transitions from the DSC.

The binary phase diagram for the transition temperatures determined by calorimetry is shown in Figure 5.21. Firstly, the results are broadly in agreement with the phase diagram obtained by microscopy, but no nematic to isotropic liquid phase transition peak could be seen for the 31.6 mol%, 63.4 mol%, and 81.2 mol% of compound **27**. Additionally, the temperatures between heating and cooling cycles show supercooling for the 50 mol% of compound **27**.

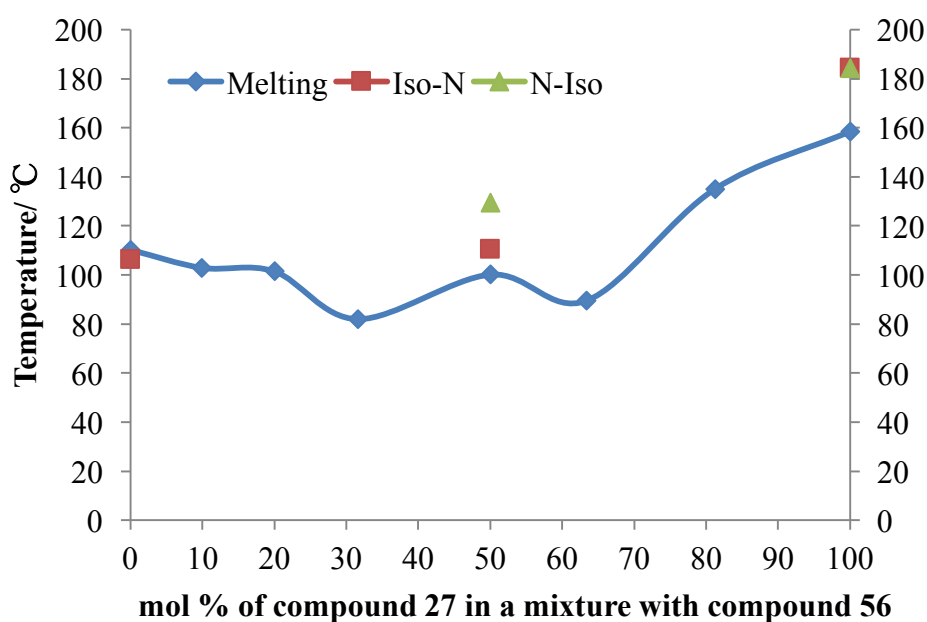


**Figure 5.21** The Gibbs phase diagram showing the biphasic region determined by DSC between heating and cooling for nematic to isotropic transition of mixtures of compounds **27** and **56**.

If we examine the values of the enthalpies of the phase transitions as a function of concentration, as shown in Figure 5.22, it can be seen that the difference in the

values of the enthalpies for the N-I phase transitions for compounds **27** and **56** are approximately not an order of magnitude different, and that the value of the enthalpies for 50 mol% show smaller difference with compound **27** compared with both compound **56**, indicating that the 50-50 mixture has a stabilised structure order.

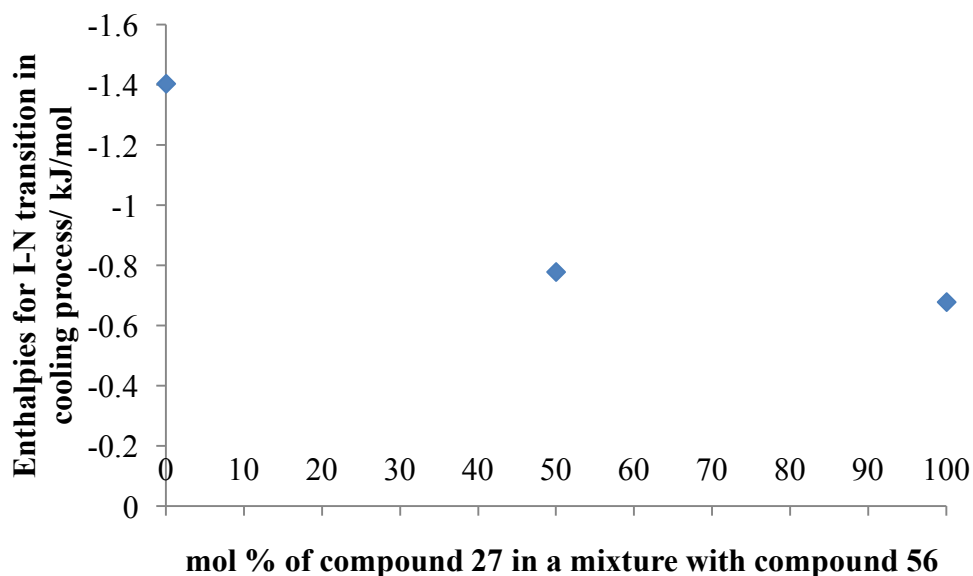
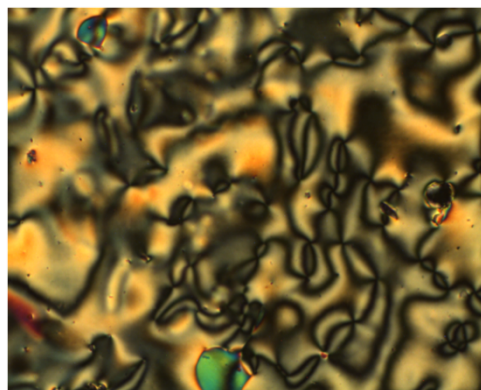
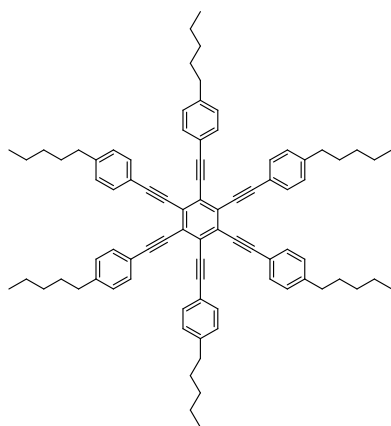


**Figure 5.22** The diagram showing the enthalpies (kJ/mol) for the nematic to isotropic liquid transition in cooling process of mixtures of **27** and **56**.

### 5.2.3 Co-miscibility of disc-like triphenylene mesogens with phenyl hexa-alkynes

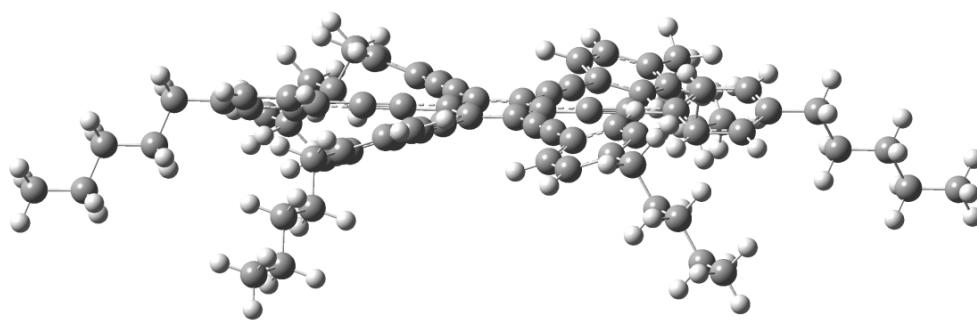
Since the phenyl tetra-esters apparently have rod-like shapes, and miscibility with hexa-substituted systems was not achieved, in the following sections it was decided to see if concentrated electron rich disc-like systems would mix with the more traditional  $\pi$ -conjugated disc-like systems. Therefore, studies of mixtures between disc-like alkyne hexa-substituted benzenes with aromatic triphenylene hexa-esters, were investigated. Sandeep Kumar has reported several new benzene hexa-alkynes and penta-alkynes which were prepared and characterized, and two of them showed very broad discotic nematic mesophase stabilities in ranges from

well below room temperature on supercooling to relatively high temperatures on heating, thereby giving the opportunity to study nematogenic mixtures over wide ranges.[92-93] These materials were prepared and used in studies of co-miscibility. The structures and phase transition temperatures, the energy minimised space-filling structures using ChemDraw3D in gas phase at absolute zero, and molecular simulations using DFT theory for compound **16** are shown in Figure 5.23 and 5.24.

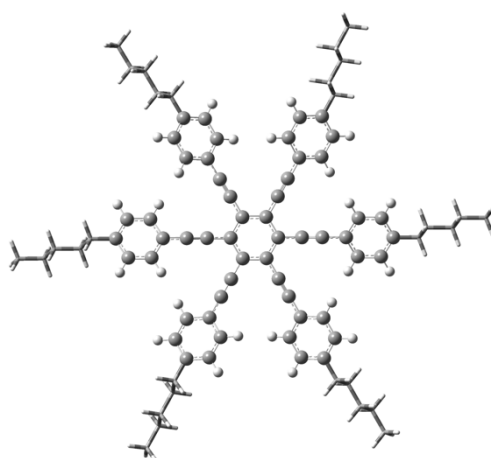


**64** K 166.0 N 183.8 °C Iso Liq

**Figure 5.23** The structure of compound **64**, and the respective photomicrograph for nematic texture at 178.0 °C.



XY-view



Z-view

**Figure 5.24** The energy minimised structures for compound **64**, at the mixed ONIOM(B3LYP/6-31G(d):PM6) Level of theory. The diameter of the material is 28.045 Å. geometry was minimised using the ONIOM method as implemented in Gaussian G09 revision D.01, with the B3LYP/6-31G(d) method used for the 'core' and the PM6 semi-empirical method used for the aliphatic chains.

### 5.2.3.1 Mixture Studies between Compounds **16** and **64**

The first binary phase diagram in this series of studies involved compounds **16** and **64**. These materials were selected for study because it was thought that the alkynic material **64** would have a flat electron concentrated disc-like structure, whereas the hexa-substituted triphenylene compound **16** would have a twisted structure due to lateral methyl groups in the peripheral rings. Thus it was expected that compound **16** would sterically interfere with the face-to-face interactions of

compound **64**, which was predicted to stabilise the formation of the nematic phase. Thus, the binary phase diagram between the two compounds is presented in Figure 5.28.

The structures and phase transition temperatures, the energy minimised space-filling structures using the MM2 force field as implemented in ChemDraw 3D in gas phase at absolute zero, and molecular simulations using DFT theory for compounds **16** and **64** are shown respectively in Figures 5.25 to 5.27.

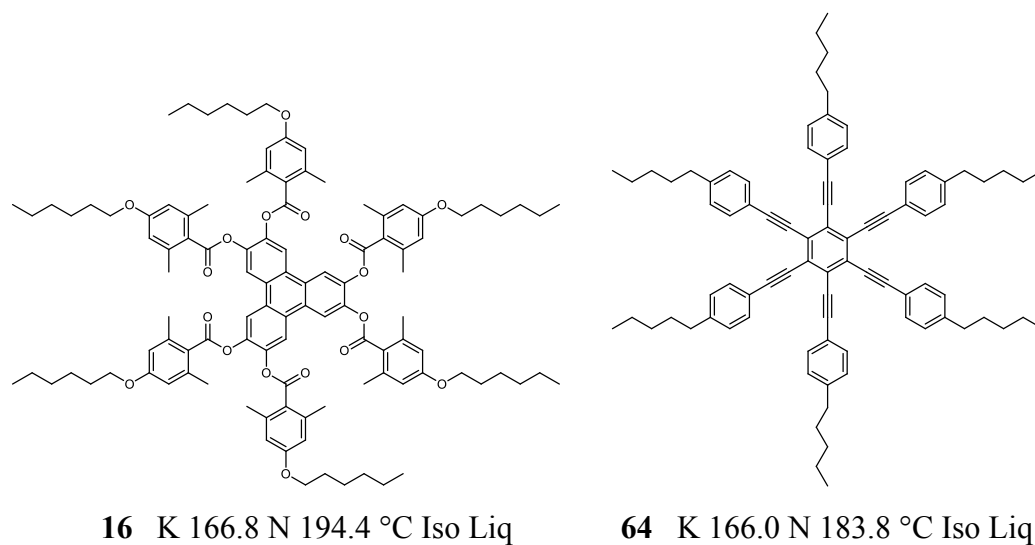
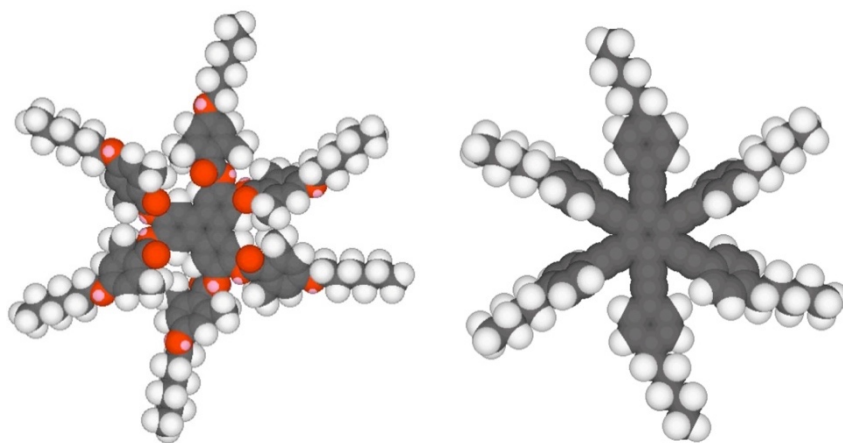


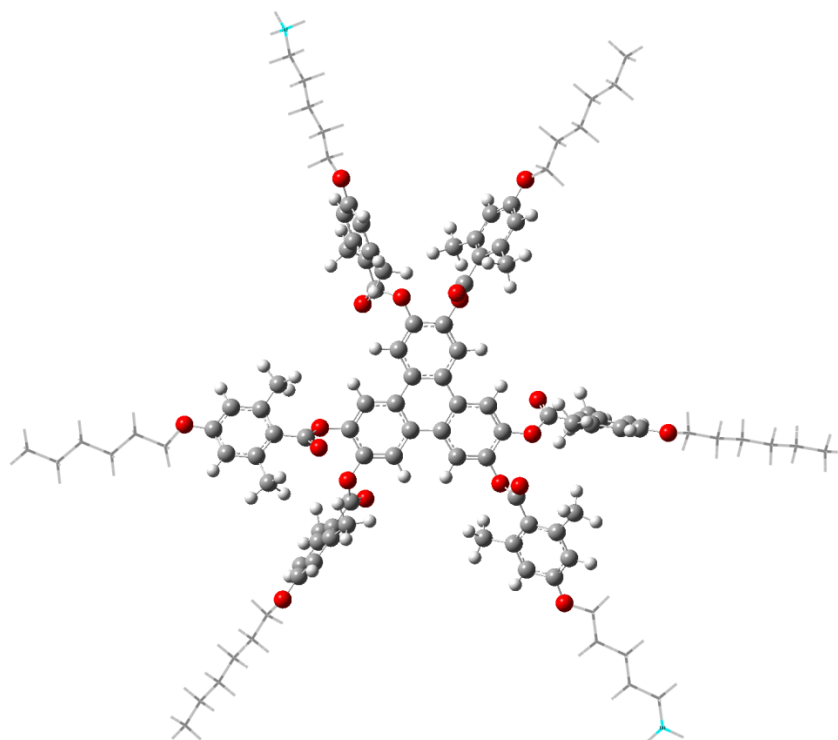
**Figure 5.25** The chemical structures and phase transitions (°C) for compounds **16** and **64**.



**16**

**64**

**Figure 5.26** The space filling structures of compounds **16** and **64** determined in gas phase at 0 K using the MM2 force field as implemented in ChemDraw 3D.



**16**

**Figure 5.27** The energy structure for compound **16**, at the mixed ONIOM(B3LYP/6-31G(d):PM6) Level of theory.

From the simulated structures, the diameter of compound **16** is 37.03 Å and the diameter of compound **64** is 28.05 Å, thus **64** is smaller than **16** and will fit in between the face-to-face packing of molecules of **64**. For compound **16**, at least in gas phase, four of the peripheral aromatic rings are twisted of the plane of the triphenylene core, whereas all of the peripheral aromatic rings and the central phenyl unit of compound **64** are co-planar and the molecular architecture is flat.

For the mixture studies, a series of mixtures (**TZ-M022-1-4**) of compounds **16** and **64** were prepared in different mol ratios of the two components and examined by POM and then by DSC. The transition temperatures for the various mixtures determined by POM are given in Table 5.10, whereas those determined from DSC, which are in agreement, are given in Table 5.11.

**Table 5.10** Compositions (mol%) and transition temperatures (°C) for binary mixtures of **16** and **64** determined by POM.

ID	<b>16</b> / mol%	K	/°C	N	/°C	Iso Liq
<b>64</b>	0	.	166.0	.	183.8	.
<b>TZ-M022-1</b>	15	.	155.6	.	187.7	.
<b>TZ-M022-2</b>	31.7	.	152.9	.	183.0	.
<b>TZ-M022-E</b>	49.4	.	140.8	.	179.7	.
<b>TZ-M022-3</b>	65	.	153.2	.	191.5	.
<b>TZ-M022-4</b>	85	.	153.2	.	195.2	.
<b>16</b>	100	.	168.8	.	194.4	.

**Table 5.11** Mixture compositions (mol%) and transition temperatures (°C) and enthalpies (J/g) both on heating and cooling for binary mixtures of **16** and **64**.

ID	16/ mol%	N-Iso/ °C	
		Heating	Cooling
<b>64</b>	0	184.76	192.80
		$\Delta H = 0.28$	$\Delta H = -0.20$
<b>TZ-M022-1</b>	15	191.01	-
		$\Delta H = 0.23$	-
<b>TZ-M022-2</b>	31.7	186.64	163.14
		$\Delta H = 0.49$	$\Delta H = -0.12$
<b>TZ-M022-E</b>	49.4	194.45	178.16
		$\Delta H = 0.29$	$\Delta H = -0.97$
<b>TZ-M022-3</b>	65	192.85	186.65
		$\Delta H = 0.22$	$\Delta H = -0.18$
<b>TZ-M022-4</b>	85	196.06	195.54
		$\Delta H = 0.18$	$\Delta H = -0.23$
<b>16</b>	100	195.21	195.15
		$\Delta H = 0.26$	$\Delta H = -0.18$

The predicted composition of the eutectic mixture (**TZ-M022-E**) was determined for the binary components using the Schröder-van Laar equation (49.4 mol% of **16**). The results obtained for the experimental ‘eutectic’ mixture were determined from POM and DSC, and are included in both tables. Interestingly, not only does the eutectic mixture have the lowest melting point with respect to the other mixtures as predicted, it also exhibits marginally the highest clearing point.

The binary phase diagram for the POM results is shown in Figure 5.28, incorporating photomicrographs of the detect textures at various concentrations in the diagram. It can be seen from the figure that on heating the N to I curve varies almost linearly with respect to concentration. Furthermore, the heating cycle results obtained from POM and DSC concur with one another. Conversely the

cooling results for the DSC data show that at the concentration of 15 mol% of **16** the I-N phase transition peak disappears. This hysteresis behaviour in the liquid to liquid crystal phase transition is exemplified in Figure 5.29, where for the cooling cycles the curve for the I-N transition suffer a depression when the mol percentage of compound **16** decreases.

In order to investigate further the phase behaviour, the enthalpies for the N-I phase transitions for each mixture from the DSC, both on heating and cooling, are shown in Figure 5.30. In the Figure it can be seen that the enthalpies for the heating process vary from 0.3 to 0.7 kJ/mol, they do not show big differences between the different concentrations. However, for the enthalpies for the cooling process at the point of 49.4 mol% of compound **16** give a larger difference compared with all the other concentrations, and also at 15 mol% of compound **16**, there is no peak value for the isotropic liquid to nematic phase transition as shown in the DSC curve for mixture **TZ-M022-1** in Figure 5.31.

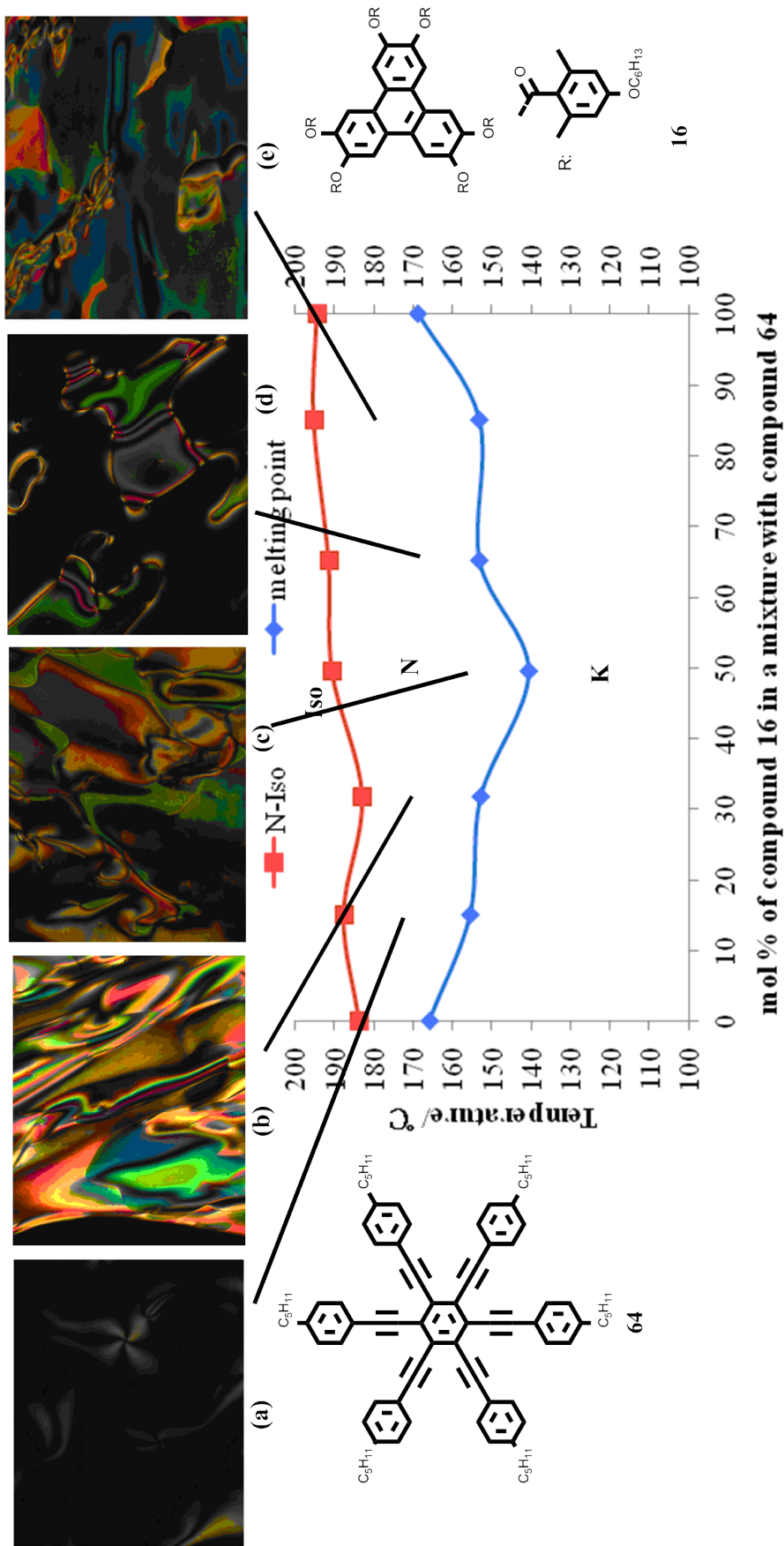


**Figure 5.28** The Gibbs phase diagram obtained from the binary mixture series **TZ-M022**. Photomicrographs (x100 magnification) showing representative optical textures for **TZ-M022**: **(a)** 15.0%, heating, 175.6 °C, N; **(b)** 31.7%, heating, 169.0 °C, N; **(c)** 49.4%, heating, 168.7 °C, N; **(e)** 65%, cooling, 153.6 °C, N; **(f)** 85%, heating, 168.8 °C, N.

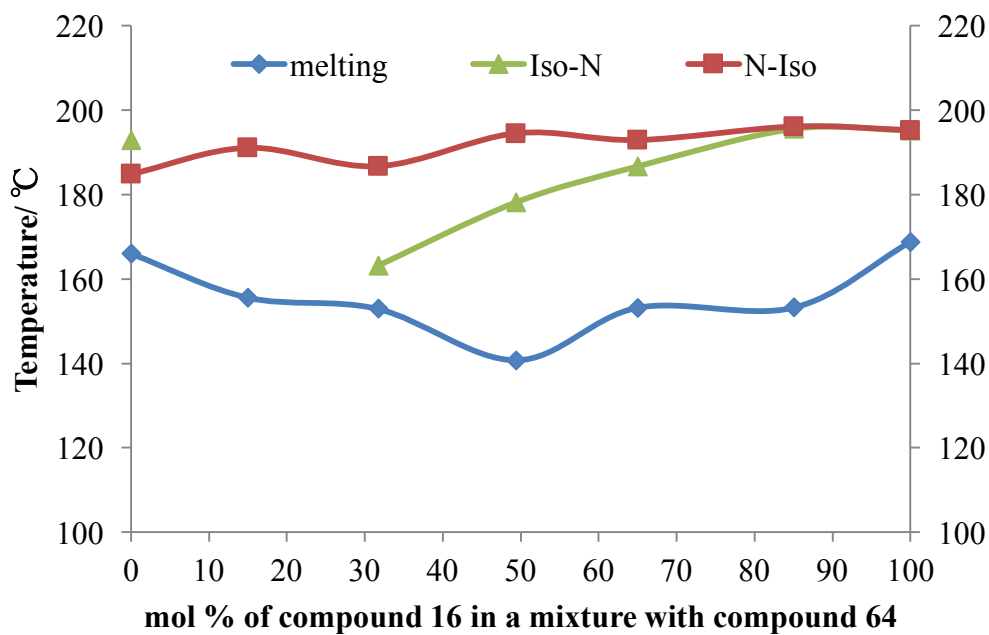


**Figure 5.29** The Gibbs phase diagram showing the biphasic region between heating and cooling for transition of mixtures of **16** and **64**.

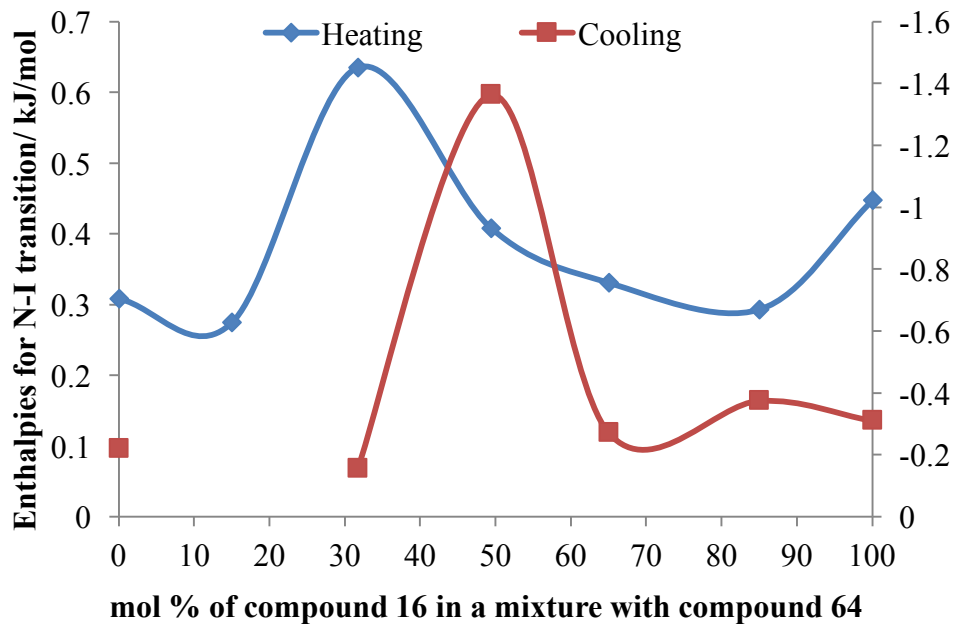


**Figure 5.30** The enthalpies (kJ/mol) for nematic to isotropic liquid transition in both heating and cooling process of the mixtures of **16** and **64**.

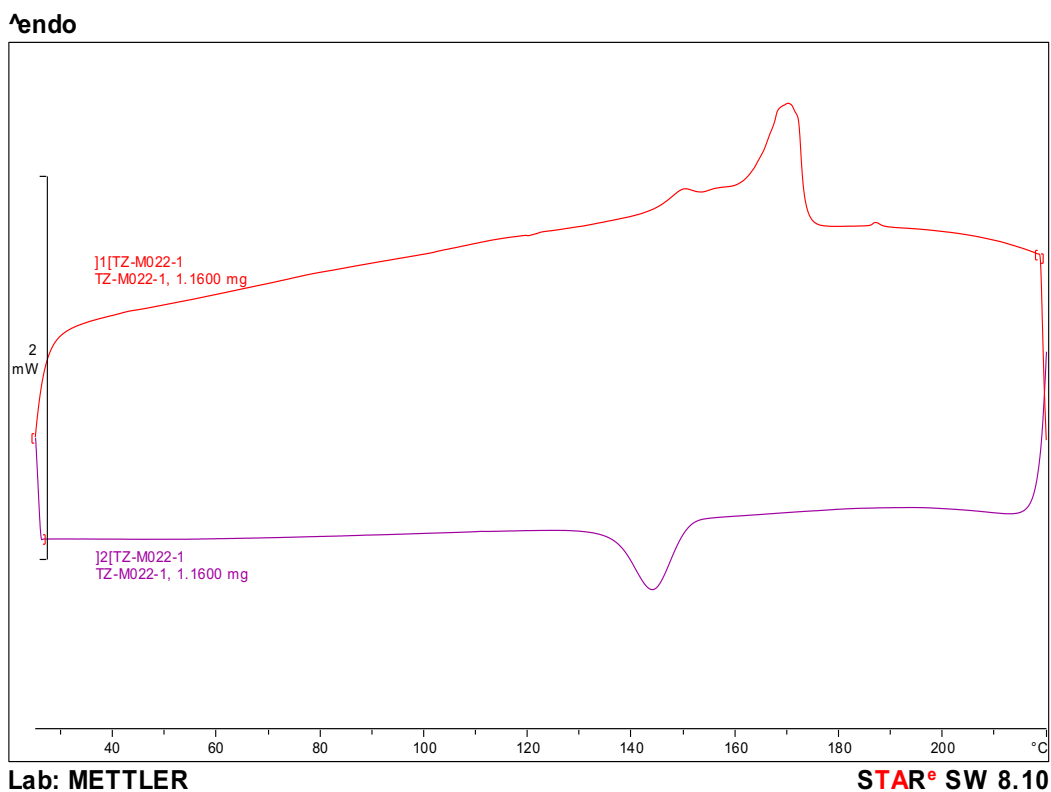
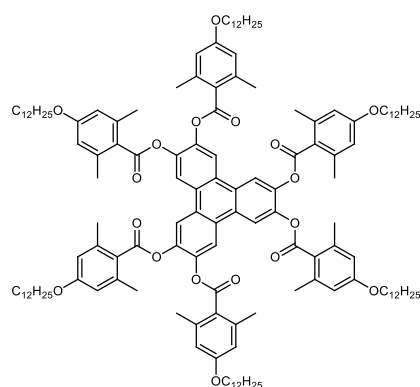


**Figure 5.31** The DSC tracing result for the mixture **TZ-M022-1** both on heating and cooling of the first cycle.

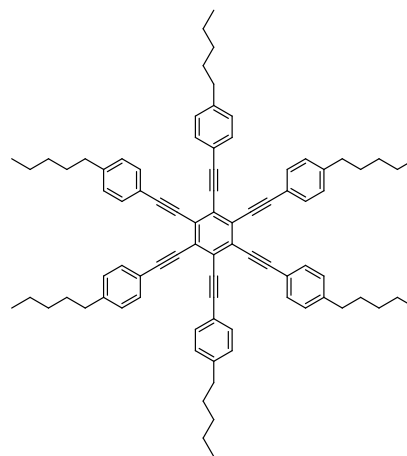
### 5.2.3.2 Mixture Studies between Compounds **18** and **64**

Following on from the previous study, a binary phase diagram between compounds **18** and **64** was constructed. Compound **64** remains the same, but compound **18** has a much larger diameter than **16** due to the longer aliphatic chains.

The structures and phase transition temperatures, the energy minimised space-filling structures using the MM2 force field as implemented in ChemDraw 3D in gas phase at absolute zero, and molecular simulations using DFT theory for compounds **18** and **64** are shown respectively in Figures 5.32 to 5.34.

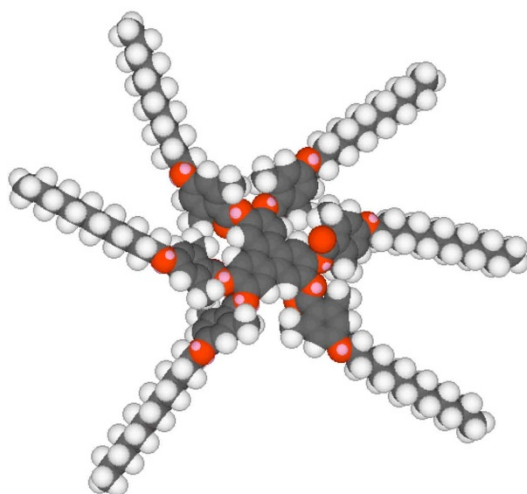


**18** K 84.2 N 91.8 °C Iso Liq

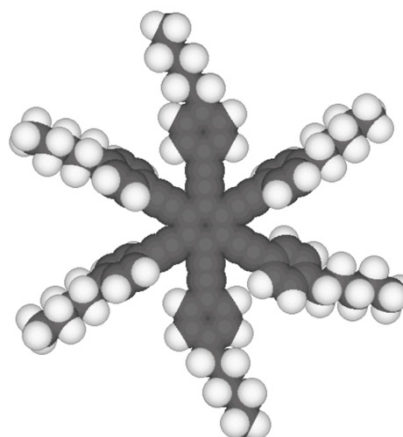


**64** K 166.0 N 183.8 °C Iso Liq

**Figure 5.32** The chemical structures and phase transitions of compound **18** and **64**.

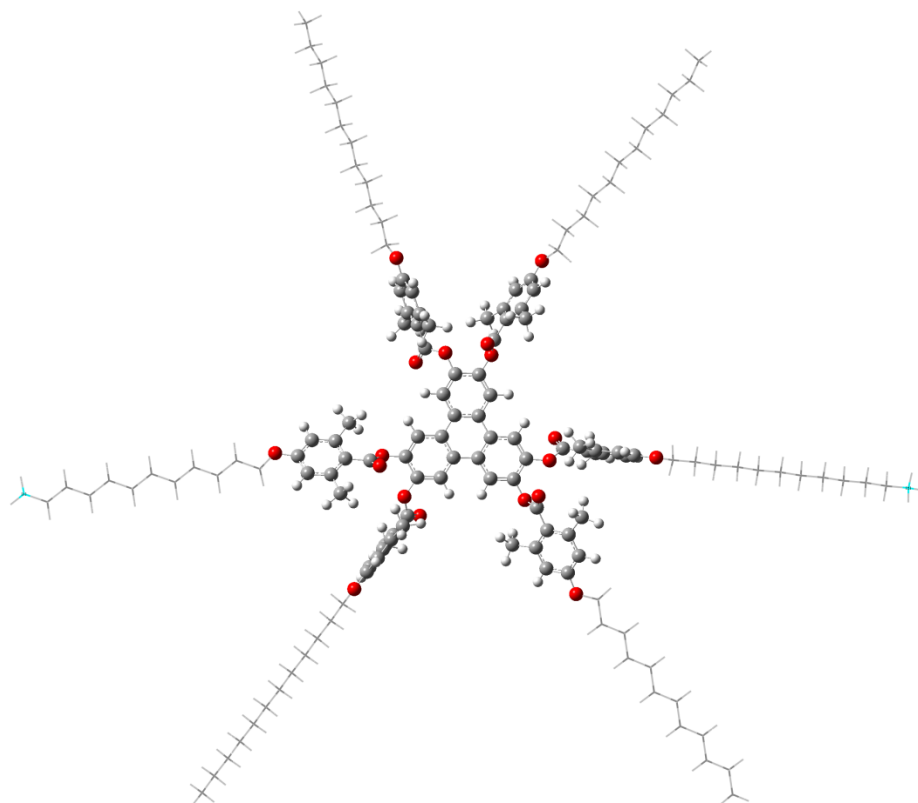


**18**



**64**

**Figure 5.33** The space filling structures of compounds **18** and **64** determined in gas phase at 0 K using the MM2 force field as implemented in ChemDraw 3D.



**18**

**Figure 5.34** The energy structure for compound **18**, at the mixed ONIOM(B3LYP/6-31G(d):PM6) level of theory.

In the simulated structures, the disc diameter of compound **18** was found to be 52.12 Å, and the disc diameter of compound **64** was 28.05 Å. Thus, compound **64** will sit well within the perimeter of **18**, and so packing of the molecules together will allow for the peripheral aliphatic chains to fill the space between the edges of the molecules. Two of the peripheral aromatic rings of compound **18** were found to be twisted at 90° out of the plane of the central triphenylene core, whereas all the peripheral aromatic rings of compound **64** were found to be in the same plane as the central benzene core. Thus the stereochemical structure of compound **18** will envelope that of compound **64** thereby allowing face-to-face packing to be favoured, particularly in binary mixtures where compound **18** is in higher concentration.

A series of mixtures (**TZ-M023-1-5**) were prepared in different mol ratios of the two components, additionally their phase behaviour was examined by POM and secondly by DSC. The transition temperatures for the series of mixtures determined by POM are given in Table 5.12, whereas those determined from DSC are shown in Table 5.13. The predicted composition of the eutectic mixture (**TZ-M023-E**) was determined for the binary components using the Schröder-van Laar equation; the phase behaviour (mp 87.6 and N to I 130 °C) was determined by both POM and DSC as shown in both Tables.

The binary phase diagram constructed for the results shown in Table 5.12 is displayed in Figure 5.35. In addition, photomicrographs of the defect textures at various concentrations are incorporated into the figure.

**Table 5.12** Compositions (mol%) and transition temperatures (°C) for binary mixtures of **18** and **64** determined by POM.

ID	18/ mol%	K	/°C	N	/°C	Iso Liq
<b>64</b>	0	.	166.0	.	183.8	.
<b>TZ-M023-1</b>	20	.	158.3	.	176.6	.
<b>TZ-M023-2</b>	40.1	.	146.1	-	-	.
<b>TZ-M023-3</b>	59.9	.	141.4	-	-	.
<b>TZ-M023-4</b>	75	.	135.7	-	-	.
<b>TZ-M023-E</b>	89.9	.	87.6	.	130.0	.
<b>TZ-M023-5</b>	95	.	87.5	.	136.0	.
<b>18</b>	100	.	84.2	.	91.8	.

**Table 5.13** Mixture compositions (mol%) and transition temperatures (°C) and enthalpies (J/g) both on heating and cooling for binary mixtures of **18** and **64**.

ID	18/ mol%	Melting/ °C	N-Iso/ °C	
			Heating	Cooling
<b>64</b>	0	166.01	184.76	192.80
		$\Delta H = 53.98$	$\Delta H = 0.28$	$\Delta H = -0.20$
<b>TZ-M023-1</b>	20	158.28	-	-
		$\Delta H = 25.50$	-	-
<b>TZ-M023-2</b>	40.1	146.12	-	-
		$\Delta H = 12.84$	-	-
<b>TZ-M023-3</b>	59.9	141.42	-	-
		$\Delta H = 5.35$	-	-
<b>TZ-M023-4</b>	75	135.66	-	-
		$\Delta H = 2.18$	-	-
<b>TZ-M023-E</b>	89.9	87.61	134.78	-
		$\Delta H = 12.28$	$\Delta H = 0.18$	-
<b>TZ-M023-5</b>	95	87.49	127.02	-
		$\Delta H = 11.74$	$\Delta H = 0.12$	-
<b>18</b>	100	84.20	94.62	98.51
		$\Delta H = 15.03$	$\Delta H = 3.39$	$\Delta H = -0.10$

The binary phase diagram shown in Figure 5.35 was not actually as the Schröder-van Laar equation predicted. From the figure, it is shown that for the high and the low concentrations of compound **18** in the mixtures nematic mesophases were displayed (below 20 mol% of **18** and above 85 mol% of **18**). However, in between 20 mol% and 85 mol% of **18**, the mixtures were liquid-like after melting. In addition, the N-I transition and melting point temperatures were deeply depressed after 70 mol% of **18**.

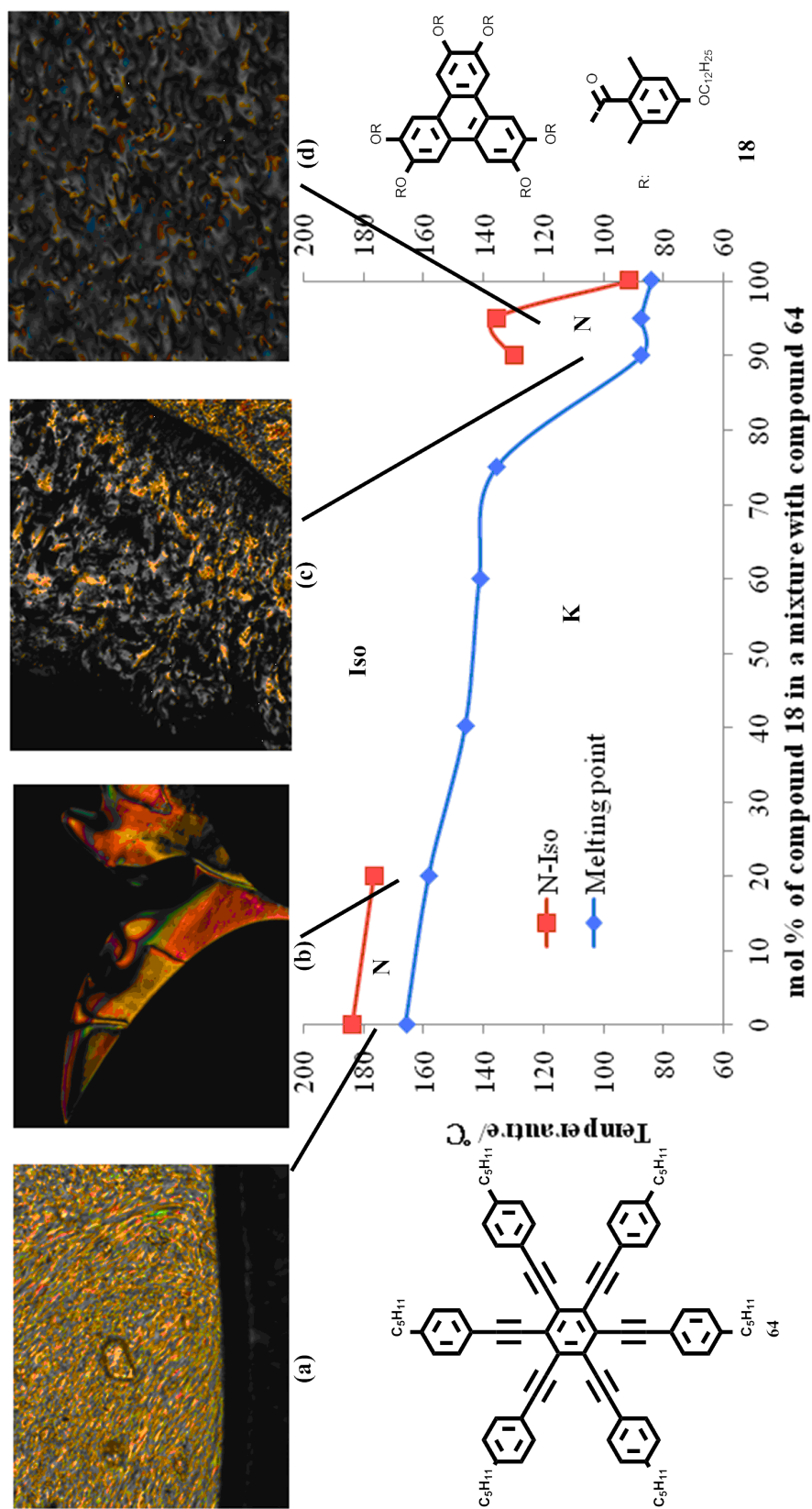


**Figure 5.35** The Gibbs phase diagram for the binary mixture series TZ-M023-1-5 of 18 and 64. Photomicrographs (x100 magnification) showing representative optical textures for TZ-M023: (a) 18, heating, 93.3 °C, N; (b) 20.0%, heating, 170.7 °C, N; (c) 89.9%, heating, 94.9 °C, N; (d) 95%, cooling, 91.1 °C, N.

In order to investigate this behaviour further, and to obtain accurate values for the transition temperatures on heating and cooling for the mixtures in the phase diagram, calorimetric studies were performed for each individual mixture; the results for which are shown in Table 5.13 along with the enthalpies for transitions.

The binary phase diagram for the transition temperatures determined by calorimetry, as shown in Figure 5.36, is broadly in agreement with the phase diagram obtained from thermal optical microscopy studies. In the region between 20 to 75 mol% of compound **18** in the phase diagram, no enthalpies for a nematic to liquid transition were detected by DSC on both heating or cooling cycles. This is in agreement with the absence of mesophases in the microscopy studies. Furthermore, between 90 to 95 mol% of compound **18**, DSC only detected the enthalpies during the heating process, but for the cooling process, no enthalpies were observed. Thus nematic phases were only observed on heating.

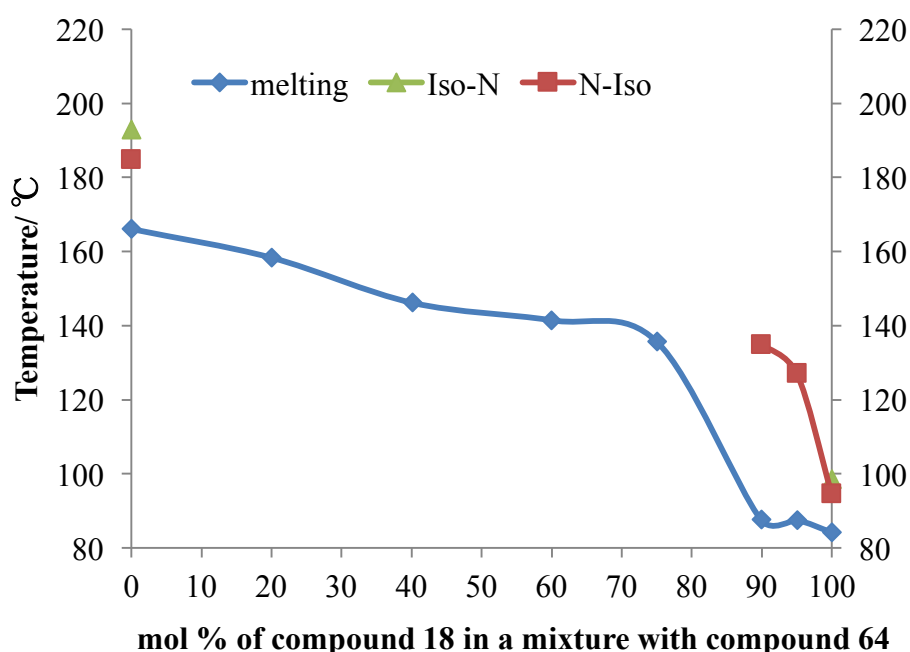


**Figure 5.36** The Gibbs phase diagram showing the biphasic region between heating and cooling for transition of mixtures of **18** and **64**.

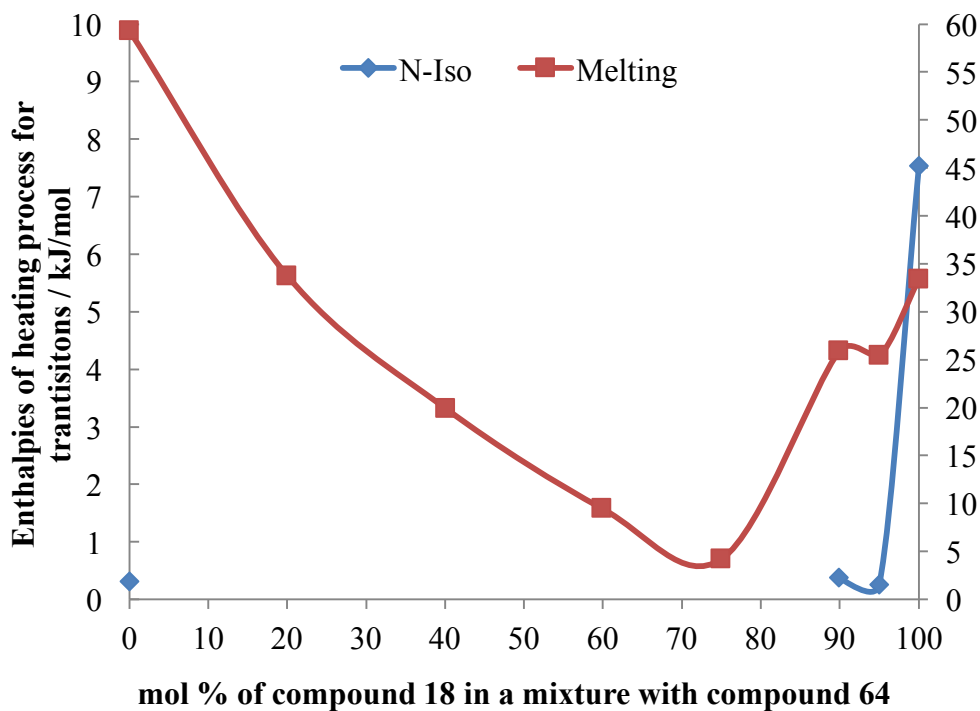


**Figure 5.37** The diagram showing the enthalpies (kJ/mol) of transitions on heating as a function of the mol concentration of compound **18** in a mixture with compound **64**.

If we create the curve of the values of enthalpies as a function of concentration of compound **16** in a mixture with compound **64**, it can be seen as in Figure 5.37, that the values of the enthalpies for the melting cycle are of magnitude larger than the N to I transitions. In addition, from the DSC thermogram of the mixture of 59.9 mol% of compound **16** (shown in Figure 5.38) it can be seen that there is no mesophase present for the **TZ-M023-3** mixture.

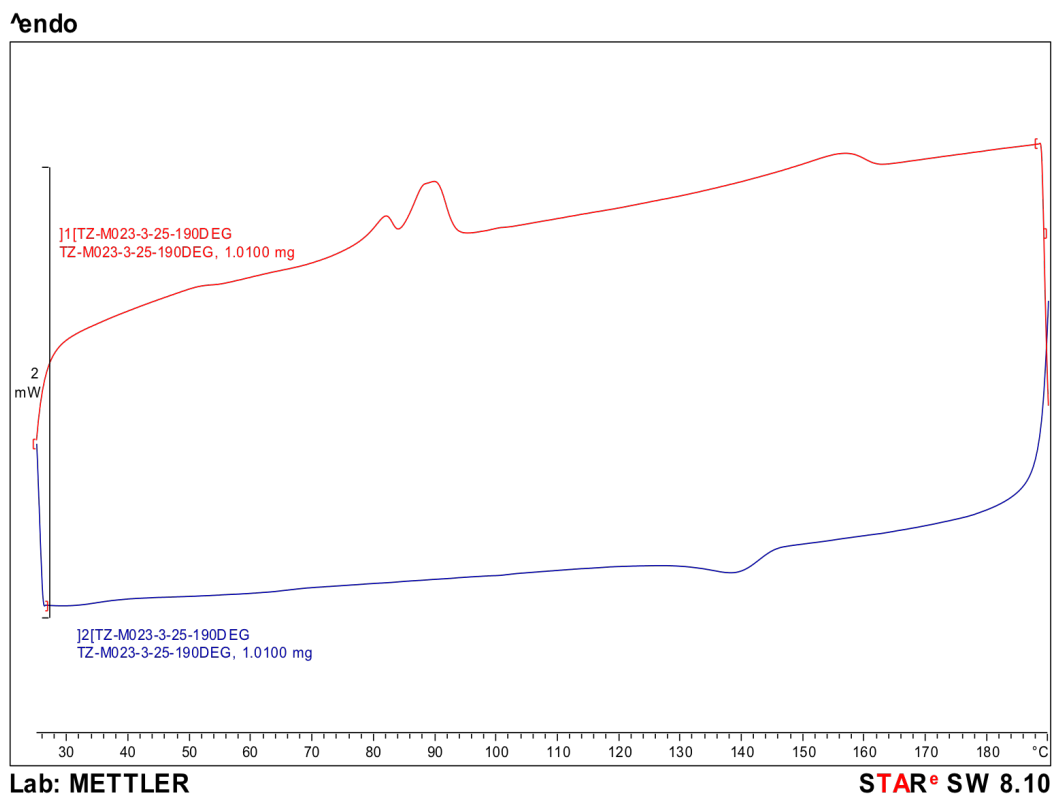


**Figure 5.38** The DSC curve for the mixture **TZ-M023-3** (59.9 mol% of compound **16**) both on heating and cooling in the first cycle..

### 5.2.3.3 Mixture Studies between Compounds **26** and **64**

The next binary phase diagram in this series of studies involves nematogenic compounds **26** and **64**. Nematogen **64** was selected as before because it has a flat electron concentrated disc-like structure, whereas the hexa-substituted triphenylene compound **26** would have a twisted structure due to lateral methyl groups in the peripheral rings, but in this case there is only one lateral methyl group per peripheral phenyl ring and so the twist will be less prevalent. Thus it was expected that compound **26** would partially sterically interfere with the face-to-face interactions of compound **64**, which it was predicted would be better in stabilising the formation of the nematic phase. Thus, the binary phase diagram between the two compounds is presented in Figure 5.42.

Thus, the structures and phase transition temperatures, the energy minimised space-filling structures using the MM2 force field as implemented in ChemDraw

3D in gas phase at absolute zero, and molecular simulations using DFT theory for compounds **26** and **64** are shown respectively in Figures 5.39 to 5.41.

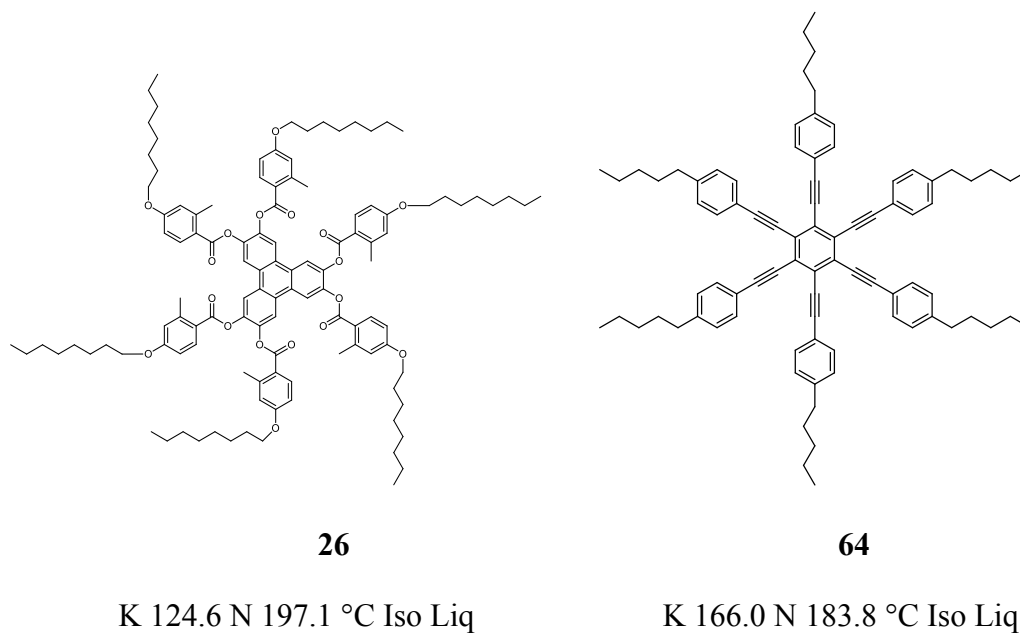


**Figure 5.39** The chemical structures and phase transitions of compound **26** and **64**.

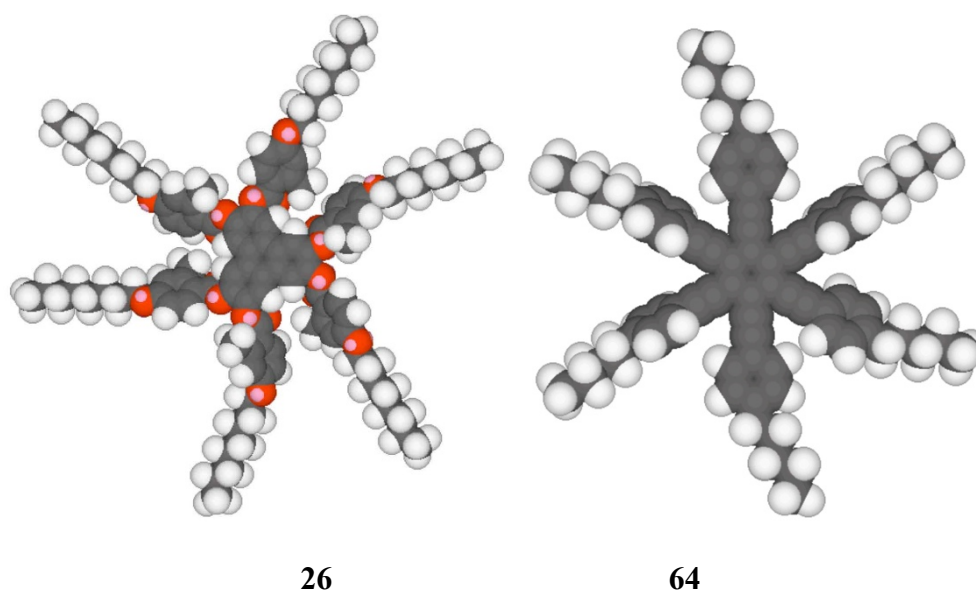
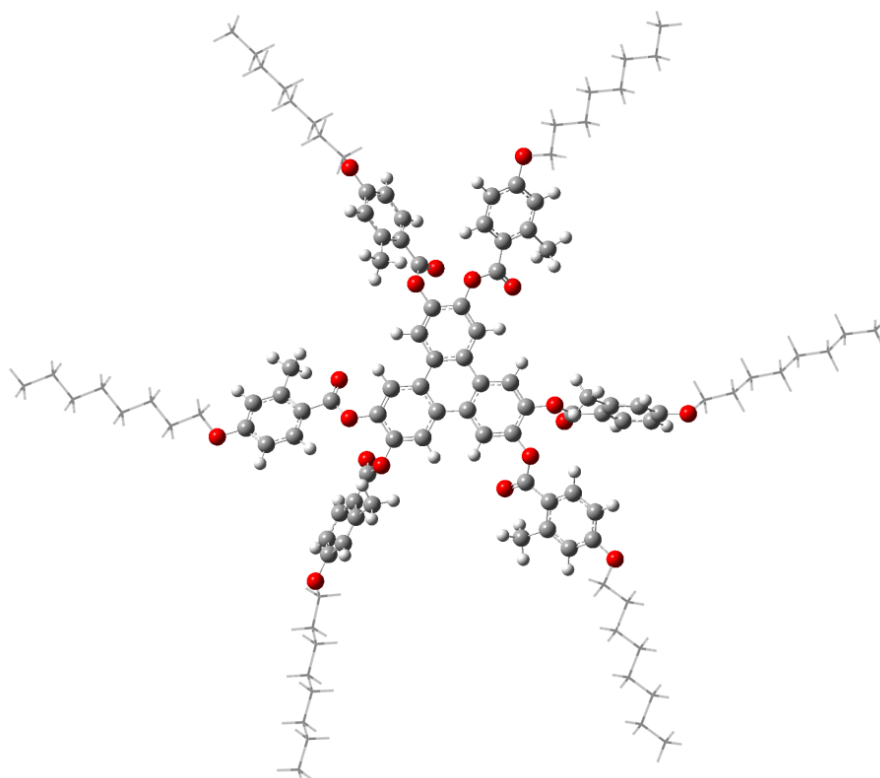


**Figure 5.40** The space filling structures of compounds **26** and **64** determined in gas phase at 0 K using the MM2 force field as implemented in ChemDraw 3D.

In the simulated structures, three of the peripheral aromatic rings are twisted out of the plane of the central triphenylene core for compound **26**, whereas the peripheral rings are in the same plane of the central benzene core for compound **64**. The diameter of compound **64** was found to be 28.05 Å, whereas the diameter for compound **26** was 41.04 Å. It appears that ratio of the diameters of compounds **64** to **26** approximately 3:2. Thus, compound **64** will pack securely within the bounds of compound **26**.



**26**

**Figure 5.41** The energy structure for compound **26**, at the mixed ONIOM(B3LYP/6-31G(d):PM6) level of theory.

Compound **26** and **64** were both found to exhibit nematic phases. In the same manner as before, a series of mixtures (**TZ-M024-1-5**) were prepared in different mol ratios of the two components, and examined by POM and then DSC. The transition temperatures for the series of mixtures determined by POM are given in Table 5.14, whereas those determined from DSC are shown together in Table 5.15.

The composition of the mixture predicted to exhibit the eutectic point for the binary components (**TZ-M024-E**) was calculated by the Schröder-van Laar equation (72 mol% of **26**), and its experimental phase behaviour was determined by POM and DSC, as shown in both Tables.

**Table 5.14** Compositions (mol%) and transition temperatures (°C) for binary mixtures of **26** and **64** determined by POM.

ID	<b>26</b> / mol%	K	/°C	N	/°C	Iso Liq
<b>64</b>	0	.	166.0	.	183.8	.
<b>TZ-M024-1</b>	14.9	.	150.7	.	176.6	.
<b>TZ-M024-2</b>	30.2	.	150.9	.	176.0	.
<b>TZ-M024-3</b>	45.3	.	146.9	.	172.9	.
<b>TZ-M024-4</b>	59.8	.	120.7	.	170.0	.
<b>TZ-M024-E</b>	72.0	.	116.3	.	181.0	.
<b>TZ-M024-5</b>	85.0	.	122.0	.	190.1	.
<b>26</b>	100	.	124.6	.	197.1	.

**Table 5.15** Mixture compositions (mol%) and transition temperatures (°C) and enthalpies both on heating and cooling for binary mixtures of **26** and **64**.

ID	26/ mol%	Melting / °C	N-Iso/ °C	
			Heating	Cooling
<b>64</b>	0	166.01	184.76	192.80
		$\Delta H= 53.98$	$\Delta H= 0.28$	$\Delta H= -0.20$
<b>TZ-M024-1</b>	14.9	150.69	-	-
		$\Delta H= 18.87$	-	-
<b>TZ-M024-2</b>	30.2	150.92	-	-
		$\Delta H= 10.34$	-	-
<b>TZ-M024-3</b>	45.3	146.9	-	-
		$\Delta H= 8.36$	-	-
<b>TZ-M024-4</b>	59.8	120.65	-	-
		$\Delta H= 16.41$	-	-
<b>TZ-M024-E</b>	72.0	116.33	-	-
		$\Delta H= 14.42$	-	-
<b>TZ-M024-5</b>	85.0	121.96	191.99	191.00
		$\Delta H= 18.74$	$\Delta H= 0.16$	$\Delta H= -0.17$
<b>26</b>	100	124.6	198.55	198.31
		$\Delta H= 23.17$	$\Delta H= 0.12$	$\Delta H= -0.12$

The binary phase diagram construction based on the results obtained by thermal optical microscopy is shown in Figure 5.42. In addition, photomicrographs of the defect textures at various points are incorporated into the phase diagrams in Figure 5.42.

In the phase diagram there is a fast reduction of the melting temperature from 45.3 mol% of **26** to 59.8 mol% of **26**, whereas the temperature for concentrations near to 100 mol% **26** fell more slowly. The results obtained for the eutectic mixture **TZ-M024-E** gave a melting point of 116.3 °C, which was the lowest value for all of the mixtures studied, indicating that it might be the real eutectic point. However, the depression in the melting point curve for the phase diagram was relatively weak,

suggesting that the calculated eutectic point may not be the actual point. The almost linear N-I transition temperature curve varies in a similar way to the melting curve and possesses a minimum point at a similar concentration to that of the calculated eutectic point.

In order to investigate this behaviour further, and to obtain accurate values for the transition temperatures on heating and cooling for the mixtures in the phase diagram, calorimetric studies were performed for each individual mixture, and the results for which are shown in Table 5.15 along with the enthalpies for transitions.

Comparing the results of Table 5.14 and 5.15, it implies that the transition temperatures by calorimetry are in agreement with those by microscopy, however, in the region between 14.9 to 85 mol% of compound **26** in the phase diagram, no enthalpies are detected DSC for the N-I phase transition, but the nematic phase could be observed to isotropic phase transition *via* microscopy as shown in Figure 5.42. This is unusual behaviour, which indicates that the organization of the molecules in the nematic phase are very similar to those in the amorphous liquid, which suggests that there is probably short range molecular clustering in the liquid state. In addition, the values of the enthalpies of the melting cycles are a magnitude larger than those of the N-I phase transitions, and when these mixtures are cooled down there are no peaks in the DSC showing any I-N transitions.

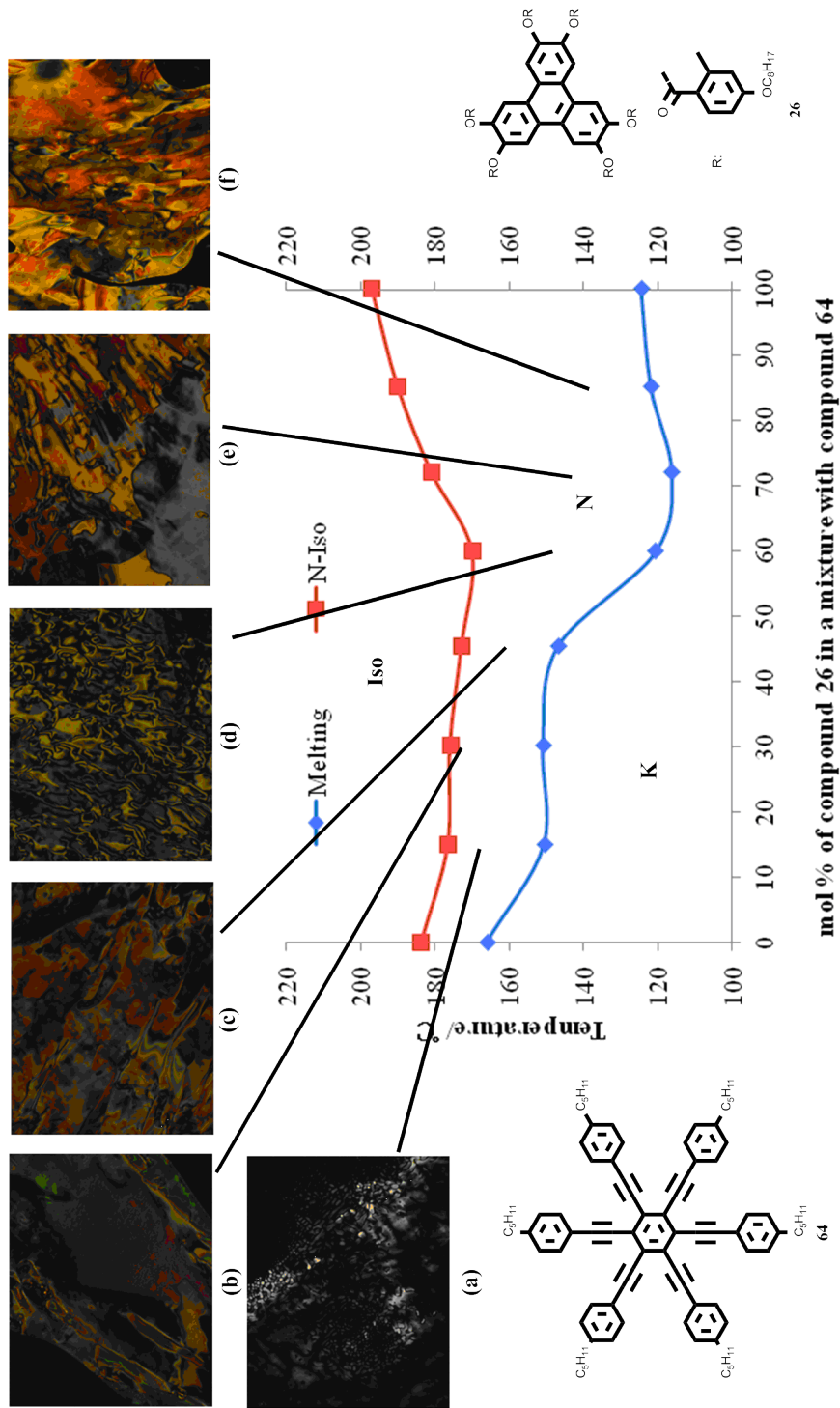
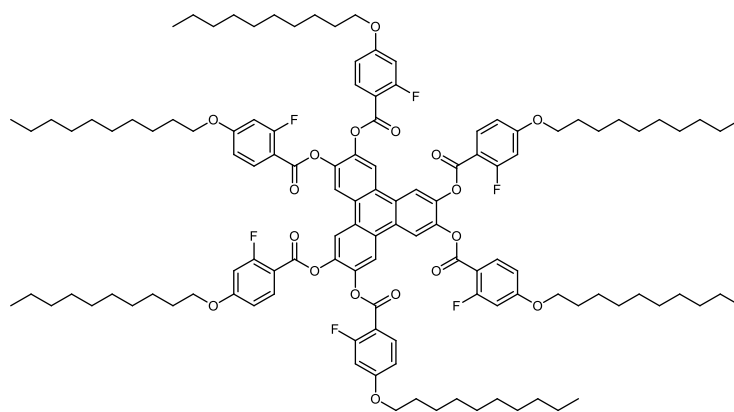


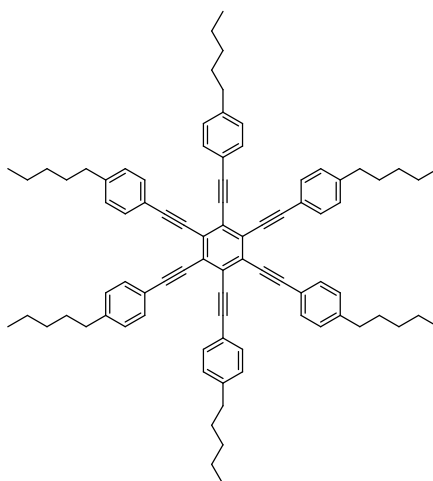
**Figure 5.42** The Gibbs phase diagram for binary mixture series TZ-M024 of 26 and 64. Photomicrographs (x100 magnification) showing representative optical textures for TZ-M024: (a) 14.9%, cooling, 160.0 °C, N; (b) 30.2%, heating, 167.0 °C, N; (c) 45.3%, cooling, 162.0 °C, N; (d) 59.8%, cooling, 155.0 °C, N; (e) 72%, cooling, 145.0 °C, N; (f) 85%, cooling, 136.9 °C, N.

#### 5.2.3.4 Mixture Studies between Compounds 27 and 64

The next step in the investigation of the miscibility of alkyne systems is to examine the interactions of  $\pi$ -rich systems (alkynes as in compound **64**) with those of electron deficient materials (fluoro-substitution as in compound **27**). The minimised structures in gas phase at absolute zero for compound **27** and **64** are shown in previous figures in section 5.2.2.3 (pp 100-102) and section 5.2.3.1 (pp 111-112), however, Figure 5.43 shows the structures and phase transitions of the two materials.



**27** K 158.7 N 184.1 °C Iso Liq



**64** K 166.0 N 183.8 °C Iso Liq

**Figure 5.43** The chemical structures and phase transitions of compound **27** and **64**.

Thus, a series of mixtures **TZ-M030-1-5** of **27** and **64** were prepared in different mol ratios and their phase behaviour was analysed by POM and DSC in order to create a binary phase diagram between compounds **27** and **64**. The transition temperatures for the series of mixtures determined by POM are shown in Table 5.16, and those determined from DSC are given in Table 5.17, and the phase diagram is shown in Figure 5.44.

The composition of the theoretically predicted eutectic mixture **TZ-M030-E** was determined by calculations from the Schröder-van Laar equation. The composition was determined to be 57.3 mol% of compound **27** in a mixture with **64**. The phase behaviour for the experimental mixture was determined by POM and DSC, and the results obtained are shown in both Tables. The binary phase diagrams for the results shown in Table 5.16 and Table 5.17 are shown respectively in Figures 5.42 and 5.43. Additionally, photomicrographs for the defect textures at various concentrations are incorporated in the phase diagram of Figure 5.42.

**Table 5.16** Compositions (mol%) and transition temperatures (°C) for binary mixtures of **27** and **64** determined by POM.

ID	27/ mol%	K	/°C	N	/°C	Iso Liq
<b>64</b>	0	.	166.0	.	183.8	.
<b>TZ-M030-1</b>	9.9	.	160.6	.	184.4	.
<b>TZ-M030-2</b>	30	.	154.7	.	181.7	.
<b>TZ-M030-3</b>	50	.	142.2	.	175.2	.
<b>TZ-M030-E</b>	57.3	.	143.2	.	170.0	.
<b>TZ-M030-4</b>	74.4	.	144.3	.	170.2	.
<b>TZ-M030-5</b>	91.2	.	144.4	.	178.4	.
<b>27</b>	100	.	158.7	.	184.0	.

**Table 5.17** Mixture compositions (mol%) and transition temperatures (°C) and enthalpies (J/g) both in heating and cooling sessions for binary mixtures of **27** and **64**.

ID	27/ mol%	N-Iso/ °C	
		Heating	Cooling
<b>64</b>	0	184.76	192.8
		$\Delta H = 0.28$	$\Delta H = -0.20$
<b>TZ-M030-1</b>	20	190.84	179.67
		$\Delta H = 0.31$	$\Delta H = -0.16$
<b>TZ-M030-2</b>	40.1	189.37	177.36
		$\Delta H = 0.22$	$\Delta H = -0.62$
<b>TZ-M030-3</b>	59.9	186.36	185.65
		$\Delta H = 0.19$	$\Delta H = -0.25$
<b>TZ-M030-E</b>	75	156.91	156.76
		$\Delta H = 0.63$	$\Delta H = -0.28$
<b>TZ-M030-4</b>	89.9	171.5	171.29
		$\Delta H = 0.31$	$\Delta H = -0.42$
<b>TZ-M030-5</b>	95	191.99	191
		$\Delta H = 0.16$	$\Delta H = -0.17$
<b>27</b>	100	184.4	184.37
		$\Delta H = 0.39$	$\Delta H = -0.34$

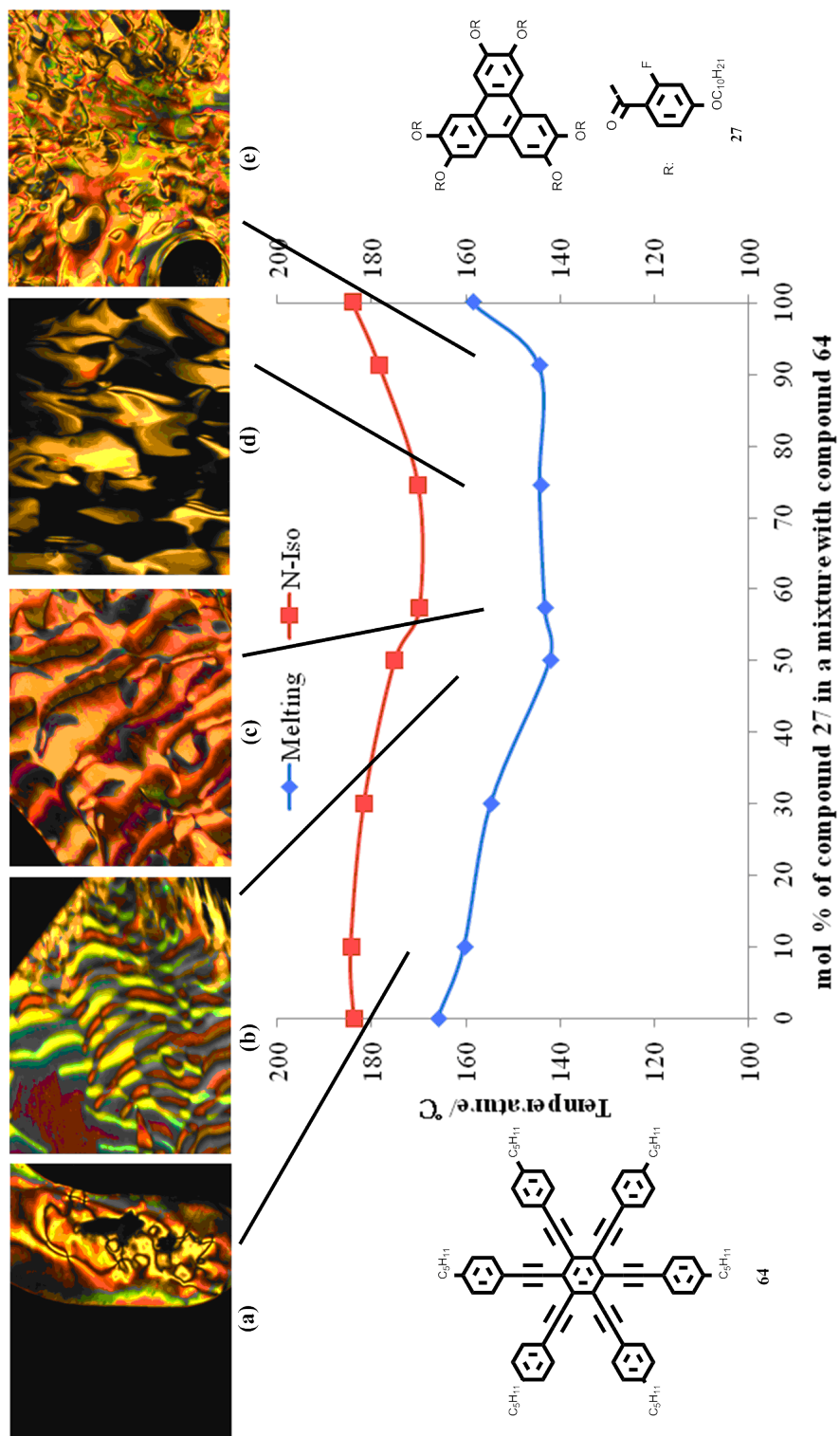


**Figure 5.44** The Gibbs phase diagram for the binary mixture series **TZ-M030** of 27 and 64. Photomicrographs (x100 magnification) showing representative optical textures for **TZ-M030**: **(a)** 9.9%, heating, 173.0 °C, N; **(b)** 50%, heating, 162.0 °C, N; **(c)** 57.3%, Heating, 158.0 °C, N; **(d)** 74.4%, heating, 170.0 °C, N; **(e)** 91.2%, Cooling, 155.5 °C, N.

Results from the binary phase diagram (Figure 5.44) show that the melting temperature and N-I transition curves exhibit similar behaviour. At the centre of the curve there is a gentle minimisation of both curves, thus the melting curve does not appear to be a normal melting curve complete with a minimum for the melting point around the calculated eutectic point. As the Schröder-van Laar equation simulated, it should be an obvious eutectic in the melting temperature curve, however, the points (50 mol% of **27** and 74.4 mol% of **27**) near the predicted point (57.3 mol% of **27**) also showed quite small differences with respect to each other. Additionally, from the N-I transition temperature curve, the lowest clearing point was of a similar value.

In order to investigate the transition behaviour further, and to obtain accurate the values for the temperature on heating and cooling for the mixtures in the phase diagram, calorimetric studies were performed for each individual mixture; the results for which are given in Table 5.17 along with the enthalpies for the transitions.

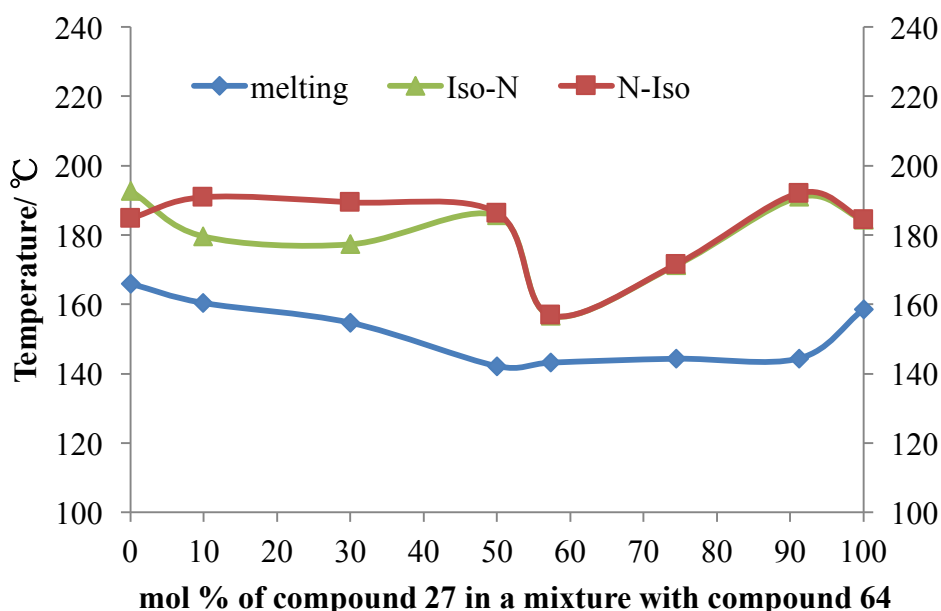


**Figure 5.45** The Gibbs phase diagram showing the biphasic region between heating and cooling for transitions for mixtures of **27** and **64**.

It is important first to note that the binary diagram for the transition temperatures determined by calorimetry, as shown in Figure 5.45, are broadly in agreement with the phase diagram obtained by microscopy shown in Figure 5.44. Secondly, there is little phase separation in the phase diagram because the temperatures for the peak maxima show little hysteresis with respect to heating and cooling cycles.

If we examine the values of the enthalpies of the phase transitions as a function of concentration, as shown in Figure 5.46, it can be seen that all of the enthalpies are of comparable values with respect to compounds **27** and **64**, except for around the predicted eutectic point, which shows the peak in the curve. The peak is probably associated with the presence of a real eutectic point that has a well-defined melting point and associated enthalpy. At this point the relative interactions between the two components are probably strong and so the nematic phase is better organized, and so from the phase transition to the liquid, the two phases either side of the transitions have greater differences in structure.

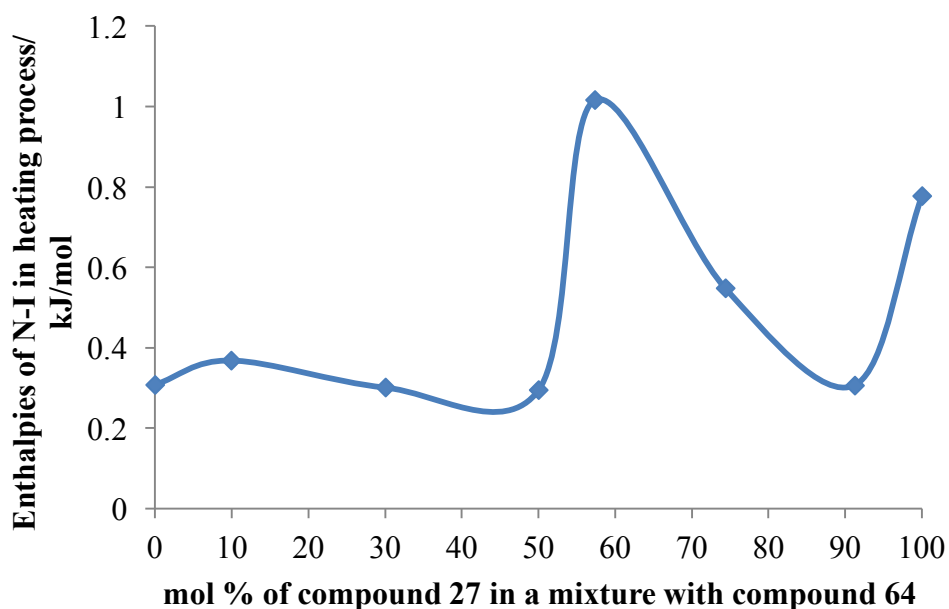


**Figure 5.46** The diagram showing the function of enthalpies (kJ/mol) of each phase transition in heating session with the mol concentration of compound **27** in a mixture with compound **64**.

Overall these studies demonstrate that the two materials are co-miscible, and that their co-miscibility is supported *via* the stronger intermolecular interactions of the two materials around the theoretical eutectic point.

#### **5.2.3.5 Mixture Studies between Compounds 22 and 64**

The next binary phase diagram in this series of studies involves nematogenic compounds **22** and **64**. In this case the two materials were selected for binary phase diagram investigations because they have a similar length for their terminal chains again the hexa-substituted triphenylene compound **22** was expected to have a twisted structure due to lateral methyl groups in the peripheral rings, but in this case there is only one lateral methyl group per peripheral phenyl ring and so the twist will be less prevalent. It was expected therefore that compound **22** would partially sterically interfere with the face-to-face interactions of, and with, compound **64**, which it was predicted would be better in stabilising the formation of the nematic phase. Thus, the binary phase diagram between the two compounds is presented in Figure 5.50.

The structures and phase transition temperatures, the energy minimised space-filling structures using the MM2 force field as implemented in ChemDraw 3D in gas phase at absolute zero, and molecular simulations using DFT theory for compounds **22** and **64** are shown respectively in Figures 5.47 to 5.49.

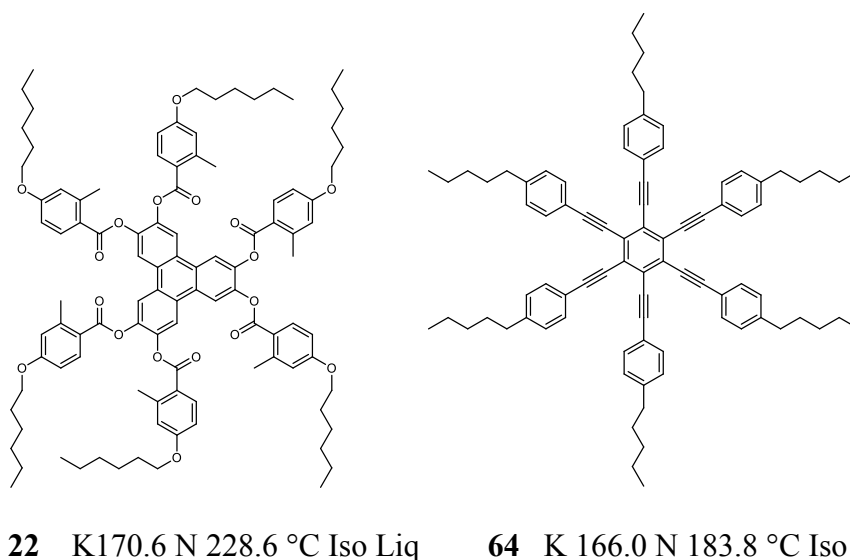


**Figure 5.47** The chemical structures and phase transition temperatures (°C) for compounds **22** and **64**.

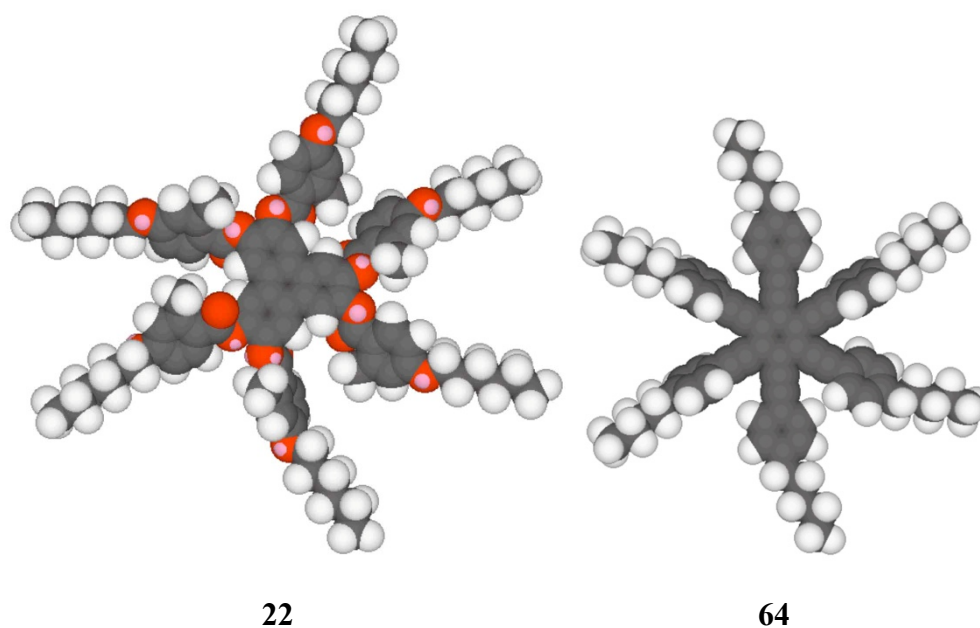
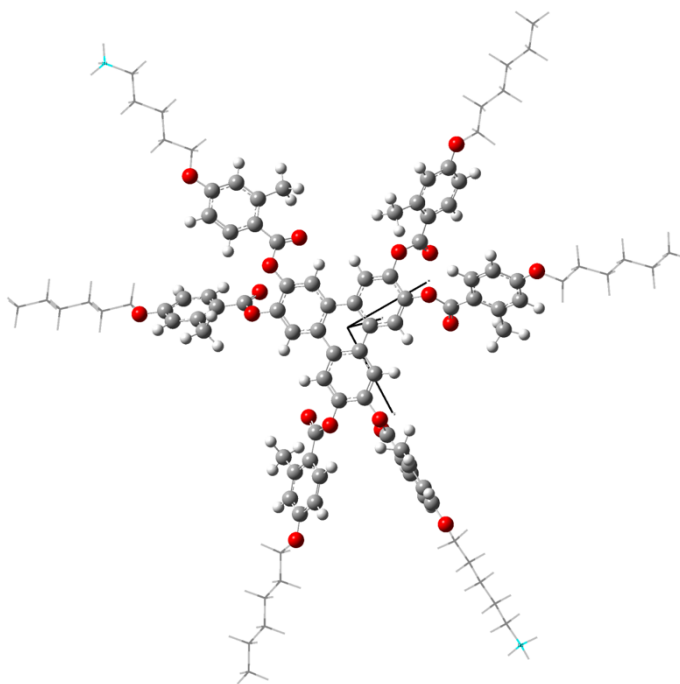


**Figure 5.48** The space filling structures of compounds **22** and **64** determined in gas phase at 0 K using the MM2 force field as implemented in ChemDraw 3D.

In the simulation results, the diameter of compound **22** is 37.05 Å whereas the diameter of compound **64** is 28.05 Å. Thus **64** is smaller than **22** and will fit in between the face-to-face packing of molecules of **64**. For compound **22**, at least in gas phase, all the six of the peripheral aromatic rings are twisted out of the plane

of the triphenylene core, however all of the peripheral aromatic rings and the central phenyl unit of compound **64** are co-planar and the molecular architecture is flat.



**22**

**Figure 5.49** The energy structure for compound **22**, at the mixed ONIOM(B3LYP/6-31G(d):PM6) level of theory.

Compounds **22** and **64** were found to exhibit nematic phase. A series of mixtures **TZ-M031-1-6** of **22** and **64** were prepared in different mol ratios of the two components, and their phase behaviour was analysed by POM and DSC. The transition temperatures for the various mixtures determined by POM are shown in Table 5.18, whereas those the results determined from DSC showed no enthalpy values for the N-I transitions. This indicates that the nematic phase probably has a very similar structure to that of the liquid or vice-versa. The predicted composition mixture (**TZ-M031-E**) for the eutectic for the binary components was determined by the calculations using the Schröder-van Laar equation (38 mol% of Compound **22**). The phase transition temperatures for the experimental eutectic mixture were determined by POM and DSC, and are shown in Table 5.18.

**Table 5.18** Compositions (mol%) and transition temperatures (°C) for binary mixtures of **22** and **64** determined by POM.

ID	27/ mol%	K	/°C	N	/°C	Iso Liq
<b>64</b>	0	.	166.0	.	183.8	.
<b>TZ-M031-1</b>	5	.	166.3	.	177.8	.
<b>TZ-M031-2</b>	15	.	160.7	.	189.0	.
<b>TZ-M031-E</b>	38	.	159.0	.	193.7	.
<b>TZ-M031-3</b>	45	.	160.2	.	194.0	.
<b>TZ-M031-4</b>	65.9	.	160.0	.	202.0	.
<b>TZ-M031-5</b>	85	.	158.4	.	203.0	.
<b>TZ-M031-6</b>	95	.	168.1	.	224.0	.
<b>22</b>	100	.	170.6	.	228.6	.

The binary phase diagram for the phase transition results shown in Table 5.18 is shown in Figure 5.50. In addition, photomicrographs of the defect textures at various points are incorporated into the phase diagram.

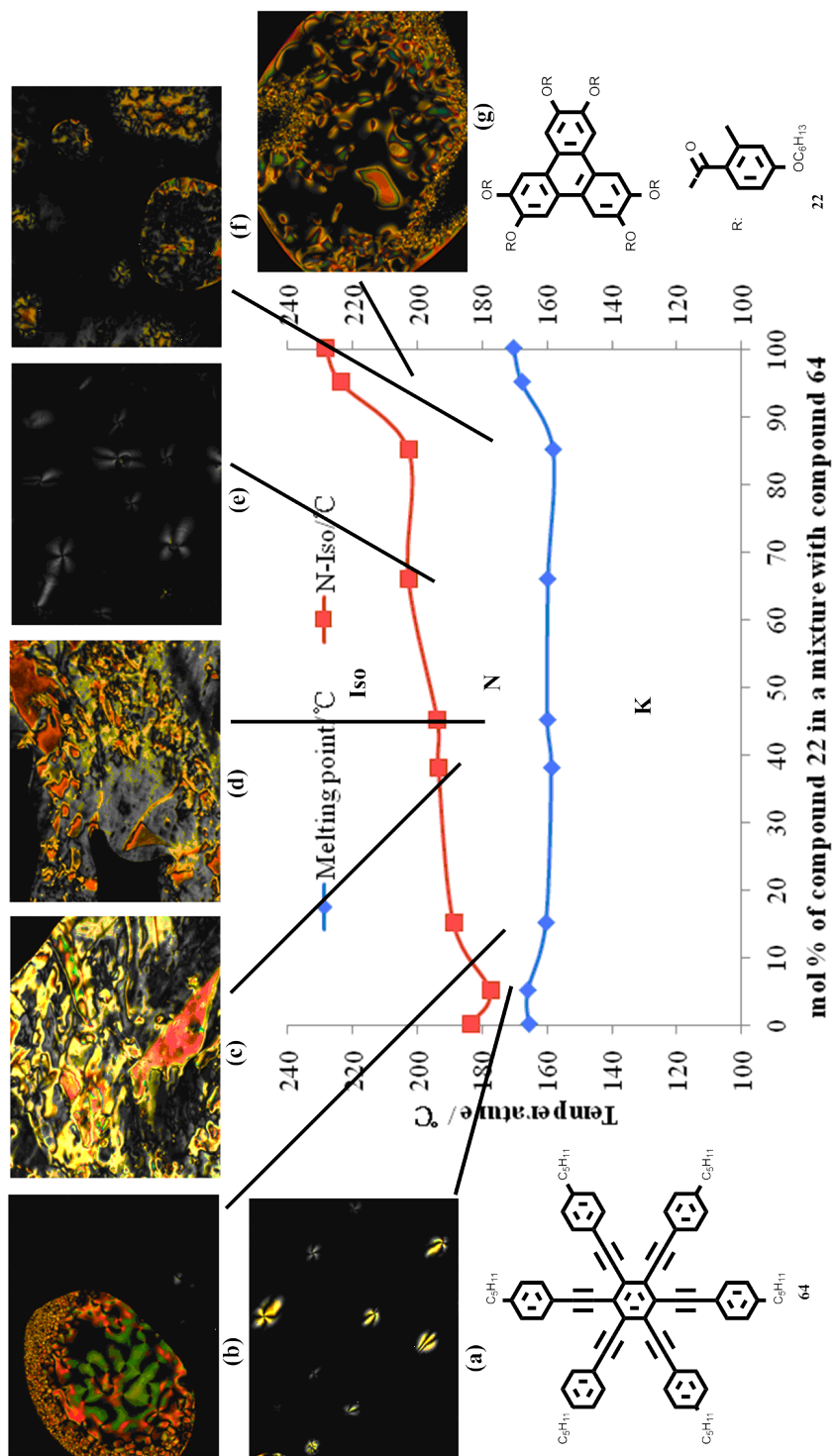


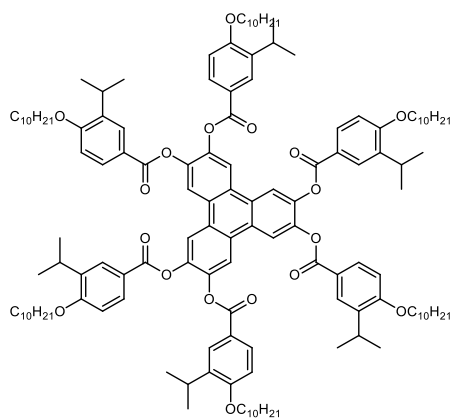
**Figure 5.50** The Gibbs phase diagram for the binary mixture series TZ-M031 of 22 and 64. Photomicrographs (x100 magnification) showing representative optical textures for mixture series TZ-M031: (a) 5.0%, heating, 175.0 °C, N; (b) 15.0%, cooling, 156.8 °C, N; (c) 38.0%, heating, 177.9 °C, N; (d) 45.0%, heating, 173.9 °C, N; (e) 65.9%, cooling, 181.0 °C, N; (f) 85%, heating, 175.9 °C, N; (g) 95%, cooling, 220.0 °C, N.

As can be seen from the data presented in Figure 5.50, the compounds **22** and **64** had similar melting temperatures, as did the mixture across the phase diagram. Thus the melting temperature curve varies almost linearly with respect to concentration. Similarly, the N-I transition temperature curve varies almost linearly as a function of concentration. Thus, no eutectic point is apparent; this is in contradiction to Schröder-van Laar equation prediction, of a eutectic point at a concentration of 38 mol% of compound **22**.

However when further attempts were made to obtain accurate values for the transition temperatures on heating and cooling for the mixtures in the phase diagram, the calorimetric studies for the melting points of each individual mixture could be determined, but as the enthalpies for the N-I transitions could not be discerned as it was not possible to determine accurately the transition temperatures. Overall, however, the two materials showed classical co-miscibility of the nematic phase.

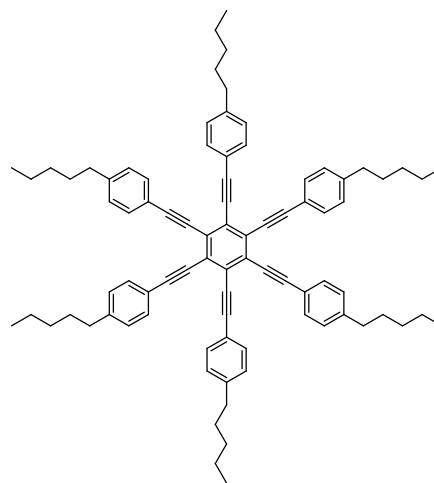
#### **5.2.3.6 Mixture Studies between Compounds 14 and 64**

The next binary phase diagram in this systematic study involves nematogenic compounds **14** and **64**. The two materials were selected for investigation of their co-miscibility because the hexa-substituted triphenylene compound **14** possesses only one lateral substituent in the peripheral rings, but the substituent (isopropyl) was effectively large and could cause twisting of the external phenyl rings which could produce steric repulsion between the two materials. The binary phase diagram between compounds **14** and **64** is shown in Figure 5.54, and the structures and phase transition temperatures, the energy minimised space-filling structures using the MM2 force field as implemented in ChemDraw 3D in gas phase at absolute zero, and molecular simulations using DFT theory for compounds **14** and **64** are shown respectively in Figures 5.51 to 5.53.



**14**

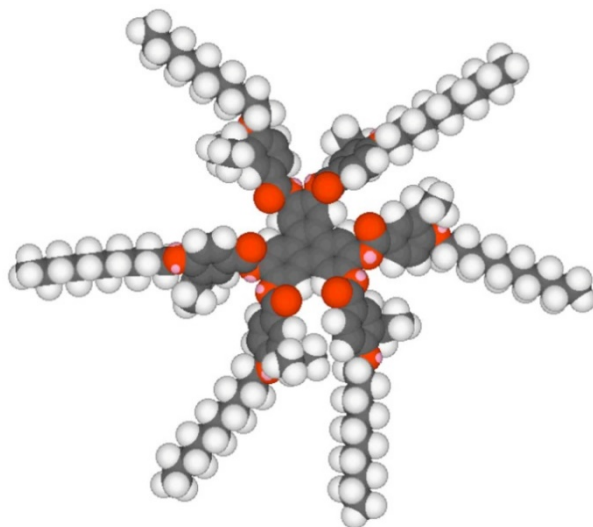
K 160.7 N 202.5 °C Iso Liq



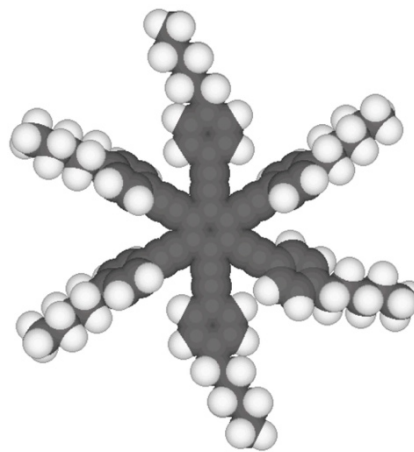
**64**

K 166.0 N 183.8 °C Iso Liq

**Figure 5.51** The chemical structures and phase transitions (°C) for compounds **14** and **64**.

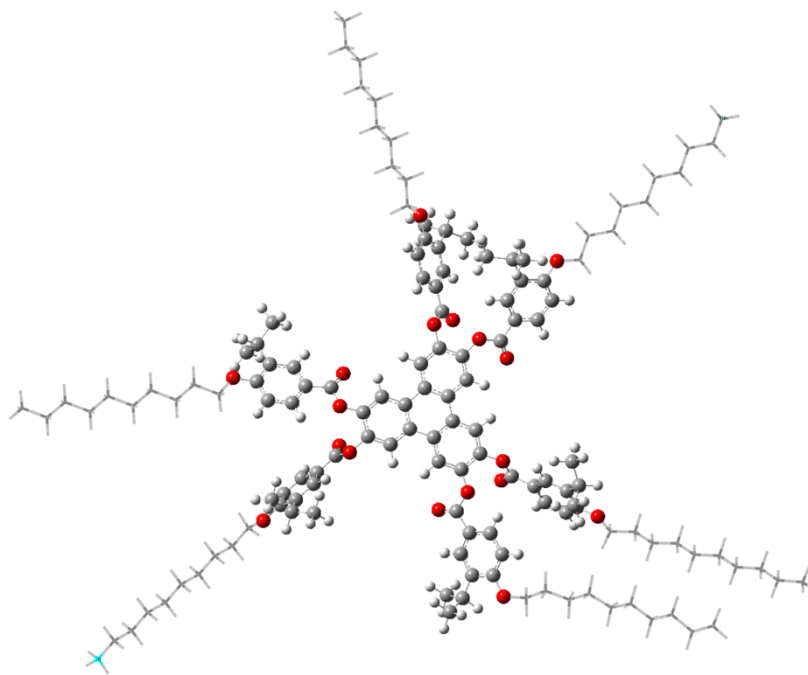


**14**



**64**

**Figure 5.52** The space filling structures of compounds **14** and **64** determined in gas phase at 0 K using the MM2 force field as implemented in ChemDraw 3D.



#### 14

**Figure 5.53** The energy structure for compound **14**, at the mixed ONIOM(B3LYP/6-31G(d):PM6) level of theory.

For the ONIOM(B3LYP/6-31G(d):PM6) simulated structures, the diameter of compound **14** was determined to be 47.36 Å whereas the diameter for compound **64** was 28.05 Å, *i.e.* **14** is almost 1.5 times larger than compound **64**. For compound **14**, the peripheral aromatic rings are twisted with respect to the triphenylene central core. However, for compound **64**, all of the peripheral aromatic rings are in the same plane as the central benzene core.

Compounds **14** and **64** were mixed together in various mol ratios to give a series of formulations **TZ-M032-1-5**. The mesophase properties of the individual mixtures were investigated by POM, and then by DSC. The transition temperatures for the various mixtures determined by POM are given in Table 5.19, and those determined from DSC are shown in Table 5.20. The theoretical composition of the eutectic mixture **TZ-M032-E** was determined *via* the Schröder-van Laar equation, and the phase behaviour of the experimental mixture was determined from POM and DSC, as shown in Tables 5.19 and 5.20. The binary phase diagrams for the

results given in Tables 5.19 and 5.20 are shown respectively in Figure 5.54 and 5.55. Additionally, photomicrographs of the detected textures at various points are incorporated into the phase diagram in Figure 5.54.

**Table 5.19** Compositions (mol%) and transition temperatures (°C) for binary mixtures of **14** and **64** determined by POM.

ID	14/ mol%	K	/°C	N	/°C	Iso Liq
<b>64</b>	0	.	166.0	.	183.8	.
<b>TZ-M032-1</b>	5	.	160.4	.	184.7	.
<b>TZ-M032-2</b>	24.6	.	152.3	.	187.3	.
<b>TZ-M032-5</b>	44.5	.	142.3	.	189.8	.
<b>TZ-M032-E</b>	55.4	.	142.1	.	167.5	.
<b>TZ-M032-3</b>	75.8	.	142.2	.	188.2	.
<b>TZ-M032-4</b>	95	.	153.4	.	197.6	.
<b>14</b>	100	.	160.7	.	202.5	.

**Table 5.20** Compositions (mol%) and transition temperatures (°C) and enthalpies (J/g) both on heating and cooling for binary mixtures of **14** and **64**.

ID	14/ mol%	N-Iso/ °C	
		Heating	Cooling
<b>64</b>	0	184.76	192.8
		$\Delta H = 0.28$	$\Delta H = -0.20$
<b>TZ-M032-1</b>	5	191.68	177.99
		$\Delta H = 0.34$	$\Delta H = -0.38$
<b>TZ-M032-2</b>	24.6	188.39	187.39
		$\Delta H = 0.58$	$\Delta H = -0.84$
<b>TZ-M032-5</b>	44.5	157.45	167.04
		$\Delta H = 4.63$	$\Delta H = -0.22$
<b>TZ-M032-E</b>	55.4	176.86	175.67
		$\Delta H = 0.33$	$\Delta H = -0.27$
<b>TZ-M032-3</b>	75.8	189.69	190.03
		$\Delta H = 0.68$	$\Delta H = -0.45$
<b>TZ-M032-4</b>	95	198.78	198.95
		$\Delta H = 0.56$	$\Delta H = -1.57$
<b>14</b>	100	202.91	202.93
		$\Delta H = 0.39$	$\Delta H = -0.35$

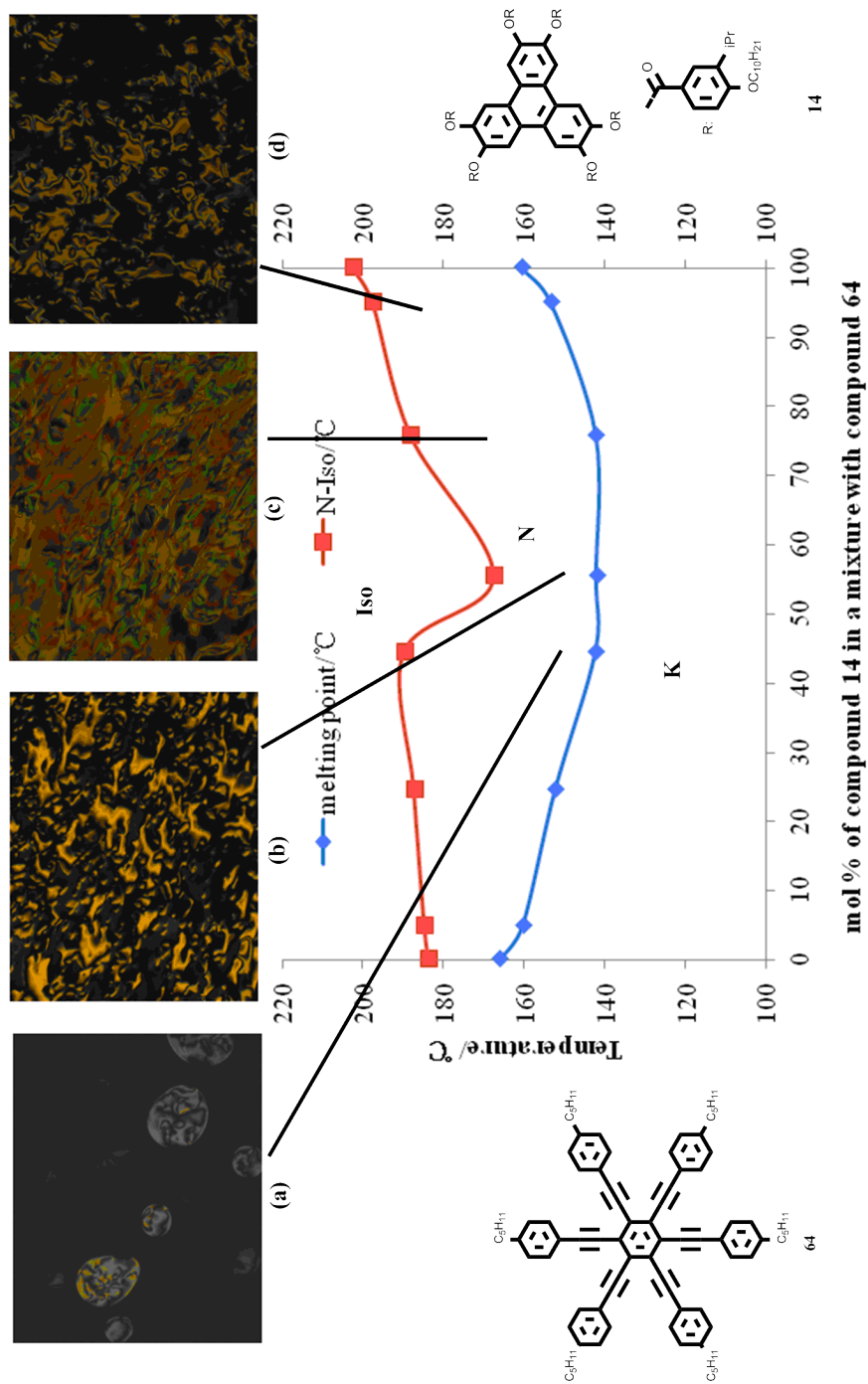


**Figure 5.54** The Gibbs phase diagram for the binary mixture series TZ-M032 of 14 and 64. Photomicrographs (x100 magnification) showing representative optical textures for TZ-M032: (a) 44.5%, cooling, 155.8 °C, N; (b) 55.4%, heating, 161.0 °C, N; (c) 75.8%, heating, 156 °C, N; (d) 95.0%, heating, 146.7 °C, N.

The binary phase diagram shows unusual behaviour. Firstly there is a minimum in the N to I curve within 10 mol% of the calculated point for the eutectic mixture. However, there was no concomitant minimum in the melting curve. For the nematic phase this result indicates that the phase must be fairly well organized, which should be reflected in the thermal analyses of the clearing point transitions of the mixture studied in the phase diagram. Thus, for further investigations and acquiring accurate values for the transition temperatures on heating and cooling for the mixtures in the phase diagram, calorimetric studies were performed for each individual mixture, and the results for which are shown in Table 5.20, along with the enthalpies for transitions.

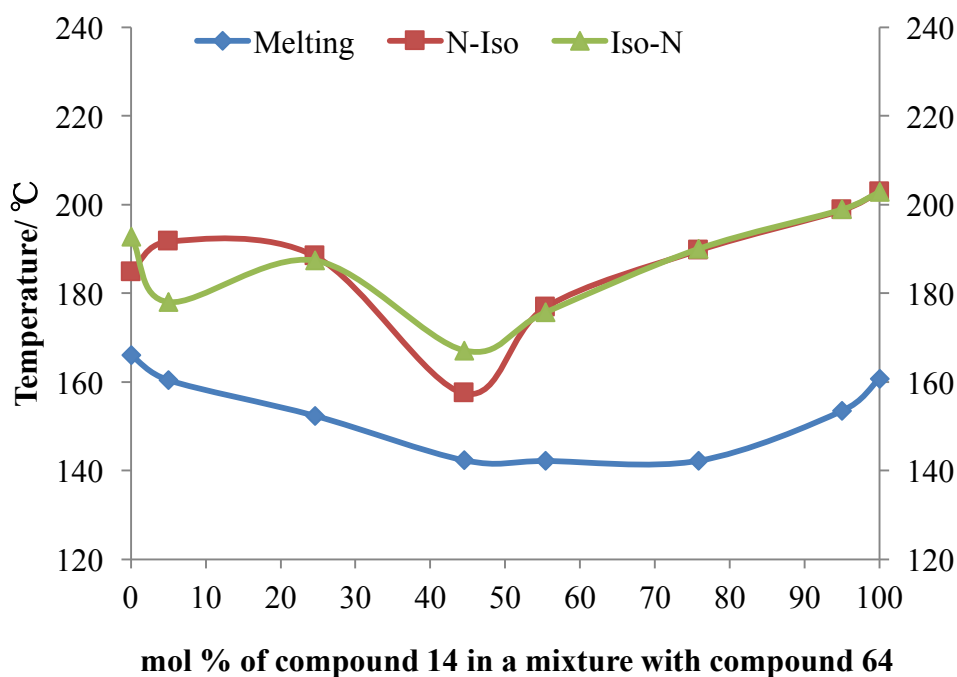


**Figure 5.55** The Gibbs phase diagram showing the biphasic region between heating and cooling for transition of mixtures of **14** and **64**.

Firstly it should be noted that the transition temperatures determined by calorimetry, as shown in Figure 5.55, are broadly in agreement with those shown in the phase diagram in Figure 5.54 obtained by microscopy. Secondly the

temperature of the peak maximums generally show little hysteresis with respect to heating and cooling cycles, which means that there is little phase separation in the phase diagram. In fact, the only large biphasic region is for 5 and 44.5 mol% of compound **14**.

If we analyse the values of the enthalpies of the phase transitions as a function of concentrations, as shown in Figure 5.56, it can be seen there is only a large peak at the point of 44.5 mol% of compound **14** which corresponds to the minima in the N to I curve. All of the other enthalpies values are similar in value, which is low.

Unlike many of the other studies performed, these investigations suggest that the behaviour of mixing the two components mixtures is different from the predictions of the Schröder van-Laar calculations.

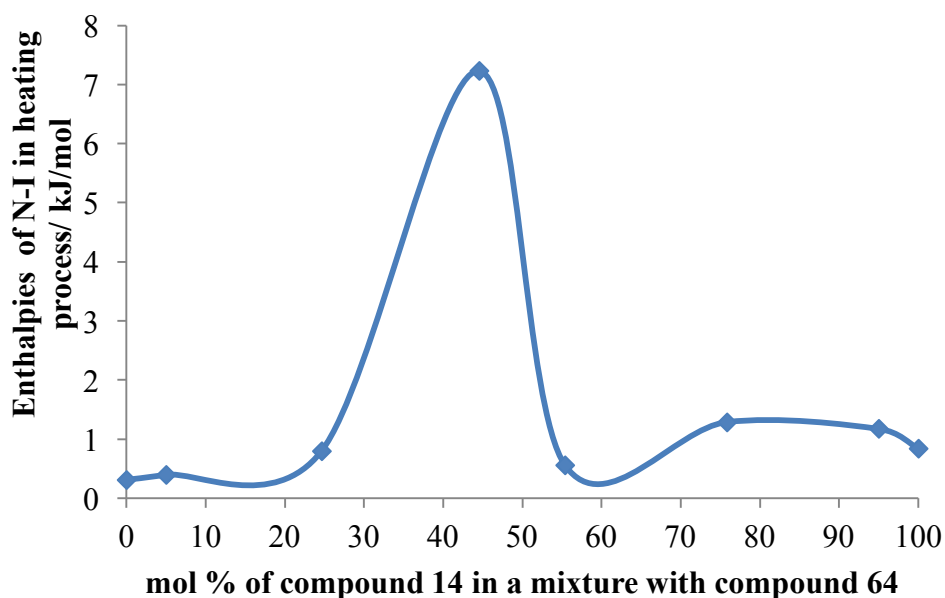


**Figure 5.56** The diagram showing the function of enthalpies (kJ/mol) of N-I phase transition in heating session with the mol concentration of compound **14** in a mixture with compound **64**.

### 5.2.3.7 Mixture Studies between Compounds 19 and 64

The binary phase diagram between compounds **19** and **64**, shown in Figure 5.60, was selected for investigation because the two compounds showed nematic phases that and exhibited similar microscopic defect textures, even though they possessed differing shapes for their chemical structures.

The binary phase diagram between compounds **19** and **64** is shown in Figure 5.60, and the structures and phase transition temperatures, the energy minimised space-filling structures using the MM2 force field as implemented in ChemDraw 3D in gas phase at absolute zero, and molecular simulations using DFT theory for compounds **19** and **64** are shown respectively in Figures 5.57 to 5.59.

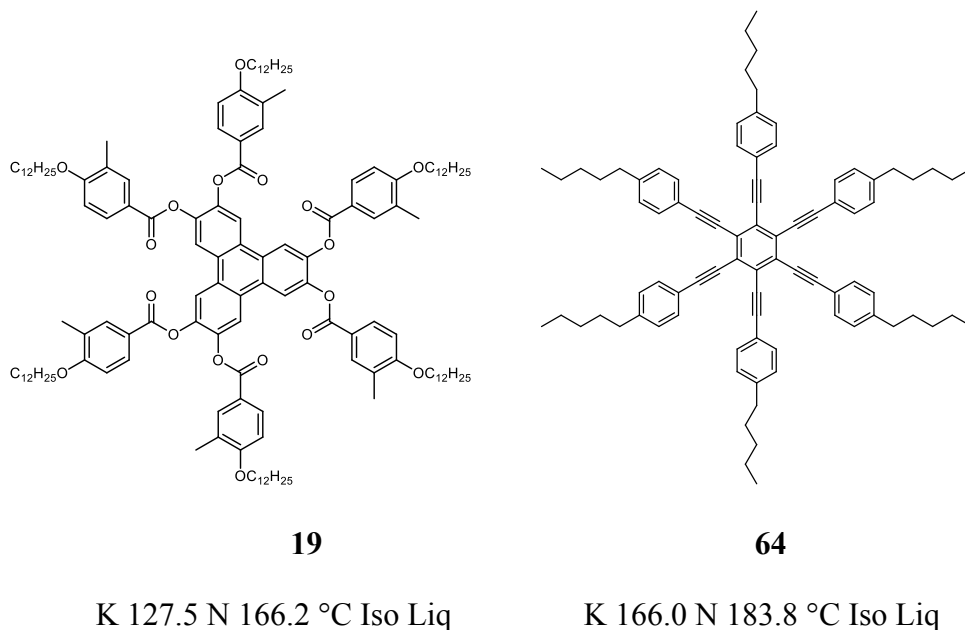


**Figure 5.57** The chemical structures and phase transitions of compounds **19** and **64**.

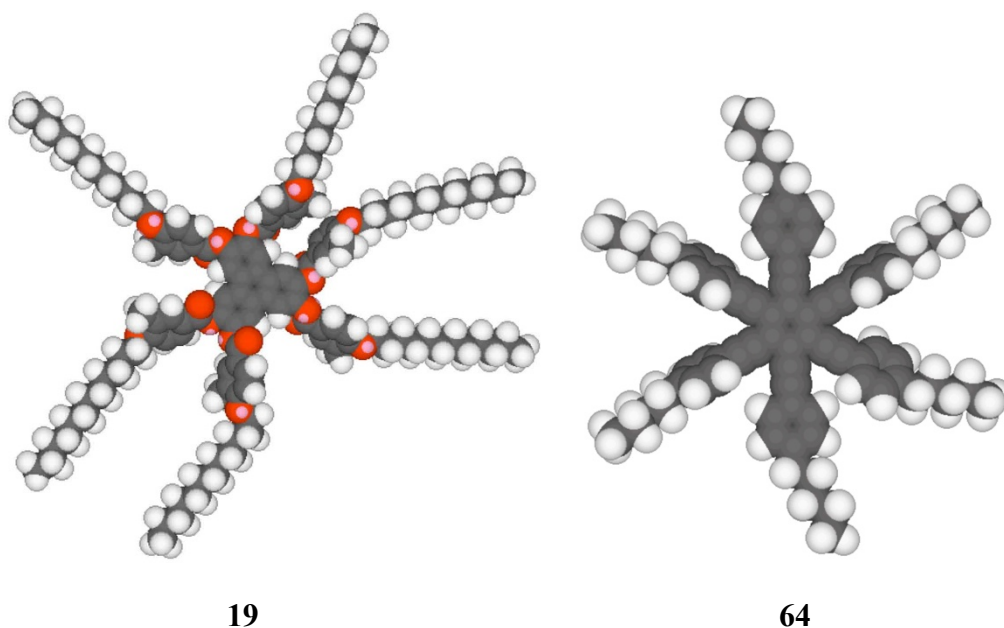
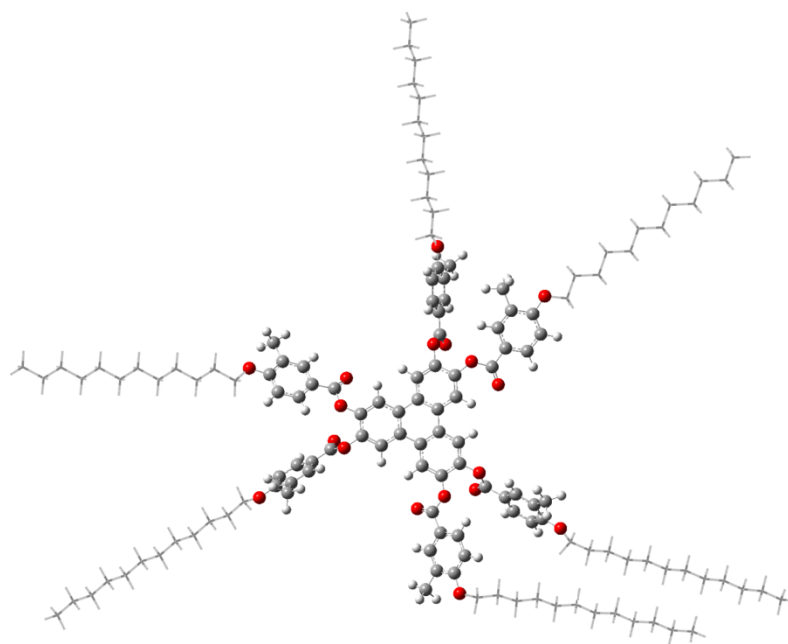


**Figure 5.58** The space filling structures of compounds **19** and **64** determined in gas phase at 0 K using the MM2 force field as implemented in ChemDraw 3D.

In the simulated structures, the diameter of compound **19** was determined to be 52.24 Å, whereas the diameter of compound **64** was 28.05 Å. For compound **19**, alternate peripheral aromatic ring was found to be twisted 90° out of the plane of the central triphenylene core. However, for compound **64** the peripheral rings were in the same plane as the central benzene core.



19

**Figure 5.59** The energy structure for compound **19**, at the mixed ONIOM(B3LYP/6-31G(d):PM6) level of theory.

A series of mixtures **TZ-M033-1-6** of **19** and **64** were prepared in different mol ratios of the two components and their phase behaviour was examined by POM and secondly by DSC. The transition temperatures for the series of mixtures determined by POM are given in Table 5.21, whereas those determined from DSC are shown together in Table 5.22. The composition of the predicted eutectic mixture (**TZ-M033-E**) was determined using Schröder-van Laar equation. POM and DSC determined the phase behaviour of the experimental mixture, based on the calculation, the results for which are given in both Tables. The binary phase diagram for the results shown in Table 5.21 and 5.22 are shown respectively in Figure 5.60 and 5.61. In addition, photomicrographs of the detected textures at various points are incorporated into the phase diagrams in Figure 5.60.

**Table 5.21** Compositions (mol%) and transition temperatures (°C) for binary mixtures of **19** and **64** determined by POM.

ID	<b>19</b> / mol%	K	/°C	N	/°C	Iso Liq
<b>64</b>	0	.	166.0	.	183.8	.
<b>TZ-M033-1</b>	5	.	162.0	.	170.1	.
<b>TZ-M033-2</b>	35.3	.	151.0	.	171.0	.
<b>TZ-M033-6</b>	50	.	103.6	.	141.2	.
<b>TZ-M033-3</b>	65	.	105.6	.	155.2	.
<b>TZ-M033-4</b>	75.7	.	103.6	.	153.9	.
<b>TZ-M033-E</b>	87.1	.	106.0	.	155.6	.
<b>TZ-M033-5</b>	94.1	.	115.6	.	163.9	.
<b>19</b>	100	.	127.5	.	166.2	.

In Figure 5.60, it illustrates that the melting temperature curve was not as predicted with a eutectic point determined by the Schröder-van Laar equation, *i.e.* 87.1 mol% of compound **19**. However, there is a prominent fall in both the melting temperature curve and the N-I transition temperature curve from the point of 35.3 mol% of compound **19** to the point of 50 mol% of compound **19**. The phase temperature range was broadened from 50 to 100 mol% of compound **19** compared with the phase range below 50 mol% of compound **19**.

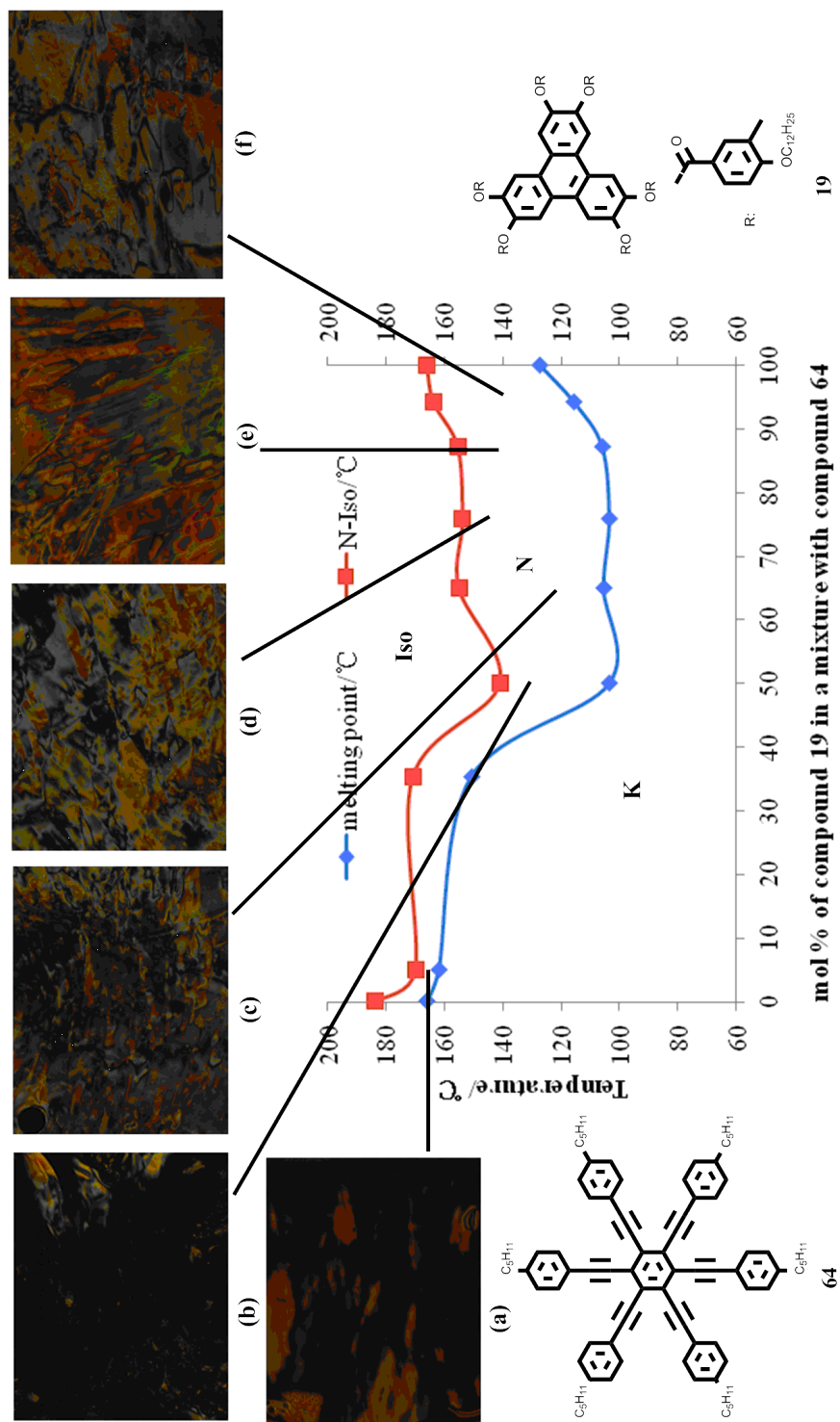


**Figure 5.60** The Gibbs phase diagram for the binary mixture series TZ-M033 of 19 and 64. Photomicrographs (x100 magnification) showing representative optical phase textures for TZ-M033: (a) 5.0%, heating, 170.7 °C, N; (b) 50.0%, cooling, 139.4 °C, N; (c) 65.0%, cooling, 123.5 °C, N; (d) 75.7%, cooling, 119.6 °C, N; (e) 87.1%, heating, 175.9 °C, N; (f) 94.1%, cooling, 126.5 °C, N.

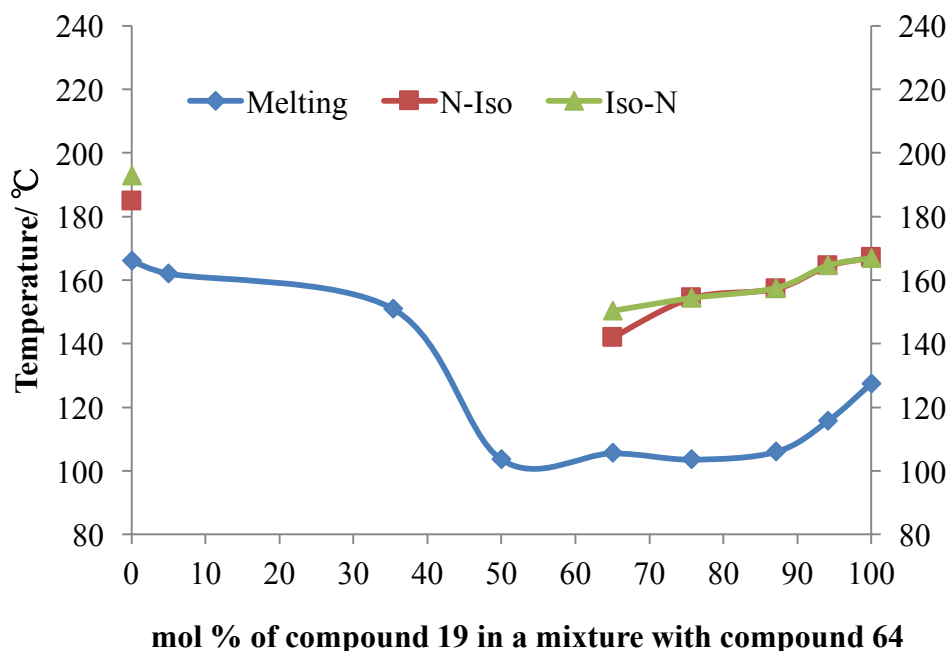
**Table 5.22** Mixture compositions (mol%) and transition temperatures (°C) and enthalpies (J/g) both on heating and cooling for binary mixtures of **19** and **64**.

ID	19/ mol%	Melting/ °C	N-I/ °C	
			Heating	Cooling
<b>64</b>	0	166.01	184.76	192.8
		$\Delta H = 53.98$	$\Delta H = 0.28$	$\Delta H = -0.20$
<b>TZ-M033-1</b>	5	162.01	-	-
		$\Delta H = 16.42$	-	-
<b>TZ-M033-2</b>	35.3	150.98	-	-
		$\Delta H = 11.12$	-	-
<b>TZ-M033-6</b>	50	103.63	-	-
		$\Delta H = 5.39$	-	-
<b>TZ-M033-3</b>	65	105.56	141.9	150.27
		$\Delta H = 3.06$	$\Delta H = 0.24$	$\Delta H = -0.12$
<b>TZ-M033-4</b>	75.7	103.61	154.33	154.32
		$\Delta H = 12.76$	$\Delta H = 0.13$	$\Delta H = -0.12$
<b>TZ-M033-E</b>	87.1	106.01	157.21	157.47
		$\Delta H = 16.35$	$\Delta H = 0.21$	$\Delta H = -0.25$
<b>TZ-M033-5</b>	94.1	115.61	164.34	164.62
		$\Delta H = 10.76$	$\Delta H = 0.11$	$\Delta H = -0.10$
<b>19</b>	100	127.46	167.04	166.89
		$\Delta H = 2.05$	$\Delta H = 0.21$	$\Delta H = -0.25$

For further investigations, and to obtain accurate values for the transition temperatures on heating and cooling for the mixtures in the phase diagram, calorimetric studies were performed for each individual mixture, the results for which are shown in Table 5.22 along with the enthalpies for transitions.

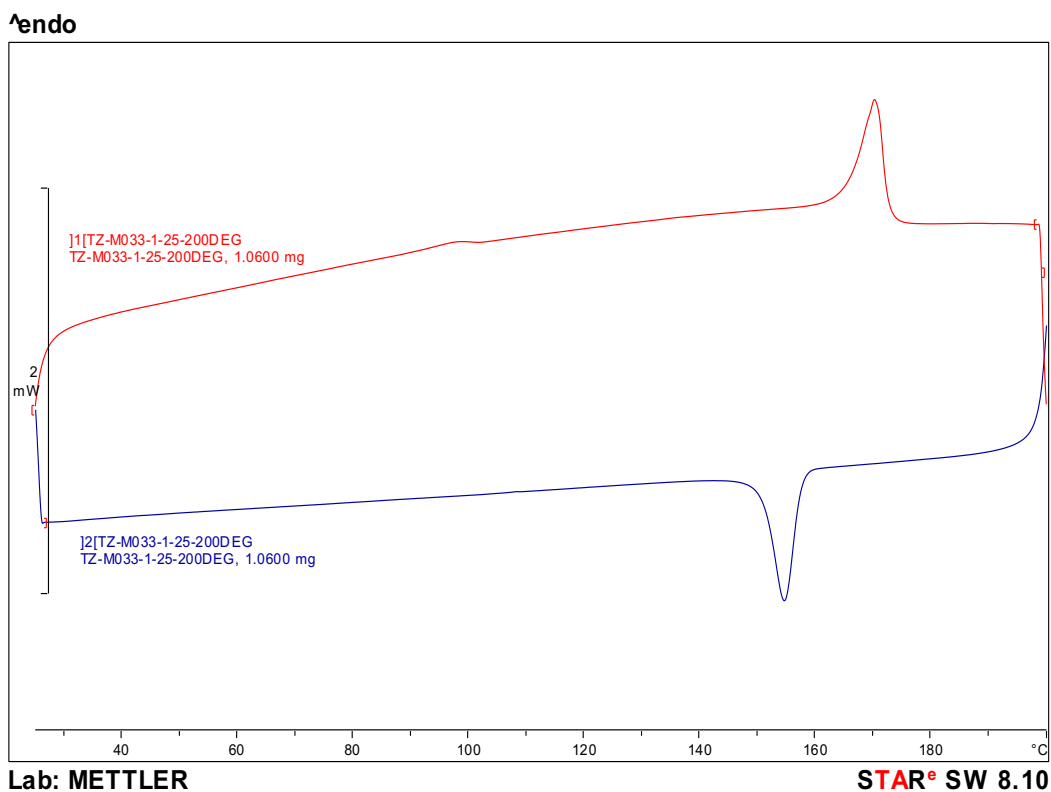
Firstly it is important to note that the binary diagram for the transition temperatures determined by calorimetry, as shown in Figure 5.61, are broadly in agreement with the phase diagram obtained by microscopy. Additionally, the temperatures of the peak maximums show little hysteresis with respect to heating and cooling cycles. It reveals that there is little phase separation in the phase diagram. Furthermore, it can be seen for the region between 5 to 50 mol% of compound **19**, the nematic phase can only be observed by microscopy with no enthalpies detected from DSC (*i.e.*

Figure 5.62 showing the DSC trace for 5 mol% of compound **19**). This may be because the mixtures are dominated by the interactions of compound **64** with itself, which involves  $\pi$ - $\pi$  stacking.



**Figure 5.61** The Gibbs phase diagram showing the biphasic region between heating and cooling for transition of mixtures of **19** and **24**.

If we examine the values of the enthalpies of phase transitions as a function of concentrations, as shown in Figure 5.63, it can be seen that the enthalpies of N-I phase transition vary between 0.03 and 0.5 kJ/mol for mixtures between 65 and 100 mol% of compound **19**, and they are of similar values to the compounds **19** and **64**. Over these values indicates that the nematic phase is stabilised by a wide temperature range, and so the nematic phase is stabilised relative to the liquid, and therefore the enthalpies are larger than for the 0 - 50 mol% concentration range.



**Figure 5.62** The DSC curve of the mixture **TZ-M033-1** showing no peaks for the N-I phase transition.

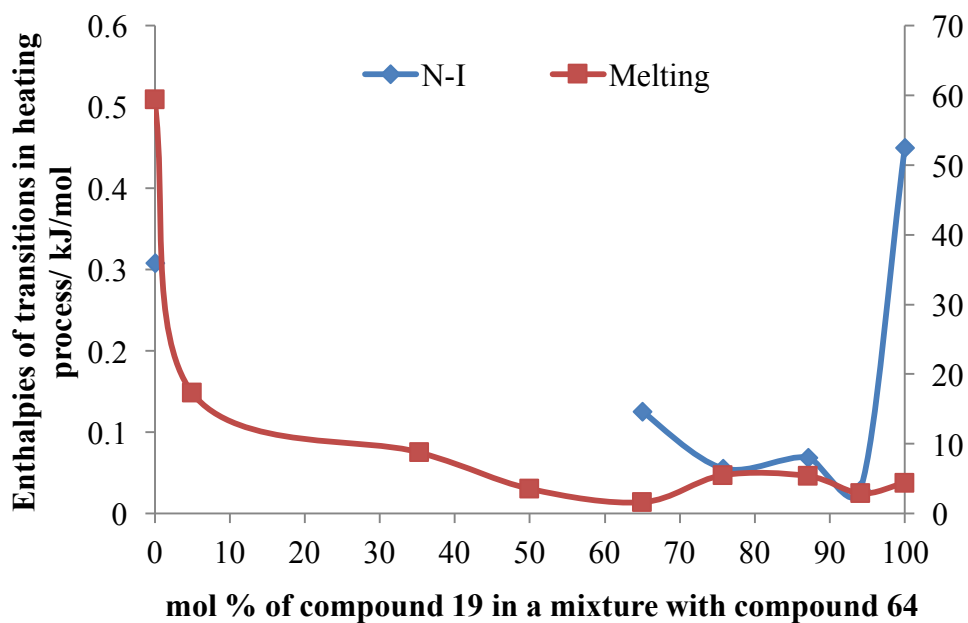


**Figure 5.63** The diagram showing the function of enthalpies (kJ/mol) of phase transitions in heating session with the mol concentration of compound **19** in a mixture with compound **64**.

### 5.2.3.8 Mixture Studies between Compounds **20** and **64**

In this study the two compounds, like others discussed previously, possess very different diameters, which have been somewhat illustrated in the comparative molecular sizes in the following three figures 5.65 to 5.67. Compound **20** was expected to possess a dynamic twisted steric structure where the peripheral rings are twisted out of the plane with respect to the triphenylene core. Compound **64** was predicted to have a relatively planar structure due to conjugative  $\pi$  effects. Thus when packing together in a nematic phase at higher concentrations of compound **20**, the self-organization process was expected to be dominated by the larger molecules, with the smaller molecules interleaving with them, as shown in Figure 5.64, and thereby having less lateral effects on the organization. Conversely, for the smaller molecules being in larger concentration, the larger molecules will still have lateral effects, which will occur through correlations between adjacent molecular clustering. One might therefore predict that the binary phase diagram would be composed of two, but unsymmetrical halves, which will be probed in this study.

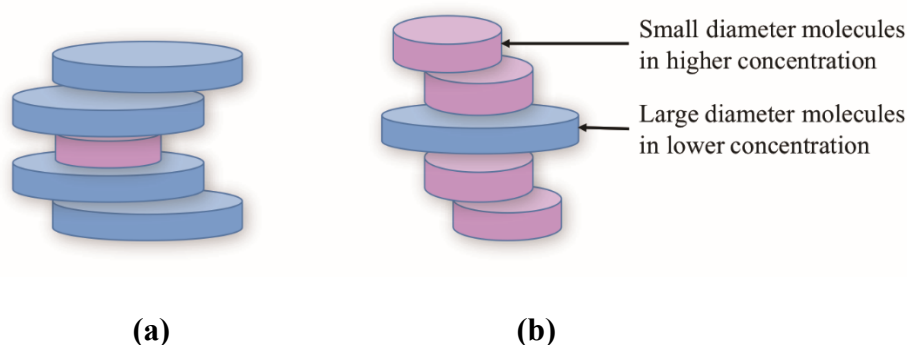
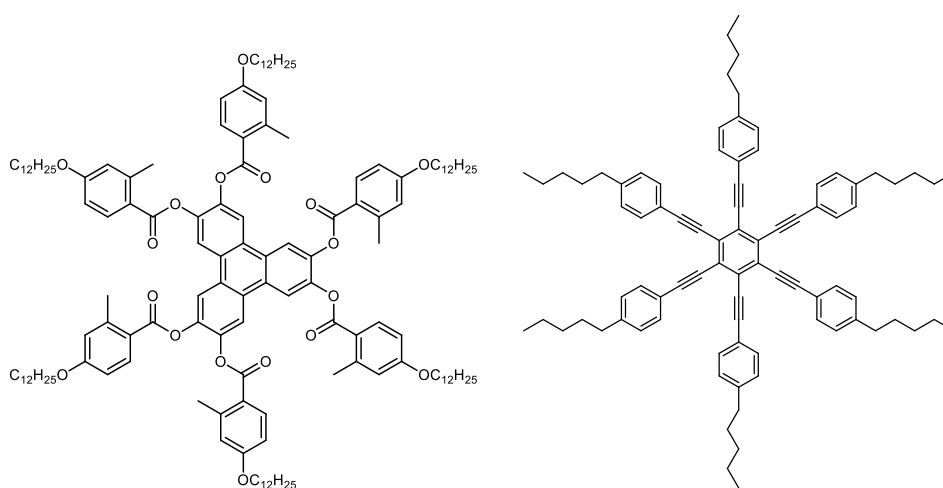


**Figure 5.64** The packing together two types of molecules that have disc-like structures of differing diameters: **(a)** Packing where the larger diameter molecules are in higher concentration; **(b)** Packing where the smaller diameter molecules are in higher concentration.

The binary phase diagram between compounds **20** and **64** is shown in Figure 5.68, and the structures and phase transition temperatures, the energy minimised space-filling structures using the MM2 force field as implemented in ChemDraw 3D in

gas phase at absolute zero, and molecular simulations using DFT theory for compounds **19** and **64** are shown respectively in Figures 5.65 to 5.67. In the figures the structures have been adjusted so they have roughly the same atom size.

From the DFT simulation results, the length of compound **20** was found to be 51.98 Å, whereas the length of compound **64** was 28.05 Å. For compound **20**, five of the peripheral aromatic rings are twisted out of the plane of the central triphenylene core as predicted, whereas for compound **64** all of the peripheral rings are in the same plane as the central benzene core as expected.



**20** K 103.7 N 128.8 °C Iso Liq

**64** K 166.0 N 183.8 °C Iso Liq

**Figure 5.65** The chemical structures and phase transitions of compounds **20** and **64**.

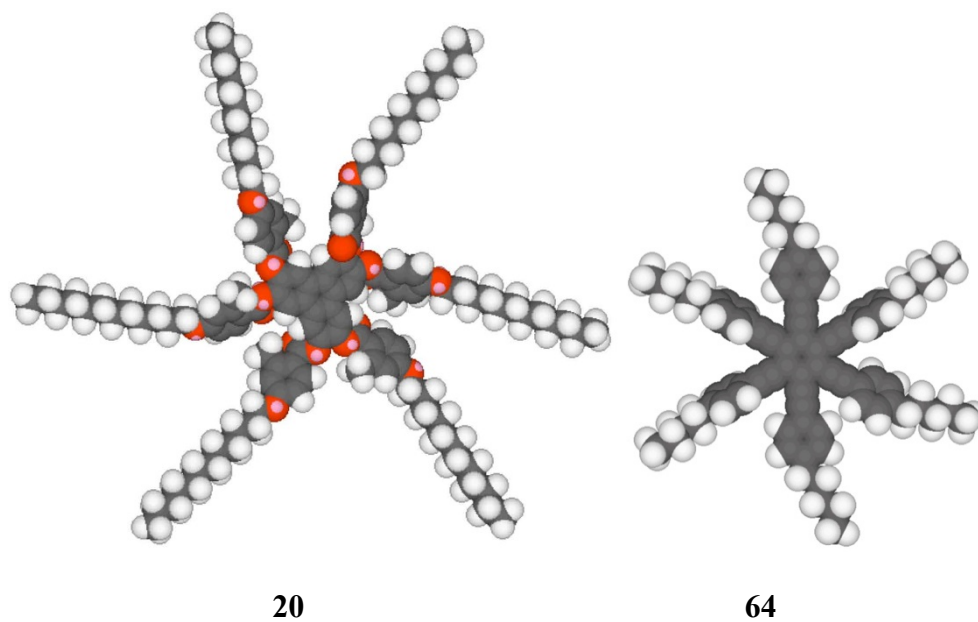
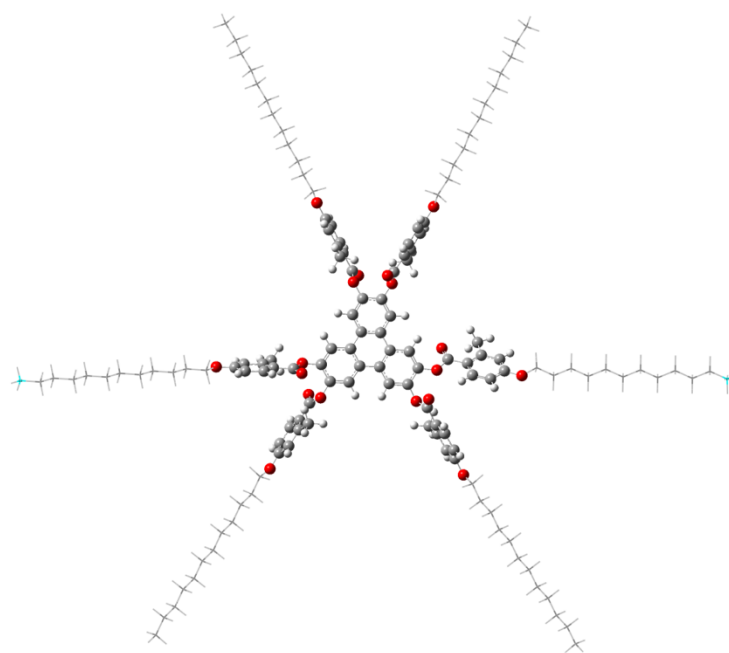


**Figure 5.66** The space filling structures of compounds **20** and **64** determined in gas phase at 0 K using the MM2 force field as implemented in ChemDraw 3D.



**20**

**Figure 5.67** The energy structure for compound **20**, at the mixed ONIOM(B3LYP/6-31G(d):PM6) level of theory.

A series of mixtures (**TZ-M034-1-5**) of **20** and **64** were prepared, and the subsequent phase behaviour was examined by POM and DSC. The transition temperatures for the various mixtures determined by POM are given in Table 5.23, whereas those determined by DSC are listed in Table 5.24. The composition of the eutectic mixture (**TZ-M034-E**) was predicted for the binary components using the Schröder-van Laar equation (83.3 mol% of compound **20**). The phase behaviour, determined by POM and DSC, for experimental mixture for the predicted eutectic are shown in both Tables. The binary phase diagrams for the results given in Table 5.23 and 5.24 are shown respectively in Figure 5.68 and 5.69. Additionally, photomicrographs of the defect textures at various concentrations are incorporated into the phase diagrams in Figure 5.68.

**Table 5.23** Compositions (mol%) and transition temperatures (°C) for binary mixtures of **20** and **64** determined by POM.

ID	<b>20</b> / mol%	K	/°C	N	/°C	Iso Liq
<b>64</b>	0	.	166.0	.	183.8	.
<b>TZ-M034-1</b>	5.1	.	164.5	.	169.5	.
<b>TZ-M034-2</b>	34.7	.	147.6	.	160.4	.
<b>TZ-M034-3</b>	54.3	.	140.2	.	155.6	.
<b>TZ-M034-4</b>	68.7	.	101.5	.	130.3	.
<b>TZ-M034-E</b>	83.3	.	102.3	.	123.7	.
<b>TZ-M034-5</b>	95	.	102.1	.	128.5	.
<b>20</b>	100	.	103.7	.	128.8	.

**Table 5.24** Mixture compositions (mol%) and transition temperatures (°C) and enthalpies (J/g) both on heating and cooling for binary mixtures of **20** and **64** by DSC.

ID	20/ mol%	Melting/ °C	N-Iso/ °C	
			Heating	Cooling
<b>64</b>	0	166.01	184.76	192.8
		$\Delta H= 53.98$	$\Delta H= 0.28$	$\Delta H= -0.20$
<b>TZ-M034-1</b>	5.1	164.45	-	-
		$\Delta H= 32.03$	-	-
<b>TZ-M034-2</b>	34.7	147.55	-	-
		$\Delta H= 12.54$	-	-
<b>TZ-M034-3</b>	54.3	140.24	-	-
		$\Delta H= 7.05$	-	-
<b>TZ-M034-4</b>	68.7	101.49	138.19	-
		$\Delta H= 16.9$	$\Delta H= 0.36$	-
<b>TZ-M034-E</b>	83.3	102.33	139.88	144.07
		$\Delta H= 17.66$	$\Delta H= 2.73$	$\Delta H= -2.76$
<b>TZ-M034-5</b>	95	102.08	129.44	129.63
		$\Delta H= 22.63$	$\Delta H= 0.15$	$\Delta H= -0.23$
<b>20</b>	100	103.66	131.58	130.32
		$\Delta H= 14.53$	$\Delta H= 0.15$	$\Delta H= -0.21$

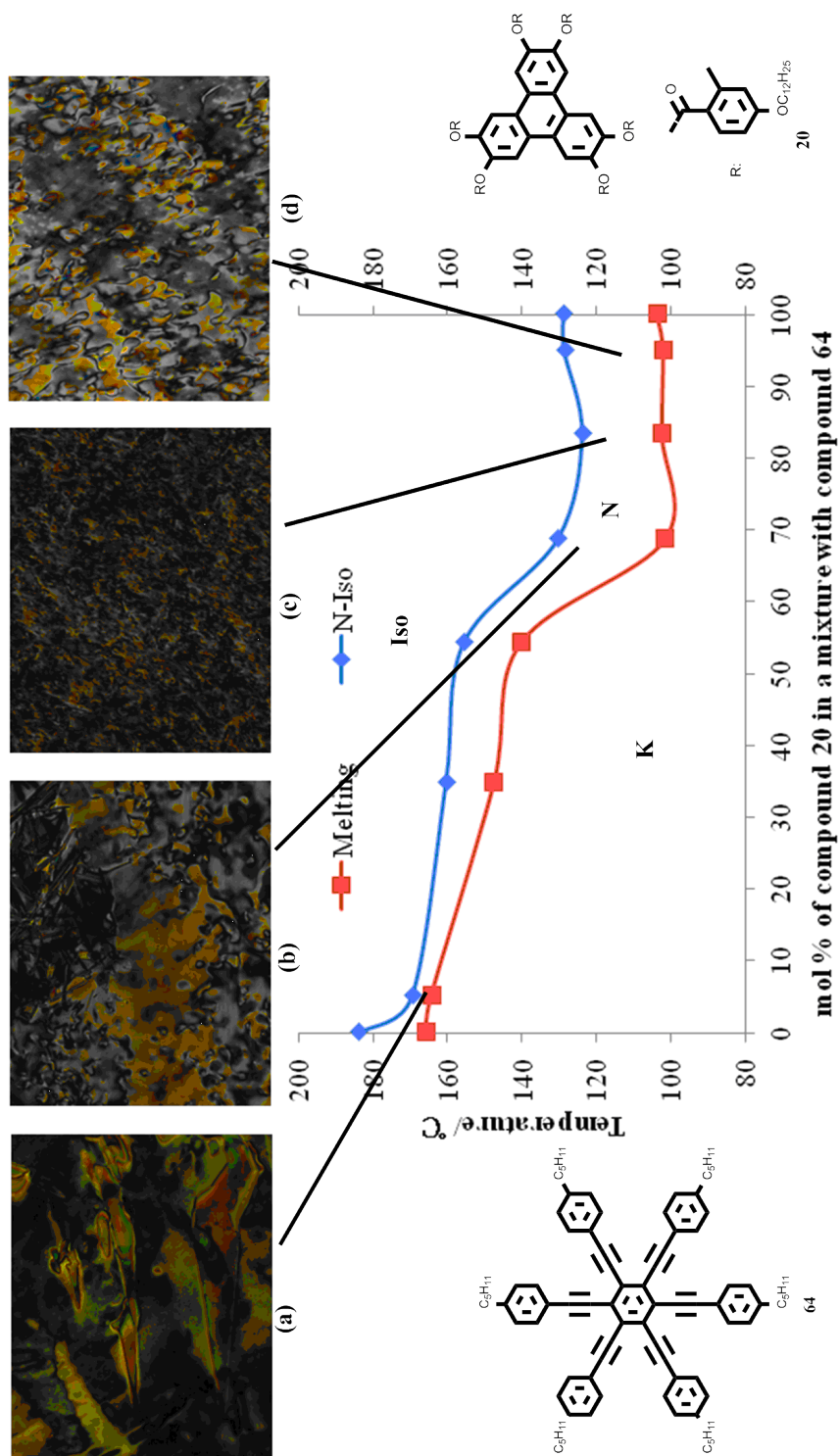


**Figure 5.68** The Gibbs phase diagram for the binary mixture series **TZ-M034** of **20** and **64**. Photomicrographs (x100 magnification) showing representative optical textures for **TZ-M034**: (a) 5.1%, heating, 172.4 °C, N; (b) 68.7%, cooling, 120.7 °C, N; (c) 83.3%, heating, 117.9 °C, N; (d) 95%, cooling, 117 °C, N.

As predicted in the introductory section, the phase diagram was one of two halves, with the one half possessing the larger molecules being of lower transition temperatures than the half dominated by the molecules of smaller diameter. As a consequence, the phase diagram was not as predicted from the Schröder-van Laar equation, and the transition temperature curves for the Gibbs phase diagram were abnormal. There was an apparent decrease from 5:95 (**20:64**) to 35:65 (**20:64**), and the eutectic point was found to be around 70 mol% of compound **20**; but above 70 mol% of compound **20** they showed similar melting temperatures as shown from the melting point curve, which is in disagreement with the calculated Schröder-van Laar equation prediction of 83.3 mol% of compound **20**. The temperature ranges for the nematic phase from 5.1 mol% of compound **20** to 70 mol% of compound **20** was relatively wide, and the N-I transition temperatures fell greatly starting from 70 mol% of compound **20**.

In order to investigate this behaviour further, and to obtain accurate values for the transition temperatures on heating and cooling for the mixtures in the phase diagram, calorimetric studies were performed for each individual mixture, the results for which are shown in Table 5.24 along with the enthalpies for transitions, and graphically in Figure 5.69.

Firstly it is important to note that the binary diagram for the transition temperatures determined by calorimetry, as shown in Figure 5.69, are broadly in agreement with the phase diagram obtained by microscopy as shown in Figure 5.68. Additionally, the temperatures of the peak maximums show little hysteresis with respect to heating and cooling cycles. This demonstrates that there is little hysteresis in the temperatures of phase changes. However, there are no enthalpies detected by DSC for the clearing points in the region of 5.1 to 54.3 mol% of compound **20**. For the 68.7 mol% of compound **20** no enthalpies were observed in the cooling cycle for the N to I transition, but the mesophase was observed *via* microscopy in this region.

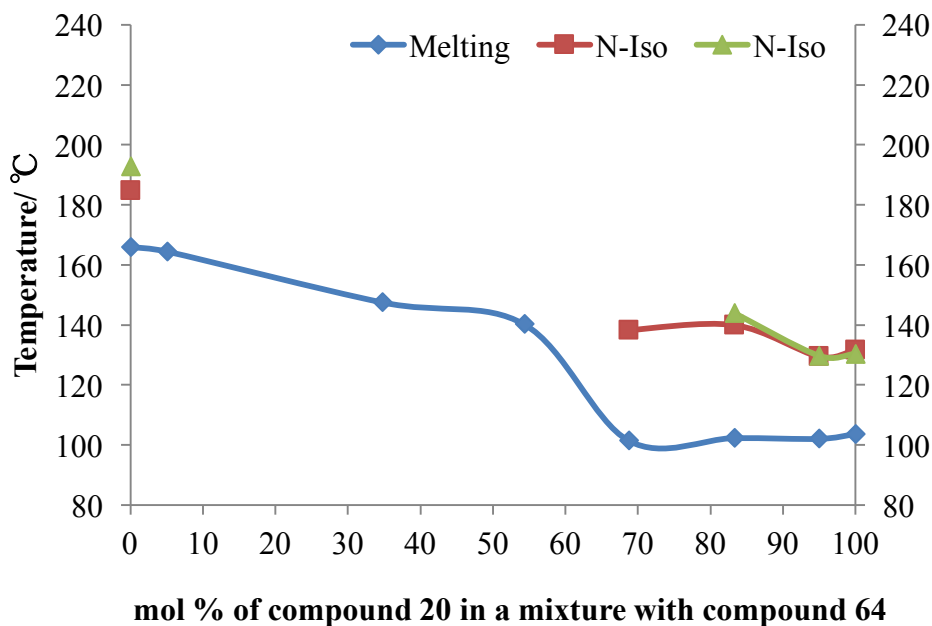


**Figure 5.69** The Gibbs phase diagram showing the biphasic region between heating and cooling for transition of mixtures of **20** and **64**.

If we now examine the values of the enthalpies for the phase transitions as a function of concentration, as shown in Figure 5.70, it can be seen that the values of enthalpies for the N-I phase transitions are relatively low except for around the value of 83.3 mol% of compound **20**, which is the predicted eutectic point. In this region the enthalpy it is almost ten times of the values for other points. As with other studies this result demonstrates that the nematic phase is fairly well-organized in this concentration range, unlike the disorganized liquid. Hence the phase transition is accompanied by a larger enthalpy. Interestingly however, the clearing temperature is relatively unaffected. Thus it appears that the smaller molecules of compound **64** sit in the packing arrangements with the larger molecules of compound **20**, depressing melting point but stabilising mesophase formation without destabilising the overall structure, in other word the **20/64** electrostatic interactions are stronger than the interactions of the individual components, but sterically compound **64** is relatively unseen.

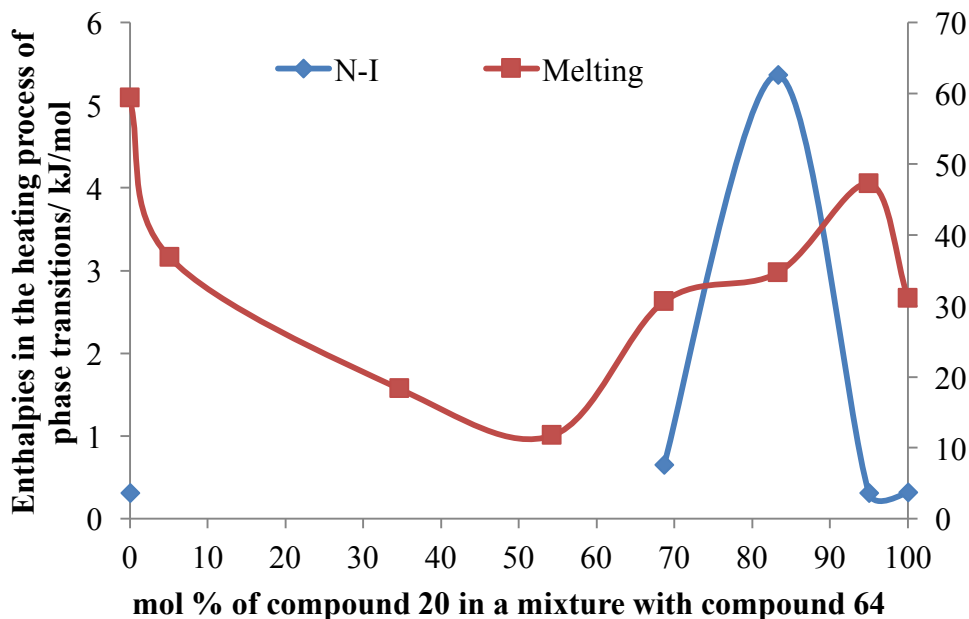
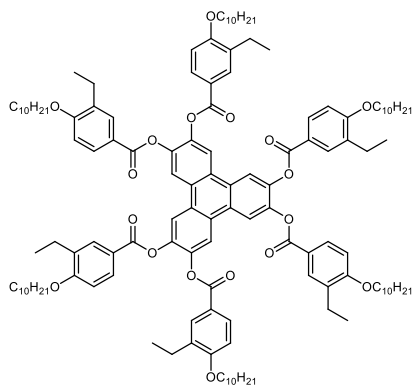


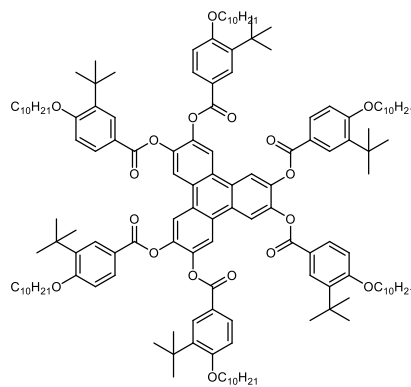
**Figure 5.70** The diagram showing the function of enthalpies (kJ/mol) of phase transitions in heating session with the mol concentration of compound **20** in a mixture with compound **64**.

### 5.2.3.9 Mixture Studies of Compounds **13**, **15** and **17** with **64**

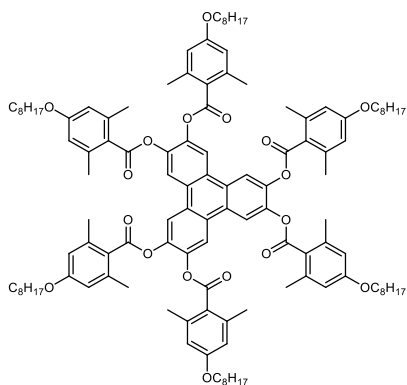
In the following section the three materials **13**, **15** and **17** all have the same triphenylene benzoate core structures with the similar peripheral aliphatic chain lengths; the only difference is the nature of lateral substituents in the outer rings. The lateral substituents were selected because they are relatively large and are expected to cause steric repulsive interactions. All of these compounds were mixed with compound **64** in order to create binary phase diagrams. Thus in the next section the structures of the materials their phase transition temperatures and computer simulations are presented, after which the individual results for the binary phase diagrams will be presented.



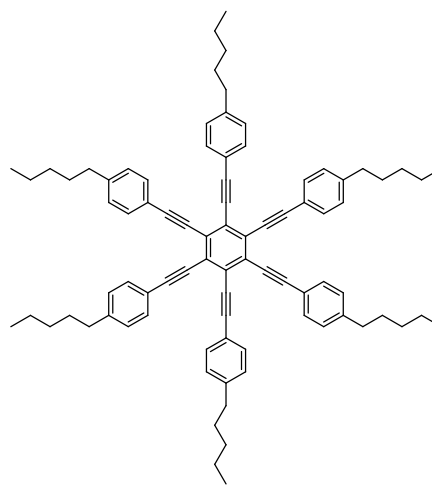
**13** K 136.4 N 207.0 °C Iso Liq



**15** K 194.0 N 224.9 °C Iso Liq



**17** K 154.1 N 169.6 °C Iso Liq



**64** K 166.0 N 183.8 °C Iso Liq

**Figure 5.71** The chemical structures and phase transition temperatures (°C) for compounds **13**, **15**, **17** and **64**.

The binary phase diagrams between compounds **13** and **64**, **15** and **64**, and **17** and **64** are shown in Figures 5.74, 5.77 and 5.80 respectively. The structures and phase transition temperatures, the energy minimised space-filling structures using the MM2 force field as implemented in ChemDraw 3D in gas phase at absolute zero, and molecular simulations using DFT theory for compounds **13** to **17** and **64** are shown respectively in Figures 5.71 to 5.74. In the figures the structures have been adjusted so they have roughly the same atom size, and therefore comparisons can be made by eye to the steric shapes of the structures.

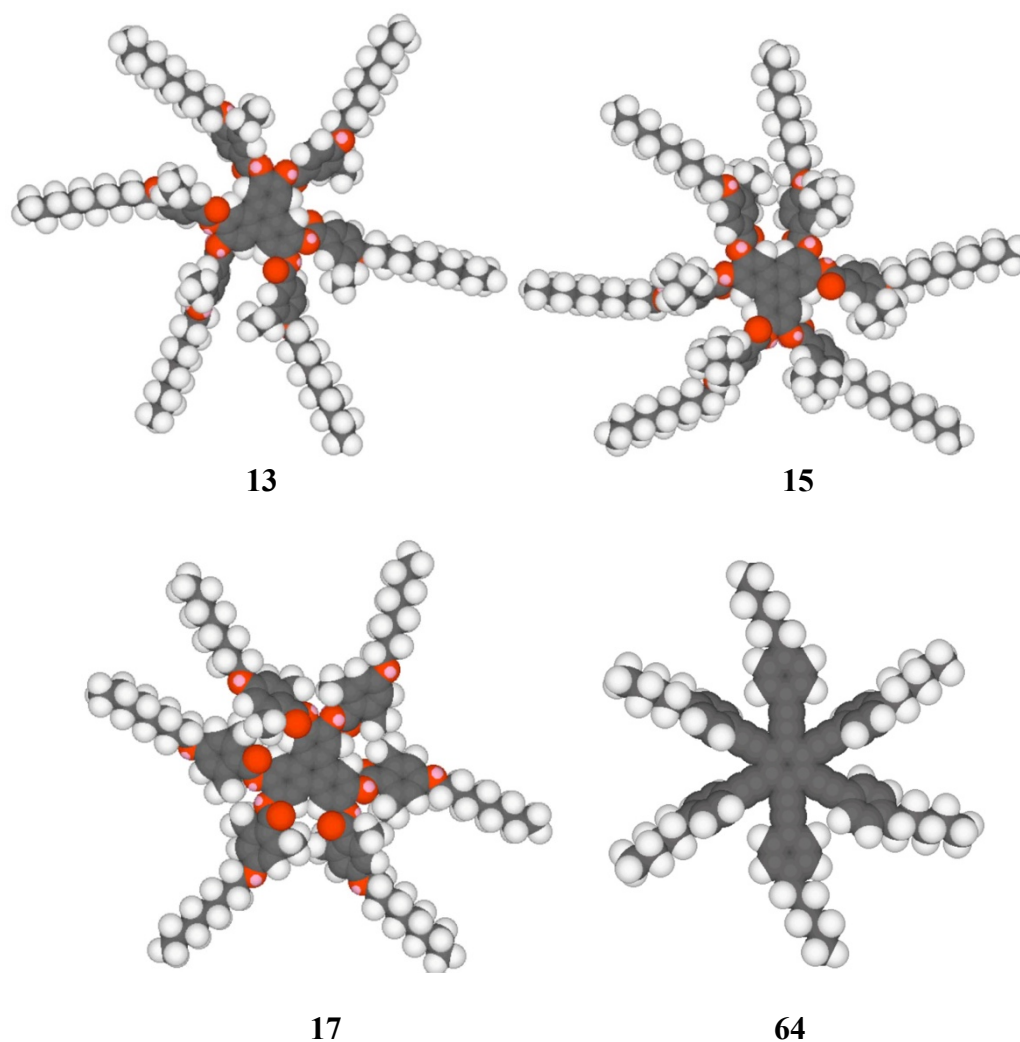
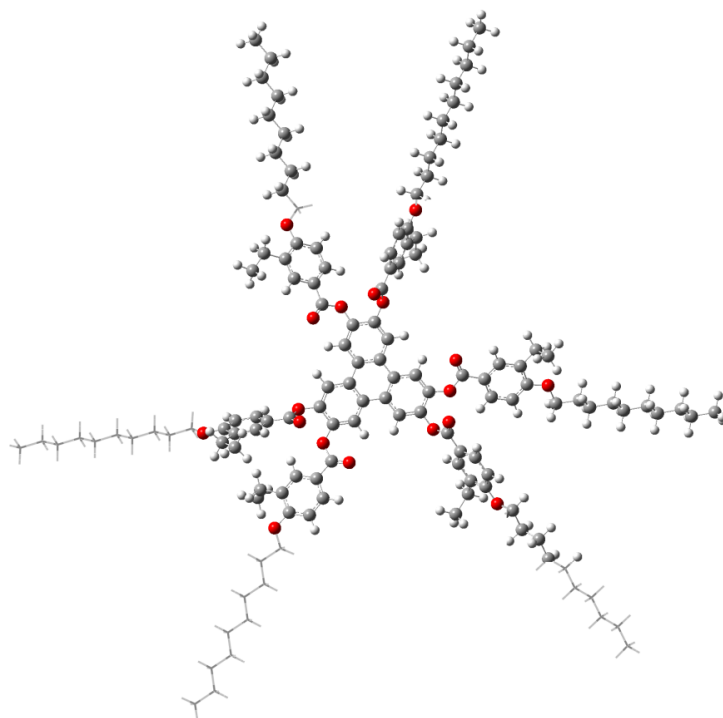
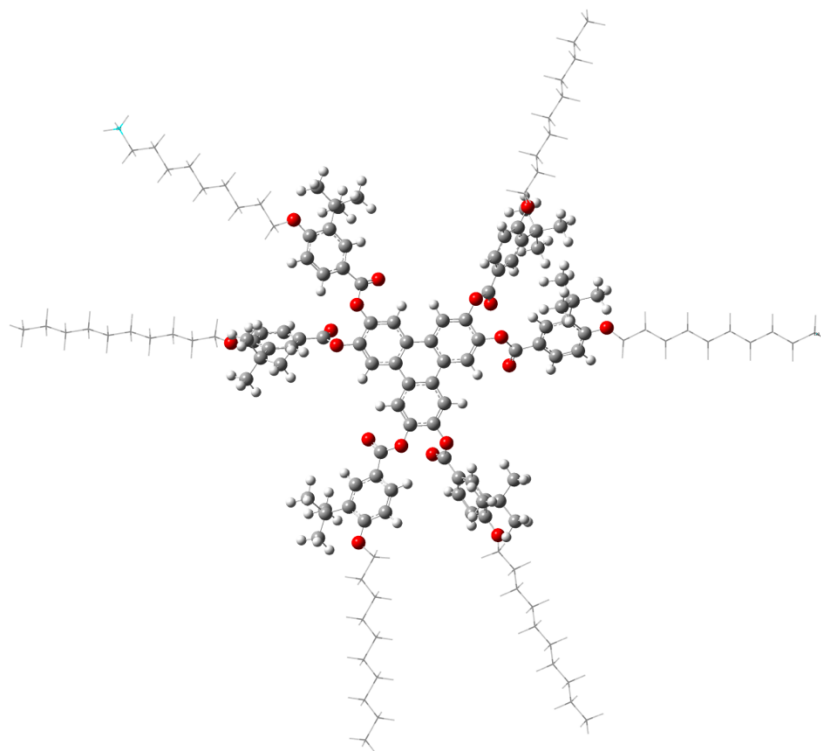


**Figure 5.72** The space filling structures of compounds **13** to **17** and **64** determined in gas phase at 0 K using the MM2 force field as implemented in ChemDraw 3D.

In the simulated structures, the diameters of the compound were as follows: **13** 47.17 Å, **15** is 43.69 Å, **17** is 42.04 Å and **64** is 28.05 Å. For all of the triphenylene based materials most of the peripheral aromatic rings were twisted out of the plane of the central triphenylene core, whereas for compound **64** all of the peripheral rings are stay as the same plane of the central benzene core.

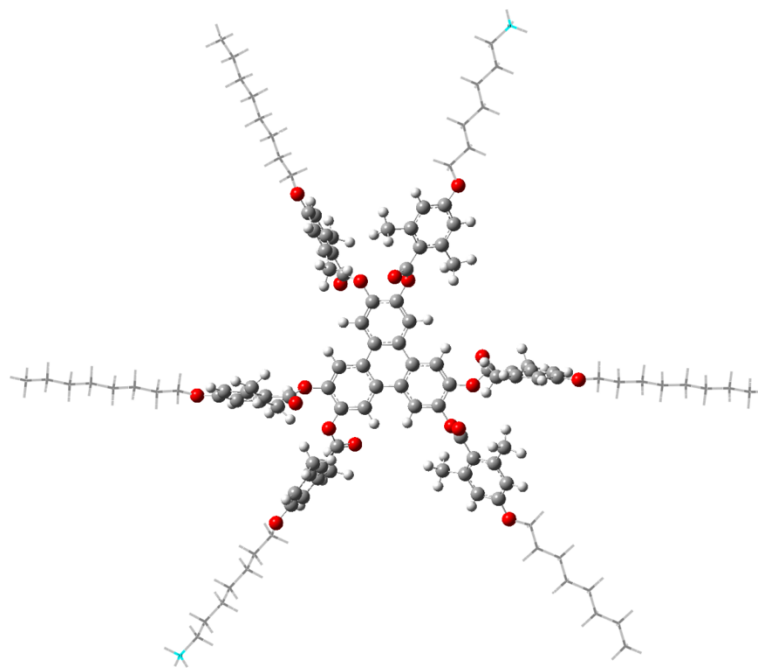


13

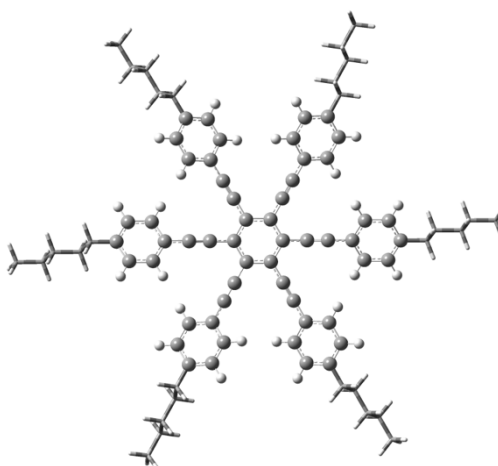


15

**Figure 5.73** The energy structures for compounds **13** and **15**, at the mixed ONIOM(B3LYP/6-31G(d):PM6) level of theory.



17



64

**Figure 5.74** The energy structure for compounds **17** and **64**, at the mixed ONIOM(B3LYP/6-31G(d):PM6) level of theory.

#### **Mixture Studies for Compound 13 with Compound 64:**

As compounds **13** and **64** were found to exhibit nematic phases it was expected that the binary phase diagram would show that they were capable of mixing even though they have different molecular shapes. Thus a series of mixtures (**TZ-M035-1-5**) of **13** and **64** were prepared, and their phase behaviour was examined firstly

by POM, and then by DSC. The transition temperatures for the mixtures determined by POM are shown in Table 5.25, whereas those determined from DSC are given together in Table 5.26. The composition of the predicted eutectic mixture (**TZ-M035-E**) was determined *via* Schröder-van Laar equation. The experimental phase behaviour was determined by POM and DSC for a mixture made up in the same proportions of the two compounds, the results for which are also shown in the Tables. The binary phase diagrams for the results shown in Table 5.25 and Table 5.26 are shown in Figures 5.75 and 5.76. In addition, photomicrographs of the defect textures at various concentrations of the two components are incorporated in the phase diagram in Figure 5.74.

**Table 5.25** Compositions (mol%) and transition temperatures (°C) for binary mixtures of **13** and **64** determined by POM.

ID	13/ mol%	K	/°C	N	/°C	Iso Liq
<b>64</b>	0	.	166.0	.	183.8	.
<b>TZ-M035-1</b>	10	.	163.8	.	169.0	.
<b>TZ-M035-2</b>	34.8	.	149.2	.	173.8	.
<b>TZ-M035-3</b>	54.3	.	124.5	.	187.6	.
<b>TZ-M035-4</b>	70.6	.	121.1	.	189.2	.
<b>TZ-M035-E</b>	83.8	.	121.6	.	196.4	.
<b>TZ-M035-5</b>	90.5	.	122.5	.	201.1	.
<b>13</b>	100	.	136.4	.	207.0	.

**Table 5.26** Mixture compositions (mol%) and transition temperatures (°C) and enthalpies (J/g) both on heating and cooling for binary mixtures of **13** and **64**.

ID	13/ mol%	Melting/ °C	N-Iso/ °C	
			Heating	Cooling
<b>64</b>	0	166.01	184.76	192.8
		$\Delta H = 53.98$	$\Delta H = 0.28$	$\Delta H = -0.20$
<b>TZ-M035-1</b>	10	163.75	-	-
		$\Delta H = 34.75$	-	-
<b>TZ-M035-2</b>	34.8	149.2	-	-
		$\Delta H = 4.42$	-	-
<b>TZ-M035-3</b>	54.3	124.53	169.98	169.08
		$\Delta H = 7.81$	$\Delta H = 0.42$	$\Delta H = -0.33$
<b>TZ-M035-4</b>	70.6	121.12	189.92	189.51
		$\Delta H = 10.37$	$\Delta H = 0.52$	$\Delta H = -0.48$
<b>TZ-M035-E</b>	83.8	121.61	196.93	197.21
		$\Delta H = 11.28$	$\Delta H = 0.73$	$\Delta H = -0.35$
<b>TZ-M035-5</b>	90.5	122.45	191.99	191
		$\Delta H = 12.43$	$\Delta H = 0.16$	$\Delta H = -0.17$
<b>13</b>	100	136.35	207	206.73
		$\Delta H = 13.24$	$\Delta H = 0.44$	$\Delta H = -0.71$

From the phase diagram of the mixtures obtained by **13** and **64**, it was revealed that when the concentration of sample **13** was increased from 38.4 to 100 mol%, the temperature ranges of the nematic phase became broader. The Schröder-van Laar equation predicted that the eutectic point occurs at 83.8 mol% of compound **13**, however, from the Gibbs phase diagram the melting temperature curve did not show any minimum 54.3 mol% of compound **13**, conversely it varied somewhat linearly. The N-I transition temperature curve exhibited ideal behaviour and varied almost linearly across the phase diagram.

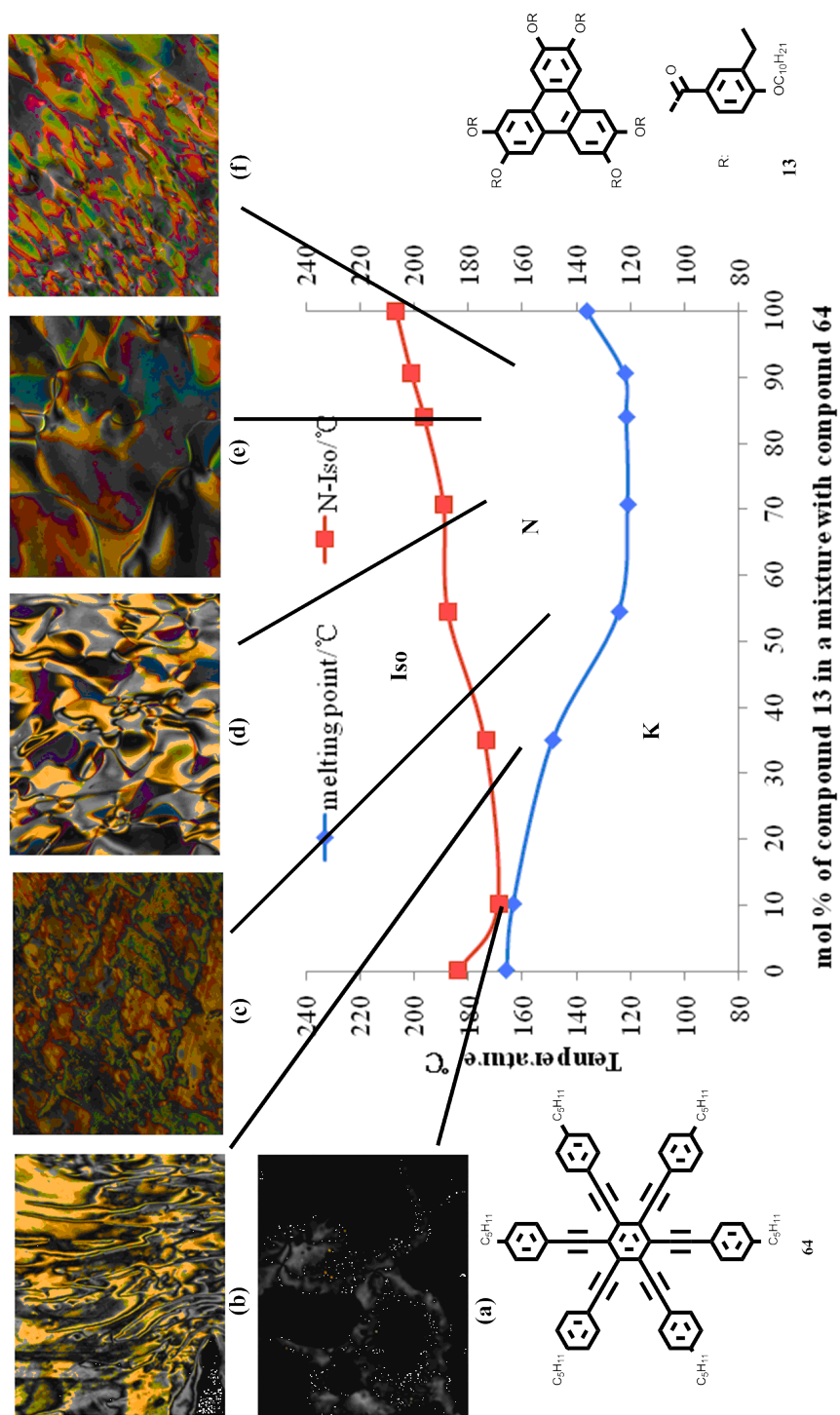


**Figure 5.75** The Gibbs phase diagram for the binary mixture series TZ-M035-1-5 of **13** and **64**. Photomicrographs (x100 magnification) showing representative optical textures for TZ-M035: (a) 10.0%, cooling, 166 °C, N; (b) 38.4%, cooling, 157.4 °C, N; (c) 54.3%, cooling, 141.8 °C, N; (d) 70.6%, heating, 147.6 °C, N; (e) 83.8%, heating, 176.4 °C, N; (f) 90.5%, heating, 172.0 °C, N.

In order to investigate this behaviour further, and to obtain accurate values for the transition temperatures on heating and cooling for the mixtures in the phase diagram, calorimetric studies were performed for each individual mixture, the results for which are shown in Table 5.26 along with the enthalpies for transitions and in Figures 5.76 and 5.77.

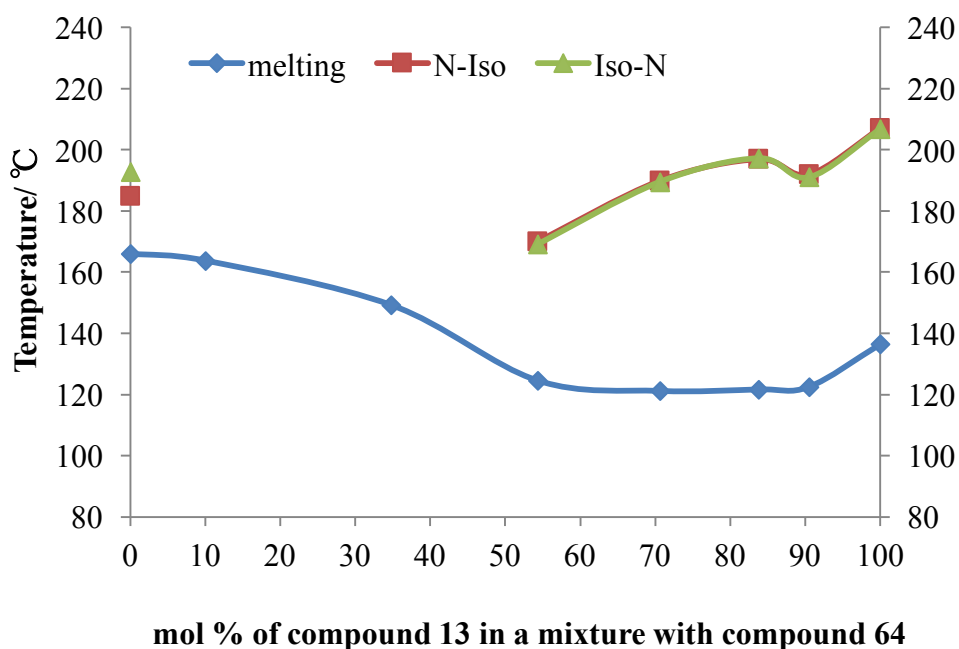


**Figure 5.76** The Gibbs phase diagram showing the biphasic region between heating and cooling for transition of mixtures of **13** and **64**.

It is important to note that the binary diagram for the transition temperatures determined by calorimetry, as shown in Figure 5.76, are broadly in agreement with the phase diagram in Figure 5.75 obtained by microscopy. Secondly, the temperatures of the peak maximums show little hysteresis with respect to heating and cooling cycles. This shows that there is little phase separation in the phase diagram. However, in the region between 10 and 38.4 mol% of compound **13** in the phase diagram, no enthalpies were detected by DSC, yet there is an indication of presence of a nematic phase as observed *via* microscopy.

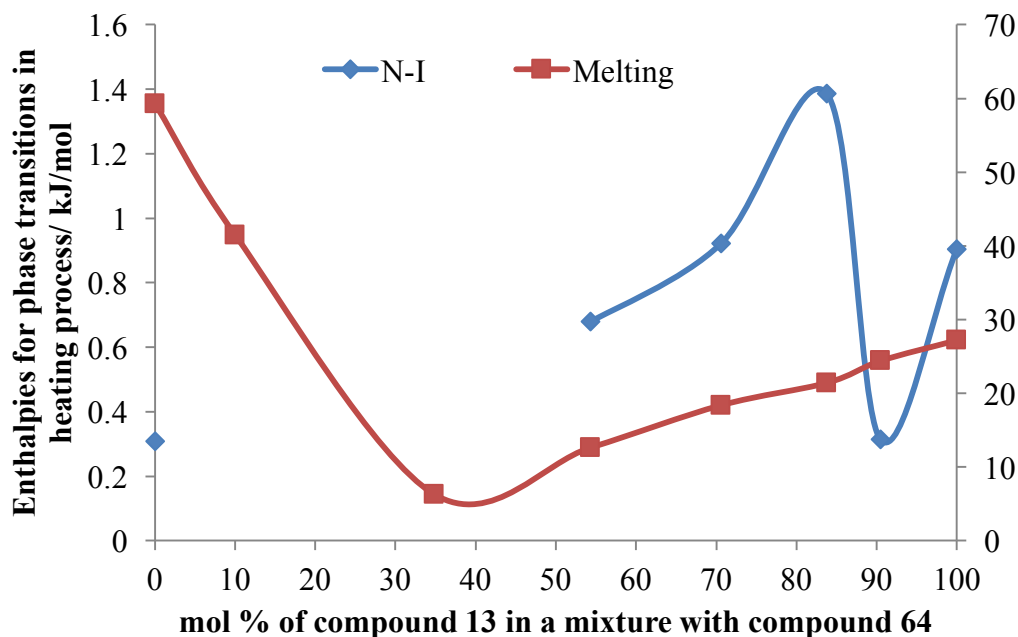


**Figure 5.77** The diagram showing the function of enthalpies (kJ/mol) of phase transitions in heating session with the mol% concentration of compound **13** in a mixture with compound **64**.

If we examine the values of the enthalpies of phase transitions as a function of concentration, as shown in Figure 5.77, it can be seen that the enthalpies for the N-I phase transition fluctuate with respect to concentration, yet their values although relatively low, vary between 0.03 to 1.4 kJ/mol. This indicates that the nematic phases, formed between the two materials at higher concentrations of compound **13**, are more ordered in the mesophase than those of low concentration. This result is in keeping with that described previously in section 5.2.3.8. Nevertheless, this result does not particularly affect the N to I transition temperature curve, and the nematic phase exhibits almost ideal behaviour across the phase diagram.

#### **Mixture Studies for Compound 15 with Compound 64:**

Compound **15** and **64** were both found to exhibit nematic phases and therefore expected to be co-miscible. Thus, a series of mixtures (**TZ-M036-1-5**) of **15** and **64** were prepared and their phase behaviour was examined by POM, and then by

DSC. The transition temperatures for the mixtures determined by POM are shown in Table 5.27, and those determined from DSC and their enthalpy values are given together in Table 5.28. The composition of the predicted eutectic mixture (**TZ-M036-E**) was found to be 25.6 mol% of compound **15**. The phase behaviour of the experimental mixture was determined by POM and DSC.

**Table 5.27** Compositions (mol%) and transition temperatures (°C) for binary mixtures of **15** and **64** determined by POM.

ID	<b>15</b> / mol%	K	/°C	N	/°C	Iso Liq
<b>64</b>	0	.	166.0	.	183.8	.
<b>TZ-M036-1</b>	9.7	.	161.8	-	-	.
<b>TZ-M036-E</b>	25.6	.	163.6	.	209.0	.
<b>TZ-M036-2</b>	45	.	163.3	.	213.0	.
<b>TZ-M036-3</b>	70	.	177.7	.	201.5	.
<b>TZ-M036-4</b>	78.5	.	185.6	.	216.5	.
<b>TZ-M036-5</b>	90	.	188.8	.	219.7	.
<b>15</b>	100	.	194.0	.	224.9	.

The binary phase diagrams for the results shown in Table 5.27 and Table 5.28 are shown respectively in Figure 5.78 and 5.79. In addition, photomicrographs of the defect textures at various concentrations are incorporated into the phase diagram in Figure 5.78.

**Table 5.28** Mixture compositions (mol%) and transition temperatures (°C) and enthalpies (J/g) both on heating and cooling for binary mixtures of **15** and **64**.

ID	15/ mol%	Melting/ °C	N-Iso/ °C	
			Heating	Cooling
<b>64</b>	0	166.01	184.76	192.80
		$\Delta H = 53.98$	$\Delta H = 0.28$	$\Delta H = -0.20$
<b>TZ-M036-1</b>	9.7	161.80	-	-
		$\Delta H = 41.34$	-	-
<b>TZ-M036-E</b>	25.6	163.60	209.86	171.12
		$\Delta H = 31.30$	$\Delta H = 15.4$	$\Delta H = -1.93$
<b>TZ-M036-2</b>	45	163.30	213.12	187.19
		$\Delta H = 25.15$	$\Delta H = 1.90$	$\Delta H = -0.51$
<b>TZ-M036-3</b>	70	177.71	204.59	202.38
		$\Delta H = 11.43$	$\Delta H = 0.49$	$\Delta H = -0.33$
<b>TZ-M036-4</b>	78.5	185.61	218.24	217.8
		$\Delta H = 15.87$	$\Delta H = 0.54$	$\Delta H = -0.57$
<b>TZ-M036-5</b>	90	188.78	221.27	221.30
		$\Delta H = 20.01$	$\Delta H = 1.07$	$\Delta H = -1.50$
<b>15</b>	100	194.03	225.46	225.43
		$\Delta H = 24.64$	$\Delta H = 0.55$	$\Delta H = -0.43$

As shown in Figure 5.78, it revealed that the melting temperature curve almost varied linearly as a function of concentration, which was not as predicted by the Schröder-van Laar equation. At the predicted eutectic point of 25.6 mol% of compound **15** eutectic phenomena was not found. However, at this point the enthalpies for the clearing points started to disappear on reducing the concentration of compound **15** in the mixtures. The nematic phase range was much wider between 25-70 mol% of compound **15** than for any of the other mixtures. These observations suggest that the phase diagram do not have a eutectic predicted by the calculation of Schröder-van Laar equation and thermal studies by calorimetry have a break in the concentration curve. Thus, in order to investigate this behaviour further, and to confirm and obtain accurate values for the transition temperatures

on heating and cooling for the mixtures in the phase diagram, calorimetric studies were performed for each individual mixture, the results for which are shown in Figure 5.79 and Table 5.28 along with the enthalpies for transitions.

Firstly, it is important to note that the binary diagram for the transition temperatures determined by calorimetry, as shown in Figure 5.79, were in agreement with the phase diagram obtained *via* microscopy. Additionally, the temperatures of heating and cooling cycles show little hysteresis in the region of 70 to 100 mol% of compound **15** but below 70 mol%, the phase segregation became much wider when the concentration of compound **15** was reduced, and the potential eutectic point was approached. Thirdly, there are no enthalpies detected by DSC at the point of 9.7 mol% of compound **15**, and moreover no mesophase behaviour was observed *via* microscopy either. If we examine the values of the enthalpies for the N to I phase transitions as a function of concentration, as shown in Figure 5.80, it can be seen that the enthalpies of N-I phase transition vary almost a linear after above 45 mol% of compound **15**, but at the predicted eutectic of 25.6 mol% of compound **15** it almost diverges, and is more than 10 times bigger than other enthalpies. This is very unusual behaviour, and potentially indicates the presence of a solid phase.

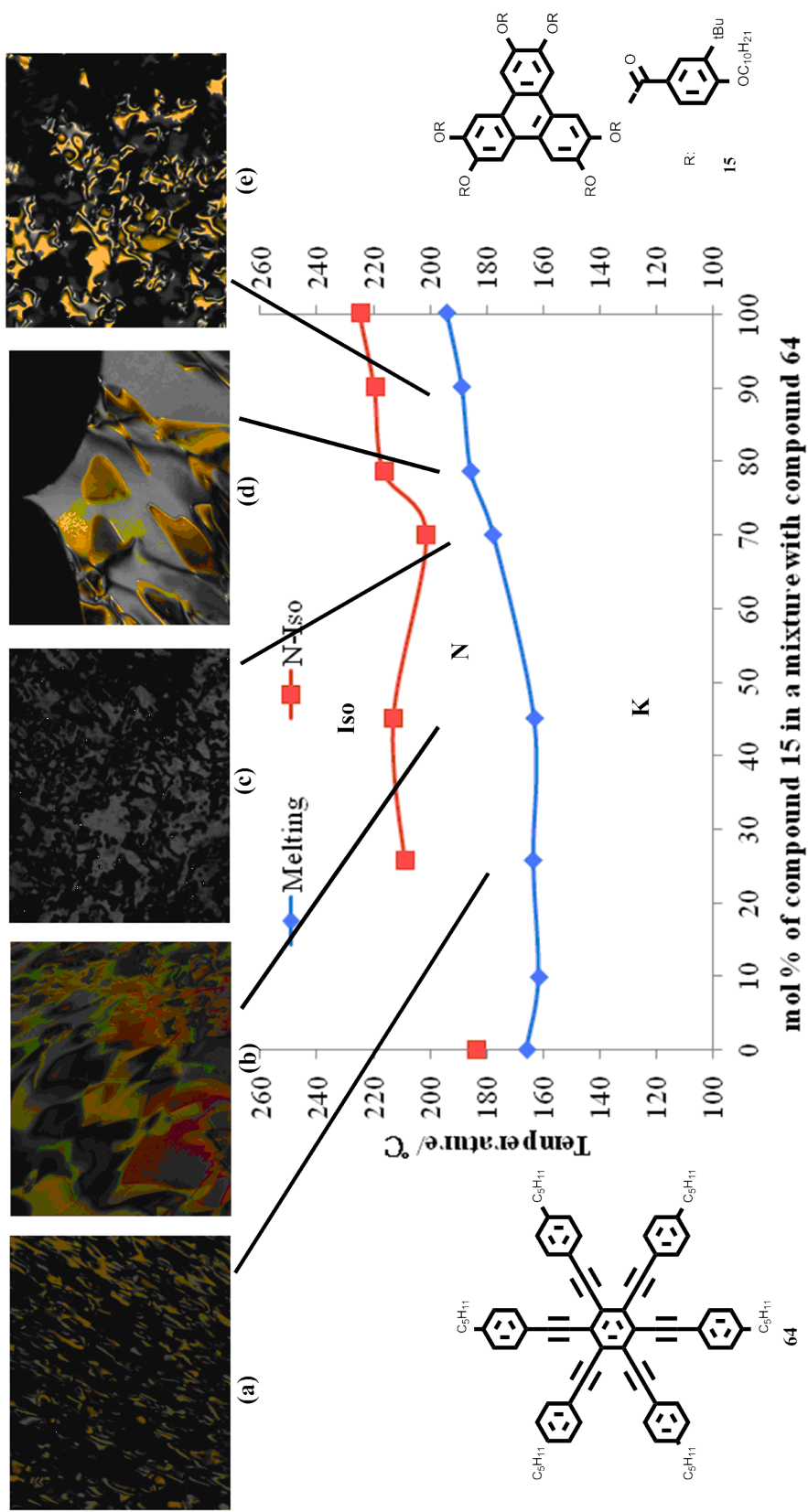


**Figure 5.78** The Gibbs phase diagram for the binary mixture series **TZ-M036** of **15** and **64**. Photomicrographs (x100 magnification) showing representative optical textures for **TZ-M036**: **(a)** 25.6%, cooling, 170.7 °C, N; **(b)** 45.0%, cooling, 182.0 °C, N; **(c)** 70.0%, cooling, 170.0 °C, N; **(d)** 78.5%, heating, 199.0 °C, N; **(e)** 90.0%, cooling, 181.0 °C, N.

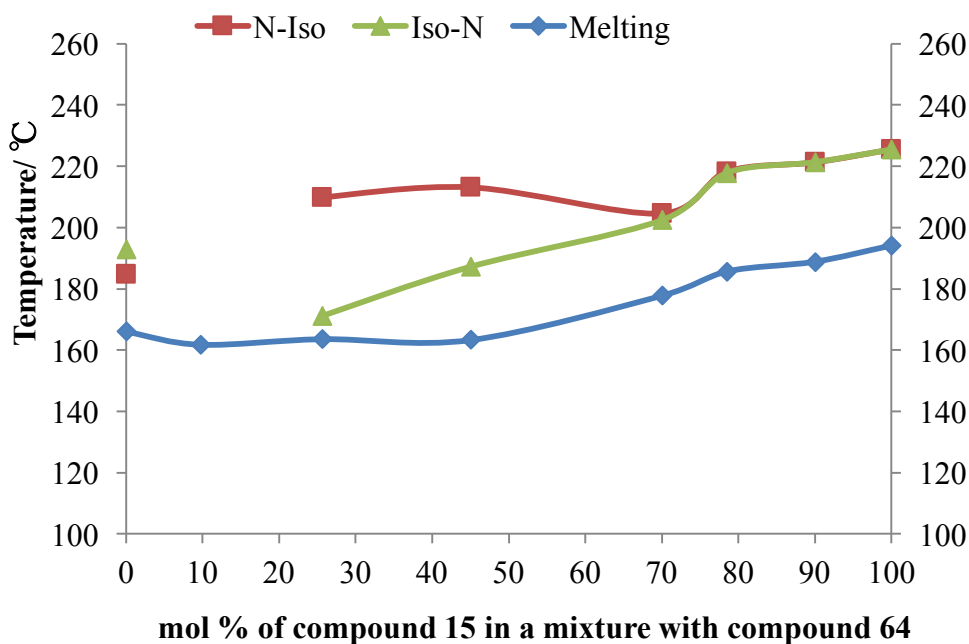


**Figure 5.79** The Gibbs phase diagram showing the biphasic region between heating and cooling (°C) for transition of mixtures of **15** and **64**.

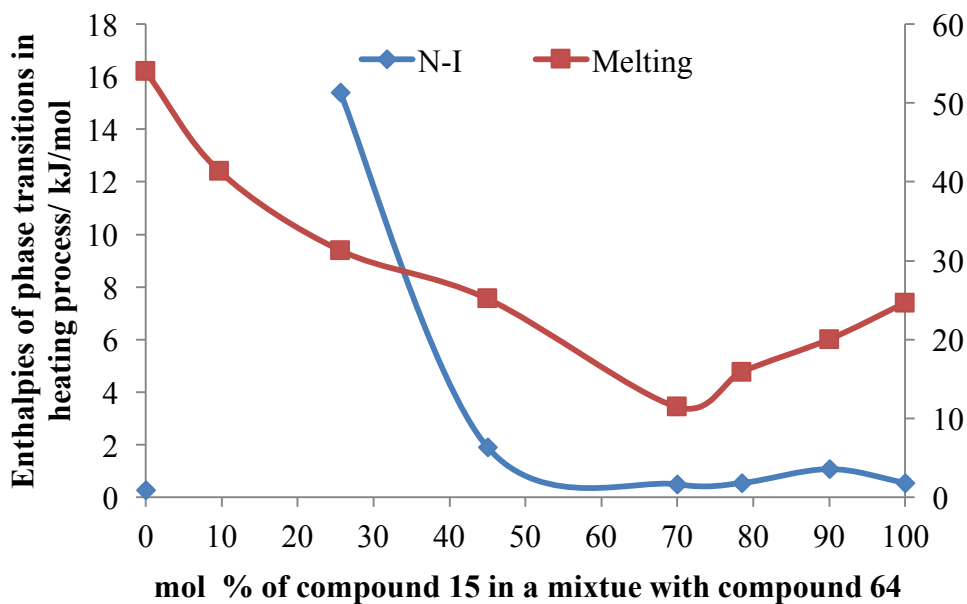


**Figure 5.80** The diagram showing the function of enthalpies (kJ/mol) of phase transitions on heating with the mol% concentration of compound **15** in a mixture with compound **64**.

### Mixture Studies for Compound 17 with Compound 64:

Compound 17 and 64 were found to exhibit nematic phase, thus it was expected a capable of mixing. Therefore, a series of mixtures (TZ-M037-1-5) of 17 and 64 were prepared and their phase behaviour was examined by POM and then DSC. The transition temperatures for the mixtures determined by POM are shown in Table 5.29, whereas those determined from DSC are given together in Table 5.30. The composition of the predicted eutectic mixture (TZ-M037-E) and the phase behaviour of the experimental mixture determined by POM and DSC are given in both Tables. The binary phase diagrams for the results shown in Table 5.29 and Table 5.30 are shown respectively in Figure 5.81 and 5.82. In addition, photomicrographs of the defect textures at various concentrations are incorporated into the phase diagram in Figure 5.81.

**Table 5.29** Compositions (mol%) and transition temperatures (°C) for binary mixtures of 17 and 64 determined by POM.

ID	17/ mol%	K	/°C	N	/°C	Iso Liq
64	0	.	166.0	.	183.8	.
TZ-M037-1	10.2	.	161.8	.	168.1	.
TZ-M037-2	34.2	.	155.4	.	163.5	.
TZ-M037-E	54.7	.	143.9	.	169.3	.
TZ-M037-3	70	.	145.1	.	168.9	.
TZ-M037-4	79.4	.	144.8	.	168.1	.
TZ-M037-5	90	.	147.8	.	169.8	.
17	100	.	154.1	.	169.6	.

**Table 5.30** Mixture compositions (mol%) and transition temperatures (°C) and enthalpies (J/g) both on heating and cooling for binary mixtures of **17** and **64**.

ID	17/ mol%	Melting/ °C	N-Iso/ °C	
			Heating	Cooling
<b>64</b>	0	166.01	184.76	192.8
		$\Delta H= 53.98$	$\Delta H= 0.28$	$\Delta H= -0.20$
<b>TZ-M037-1</b>	10.2	161.83	-	-
		$\Delta H= 29.88$	-	-
<b>TZ-M037-2</b>	34.2	155.4	-	-
		$\Delta H= 11.84$	-	-
<b>TZ-M037-E</b>	54.7	143.92	168.18	165.82
		$\Delta H= 11.27$	$\Delta H= 0.26$	$\Delta H= -0.31$
<b>TZ-M037-3</b>	70	145.14	169.72	168.58
		$\Delta H= 27.45$	$\Delta H= 0.28$	$\Delta H= -0.31$
<b>TZ-M037-4</b>	79.4	144.75	169.18	168.93
		$\Delta H= 23.27$	$\Delta H= 0.28$	$\Delta H= -0.50$
<b>TZ-M023-5</b>	90	147.83	170.69	170.99
		$\Delta H= 24.71$	$\Delta H= 0.37$	$\Delta H= -0.57$
<b>17</b>	100	154.09	170.12	170.08
		$\Delta H= 21.23$	$\Delta H= 0.14$	$\Delta H= -0.19$

As with some of the earlier phase diagrams continual miscibility of the nematic phase was observed across the concentration range of the phase diagram. In the region between the 10.2 mol% and 34.2 mol% concentration of compound **17** the temperature ranges of the nematic phase narrowed, but at higher concentrations of compound **17** the range increased substantially. At the predicted concentration for the eutectic mixture of 54.7 mol% of compound **17** no phenomena was observed in the phase diagram. Again, the left and right hand sections of the phase diagram (shown in the Figure 5.80) exhibit different properties, with the left hand segment showing a greater depression in the N to I values than the right hand side. The right hand part is dominated by the packing of the molecules with larger diameters, whereas the reverse is the case for the left hand side. In order to investigate this

behaviour further, and to obtain accurate values for the transition temperatures on heating and cooling for the mixtures in the phase diagram, calorimetric studies were performed for each individual mixture, the results for which are shown in Figure 5.81 and Table 5.30 along with the enthalpies for transitions.

Importantly the transition temperatures for the binary diagram for determined by calorimetry, as shown in Figure 5.81, are broadly in agreement with those in the phase diagram, which were obtained by microscopy. Secondly, the temperatures of the peak maximums show little hysteresis with respect to heating and cooling cycles, thus it means that there is little phase segregation in the phase diagram. Furthermore, for the region between 10.2 and 34.2 mol% of compound **17** in the phase diagram, no enthalpies were detected by DSC. However, there was an indication of mesophase presence as observed *via* microscopy, even though the phase exhibited was short lived.

If we examine the values of the enthalpies of phase transitions as a function of concentrations, as shown in Figure 5.82, the enthalpies for the N-I phase transition vary in the region of 0.3 to 0.7 kJ/mol above 50 mol% concentration of compound **17**, whereas for concentrations below 50 mol% of compound **17** no enthalpies could be detected. Although microscopy shows that the nematic phase is continually miscible across the phase diagram, the higher enthalpies in the region of higher concentrations of compound **17** indicate that the nematic phase structure is slightly different from the structure at lower concentrations; even though there is no appreciable change in the N to I curve. These results seem to have commonality across the various series of mixtures studied.

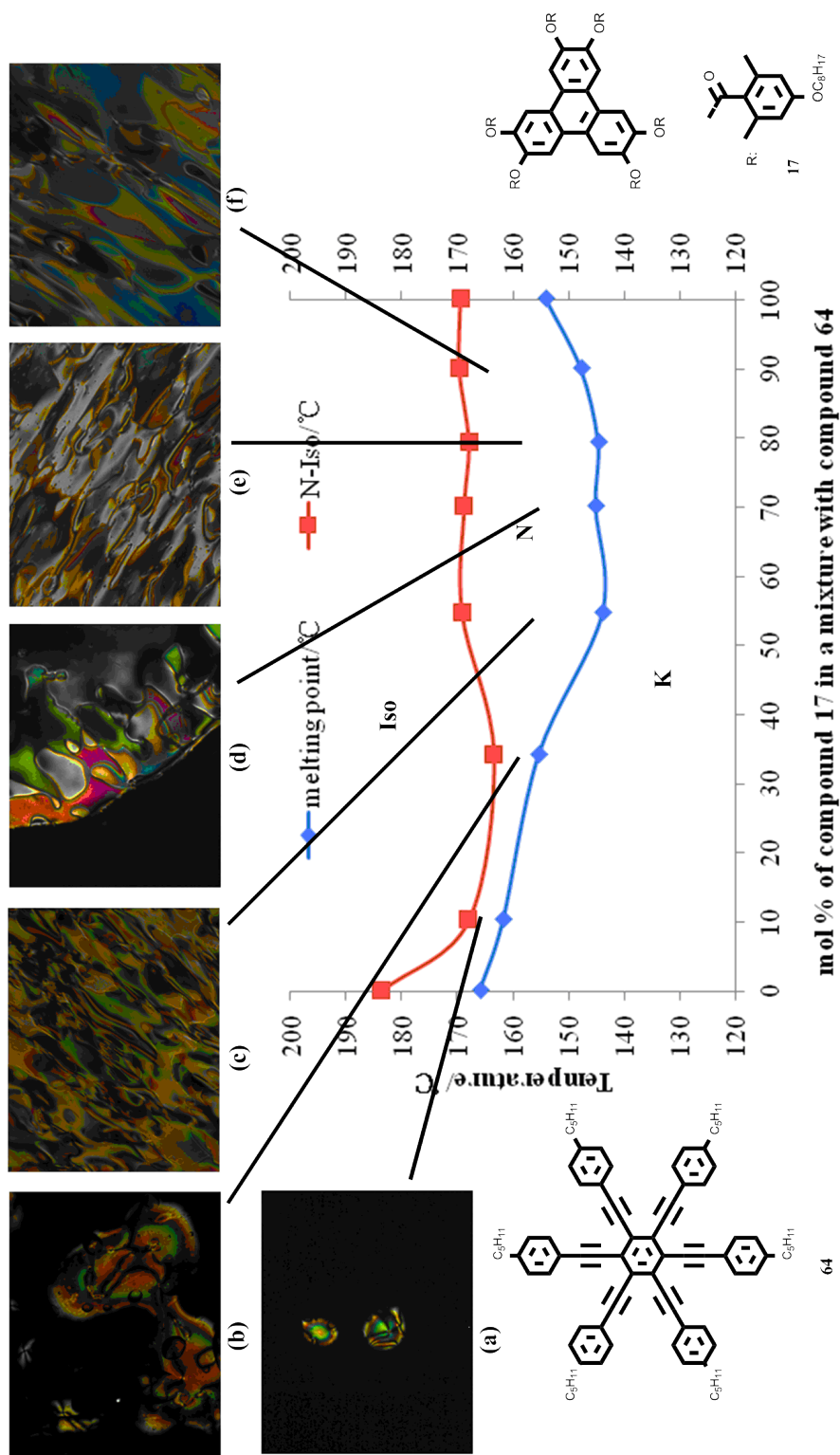


**Figure 5.81** The Gibbs phase diagram for the binary mixture series **TZ-M037** of **17** and **64**. Photomicrographs (x100 magnification) showing representative optical textures for **TZ-M037**: **(a)** 10.2%, heating, 170.0 °C, N; **(b)** 34.2%, cooling, 152.7 °C, N; **(c)** 54.7%, heating, 157.9 °C, N; **(d)** 70.0%, cooling, 149.0 °C, N; **(e)** 79.4%, heating, 154.2 °C, N; **(f)** 90.0%, heating, 166.0 °C, N.

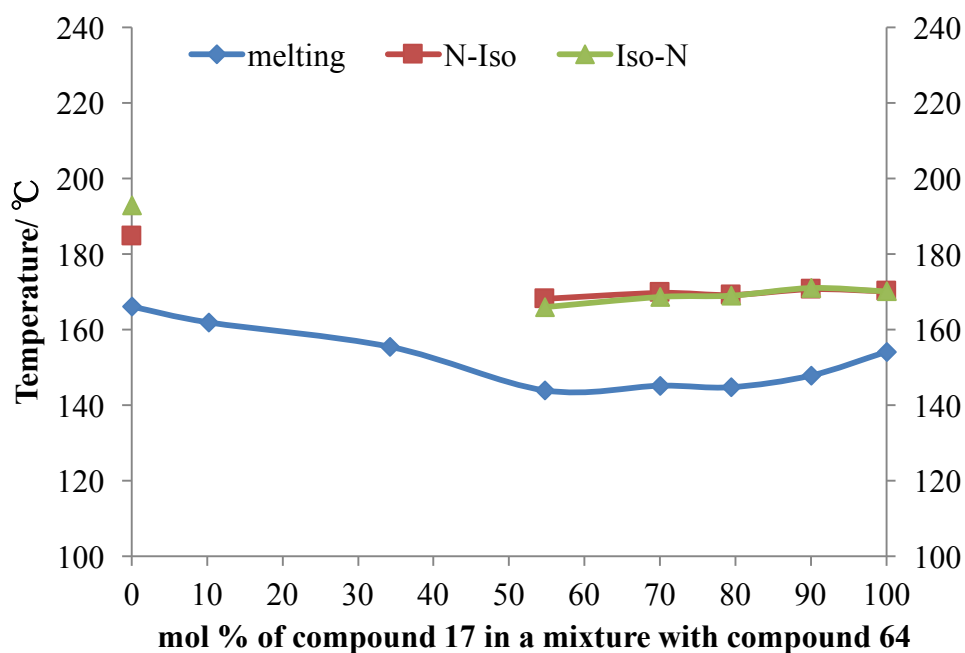


**Figure 5.82** The Gibbs phase diagram showing the biphasic region between heating and cooling cycles for phase transitions for mixtures of **17** and **64**.

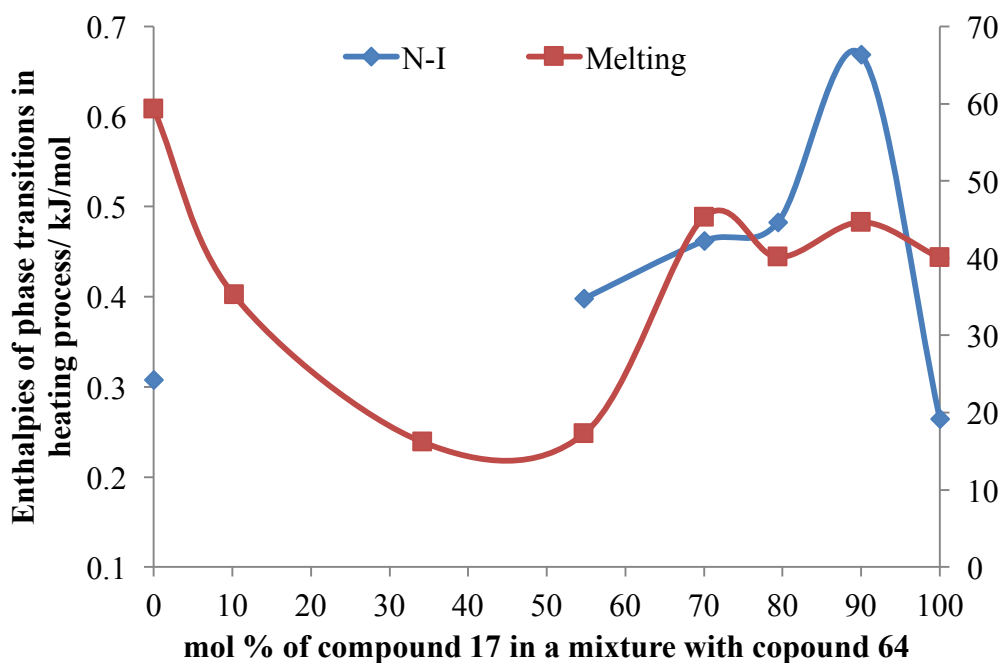


**Figure 5.83** The diagram showing the function of enthalpies (kJ/mol) of phase transitions in heating process with the mol% concentration of compound **17** in a mixture with compound **64**.

### 5.3 Summary

In this chapter, co-miscibilities of nematogens of disc-like triphenylene derivatives with each other, with rod-like tetra-benzoate molecules and with phenyl hexa-alkynes are investigated and discussed based on phase diagrams. For the nematic discotic triphenylene derivatives, they have similar behaviour as rod-like systems. However, when the smaller molecules such as rod-like tetra-benzoate molecules and phenyl hexa-alkynes are added into the discotic triphenylene derivatives system, they show different behaviour as rod-like systems.

## **Chapter 6: Phase Diagrams of Columnar Disc-like Materials**

## Chapter 6: Phase Diagrams of Columnar Disc-like Materials

### 6.1 Introduction

In the previous chapter miscibility studies and binary phase diagrams were developed for disc-like nematogenic materials in order to examine how well fluid-like mesophases mix. It appeared that disc-like materials formed mixtures relatively easily, whereas mesogens possessing disc-like and x-shaped molecular architectures did not. In the following chapter the mixing of materials that exhibit columnar phases will be investigated in order to investigate how such systems those have 2D crystal structures might mix or phase segregate. These studies will ultimately provide insights into the nature of crystallinity versus true liquid-crystallinity. Again the chapter is divided into the following sections:

1. Phase behaviour of columnars of disc-like triphenylene derivatives.
2. Phase behaviour of columnars of discotic triphenylene derivatives with rod-like tetra-benzoate molecules.
3. Phase behaviour of columnars of disc-like triphenylene mesogens with phenyl hexa-alkynes.

### 6.2 Structures of Columnar Liquid Crystals

In the following sections the materials investigated have been said to exhibit hexagonal columnar liquid crystal phases, and from microscopy many have been said to exhibit disordered columnar structures, for which the molecules are disordered along the column axes. In this case the structural order is that of a 2D crystal in the plane normal to the columnar axes ( $\text{Col}_{\text{hd}}$ ). However, there is also the possibility that the molecules are ordered ( $\text{Col}_{\text{ho}}$ ), in which case the mesophases should be considered as 3D soft crystal phases. These phases are shown together in Figure 6.1. In the classification of such phases, unlike that of calamitic phases,

miscibility studies have been effectively absent with respect to phase identification. In addition, the use of X-ray diffraction has been limited.

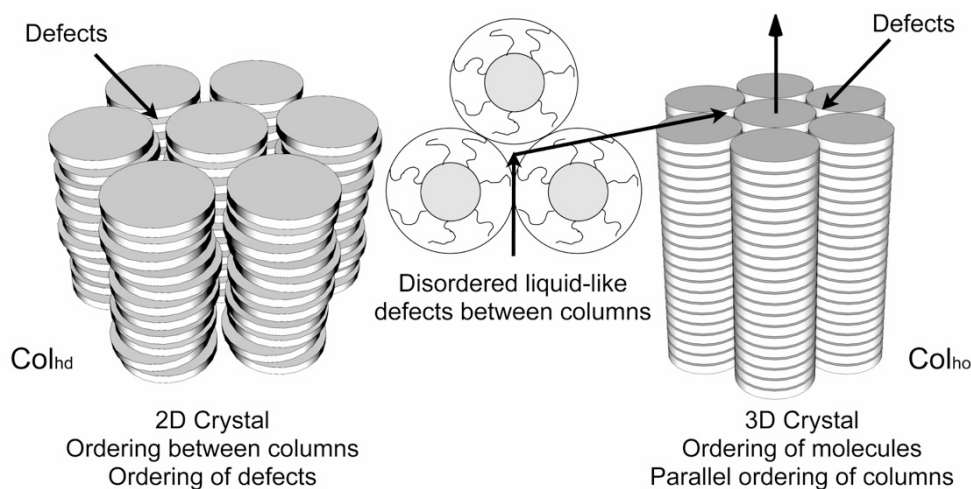


**Figure 6.1** The structures of the disordered and ordered columnar mesophases.[87]

### 6.3 Phase Behaviour of Binary Columnar Systems

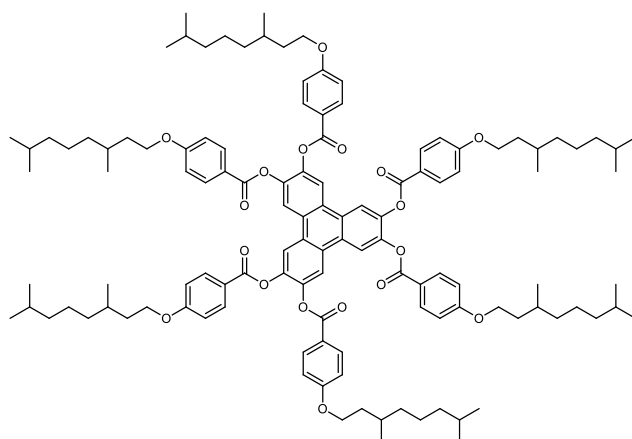
It seems the binary mixtures of nematic triphenylene derivatives exhibited similar properties to the calamitic systems containing rod-like molecules; however, there is no research about the binary mixtures of discotic columnar compounds for these systems. Thus to investigate them further, a series of mixtures were prepared and examined by polarized optical microscopy and differential scanning calorimetry.

#### 6.3.1 Mixture Studies of Compounds **21** with **32**

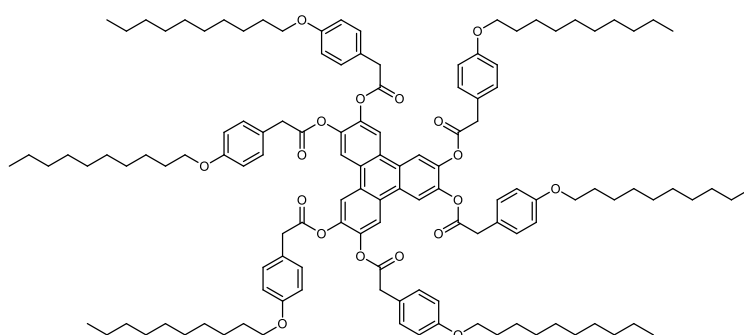
The structures and phase transitions of compounds **21** and **32** are shown in Figure 6.2. Both materials have been shown to exhibit columnar but not nematic phases. The two materials were selected for investigation because they have similar chemical structures, with triphenylene core units and peripheral aliphatic chains, but differing between the methyl branching of compound **21** and unbranched (normal) chains of compound **32**. In both cases simulations show that the peripheral rings are twisted out of the plane of the triphenylene core. This twist is

thought to assist in the columns being disordered along the column axes, thereby supporting the formation of columnar disordered phases.

The transition temperatures ( $^{\circ}\text{C}$ ), the space filling minimised structures determined using the MM2 force field as implemented in ChemDraw 3D in gas phase at absolute zero, and simulations based on DFT theory to show the stereochemical structures for compounds **21** and **32** are shown together in Figures 6.2 to 6.4 respectively. (Note the structure of compound **32** proved to be too complex for minimization using DFT theory at the mixed ONIOM(B3LYP/6-31G(d):PM6) level of theory because of its flexible structure producing a large number of conformers).

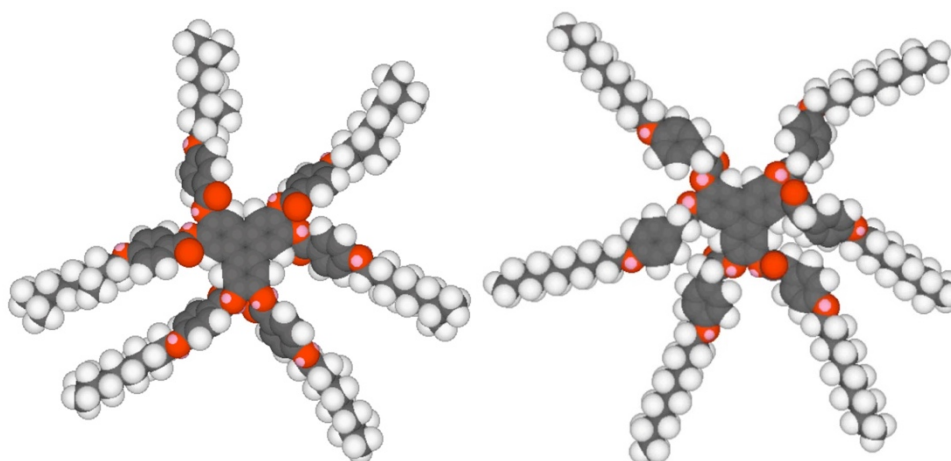


**21** K 128.2 Col<sub>h</sub> 208.4 °C Iso Liq



**32** K 106.6 Col<sub>h</sub> 169.0 °C Iso Liq

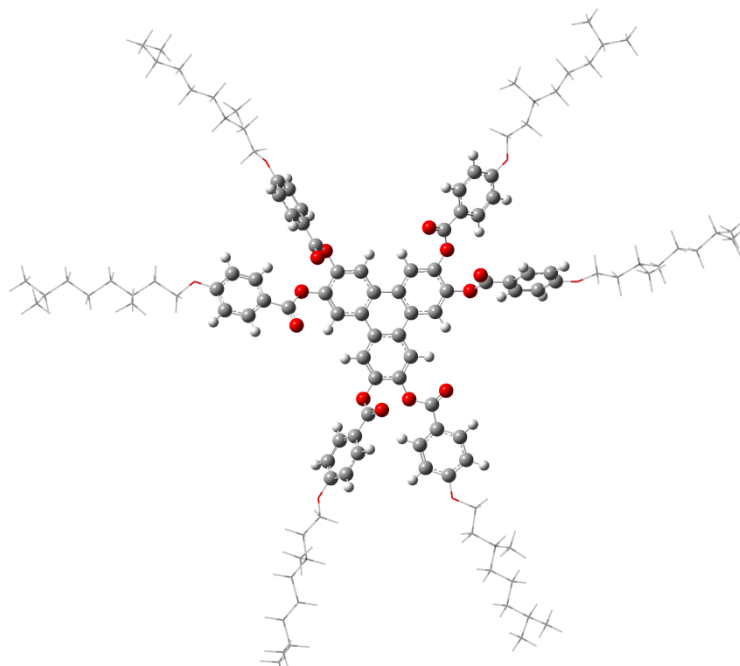
**Figure 6.2** The chemical structures and phase transitions of compounds **21** and **32**.



**21**

**32**

**Figure 6.3** The space filling structures of compounds **21** and **32** determined in gas phase at 0 K using the MM2 force field as implemented in ChemDraw 3D.



**21**

**Figure 6.4** The energy structure for compound **21** at the mixed ONIOM(B3LYP/6-31G(d):PM6) level of theory.

A series of mixtures (**TZ-M003-1-5**) of compounds **21** and **32** were prepared and their phase behaviour was examined firstly using POM and then by DSC. The transition temperatures for the mixtures determined by POM are shown in Table 6.1, whereas those determined from DSC are given together in Table 6.2. As before with these studies, the composition of the predicted eutectic mixture (**TZ-M003-E**) was determined *via* the Schröder-van Laar equation, with a value of 78.3 mol% of compound **21** being found. The results for the phase behaviour of the experimental eutectic mixture determined by POM and DSC are shown in both Tables. The binary phase diagrams for the results given in Tables 6.1 and 6.2 are shown diagrammatically in Figures 6.5 and 6.6 respectively. In addition, photomicrographs of the detected textures at various points are incorporated into the phase diagrams.

**Table 6.1** Mixture compositions (mol%) and transition temperatures (°C) for binary mixtures of compounds **21** and **32**.

ID	<b>21</b> / mol%	K	/°C	Col <sub>h</sub>	/°C	Iso Liq
<b>32</b>	0	.	106.6	.	169.0	.
<b>TZ-M003-1</b>	19.6	.	100.5	.	142.5	.
<b>TZ-M003-2</b>	38.6	.	88.2	.	115.3	.
<b>TZ-M003-3</b>	56.1	.	81.0	-	-	.
<b>TZ-M003-4</b>	68.2	.	89.3	.	149.0	.
<b>TZ-M003-E</b>	78.3	.	76.9	.	168.9	.
<b>TZ-M003-5</b>	84.9	.	91.7	.	184.2	.
<b>21</b>	100	.	128.2	.	208.4	.

**Table 6.2** Mixture compositions (mol%) and phase transition temperatures (°C) and enthalpies (J/g) both in heating and cooling session for binary mixtures of **21** and **32**.

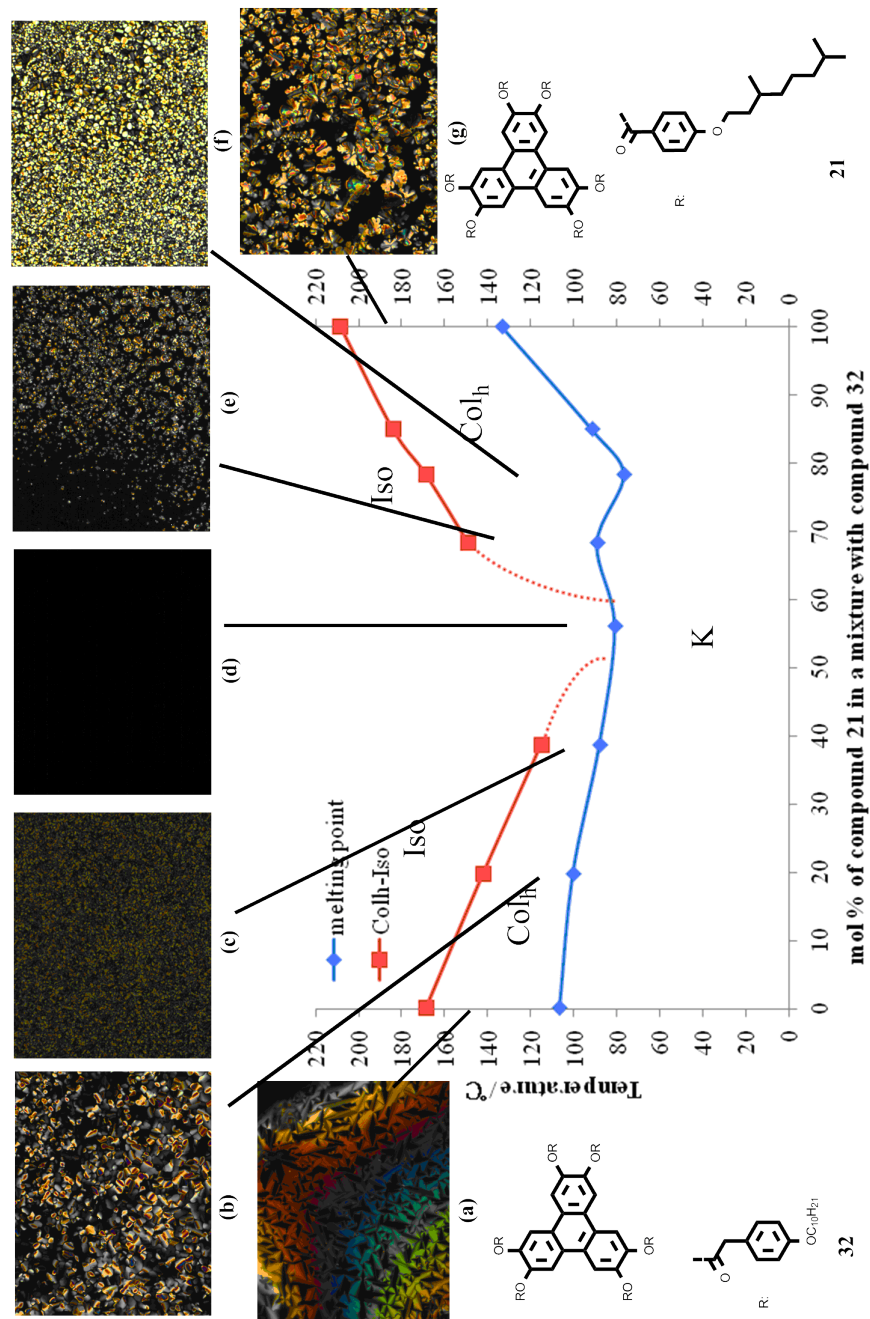
ID	21/ mol%	Melting/ °C	Col <sub>h</sub> -Iso	
			Heating/ °C	Cooling/ °C
<b>32</b>	0	106.62	176.7	174.93
		$\Delta H = 10.75$	$\Delta H = 2.59$	$\Delta H = -2.28$
<b>TZ-M003-1</b>	19.6	100.54	142.52	139.63
		$\Delta H = 9.50$	$\Delta H = 0.39$	$\Delta H = -0.37$
<b>TZ-M003-2</b>	38.6	88.19	122.71	119.37
		$\Delta H = 5.24$	$\Delta H = 1.38$	$\Delta H = -1.49$
<b>TZ-M003-3</b>	56.1	81.04	-	-
		$\Delta H = 1.61$	-	-
<b>TZ-M003-4</b>	68.2	89.26	169.6	158.91
		$\Delta H = 2.87$	$\Delta H = 1.56$	$\Delta H = -1.42$
<b>TZ-M003-E</b>	78.3	76.93	183.53	179.31
		$\Delta H = 1.02$	$\Delta H = 2.54$	$\Delta H = -2.44$
<b>TZ-M003-5</b>	84.9	91.74	180.31	173.53
		$\Delta H = 0.31$	$\Delta H = 1.76$	$\Delta H = -2.04$
<b>21</b>	100	133.47	209.69	205.73
		$\Delta H = 12.25$	$\Delta H = 5.38$	$\Delta H = -6.30$

Figure 6.5 shows the binary phase diagram for mixtures of compounds **21** and **32** that was produced from the results obtained by POM on the various mixtures. The diagram shows that, even though both compounds exhibit hexagonal columnar phases on their own, upon mixing the hexagonal columnar to the isotropic liquid phase transition is suppressed rapidly and disappears in the centre of the phase diagram. This indicates that the two compounds are not miscible across all of the concentration range. The Schröder-van Laar equation predicted a eutectic at 78.3 mol% compound **21** in the mixture, and it can be seen that there is a weak depression in the melting point curve at this value. However, the disappearance of the columnar phase appears to occur in the range of 38 to 56 mol% of compound

**21**. This behaviour is exemplified in Figure 6.6 where the texture, or lack of a texture, shown for the mixture at the centre of the phase diagram. This indicates that a columnar phase is not present. Thus, the Gibbs phase diagram reveals unexpected behaviour, and it also demonstrates that the isotropic to columnar transition does not behave in a comparable way with miscibility phase diagrams of calamitic nematic or smectic phases, and it appears more like classical behaviour for the melting of a soft crystal.

Another viewpoint is that the observations of the depression in the clearing point transitions could be due to phase segregation between the two compounds. However, the transition temperatures to the solid state across the concentration range vary almost linearly with respect to the concentration. This observation suggests that the two materials ideally mix and do not segregate. Again this shows that the system is acting more like a classical phase diagram for two solids, as shown in Figure 6.7, where A is compound **32** and B is compound **21**, and the Solid A-Solid B line is the equivalent to the melting point curve in the phase diagram.

In order to investigate this behaviour further, and to obtain accurate values for the transition temperatures on heating and cooling for the mixtures in the phase diagrams, calorimetric studies were performed for each individual mixture, and the results for which are shown in Table 6.2 and Figure 6.8, along with the enthalpies for the phase transitions, see Figure 6.9.



**Figure 6.5** The Gibbs phase diagram for the binary mixture series **TZ-M003** of **21** and **32**. Photomicrographs (x 100 magnification) showing representative optical textures for **TZ-M003**: **(a)** **32**, cooling, 147.5 °C, Col<sub>h</sub>; **(b)** 19.6%, cooling, 113.8 °C, Col<sub>h</sub>; **(c)** 38.6%, cooling, 110.2 °C, Col<sub>h</sub>; **(d)** 56.1%, cooling, 110.0 °C, non-mesogenic; **(e)** 68.2%, cooling, 135.0 °C, Col<sub>h</sub>; **(f)** 78.3%, cooling, 165.1 °C, Col<sub>h</sub>; **(g)** **21**, cooling, 186.3 °C, Col<sub>h</sub>.

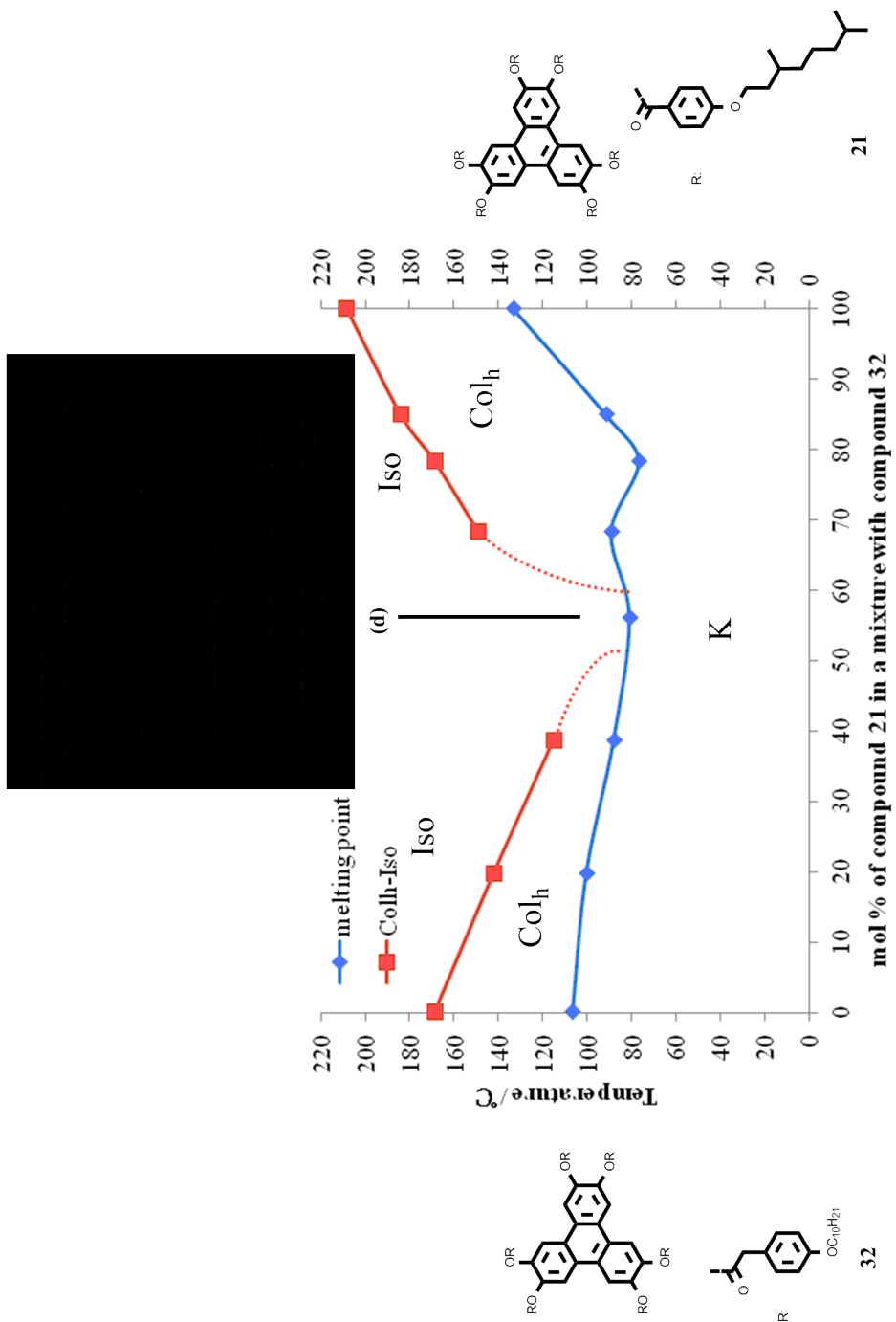


**Figure 6.6** The microscopy showing the phase texture for the concentration of 56.1 mol% of compound 21 in the mixture with compound 32.

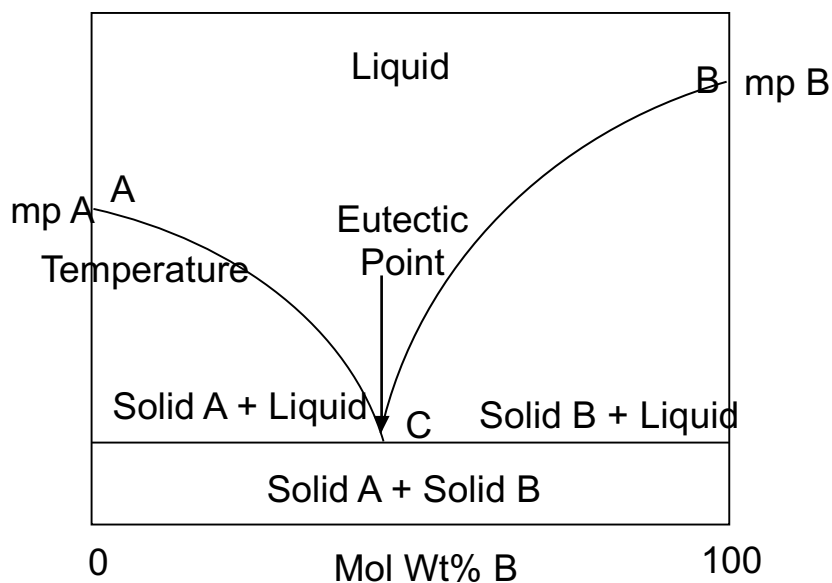


**Figure 6.7** Classical phase diagram for a binary mixture showing ideal behaviour.

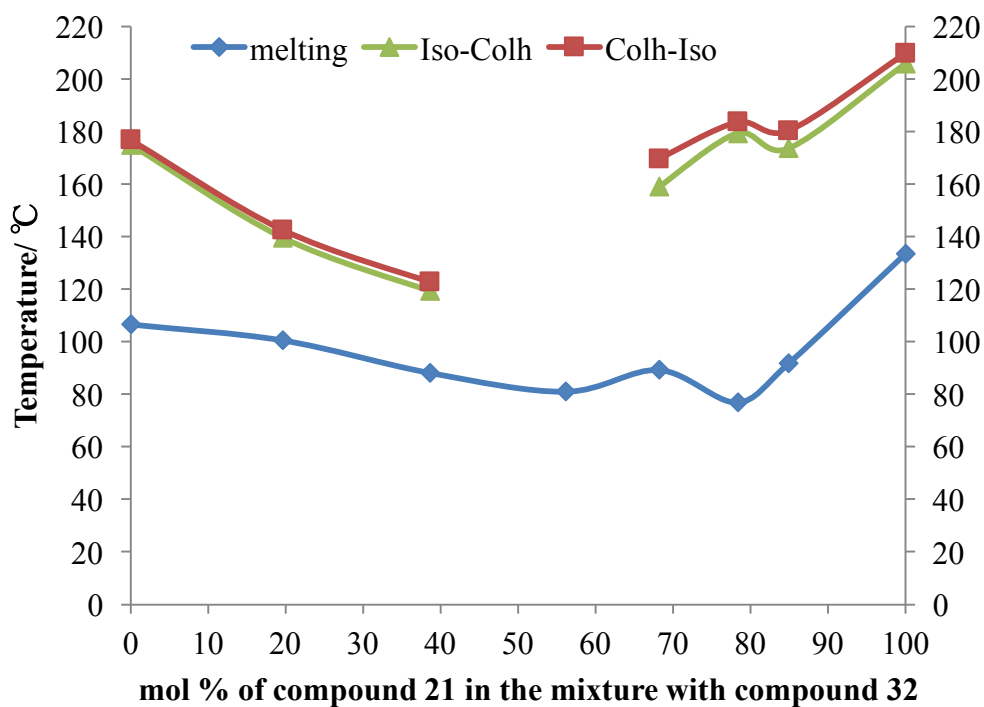


**Figure 6.8** The Gibbs phase diagram showing the biphasic region between heating and cooling for hexagonal columnar to isotropic liquid transition of mixtures of **21** and **32**.

Firstly, it is important to note that the binary diagram for the transition temperatures determined by calorimetry, as shown in Figure 6.8, is broadly in agreement with the phase diagram obtained by microscopy. Secondly, the temperatures of the peak maximums show little hysteresis with respect to heating and cooling cycles. This shows that there is little phase separation in the phase diagram. Additionally, the solid to liquid crystal phase transition curve shows a depression associated with eutectic behaviour at the point of approximately 56.1 mol% of compound **21**, whereas the melting point curve also shows a depression at 78.3 mol% of compound **21**, which is the point that was predicted from the Schröder-van Laar equation to exhibit a eutectic predicted. The enthalpic DSC studies tend to support these observations, in that no extra peaks were found for the liquid crystal underlying the columnar phase around the centre of the phase diagram as shown in Figure 6.9.

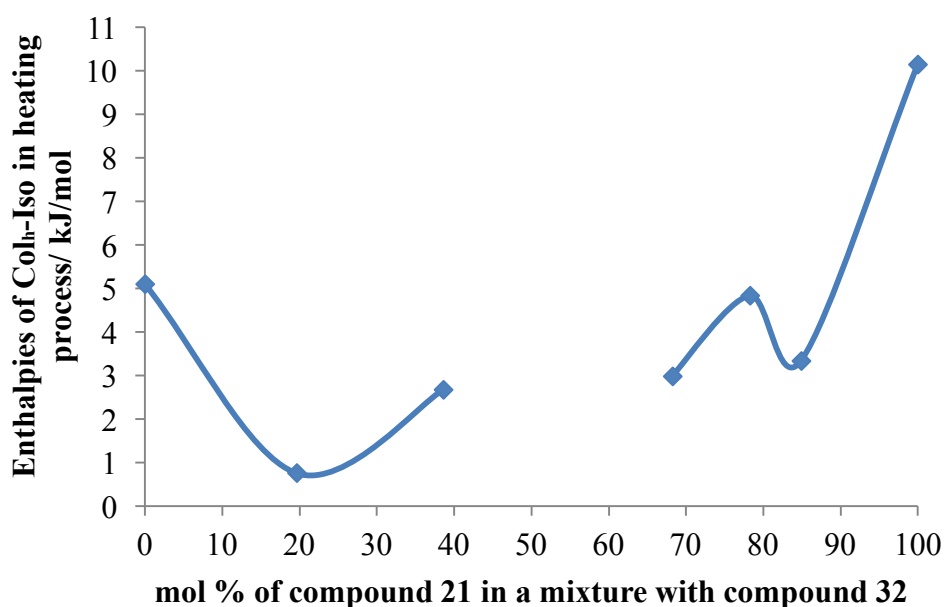


**Figure 6.9** Diagram showing the enthalpies (kJ/mol) for the columnar phase to isotropic liquid transitions on heating cycles for binary mixtures between compounds **21** and **32** as a function of the concentration of **21** (mol%).

If we examine the values of the enthalpies of the phase transitions as a function of concentration, as shown in Table 6.2 and Figure 6.9, it can be seen that the

enthalpies for the Col<sub>h</sub>-I phase transition vary below 11.0 kJ/mol, and no enthalpies were detected by DSC at the point of 56.1 mol% of compound **21**. Thus the phase diagram does in fact resemble a classical melting for a soft crystal, thereby indicating that the columnar phase is also in nature a soft crystal.

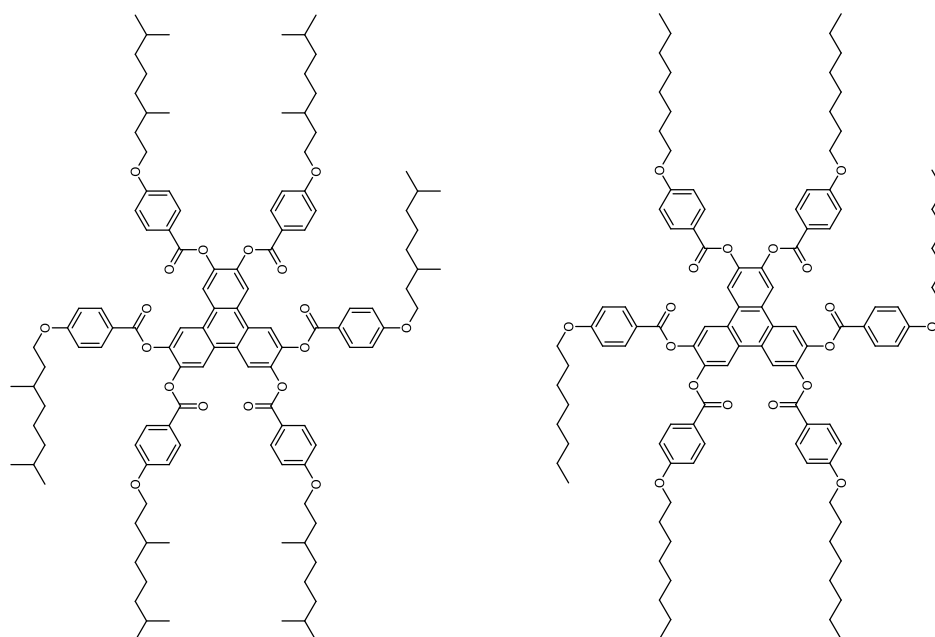
## **6.4 Phase Behaviour of Mixed Nematic and Columnar Systems**

### **6.4.1 Phase Behaviour of Nematic and Columnar Triphenylene Derivatives**

In the following subsections, the co-miscibility between columnar hexagonal phases is examined in the presence of a nematic phase exhibited by one of the materials. In this case compound **21** was selected as the material that exhibits a columnar phase, and it is mixed with compound **24**, which exhibits both nematic and columnar phases. However, compound **21** was also selected because it is a derivative of citronellol, which is optically active, and therefore will have the capability of inducing helicity into the structure of the nematic phase. This will have the effect of changing the defect textures and make it easier to discern the phase transitions.

#### **6.4.1.1 Mixture Studies between Compounds 21 and 24**

The chemical structures and transition temperatures (°C), the space filling minimised structures determined using the MM2 force field as implemented in ChemDraw 3D in gas phase at absolute zero, and simulations based on DFT theory to show the stereochemical structures for compound **21** and **24** are shown together in Figures 6.10 to 6.12 respectively. The binary phase diagram between the two compounds is shown in Figure 6.13.



**21** K 128.2 Col<sub>h</sub> 208.4 °C Iso Liq    **24** K 147.5 Col<sub>h</sub> 168.3 N 238.8 °C Iso Liq

**Figure 6.10** The chemical structures and phase transitions of compounds **21** and **24**.

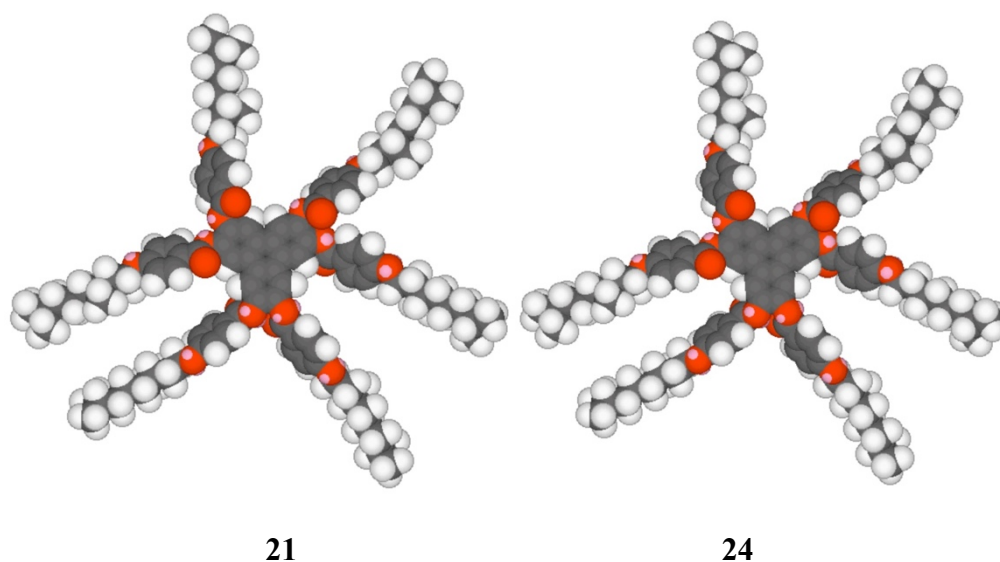
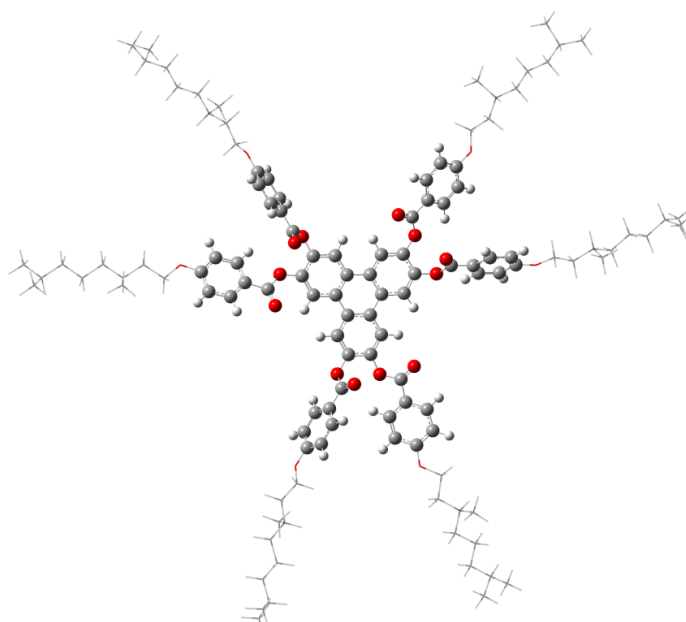


**Figure 6.11** The space filling structures of compounds **21** and **24** determined in gas phase at 0 K using the MM2 force field as implemented in ChemDraw 3D.

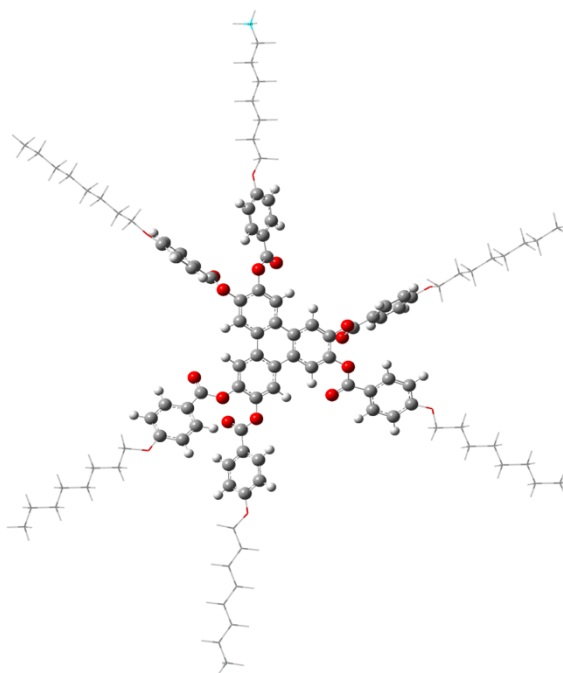
For the DFT simulated structures the disc diameters are almost identical for compounds **21** and **24**. Moreover, the peripheral aromatic rings are twisted slightly out of the plane of the central triphenylene core due to the stereochemistry of the

linking ester functional groups. However, this does induce differences in disc thickness when the two materials are compared. The terminal aliphatic chains although branched for compound **21**, and with no branching for compound **24** do not show appreciable differences with respect to packing volumes or filling space between the arms of the peripheral group. Thus, it might be expected that the two materials are compatible as far as molecular structure is concerned, and therefore one would predict that in their liquid crystal phases they should be co-miscible.

As compound **24** was found to exhibit nematic and hexagonal columnar phases, whereas **21**, only exhibits a hexagonal columnar phase, the phase diagram was expected to show a chiral nematic phase (supported through the chiral chemical structure of compound **21**) slowly disappearing as a function of concentration of **21**.



**21**



**24**

**Figure 6.12** The energy structures for compounds **21** and **24**, at the mixed ONIOM(B3LYP/6-31G(d):PM6) level of theory.

A Series of mixtures (**TZ-M040-1-8**) of **21** and **24** were prepared and their phase behaviour was firstly examined by polarized light, thermal, microscopy (POM),

and secondly by differential scanning calorimetry (DSC). The transition temperatures for the various mixtures determined by POM are given in Table 6.3, whereas those determined from DSC are shown together in Table 6.4. The composition of the mixture (**TZ-M040-E**) predicted to exhibit the eutectic for the binary components was calculated from the melting enthalpies of compounds **21** and **24** using Schröder-van Laar equation. The phase behaviour of the experimental mixture was determined by POM and DSC, the results being shown in both Tables. The binary phase diagrams for the results shown in Table 6.3 and 6.4 are shown respectively in Figures 6.13 and 6.14. In addition, photomicrographs of the defect textures at various concentrations are incorporated into the phase diagrams.

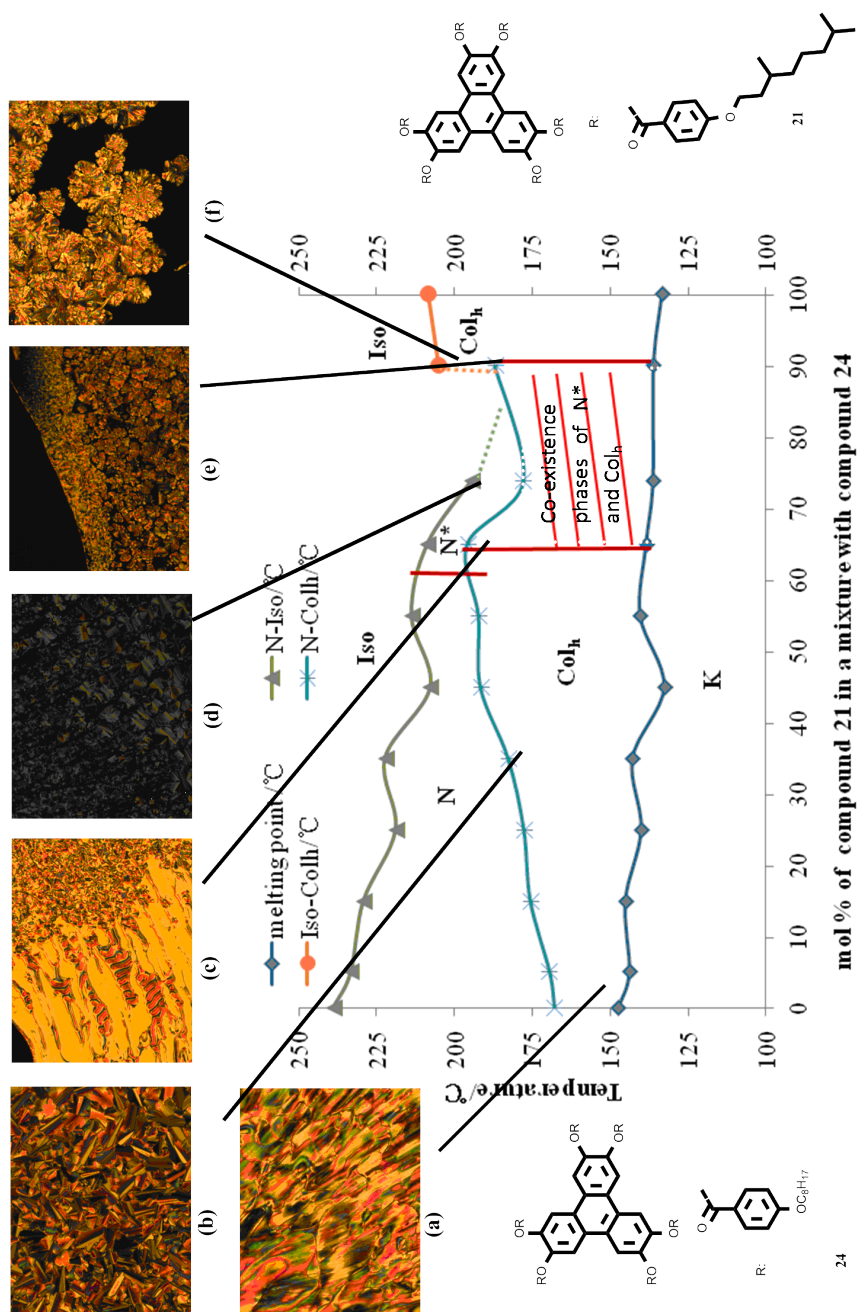
**Table 6.3** Compositions (mol%) and transition temperatures (°C) determined by POM for binary mixtures of compounds **21** and **24**.

ID	21/mol%	K	/°C	Col <sub>h</sub>	/°C	N	/°C	Iso
<b>24</b>	0	.	147.5	.	168.3	.	238.8	.
<b>TZ-M040-1</b>	5	.	144	.	170.4	.	233.2	.
<b>TZ-M040-2</b>	15	.	145.3	.	175.6	.	229.2	.
<b>TZ-M040-3</b>	25	.	140.1	.	177.4	.	218.8	.
<b>TZ-M040-4</b>	35	.	143	.	183.2	.	222.2	.
<b>TZ-M040-5</b>	45	.	132.7	.	191.6	.	207.7	.
<b>TZ-M040-6</b>	55	.	140.5	.	191.7	.	213.7	.
<b>TZ-M040-7</b>	65	.	138.6	.	196.0	.	208.7	.
<b>TZ-M040-E</b>	73.9	.	136.3	.	194.5	.	177.9*	.
<b>TZ-M040-8</b>	90	.	136.1	.	205.2	.	187.0*	.
<b>21</b>	100	.	128.2	.	208.4	-	-	.

(\*The temperatures showing when the N\* phase were observed only in microscopy in the phase separation region\*.)

**Table 6.4** Mixture compositions (mol%) and transition temperatures (°C) and enthalpies (J/g) both in heating and cooling cycles for binary mixtures of **21** and **24**.

ID	21/ mol %	Melting /°C	Col <sub>h</sub> -N/ °C		N-Iso Liq/°C	
			Heating	Cooling	Heating	Cooling
<b>24</b>	0	147.52	169.50	166.22	239.75	239.69
		$\Delta H = 14.52$	$\Delta H = 5.38$	$\Delta H = -5.26$	$\Delta H = 0.46$	$\Delta H = -0.54$
<b>TZ- M040-1</b>	5	143.97	171.74	168.82	236.29	235.76
		$\Delta H = 9.37$	$\Delta H = 2.99$	$\Delta H = -3.06$	$\Delta H = 0.40$	$\Delta H = -1.16$
<b>TZ- M040-2</b>	15	145.32	177.39	174.66	230.17	230.36
		$\Delta H = 14.03$	$\Delta H = 3.49$	$\Delta H = -4.17$	$\Delta H = 0.41$	$\Delta H = -0.66$
<b>TZ- M040-3</b>	25	140.27	180.61	176.94	225.50	225.26
		$\Delta H = 10.25$	$\Delta H = 3.70$	$\Delta H = -3.78$	$\Delta H = 0.38$	$\Delta H = -0.22$
<b>TZ- M040-4</b>	35	143.00	185.86	182.10	224.21	223.48
		$\Delta H = 9.59$	$\Delta H = 3.88$	$\Delta H = -4.13$	$\Delta H = 0.34$	$\Delta H = -0.29$
<b>TZ- M040-5</b>	45	132.73	194.59	190.55	209.62	209.05
		$\Delta H = 9.07$	$\Delta H = 4.10$	$\Delta H = -4.08$	$\Delta H = 0.20$	$\Delta H = -0.19$
<b>TZ- M040-6</b>	55	140.49	195.28	191.00	215.06	214.75
		$\Delta H = 9.51$	$\Delta H = 3.80$	$\Delta H = -3.88$	$\Delta H = 0.26$	$\Delta H = -0.17$
<b>TZ- M040-7</b>	65	138.56	199.36	194.76	210.05	209.59
		$\Delta H = 9.76$	$\Delta H = 4.17$	$\Delta H = -4.33$	$\Delta H = 0.25$	$\Delta H = -0.24$
<b>TZ- M040-E</b>	73. 9	136.33	198.88	194.48	-	168.20
		$\Delta H = 1.31$	$\Delta H = 0.31$	$\Delta H = -0.80$	-	$\Delta H = -0.22$
<b>TZ- M040-8</b>	90		Col <sub>h</sub> -Iso	Iso-Col <sub>h</sub>		
		136.13	207.42	204.00	-	-
<b>21</b>	100		Col <sub>h</sub> -Iso	Iso-Col <sub>h</sub>		
		133.47	209.69	205.73	-	-
		$\Delta H = 12.25$	$\Delta H = 5.38$	$\Delta H = -6.30$	-	-



24

**Figure 6.13** The Gibbs phase diagram for the binary mixture series TZ-M040-1-8 of 21 and 24. Photomicrographs (x 100 magnification) showing representative optical textures for TZ-M040: (a) 5%, heating, 151.9 °C, N; (b) 35%, cooling, 179.4 °C, Col<sub>h</sub>; (c) 65%, cooling, 185.8 °C, co-existence phases N\* and Col<sub>h</sub>; (d) 73.9%, cooling, 200.3 °C, co-existence phases N\* and Col<sub>h</sub>; (e) 90%, cooling, 186.0 °C, co-existence phases N\* and Col<sub>h</sub>; (f) 90%, cooling, 205.0 °C, Col<sub>h</sub>.

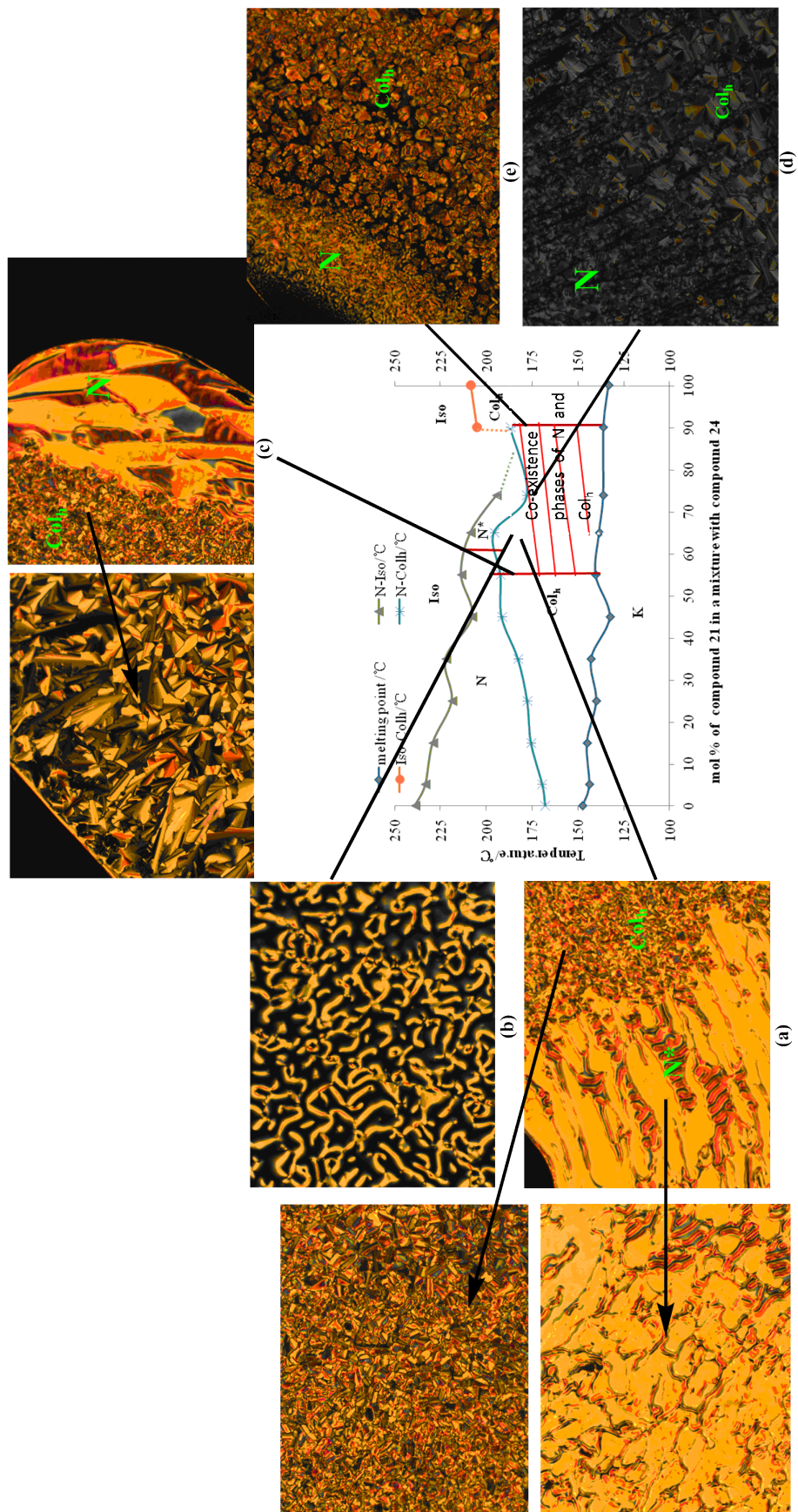
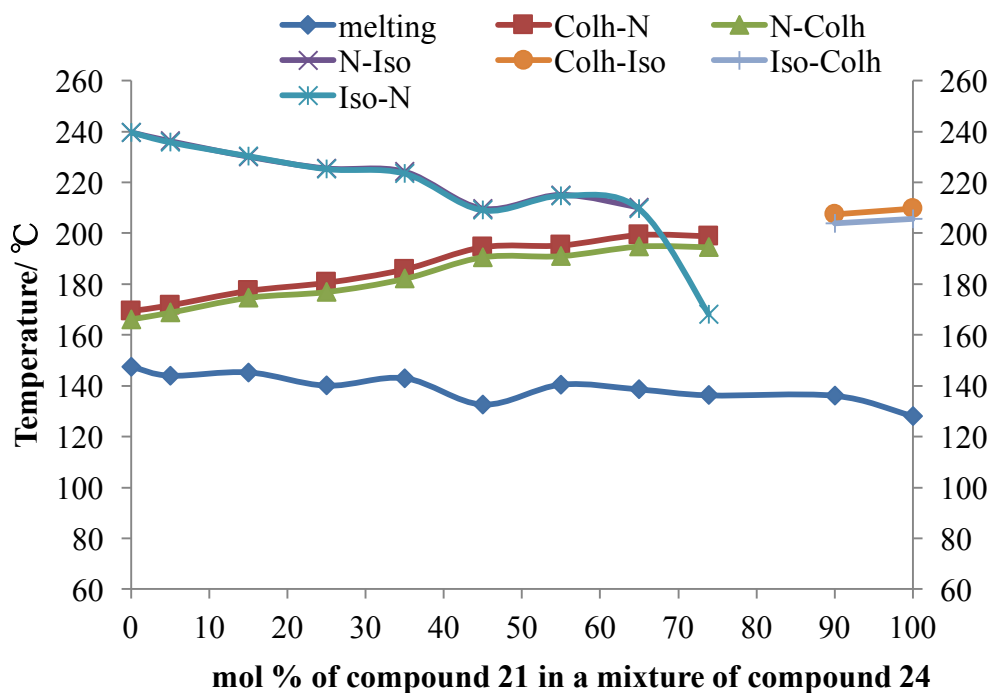


Figure 6.14 The representative optical textures for the co-existence phase region.

It was expected that the two columnar phases of compounds **21** and **24** would show continued miscibility rising across the phase diagram, and that the N to I curve would fall steadily as the concentration of **21** increased. The melting behaviour was expected to form a depression in the melting point curve as the eutectic point was approached. This is what generally happens up to the point where the N to I curve falls below the I or N to columnar transition curve. At this point there was complicated phase behaviour and segregation in the columnar region of the phase diagram. As expected there was a steady fall in the N-I values as the concentration of compound **21** was increased, with the observed disappearance of the nematic phase at 73.9 mol% of compound **21**, whereas above 90 mol% of compound **21** in the binary mixtures an increase in the Iso-Col<sub>h</sub> values was found. In between these two values however, there appeared to be a coexistence of mesomorphic properties. For example, during the cooling process, there was an increase in the N-Col<sub>h</sub> temperatures and above 90 mol% of compound **21** there was a Col<sub>h</sub> phase after cooling from isotropic liquid, but when the temperature cools as low as 187 °C there was a chiral nematic phase at the edge of the sample around the Col<sub>h</sub> phase, as shown in the photomicrograph in Figure 6.13(e). More detailed photomicrographs are shown in Figure 6.14, from which it is relatively easy to identify the various mesophases from their defect textures. Phase separated domains of chiral nematic and hexagonal columnar phase are also observed in the region of between 60-90 mol% of compound **21**. These observations suggest that phase separation occurs between the two materials, and which might be due to poor mixing of the two materials. However, the transition temperatures to the solid state vary almost linearly with respect to concentration. This is the case even for the eutectic mixture predicted from the Schröder-van Laar equation. This observation suggests that demixing had not occurred.

In order to investigate this behaviour further, and to obtain accurate values for the transition temperatures on heating and cooling for the mixtures in the phase diagram, calorimetric studies were performed for each individual mixture, the results for which are shown in Table 6.4 along with the enthalpies for transitions, and a graphical representation in Figure 6.15.



**Figure 6.15** The Gibbs phase diagram showing the biphasic region between heating and cooling for transition of mixtures of **21** and **24**.

Firstly, it is important to note that the transition temperatures determined by calorimetry, as shown in Figure 6.15, are broadly in agreement with those shown in the phase diagram obtained by microscopy shown in Figure 6.13. Secondly, the temperatures of the peak maxima show little hysteresis with respect to heating and cooling cycles. This shows that there is little phase segregation in the phase diagram. Furthermore, the solid to liquid crystal temperature curve shows a depression associated with the predicted eutectic point, and again there is little or no phase separation. This implies that either the solid is not truly solid, but another form of liquid crystal, or that this is really the solid state for the mixtures of **21** and **24**. The DSC studies tend to support the second suggestion, in that no extra peaks were found for liquid crystals underlying the columnar phases for the pure materials. Thirdly in the region between 79 and 90 mol% of compound **21** in the phase diagram, no enthalpies are detected by DSC, yet there is an indication of mesophase presence observed *via* microscopy.

If we examine the values of the enthalpies of phase transitions as a function of concentration, as shown in Figure 6.16, it can be seen that the enthalpies for the N-I phase transition vary almost linearly with respect to concentration, and that their values are relatively low. This indicates that the nematic phase formed between the two materials exhibits almost ideal behaviour, for example, the materials mix well, which is not surprising as they have very similar chemical structures. The low values of the enthalpies indicate that the structure of the nematic phase is not so dissimilar from that of the liquid.

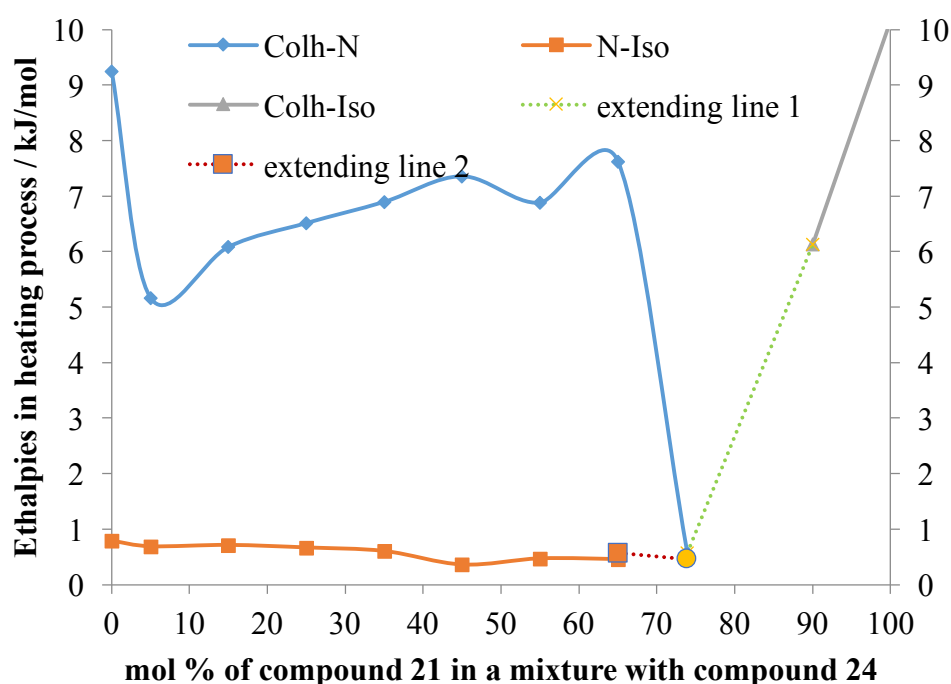


**Figure 6.16** The diagram showing the function of enthalpies (kJ/mol) of each phase transition in heating cycle with the mol% concentration of compound **21** in a mixture with compound **24**.

Conversely, the enthalpies for the columnar to nematic phase transition are much larger than the nematic transitions to the liquid (approximately 5 to 10x). Again they vary almost linearly up to the point from 5 to 65 mol% of compound **21**, where there is a break in the phase diagram at 70 to 90 mol% of compound **21**, whereby the enthalpies drop to a value similar to that of the transition to the liquid. Clearly there is no columnar phase in this region. If the line for the transition to

the columnar phase is extended for the right-hand side of the phase diagram, then the columnar transition line starts to take on the appearance of a eutectic in the phase diagram, and at the value determined *via* the Schröder-van Laar modelling.

Again these studies suggest that either the two columnar phases have differing structures, or that the columnar phases have structural features, which are more similar to those of solid than a liquid whereby a quasi eutectic is formed. Certainly, the absence of demixing in the biphasic region of the phase diagram indicates that the columnar phases are immiscible in the 70 to 90 mol% of compound **21** in the phase diagram.

#### **6.4.2 Phase Behaviour of Tetra-benzoate Esters and Columnar Triphenylene Hexa-esters**

In the following section three compounds were selected that exhibited the columnar hexagonal phase but no nematic phase, and they were mixed with nematogenic materials that possessed various forms of board or X-shaped molecular architectures. The mixtures were used to construct binary phase diagrams with the objective of investigating if columnar phases could be induced into board-like systems. In the previous studies in Chapter 5 it was found that the nematic phases of disc-like systems could not be forced to induce discotic nematic phases into board-like systems. In these studies, the board-like materials have some flexibility in their molecular architectures in order to allow ease of packing of the molecules together.

In the first set of study, investigations were made with tetra esters of benzene because of the ability of the ester function to rotate about its various bonds. This material was mixed with the benzyl esters of triphenylene because it also has a flexible structure around the central core unit.

Firstly, some eutectic mixtures are prepared following the calculation by the Schröder-van Laar equation and analysed by POM and DSC to get a general idea for the systems, which were selected to be investigated in the following sections. The components of the binary mixtures and the transition temperature are shown in Table 6.6.

**Table 6.5** The components and concentrations (mol%), the phase classifications and transition temperatures (°C) of the eutectic mixtures by columnar triphenylene hexa-esters and tetra-benzoate esters.

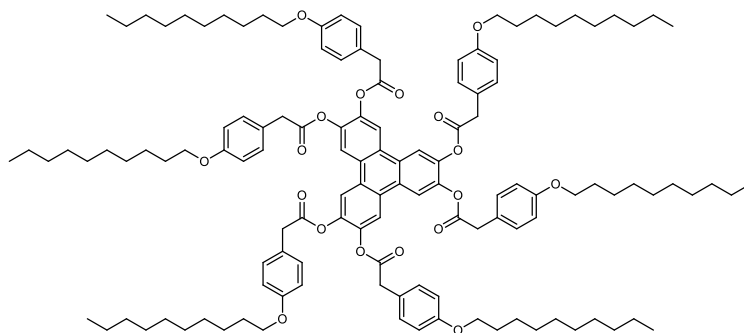
Title	A/ mol%	B	Predicted mp/ °C	Transition temperature/ °C
<b>TZ-M009-E</b>	<b>32/ 58.3</b>	<b>38</b>	78.9	K 86.3 Iso
<b>TZ-M018-E</b>	<b>21/ 89.5</b>	<b>40</b>	78.9	K 167.3 Iso
<b>TZ-M010-E</b>	<b>32/ 42.2</b>	<b>44</b>	63.3	K 71.7 Iso
<b>TZ-M016-E</b>	<b>32/ 23.9</b>	<b>52</b>	98.7	K 101.2 Iso
<b>TZ-M017-E</b>	<b>32/ 42.0</b>	<b>44</b>	63.3	K 109.0 Iso

The results in the Table 6.5 indicated that all of the eutectic mixtures predicted by Schröder-van Laar equation are non-mesogenic. None liquid crystal phases can be observed by POM and DSC. For intensive studies about the nature of the mixed systems, different mol ratio mixtures are prepared and analysed by POM and DSC, and the Gibbs phase diagrams are formed to discuss the abilities of the mixture systems in the next following sections.

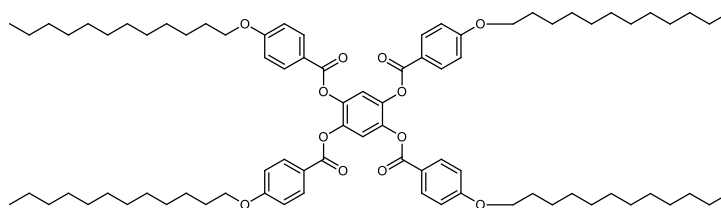
#### 6.4.2.1 Mixture Studies between Compounds 32 and 52

The binary phase diagram between compounds **32** and **52** is shown in Figure 6.20, and the structures and phase transition temperatures, the energy minimised space-filling structures using the MM2 force field as implemented in ChemDraw 3D in gas phase at absolute zero, and molecular simulations using DFT theory for compounds **32** and **52** are shown respectively in Figures 6.17 to 6.19, except for the DFT simulation for compound **32** which was not able to give a conclusive

minimum energy state because of its flexible structure producing a large number of conformers. In the figures the structures have been adjusted so they have roughly the same atom size.



**32** K 106.6 Col<sub>h</sub> 169.0 °C Iso Liq



**52** K 102.3 (SmC 90.4 N 101.5) °C Iso Liq

**Figure 6.17** The chemical structures and phase transition temperatures (°C) for compounds **32** and **52**.

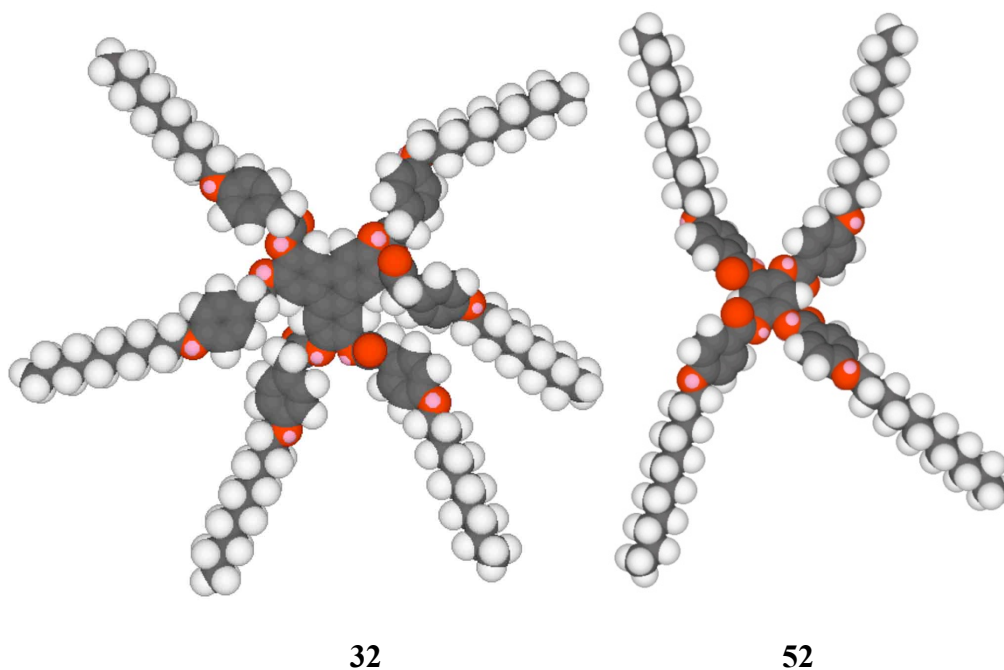


**Figure 6.18** The space filling structures of compounds **32** and **52** determined in gas phase at 0 K using the MM2 force field as implemented in ChemDraw 3D.

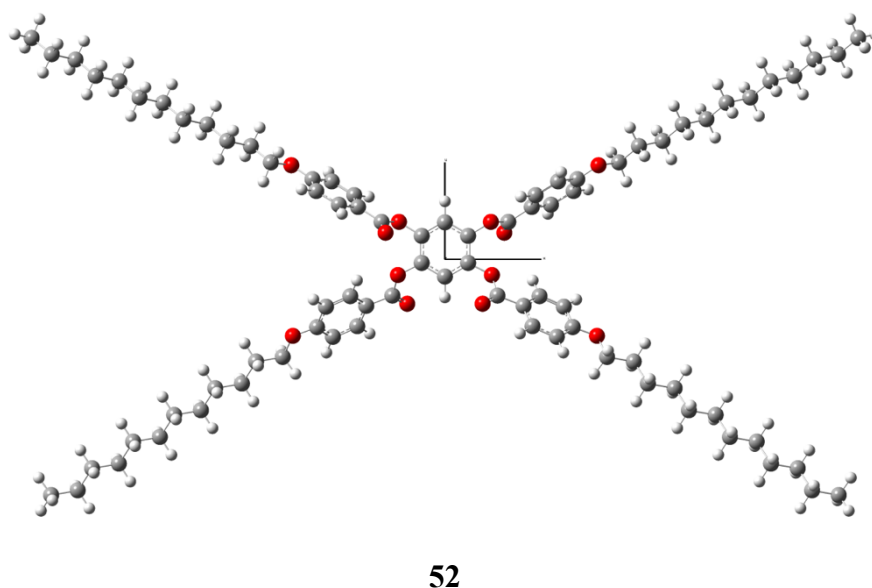


**Figure 6.19** The minimised energy structure for compound **52**, at the mixed ONIOM(B3LYP/6-31G(d):PM6) level of theory.

In this study compound **32** exhibits a columnar phase, whereas compound **52** exhibits a nematic and smectic C phase. This suggests that compound **52** has a rod-like conformational structure, and so the investigation becomes one of seeing if

the disc-like molecules of compound **32** can induce the molecular architecture of compound **52** to also become disc-like.

Thus a series of mixtures (**TZ-M016-1-3**) of **32** and **52** were prepared and their phase behaviour was examined by polarized light, thermal, microscopy (POM), and then by differential scanning calorimetry (DSC). The transition temperatures for the various mixtures determined by POM are given in Table 6.6, and the results determined from DSC were found to be in agreement with them, and so were not recorded, but are available as raw data files. The composition of the theoretical eutectic mixture (**TZ-M016-E**) was determined using the Schröder van-Laar equation, and the phase behaviour of the experimental mixture being determined by POM and DSC, with the results also being shown in Table 6.6. The binary phase diagram for the results obtained is shown in Figure 6.20. In addition, photomicrographs of the defect textures at various concentrations are included in the Figure.

**Table 6.6** Mixture compositions (mol%) and transition temperatures (°C) for binary mixtures of compounds **32** and **52**.

ID	<b>32</b> / mol%	K	/°C	Sm C	/°C	N	/°C	Col <sub>h</sub>	/°C	I
<b>52</b>	0	.	102.3	.	(90.4)	.	(101.5)	.	-	.
<b>TZ- M016-3</b>	10	.	99.2	-	-	-	-	-	-	.
<b>TZ- M016- E</b>	23.9	.	99.2	-	-	-	-	-	-	.
<b>TZ- M016-1</b>	50.1	.	97.1	-	-	-	-	-	-	.
<b>TZ- M016-2</b>	74.9	.	93.5	-	-	-	-	.	159.4	.
<b>32</b>	100	.	106.6	-	-	-	-	.	169.0	.

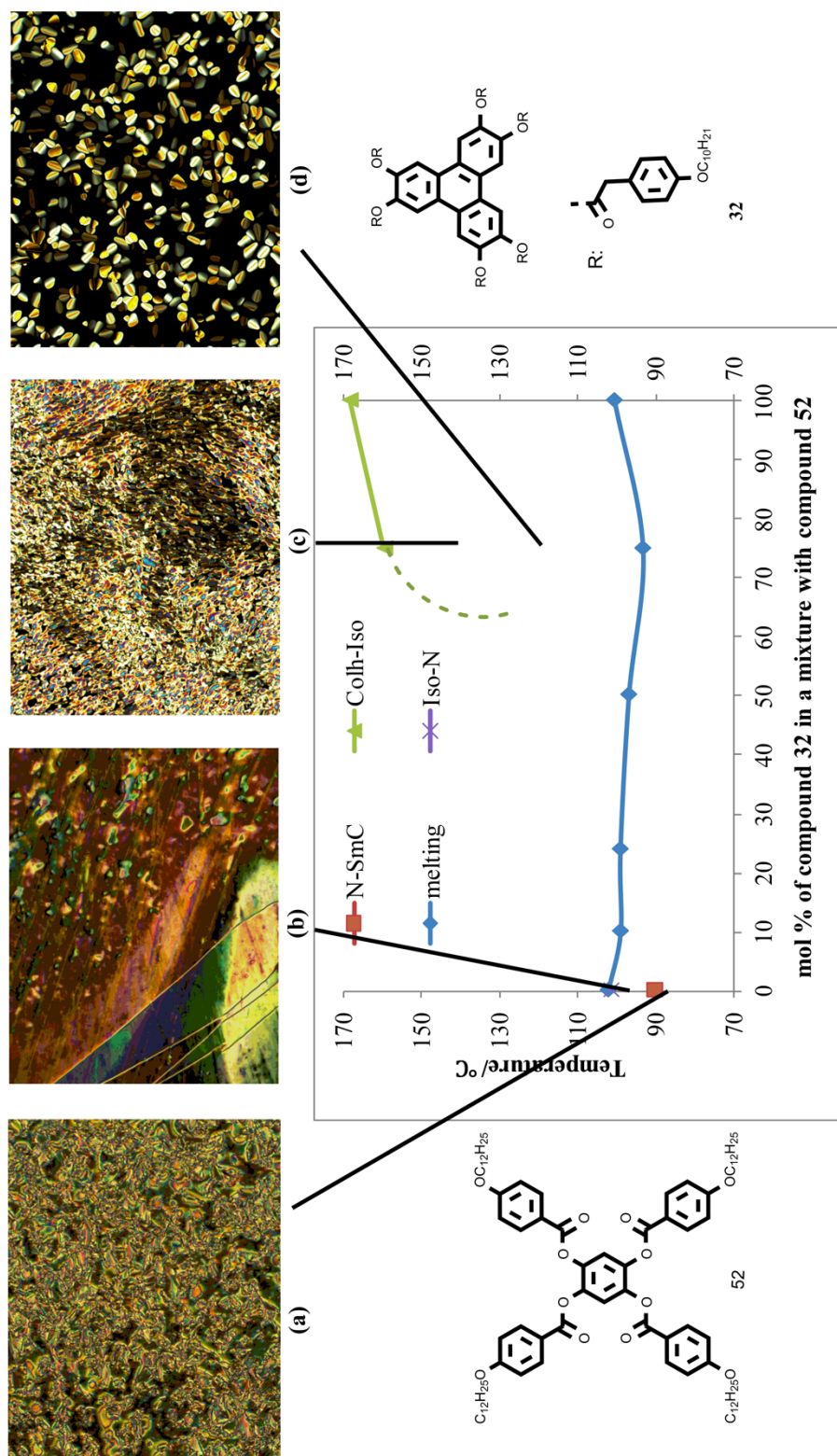
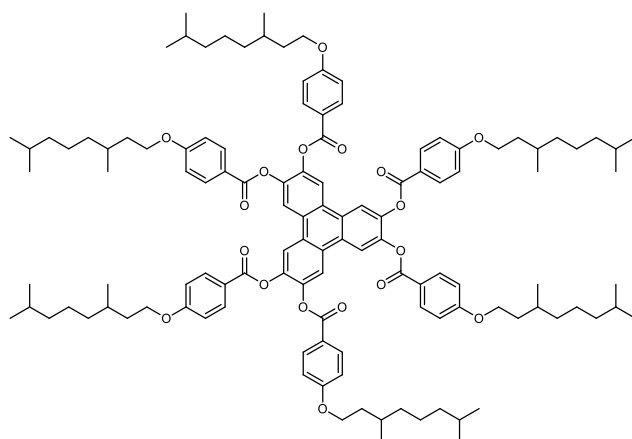


**Figure 6.20** The Gibbs phase diagram for the binary mixture series **TZ-M016** and photomicrographs (x100 magnification) of **32**, **52** and mixture **TZ-M016** showing representative optical textures: **(a)** **52**, Cooling, 88.6 °C, SmC; **(b)** **52**, Cooling, 94.4 °C, N; **(c)** 74.9%, Heating, 150.0 °C, Col<sub>h</sub>; **(d)** 74.9%, Cooling, 125.5 °C, Col<sub>h</sub>.

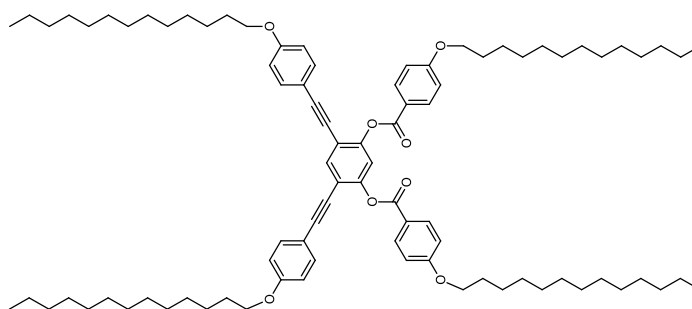
The binary phase diagram in Figure 6.20 shows that mesomorphic behaviour is suppressed. The calamitic nematic and smectic phases are not observed in any of the mixtures studied, whereas the columnar phase is only found in mixtures containing more than ~75 mol% of compound **32**. This indicates that the conformational structure of compound **52** is essentially not induced into being disc-like by compound **32**. This confirms the results in Chapter 5 that the X-shaped molecules prefer to be calamitic, and in mixtures with discotic nematic phases the depression in the phase transitions such that co-miscibility of the nematic phase is not observed also indicates that biaxial nematic phases are also unlikely to be found.

#### **6.4.2.2 Mixture Studies between Compounds 21 and 40**

The next study was between compounds **21** and **40**. Compound **21** was selected for study because it possesses a relatively high clearing temperature and a broad temperature range for the columnar mesophase stability. In contrast compound **40** has a monotropic nematic phase, and no smectic tendency. However, it does possess two alkynic units attached to the central phenyl ring, which gives it a more rigid bent structure, with two additional conformational disordered arms. The binary phase diagram between compounds **21** and **40** is shown in Figure 6.24, and the structures and phase transition temperatures, the energy minimised space-filling structures using the MM2 force field as implemented in ChemDraw 3D in gas phase at absolute zero, and molecular simulations using DFT theory for compounds **21** and **40** are shown respectively in Figures 6.21 to 6.23. In the figures the structures have been adjusted so they have roughly the same atom size.

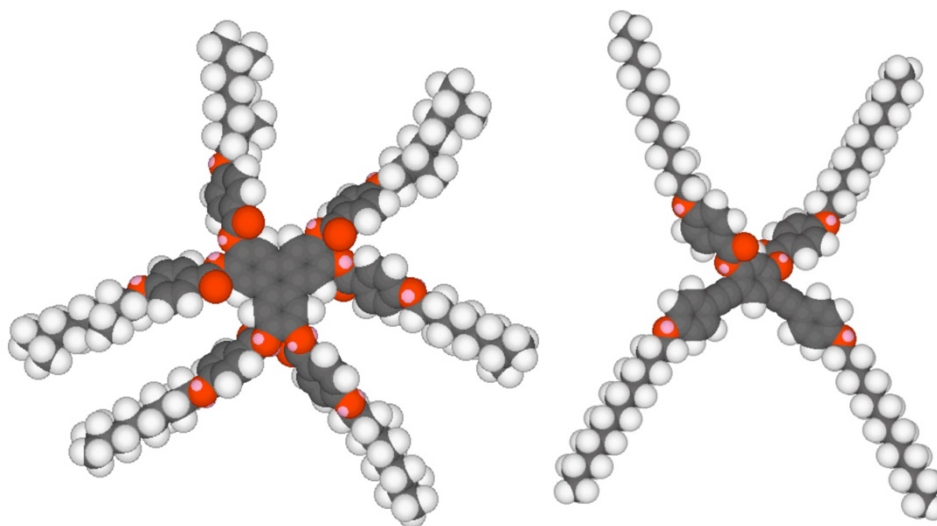


**21** K 128.2 Col<sub>h</sub> 208.4 °C Iso Liq



**40** K 106.9 N (103.3) °C Iso Liq

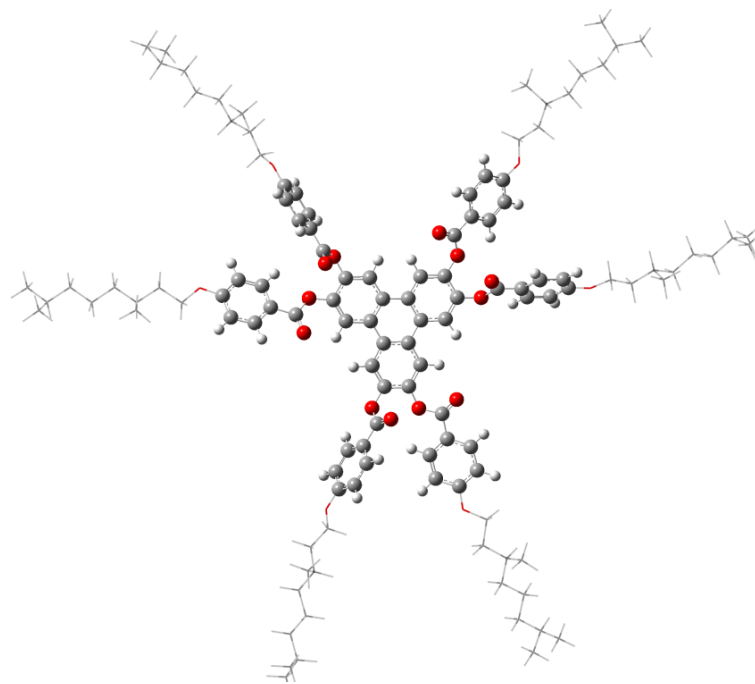
**Figure 6.21** The chemical structures and phase transitions of compounds **21** and **40**.



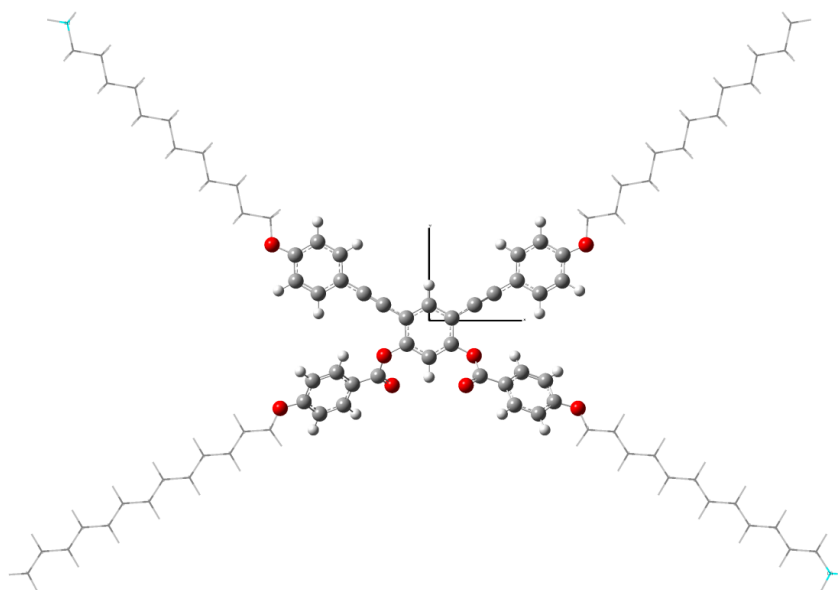
**21**

**40**

**Figure 6.22** The space filling structures of compounds **21** and **40** determined in gas phase at 0 K using the MM2 force field as implemented in ChemDraw 3D.



21



40

**Figure 6.23** The energy structures for compounds **21** and **40**, at the mixed ONIOM(B3LYP/6-31G(d):PM6) level of theory.

In the simulated structures, the diameter of compound **21** is 40.91 Å, whereas the length of compound **40** is 50.76 Å. For compound **21**, three of the peripheral aromatic rings are twisted slightly out of the plane of the central triphenylene core,

whereas for compound **40** all of the peripheral rings are effectively in the same plane of the central benzene core.

Thus, mixtures (**TZ-M018-1-4**) of **21** and **40** were prepared, and their phase properties were examined by POM and DSC. The transition temperatures for the various mixtures determined by POM are given in Table 6.7, whereas those determined from DSC are shown together in Table 6.8. The composition of the theoretical eutectic mixture (**TZ-M018-E**) was predicted using the Schröder-van Laar equation. The phase properties of the experimental equivalent were determined by POM and DSC, the results for which being shown in both Tables. The binary phase diagrams for the results shown in Table 6.7 and Table 6.8 are shown respectively in Figures 6.24 and 6.25. In addition, photomicrographs of the defect textures at various concentrations are included in the phase diagram Figure 6.24.

**Table 6.7** Compositions (mol %) and transition temperatures (°C) for binary mixtures of **21** and **40** determined by POM.

ID	<b>21</b> / mol%	K1	/°C	K2	/°C	Col <sub>h</sub>	/°C	N	/°C	I
<b>40</b>	0	.	106.9	-	-	-	-	.	(103.3)	.
<b>TZ-M018-4</b>	24.9	.	104.3	-	-	.	111	-	-	.
<b>TZ-M018-3</b>	49.7	.	105.5	.	112.8	.	135.5	-	-	.
<b>TZ-M018-2</b>	74.9	.	103.7	.	110.7	.	169.6	-	-	.
<b>TZ-M018-E</b>	89.5	.	94.7	-	-	.	185.4	-	-	.
<b>TZ-M018-1</b>	95	.	115.5	-	-	.	200.6	-	-	.
<b>21</b>	100	.	128.4	-	-	.	208.4	-	-	.

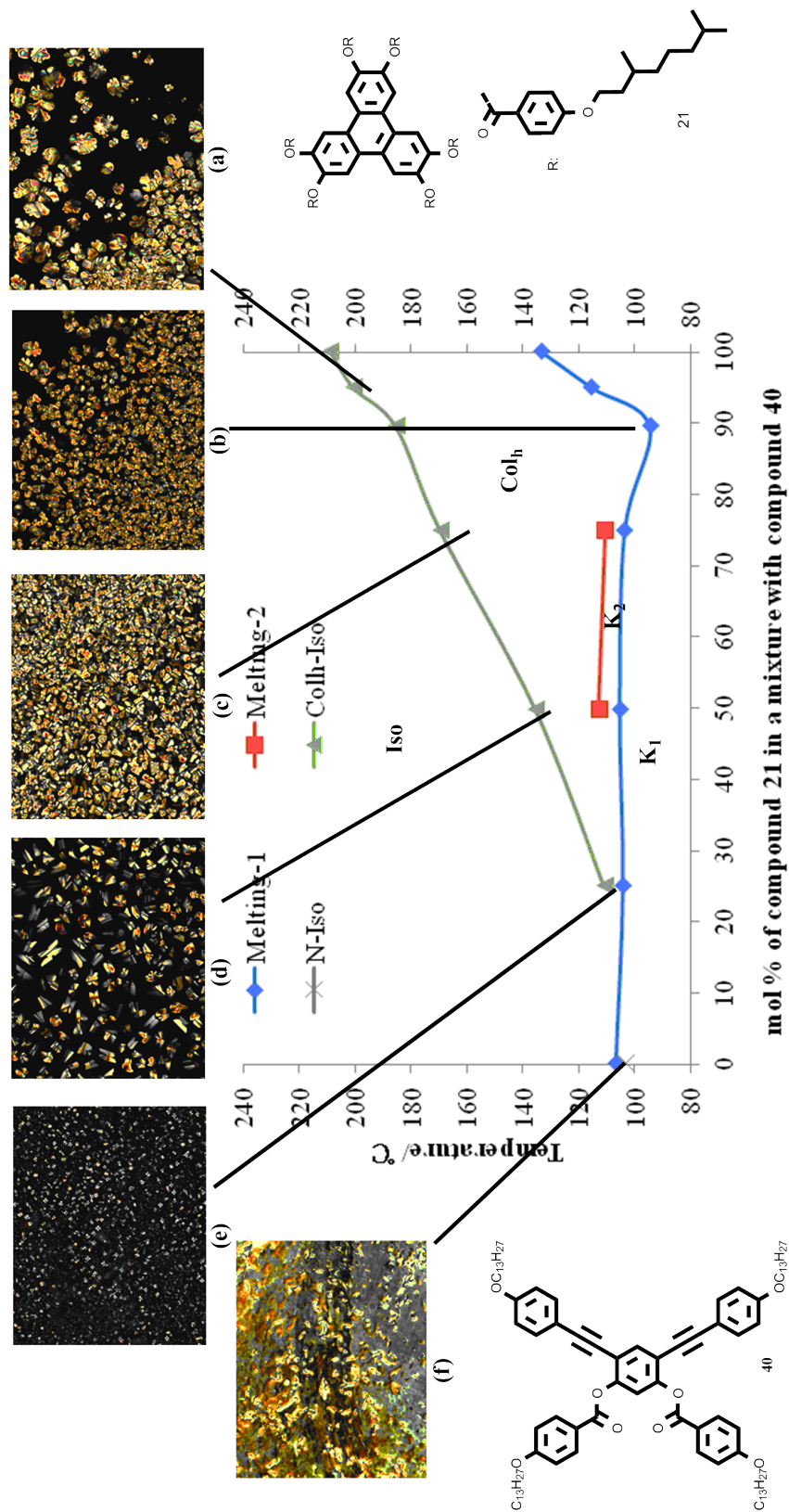


**Figure 6.24** The Gibbs phase diagram for the binary mixture series **TZ-M018** and photo micrographs (x100 magnification) of the series of mixture **TZ-M018** showing representative optical textures: **(a)** 95.0%, cooling, 198.9 °C, Col<sub>h</sub>; **(b)** 89.5%, cooling, 91.0 °C, Col<sub>h</sub>; **(c)** 74.9%, cooling, 167.6 °C, Col<sub>h</sub>; **(d)** 49.7%, cooling, 132.4 °C, Col<sub>h</sub>; **(e)** 24.9%, cooling, 108.3 °C, Col<sub>h</sub>; **(f)** 40, cooling, 100.1 °C, N.

**Table 6.8** Mixture compositions (mol%) and nematic to isotropic liquid and hexagonal columnar to isotropic liquid transition temperatures (°C) and enthalpies (J/g) both in heating and cooling cycles for binary mixtures of **21** and **40**.

ID	21/mol%	Col <sub>h</sub> -Iso/°C		N-Iso/°C	
		Heating	Cooling	Heating	Cooling
<b>40</b>	0	-	-	-	102.28
		-	-	-	$\Delta H = -1.07$
<b>TZ-M018-4</b>	24.9	-	-	-	-
		-	-	-	-
<b>TZ-M018-3</b>	49.7	123.12	130.37	-	-
		$\Delta H = 0.12$	$\Delta H = -0.83$	-	-
<b>TZ-M018-2</b>	74.9	163.58	163.52	-	-
		$\Delta H = 0.34$	$\Delta H = -0.70$	-	-
<b>TZ-M018-E</b>	89.5	191.02	182.70	-	-
		$\Delta H = 2.74$	$\Delta H = -2.87$	-	-
<b>TZ-M018-1</b>	95	201.41	194.70	-	-
		$\Delta H = 4.65$	$\Delta H = -3.80$	-	-
<b>21</b>	100	209.69	205.73	-	-
		$\Delta H = 5.38$	$\Delta H = -6.30$	-	-

The mixture studies revealed that upon mixing the nematic phase of compound **40** is not observed in any of the mixtures. The columnar phase is also rapidly suppressed as the mixtures become less based on triphenylene esters. Once again this shows that the two systems are in conflict with each other and extinguish phase formation. However, the melting point does not vary much across the phase diagram although there does appear to be a minimum at approximately 95 mol% of compound **21**, which is similar to the value determined for the eutectic point by the Schröder-van Laar equation.

In order to investigate this behaviour further, and to obtain accurate values for the transition temperatures on heating and cooling for the mixtures in the phase diagram, calorimetric studies were performed for each individual mixture, and the results for which are shown in Table 6.8 along with the enthalpies for transitions. A graphical representation for the transition temperatures obtained *via* DSC studies is shown in Figure 6.25.

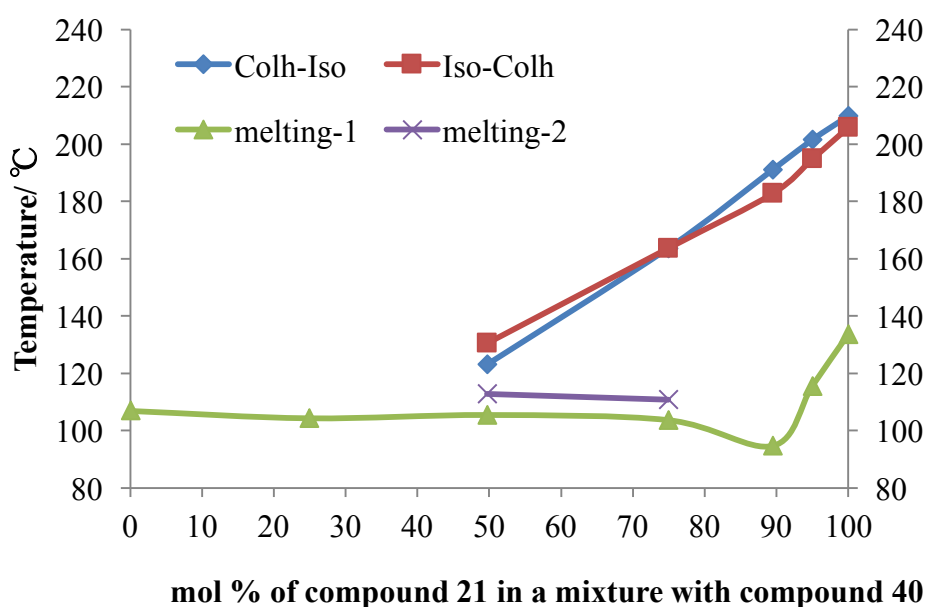


**Figure 6.25** The Gibbs phase diagram showing the biphasic region between heating and cooling for hexagonal columnar phase to isotropic transition temperatures (°C) for mixtures of compounds **21** and **40**.

It is important to note that the binary diagram for the transition temperatures determined by calorimetry, as shown in Figure 6.25, are in agreement with the phase diagram, Figure 6.24, obtained from microscopy. Additionally, the temperatures of the peak maximums show little hysteresis with respect to heating and cooling cycles. This indicates that there is little phase separation in the phase diagram. Furthermore, in the region below 50 mol% of compound **21** in the phase diagram, no enthalpies for the peak of hexagonal columnar phase to isotropic liquid transition are detected by DSC, but at the 24.9 mol% of compound **21** optical textures are observed *via* microscopy.

If we examine the values of the enthalpies of phase transitions as a function of concentrations (Figure 6.26) it can be seen that the enthalpies for the Col<sub>h</sub>-I phase transition are rapidly depressed when the concentrations of compound **21** decreased. This again shows that the materials are immiscible.

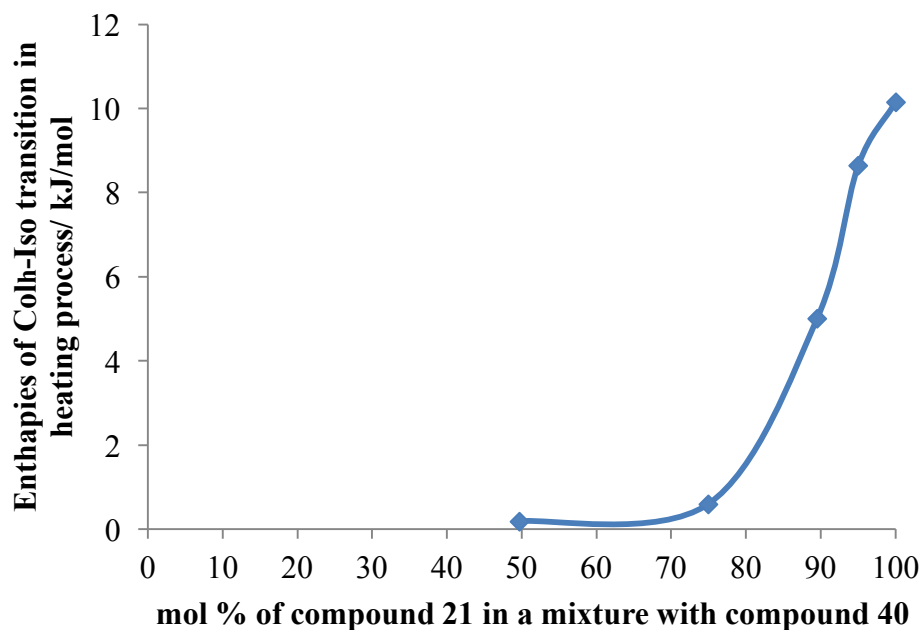
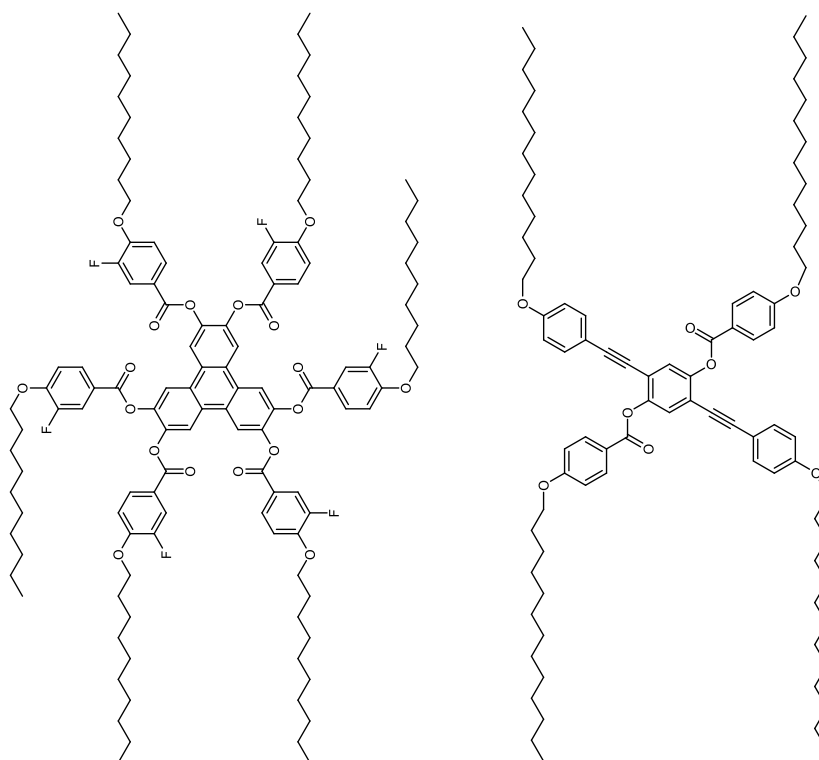


**Figure 6.26** The diagram showing the enthalpies (kJ/mol) for the hexagonal columnar phase to isotropic liquid transition in heating process of mixtures TZ-M018 with a function of mol percentage of compound **21**.

#### 6.4.2.3 Mixture Studies between Compounds **29** and **41**

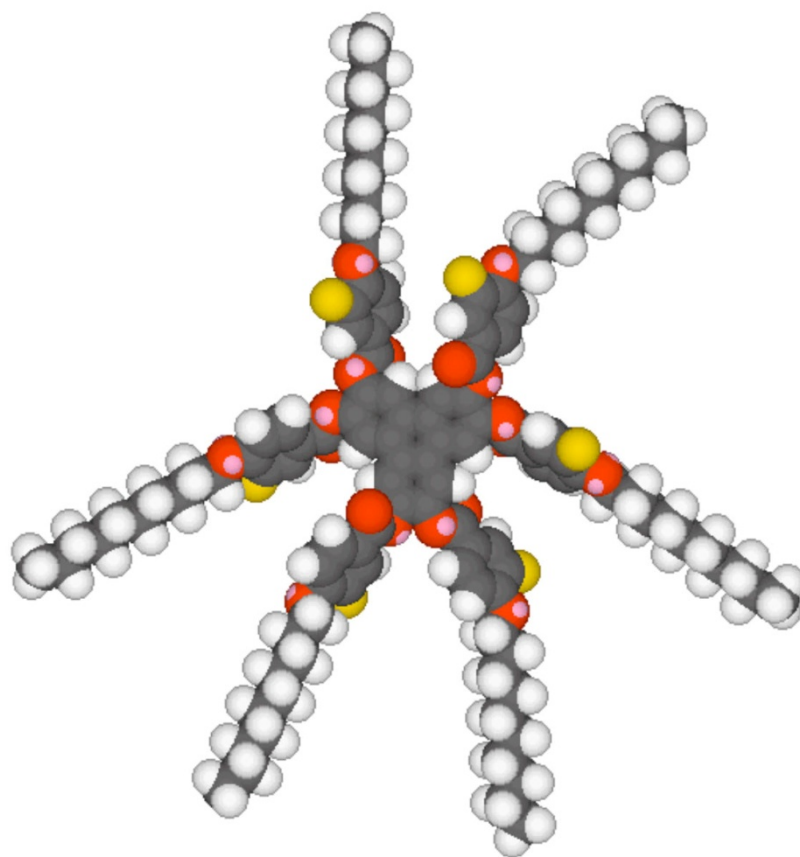
The last study in this sequence was between compounds **29** and **41**. Compound **29** was selected for study because it possesses a relatively high clearing point temperature and a broad temperature range for the columnar mesophase stability. In addition, it possesses fluoro-substituents in the peripheral rings, which were expected to give stronger intermolecular interactions with electron rich  $\pi$  systems. In contrast compound **41** has a monotropic nematic phase, and no smectic tendency. However, it does possess two alkyne units attached to the central phenyl ring in a

linear arrangement, and therefore it possesses an extended  $\pi$  structure, which gives it a more rigid linear structure, but with two additional conformational disordered arms. The binary phase diagram between compounds **29** and **41** is shown in Figure 6.30, and the structures and phase transition temperatures, the energy minimised space-filling structures using the MM2 force field as implemented in ChemDraw 3D in gas phase at absolute zero, and molecular simulations using DFT theory for compounds **29** and **41** are shown respectively in Figures 6.27 to 6.29.

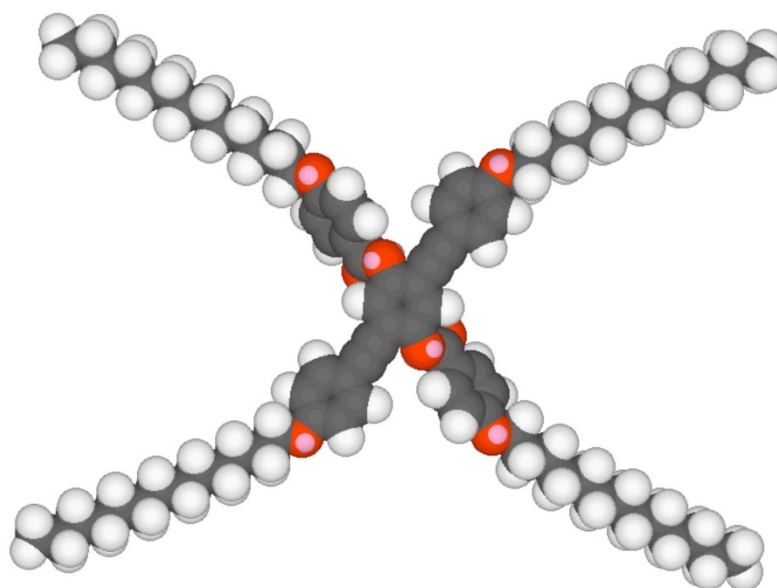


**29** K 200.7 Col<sub>h</sub> 222.9 °C Iso Liq      **41** K 108.7 (N 100.9) °C Iso Liq

**Figure 6.27** The chemical structures and phase transition temperatures (°C) for compounds **29** and **41**.

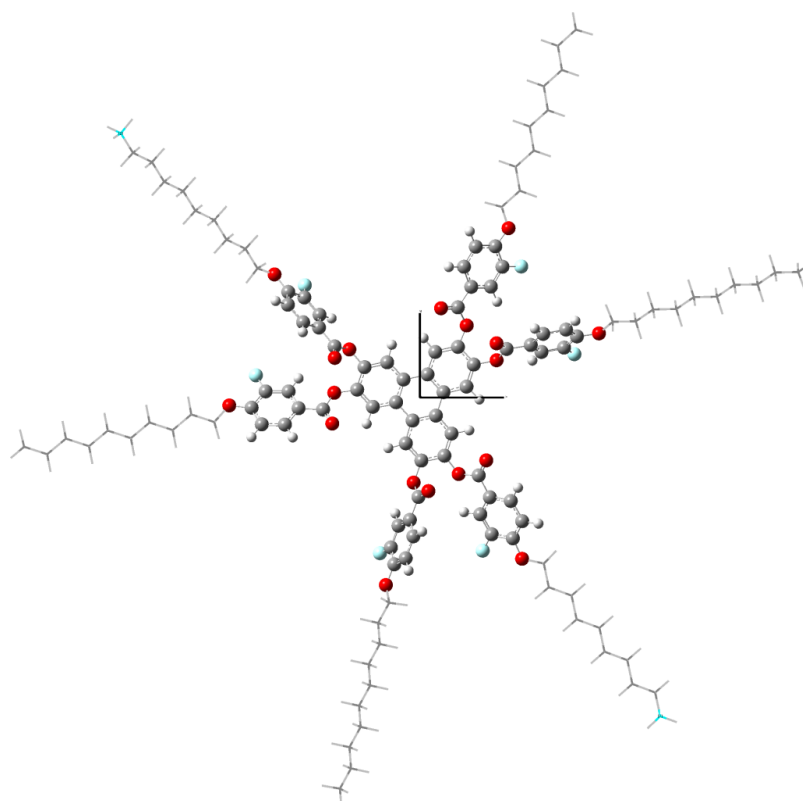


29

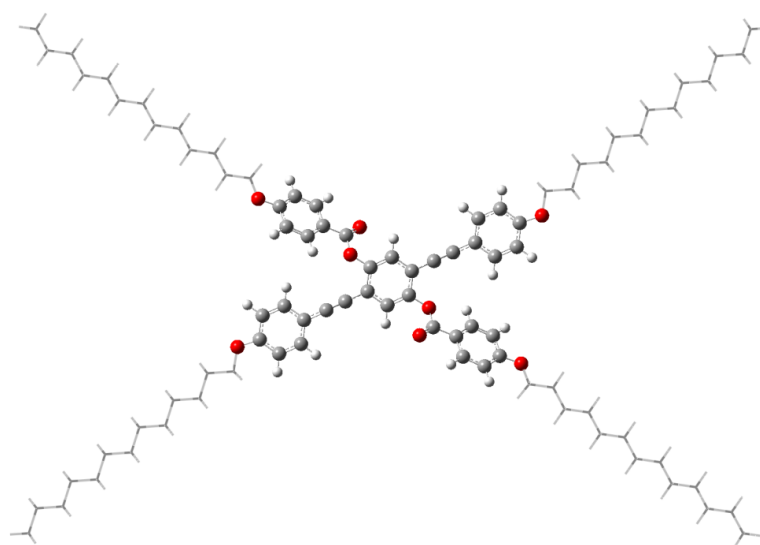


41

**Figure 6.28** The space filling structures of compounds **29** and **41** determined in gas phases at 0 K using the MM2 force field as implemented in ChemDraw 3D.



**29**



**41**

**Figure 6.29** The energy structures for compounds **29** and **41**, at the mixed ONIOM(B3LYP/6-31G(d):PM6) level of theory.

In the simulated structures, the diameter of compound **29** is 24.24 Å, whereas the length of compound **41** is 50.65 Å (benzoate-to-benzoate) or 51.28 Å (tolyl-to-

tolyl), it is longer along the alkyne axis than the ester. For compound **29**, three of the peripheral aromatic rings are twisted slightly out of the plane of the central triphenylene core, whereas for compound **41** all of the peripheral rings are in the same plane as the central benzene core. In a similar manner as previously, a series of mixtures (**TZ-M020-1-5**) of **29** and **41** were prepared and their phase behaviour was examined POM, and then by DSC. The transition temperatures for the various mixtures determined by POM are given in Table 6.9, whereas those determined from DSC are shown together in Table 6.10. The binary phase diagrams for the results for the two Tables are shown respectively in Figure 6.30 and 6.31.

**Table 6.9** Mixture compositions (mol%) and transition temperatures (°C) for binary mixtures of **29** and **41**.

ID	<b>29</b> / mol%	K	/°C	N	/°C	Col <sub>h</sub>	/°C	Iso
<b>41</b>	0	.	108.7	.	(100.9)	-	-	.
<b>TZ-M020-1</b>	11.2	.	109.3	-	-	.	215.5	.
<b>TZ-M020-2</b>	20	.	109.3	-	-	.	216.0	.
<b>TZ-M020-6</b>	31.5	.	108.8	-	-	.	215.4	.
<b>TZ-M020-3</b>	50.1	.	102.9	-	-	.	209.0	.
<b>TZ-M020-4</b>	64.7	.	97.4	-	-	.	222.4	.
<b>TZ-M020-5</b>	85	.	107.3	-	-	.	212.8	.
<b>29</b>	100	.	200.7	-	-	.	222.9	.

The phase diagram was expected to exhibit continuous miscibility of the columnar phases across all the concentrations, whereas the nematic phase was expected to disappear as a function of the concentration of compound **29**. The melting behaviour was expected to be linear as a function of concentration for the mixtures

and no eutectic point was predicted. In order to investigate this behaviour further, and to obtain accurate values for the transition temperatures on heating and cooling for the mixtures in the phase diagram, calorimetric studies were performed for each individual mixture, and the results for which are shown in Table 6.10.

**Table 6.10** Mixture compositions (mol%) and nematic to isotropic liquid and hexagonal columnar to isotropic liquid transition temperatures (°C) and enthalpies (J/g) both in heating and cooling cycles for binary mixtures of **29** and **41**.

ID	29/ mol%	Col <sub>h</sub> -Iso/°C		N-Iso/°C	
		Heating	Cooling	Heating	Cooling
<b>41</b>	0	-	-	-	100.41
		-	-	-	$\Delta H = -0.69$
<b>TZ- M020-1</b>	11.2	216.72	208.46	-	-
		$\Delta H = 0.17$	$\Delta H = -0.16$	-	-
<b>TZ- M020-2</b>	20	-	-	-	-
		-	-	-	-
<b>TZ- M020-6</b>	31.5	216.17	215.89	-	-
		$\Delta H = 0.41$	$\Delta H = -0.35$	-	-
<b>TZ- M020-3</b>	50.1	210.66	210.03	-	-
		$\Delta H = 0.20$	$\Delta H = -0.22$	-	-
<b>TZ- M020-4</b>	64.7	-	203.95	-	-
		-	$\Delta H = -0.13$	-	-
<b>TZ- M020-5</b>	85	213.88	212.85	-	-
		$\Delta H = 0.32$	$\Delta H = -0.31$	-	-
<b>29</b>	100	-	222.25	-	-
		-	$\Delta H = -0.14$	-	-

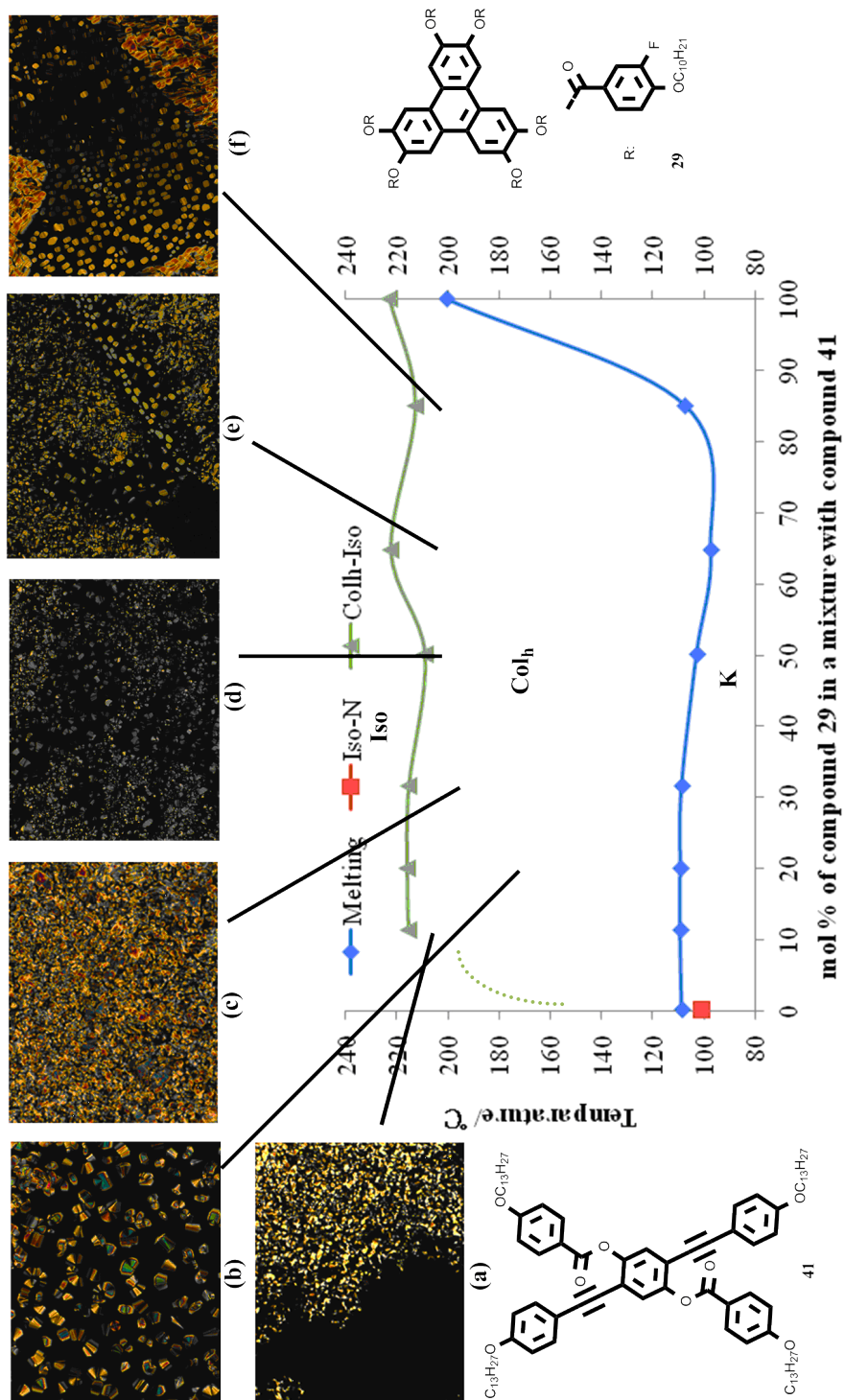


**Figure 6.30** The Gibbs phase diagram for binary mixture series TZ-M020 and photo micrographs (x100 magnification) of the series of mixture TZ-M020 showing representative optical textures: (a) 11.2%, heating, 218.4 C, Col<sub>h</sub>; (b) 20%, cooling, 172.1 C, Col<sub>h</sub>; (c) 31.5%, cooling, 195.6 C, Col<sub>h</sub>; (d) 50.1%, heating, 215.1 C, Col<sub>h</sub>; (e) 64.7%, Cooling, 206.0 C, Col<sub>h</sub>; (f) 85%, heating, 212.5 C, Col<sub>h</sub>.

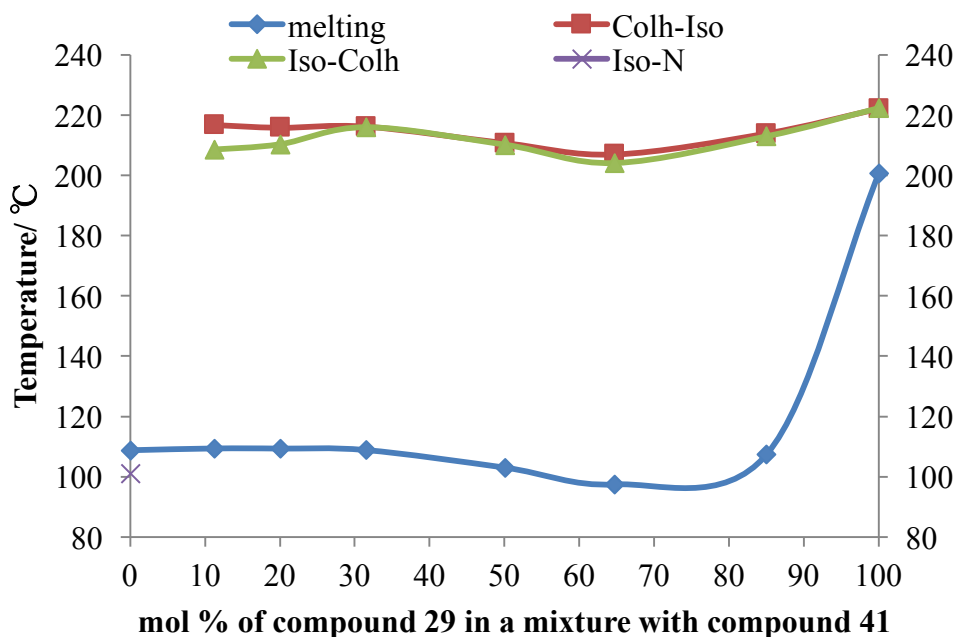


**Figure 6.31** The Gibbs phase diagram showing the biphasic region between heating and cooling for transitions of mixtures **TZ-M020** with a function of mol percentage of compound **29**.

Firstly, the binary diagram for the transition temperatures determined by calorimetry, as shown in Figure 6.31, are in agreement with the phase diagram obtained by microscopy. Secondly, the temperatures of the peak maximums show little hysteresis with respect to heating and cooling cycles, which means that there is little phase segregation in the phase diagram. In addition, for the mixtures no enthalpies for nematic to isotropic liquid transitions were detected by DSC, and no N-I phase transitions were observed *via* microscopy.

If we examine the values of the enthalpies of phase transitions as a function of concentrations, as shown in Figure 6.32, it can be seen that the enthalpies for the Col<sub>h</sub>-I phase transition vary within -0.6 kJ/mol and the enthalpies are low in value. However, as with the other studies in this section full co-miscibility was not achieved, but unlike the other studies the columnar phase was detected in all of the mixtures studied implying that compound **41** has a latent columnar phase. This

result is very interesting as it could mark a starting point for the investigation of biaxial nematic phases.

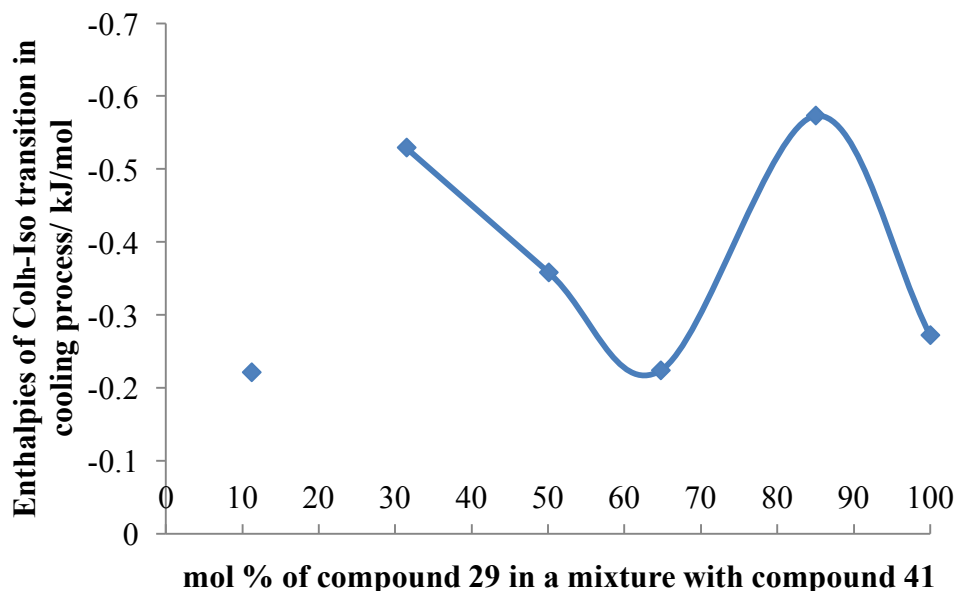


**Figure 6.32** The diagram showing the enthalpies (kJ/mol) of the hexagonal columnar phase to isotropic liquid transition in cooling process of mixtures of **29** and **41** with a function of mol percentage of compound **29**.

#### 6.4.3 Phase Behaviour of Nematogenic Phenyl Hexa-alkynes and Columnar Triphenylene Hexa-esters

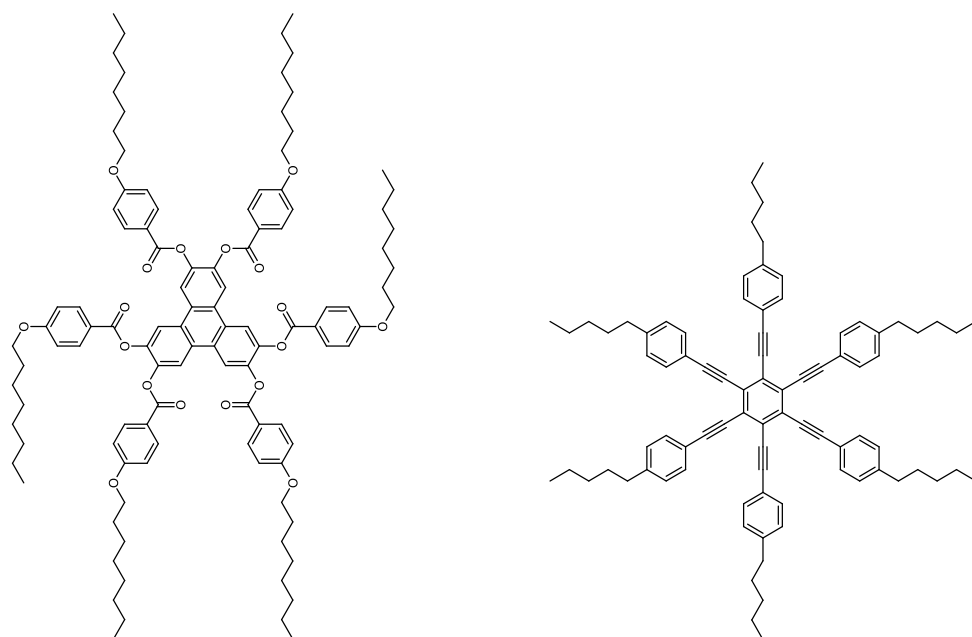
In the following section three compounds with disc-like molecular structures were selected that exhibited columnar hexagonal phases with two of them also possessing nematic phases. These materials were mixed with purely nematogenic materials that also possessed disc-like molecules. The objective of these studies was to investigate if the materials that exhibited columnar phases could induce purely nematogenic materials to exhibit columnar phases through stronger face-to-face interactions of the discs.

As with Chapter 5 triphenylene hexa-esters that exhibited columnar phases were mixed with benzene hexa-ynes because these materials were exclusively

nematogenic. As the hexa-ynes possess delocalised  $\pi$  systems across effectively flat molecular architectures it was expected that they had the potential of strongly interacting in a face-to-face mode with the hexa-phenyl esters of triphenylene to form columnar structures. Moreover, as the hexa-ynes have smaller molecular disc diameters it was thought that they would form columns easier.

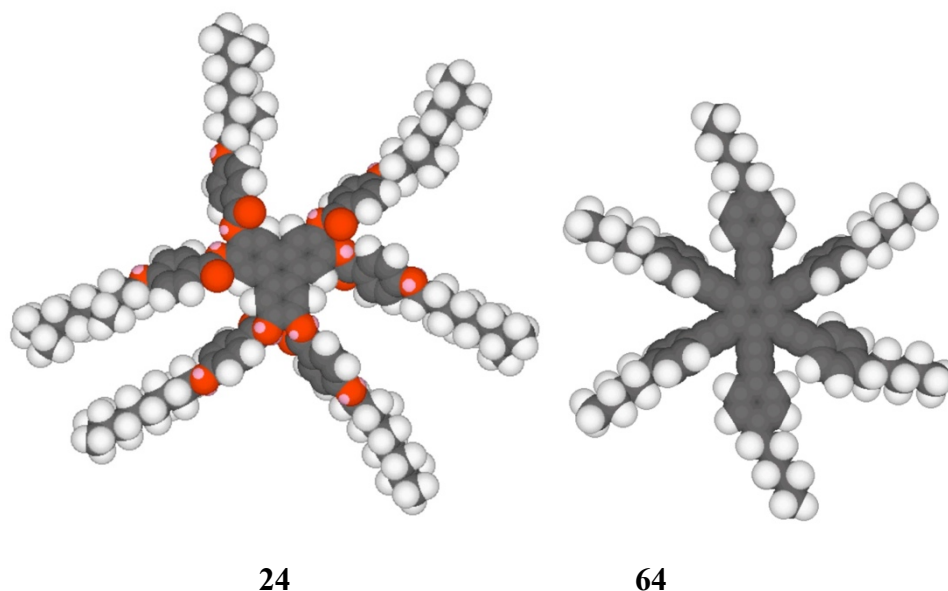
#### **6.4.3.1 Mixture Studies of Compounds 24 and 64**

The first study made was between compounds **24** and **64**, the structures of which are shown in Figure 6.33. Compound **24** was found to exhibit a nematic and a hexagonal columnar phase, whereas **64**, only exhibits a nematic phase. Thus in the phase diagram it was expected that continuous miscibility of the nematic phase would be found, but that the columnar phase would disappear as the concentration of compound **64** in the binary mixtures was increased. The structures and phase transition temperatures, the energy minimised space-filling structures using the MM2 force field as implemented in ChemDraw 3D in gas phase at absolute zero, and molecular simulations using DFT theory for compounds **24** and **64** are shown respectively in Figures 6.33 to 6.35.



**24** K 147.5 Col<sub>h</sub> 168.3 N 238.8 °C Iso Liq      **64** K 166.0 N 183.8 °C Iso Liq

**Figure 6.33** The chemical structures and phase transitions of compounds **24** and **64**.



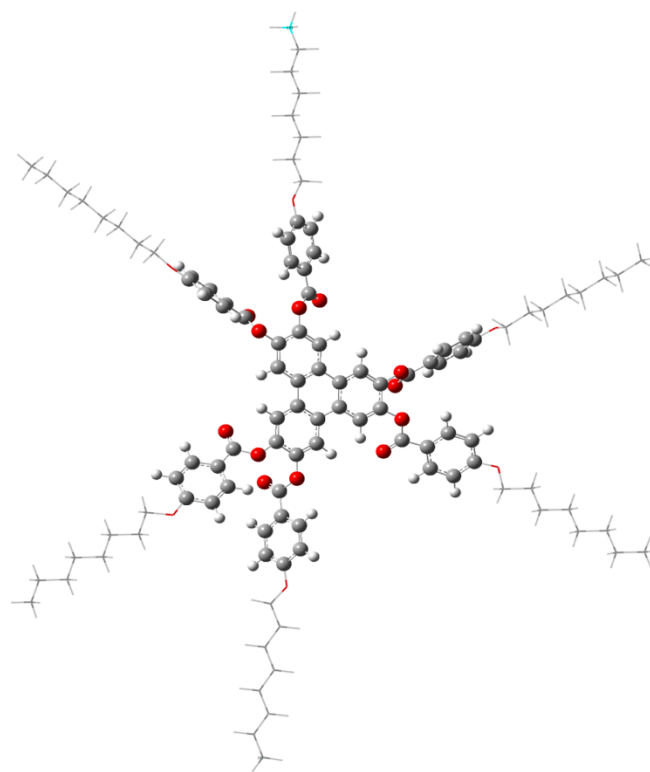
**24**

**64**

**Figure 6.34** The space filling structures of compounds **24** and **64** determined in gas phase at 0 K using the MM2 force field as implemented in ChemDraw 3D.

In the simulated structures, Compound **64** can be found as planar or twisted because the triple bond is sp hybridised and so conjugation can occur for planar or

twisted structures to a similar extent. Moreover, at the temperatures that the material exhibits liquid crystallinity the rings will be rotating relative to one another, *i.e.* they will not be static and have a flat structure. Secondly the diameter of compound **24** is 42.19 Å whereas the length of compound **64** is 28.05 Å. For compound **24**, three of the peripheral aromatic rings were twisted out of the plane of the central triphenylene core, whereas for compound **64** all of the peripheral rings are in the same plane of the central benzene core in the DFT theory, see Figure 6.35.



## 24

**Figure 6.35** The energy structure for compound **24**, at the mixed ONIOM(B3LYP/6-31G(d):PM6) level of theory.

A Series of mixtures (**TZ-M027-1-5**) of **24** and **64** were prepared and their phase behaviour was examined by POM, and then by DSC. The transition temperatures for the various mixtures determined by POM are given in Table 6.11, whereas those determined from DSC are shown together in Table 6.12. The composition of the theoretical eutectic mixture (**TZ-M027-E**) was predicted using Schröder-van Laar equation to be 71.1 mol% of compound **24** in a binary mixture with

compound **64**. The phase behaviour of the experimental eutectic mixture was determined by POM and DSC, the results being shown in the Tables.

The binary phase diagrams for the results shown in Table 6.10 and Table 6.11 are shown respectively in Figures 6.36 and 6.37. In addition, photomicrographs of the defect textures at various concentrations included in the phase diagram Figure 6.36.

**Table 6.11** Compositions (mol%) and transition temperatures (°C) for binary mixtures of compounds **24** and **64** determined by POM.

ID	<b>24</b> / mol%	K	/ °C	Col <sub>h</sub>	/°C	N	/ °C	Iso
<b>64</b>	0	•	166.0	-	-	•	183.8	•
<b>TZ-M027-1</b>	5	•	159.0	-	-	•	181	•
<b>TZ-M027-2</b>	25	•	148.0	-	-	•	190.8	•
<b>TZ-M027-3</b>	70.9	•	138.0	-	-	•	222.8	•
<b>TZ-M027-E</b>	71.1	•	136.8	-	-	•	221.2	•
<b>TZ-M027-4</b>	85	•	135.3	-	-	•	230.5	•
<b>TZ-M027-5</b>	88.9	•	136.4	-	-	•	229.9	•
<b>24</b>	100	•	147.5	•	168.3	•	238.8	•

The phase diagram that was expected from optical microscopy was to observe continuous miscibility of the nematic phases across all the concentrations, whereas the hexagonal columnar phase was expected to disappear as a function of the concentration of compound **24**. In practice, the melting behaviour varied essentially linearly in melting and no obvious eutectic point was found. The remainder of the phase diagram was found to be as predicted, see Figure 6.36, with continuous miscibility of the nematic phase as shown by the *schlieren* textures of the nematic phase shown for each mixture in the phase diagram. The columnar phase showed no stability across the phase diagram, with no mixtures exhibiting a columnar phase.

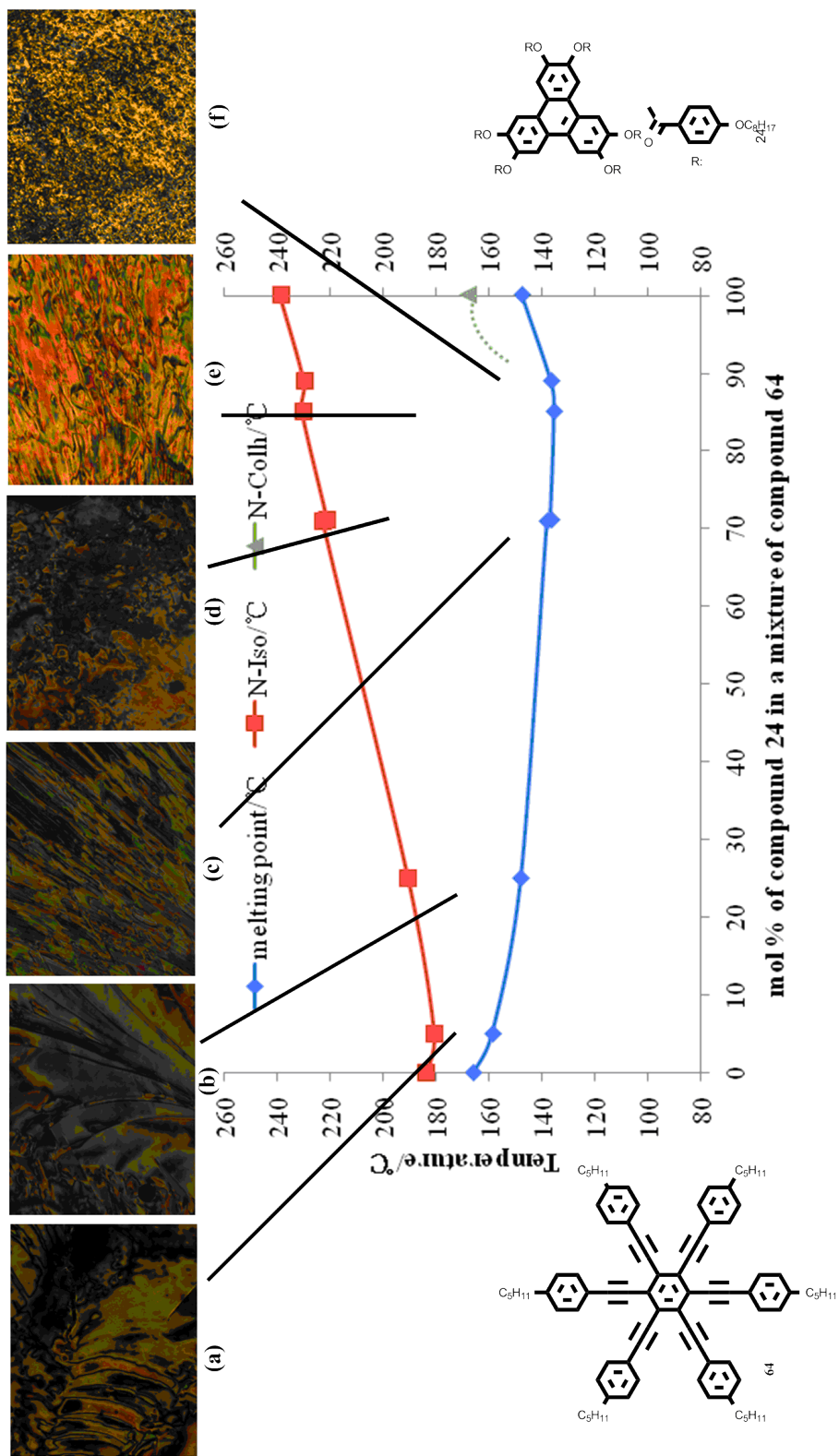


**Figure 6.36** The Gibbs phase diagram obtained from the binary mixture series **TZ-M027**. The micrographs (x100 magnification) of the series of mixture **TZ-M027** obtained from **(a)** 5.0%, heating, 176.4 °C, N; **(b)** 25.0%, heating, 170.2 °C, N; **(c)** 70.9%, heating, 155.2 °C, N; **(d)** 71.1%, heating, 189.0 °C, N; **(e)** 85.0%, heating, 176.3 °C, N; **(f)** 88.9%, cooling, 157.2 °C, N.

**Table 6.12** Mixture compositions (mol%) and transition temperatures (°C) and enthalpies (J/g) both on heating and cooling cycles for binary mixtures of compounds **24** and **64**.

ID	24/ mol%	Col <sub>h</sub> -N		N-Iso	
		Heating /°C	Cooling /°C	Heating/°C	Cooling/°C
<b>64</b>	0	-	-	185.61	186.40
		-	-	$\Delta H = 0.28$	$\Delta H = -0.20$
<b>TZ-M027-1</b>	5	-	-	-	-
		-	-	-	-
<b>TZ-M027-2</b>	25	-	-	-	-
		-	-	-	-
<b>TZ-M027-3</b>	70.9	-	-	215.72	211.70
		-	-	$\Delta H = 0.30$	$\Delta H = -0.25$
<b>TZ-M027-E</b>	71.1	-	-	213.56	197.41
		-	-	$\Delta H = 0.30$	$\Delta H = -0.26$
<b>TZ-M027-4</b>	85	-	-	231.22	230.87
		-	-	$\Delta H = 0.27$	$\Delta H = -3.32$
<b>TZ-M027-5</b>	88.9	-	-	230.45	230.26
		-	-	$\Delta H = 0.21$	$\Delta H = -0.74$
<b>24</b>	100	169.50	166.22	239.75	239.69
		$\Delta H = 5.38$	$\Delta H = -5.26$	$\Delta H = 0.46$	$\Delta H = -0.54$

In order to investigate this behaviour further, and to obtain accurate values for the transition temperatures on heating and cooling for the mixtures in the phase diagram, calorimetric studies were performed for each individual mixture, and the results for which are shown in Table 6.12 along with the enthalpies of transition, and in Figures 6.37 and 6.38.

Firstly, it is important to note that the binary diagram for the transition temperatures determined by calorimetry, as shown in Figure 6.37, are in agreement with those in the phase diagram obtained by POM. Secondly, the temperatures of

the peak maximums show little hysteresis with respect to heating and cooling cycles. This shows that there is little phase separation in the phase diagram. Thirdly in the region between 5 and 25 mol% of compound **24**, no enthalpies were detected by DSC, but there is an indication of the presence of a nematic phase which was observed *via* microscopy. If the values of the enthalpies of phase transitions are examined as a function of concentration, as shown in Figure 6.38, it can be seen that the enthalpies for the N-I phase transition vary with respect to concentration, with the values of the enthalpies, which are low, ranging from between 0.30 to 0.80 KJ/mol.

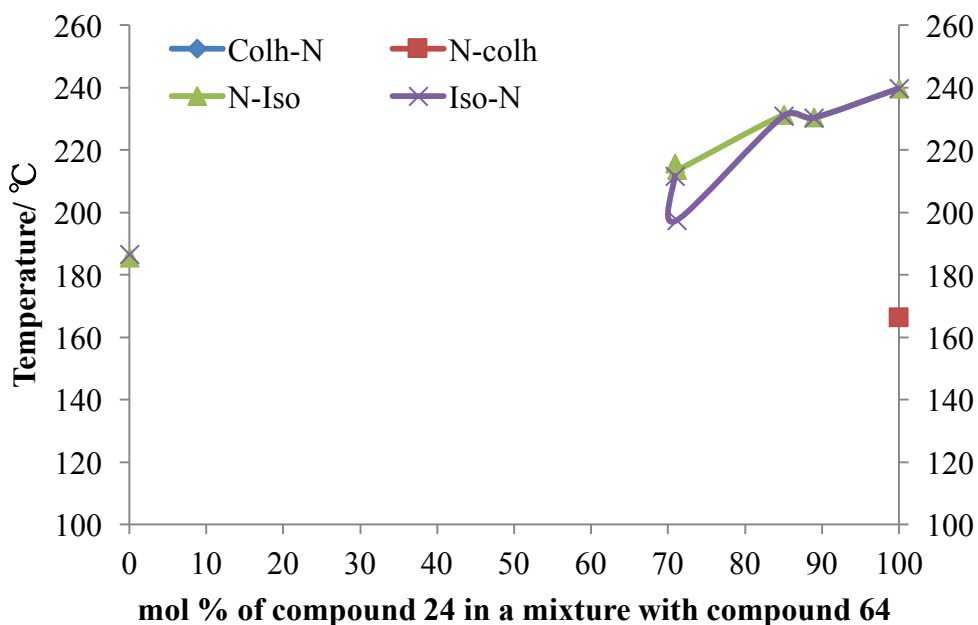


**Figure 6.37** The Gibbs phase diagram showing the biphasic region between heating and cooling for phase transitions of mixtures of the series **TZ-M027**.

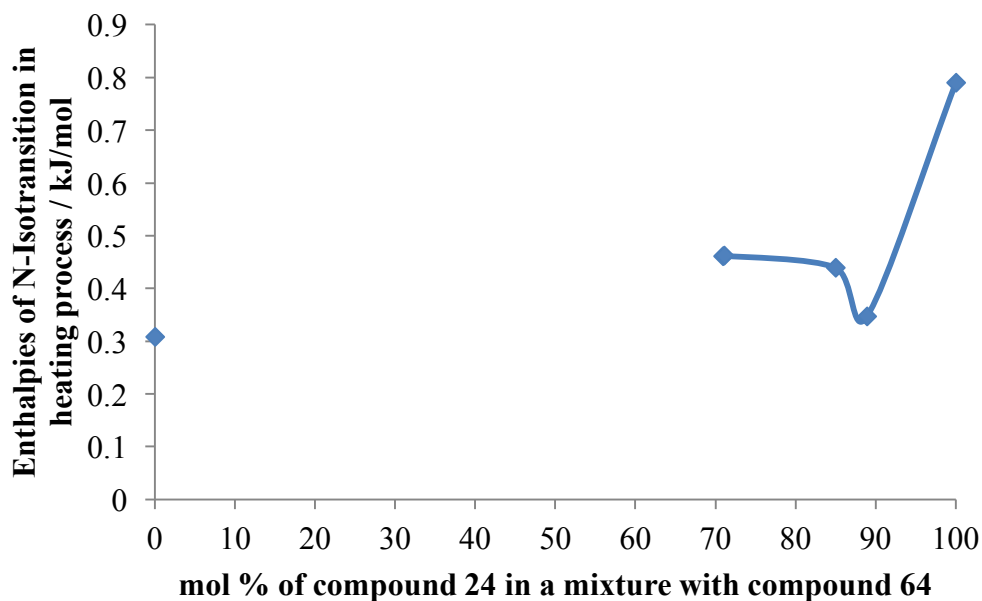


**Figure 6.38** The diagram showing the function of enthalpies (kJ/mol) of mixtures exhibiting nematic to isotropic liquid transitions on heating cycles with respect to the mol concentration of compound **24** in a mixture with compound **64**.

#### 6.4.3.2 Mixture Studies of Compounds **21** and **64**

The next study was between compounds **21** and **64**. Compound **21** was selected for study because it possesses a relatively high clearing point temperature and a broad temperature range for the columnar mesophase stability. In addition, the material is chiral and can therefore induce chirality into the discotic nematic phase of binary mixtures. This aids in the identification of phase types through the formation of finger print textures seen by POM. In contrast compound **64** has exhibits a nematic phase at a fairly high temperature. It also possesses alkynic units around the central phenyl ring, which gives it a more rigid disc-like structure and ability to interact more strongly face-to-face because of the extended polarizable delocalised  $\pi$  electrons. The binary phase diagram between compounds **21** and **64** is shown in Figure 6.42, and the structures and phase transition temperatures, the energy minimised space-filling structures using the MM2 force field as implemented in ChemDraw 3D in gas phase at absolute zero, and molecular simulations using DFT theory for compounds **21** and **64** are shown respectively in

Figures 6.39 to 6.41. In the figures the structures have been adjusted so they have roughly the same atom size.

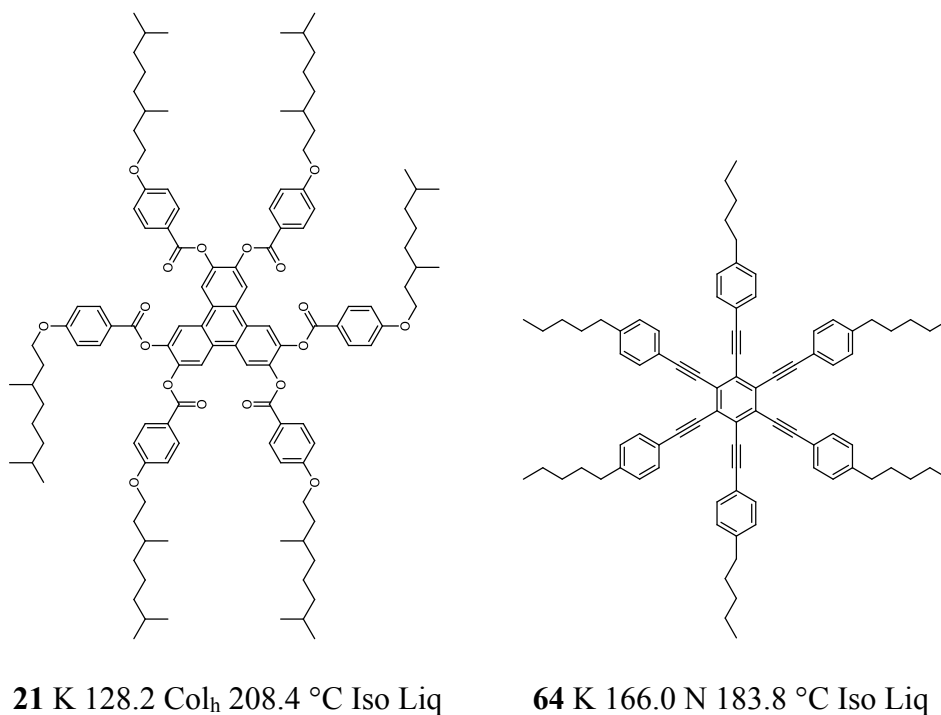


**Figure 6.39** The chemical structures and phase transitions for compounds **21** and **64**.

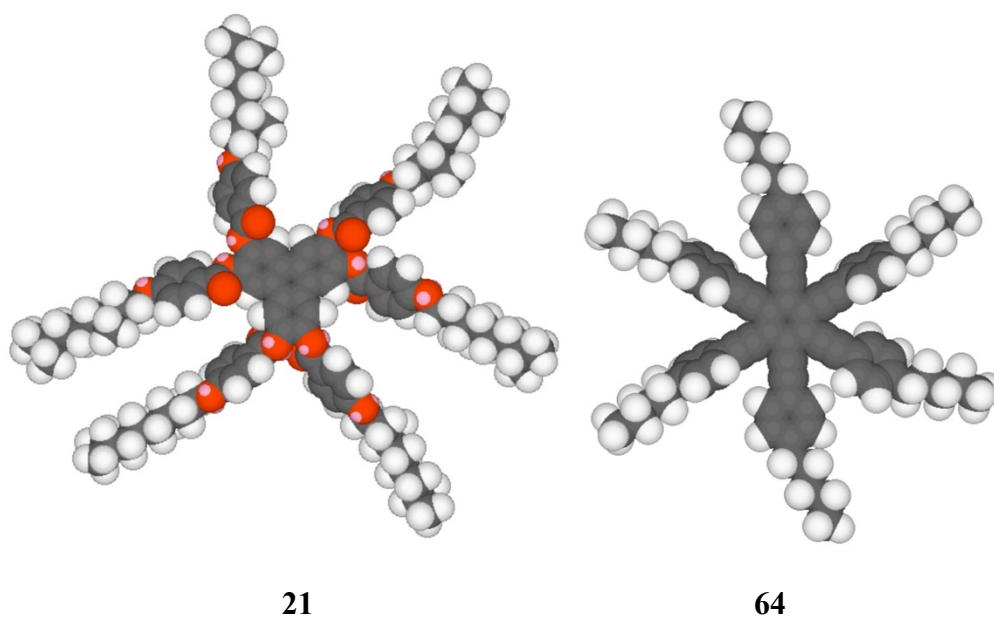
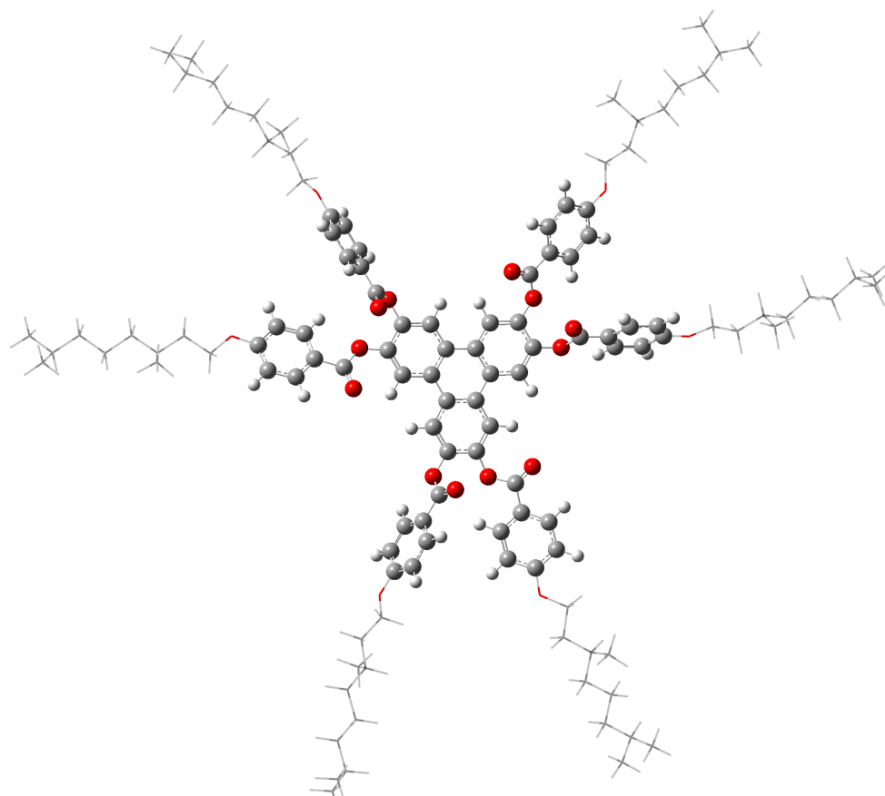


**Figure 6.40** The space filling structures of compounds **21** and **64** determined in gas phase at 0 K using the MM2 force field as implemented in ChemDraw 3D.



## 21

**Figure 6.41** The minimised energy structures for compounds **21**, at the mixed ONIOM(B3LYP/6-31G(d):PM6) level of theory.

In the simulated structures, compound **64** is planar in the DFT theory but twisted using ChemDraw 3D (see Figure 5.24 and Figure 5.26). Secondly the diameter of compound **21** is 40.91 Å, whereas the diameter of compound **64** is 28.05 Å. For compound **21**, three of the peripheral aromatic rings are twisted out of the plane of the central triphenylene core, whereas for compound **64** all of the peripheral rings are in the same plane as the central benzene core, as shown by DFT theory.

As compound **21** was found to exhibit a hexagonal columnar phase, and compound **64** exhibits a nematic phase, therefore it was expected that the two materials would be immiscible and binary mixtures at the middle of the phase diagram would not be mesomorphic. However, the following will show that this is not the case.

In the same manner with previous experiments, a series of mixtures (**TZ-M028-1-8**) of **21** and **64** were prepared and their phase behaviour was firstly examined by POM, and secondly by DSC. The transition temperatures for the various mixtures determined by POM are given in Table 6.13, whereas those determined from DSC are shown together in Table 6.14. The composition of the mixture (**TZ-M028-E**) predicted to exhibit the eutectic for the binary components was calculated from the melting enthalpies of compounds **21** and **64** using Schröder-van Laar equation, and its experimental phase behaviour determined by POM and DSC is shown in both Tables. The binary phase diagrams for the results shown in Table 6.13 and Table 6.14 are shown respectively in Figure 6.42 and 6.44. In addition, photomicrographs of the defect textures for various concentrations are incorporated into the phase diagrams in Figure 6.42 and 6.43.

**Table 6.13** Compositions (mol%) and transition temperatures (°C) for binary mixtures of compounds **21** and **64** determined by POM.

ID	21/mol%	K	/°C	N	/°C	Col <sub>h</sub>	/°C	Iso
<b>64</b>	0	.	166.0	.	183.8	-	-	.
<b>TZ-M028-1</b>	5	.	165.2	.	176.9	-	-	.
<b>TZ-M028-2</b>	35	.	150.9	.	175.4	-	-	.
<b>TZ-M028-3</b>	65	.	149.1	.	182.4	-	-	.
<b>TZ-M028-7</b>	70	.	146.3	.	175.5	.	175.5	.
<b>TZ-M028-8</b>	75	.	146.1	.	181.1	.	181.1	.
<b>TZ-M028-4</b>	80.9	.	149.8	-	-	.	180.5	.
<b>TZ-M028-E</b>	89	.	146.2	-	-	.	183.0	.
<b>TZ-M028-5</b>	95.3	.	148.8	-	-	.	192.5	.
<b>21</b>	100	.	128.4	-	-	.	208.4	.

**Table 6.14** Mixture compositions (mol%) and transition temperatures (°C) and enthalpies (J/g) in heating and cooling cycles for binary mixtures of compounds **21** and **64**.

ID	21/ mol %	Melting /°C	Col <sub>h</sub> -Iso/°C		N-Iso/°C	
			Heating	Cooling	Heating	Cooling
<b>64</b>	0	166.01	-	-	185.61	186.40
		$\Delta H= 53.98$	-	-	$\Delta H= 0.28$	$\Delta H= -0.20$
TZ- M028- 1	5	165.18	-	-	-	-
		$\Delta H= 37.30$	-	-	-	-
TZ- M028- 2	35	150.92	-	-	176.22	172.69
		$\Delta H= 20.16$	-	-	$\Delta H= 0.13$	$\Delta H= -0.15$
TZ- M028- 3	65	149.12	-	-	-	171.91
		$\Delta H= 8.42$	-	-	-	$\Delta H= -0.12$
TZ- M028- 7	70	146.34	178.04	176.03	178.04	176.03
		$\Delta H= 6.84$	$\Delta H= 0.47$	$\Delta H= -0.57$	$\Delta H= 0.47$	$\Delta H= -0.57$
TZ- M028- 8	75	146.07	185.99	184.52	185.99	184.52
		$\Delta H= 8.01$	$\Delta H= 0.56$	$\Delta H= -0.33$	$\Delta H= 0.56$	$\Delta H= -0.33$
TZ- M028- 4	80.9	149.83	182.20	171.11	-	-
		$\Delta H= 5.43$	$\Delta H= 0.73$	$\Delta H= -0.75$	-	-
TZ- M028- E	89	146.24	193.22	180.13	-	-
		$\Delta H= 2.63$	$\Delta H= 1.17$	$\Delta H= -1.55$	-	-
TZ- M028- 5	95.3	148.78	203.57	197.35	-	-
		$\Delta H= 8.28$	$\Delta H= 2.52$	$\Delta H= -2.54$	-	-
<b>21</b>	100	133.47	209.69	205.73	-	-
		$\Delta H= 12.25$	$\Delta H= 5.38$	$\Delta H= -6.30$	-	-

For the binary phase diagram for compounds **21** and **64** shown in Figure 6.42, and the more detailed Figure 6.43, below 65 mol% of **21** in the mixtures only a nematic phase is exhibited whereas above 81 mol% of **21**, the mixtures only show a hexagonal columnar phase. At the point of 70 mol% of **21** and 75 mol% of **21**, there is no miscibility of the compounds. Phase separated domains of nematic phase and hexagonal columnar phase are observed. The predicted eutectic mixture, from Schröder-van Laar equation, is 89 mol% of compound **21**. However, no

distinct eutectic point was observed in this region in the phase diagram. In fact, the melting points vary almost linearly with concentration.

These observations suggest that phase separation occurs between the two materials. However, the transition temperatures to the solid state vary almost linearly with respect to concentration. This is the case even for the eutectic mixture predicted by Schröder-van Laar equation. This observation suggests that demixing had not occurred.

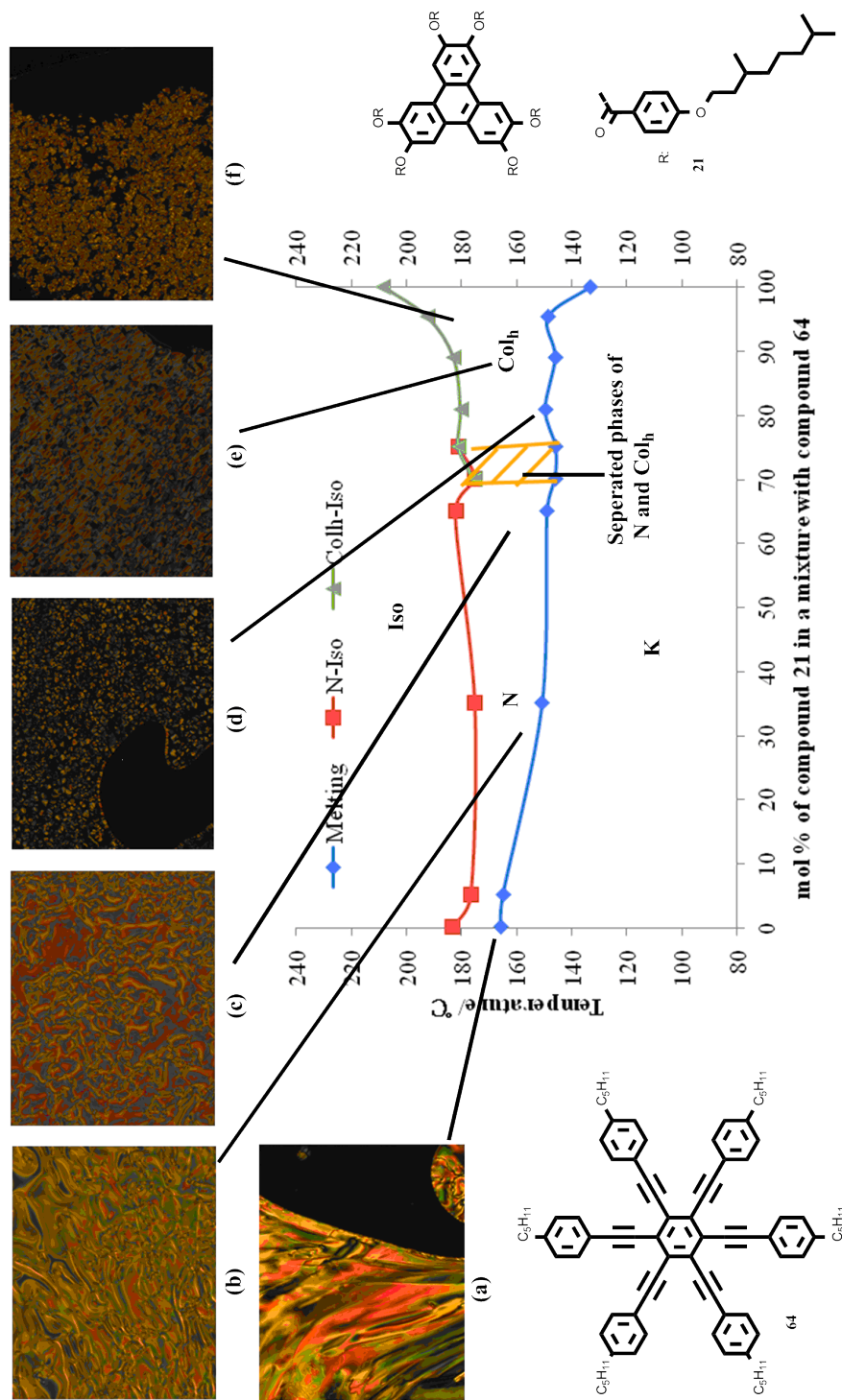


**Figure 6.42** The Gibbs phase diagram for the binary mixture series **TZ-M028** and the photo micrographs (x100 magnification) of the series of mixture **TZ-M028** showing representative optical textures: **(a)** 5.0%, heating, 169.3 °C, N; **(b)** 35.0%, heating, 170.5 °C, N; **(c)** 65.0%, cooling, 169 °C, N; **(d)** 89.9%, cooling, 158.0 °C, Col<sub>h</sub>; **(e)** 80.9%, cooling, 176.0 °C, Col<sub>h</sub>; **(f)** 95.3%, cooling, 180.8 °C, Col<sub>h</sub>.

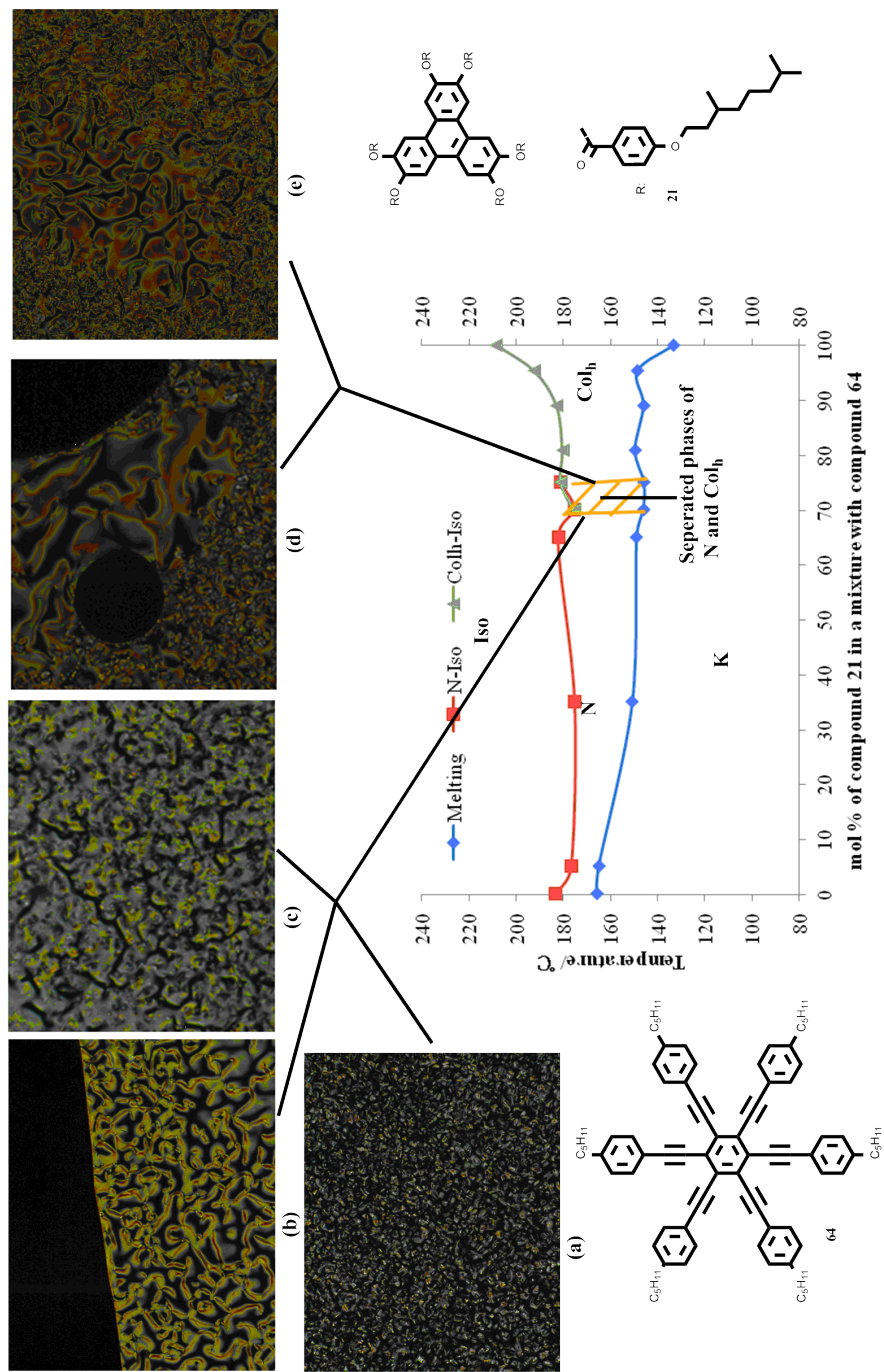


**Figure 6.43** The micrographs (x100 magnification) of the series of mixture **TZ-M028** showing representative optical separated phases textures: **(a)** **(b)** **(c)** 70.0%, cooling, 170.0 °C, separated N and Col<sub>h</sub>; **(d)** 75.0%, cooling, 182.0 °C, separated N and Col<sub>h</sub>.

In order to investigate this behaviour further, and to obtain accurate values for the transition temperatures on heating and cooling for the mixtures in the phase diagram, calorimetric studies were performed for each individual mixture, the results for which are shown in Table 6.14 along with the enthalpies for transitions.

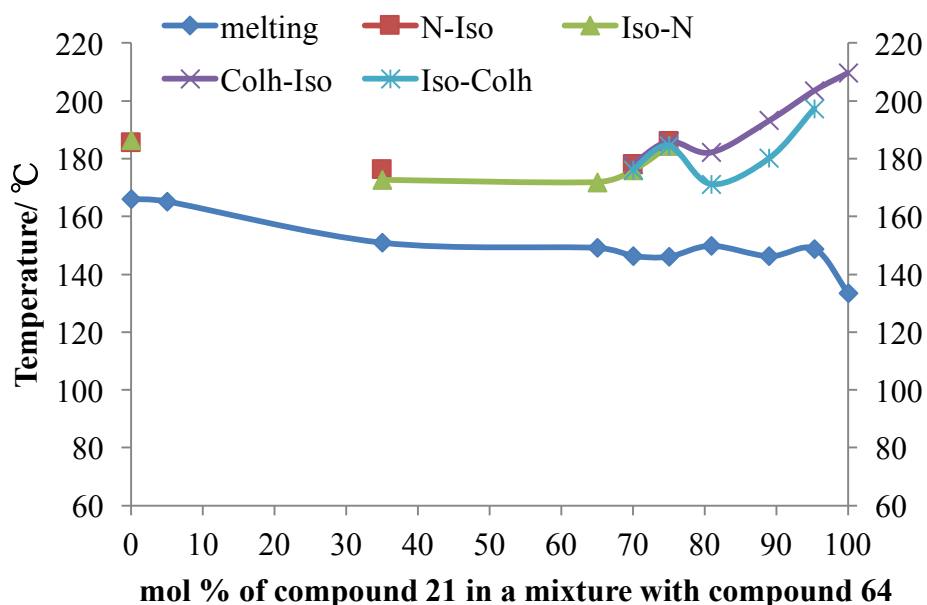


**Figure 6.44** The Gibbs phase diagram showing the biphasic region between heating and cooling for nematic to isotropic liquid and hexagonal columnar to isotropic liquid transitions of mixtures of **21** and **64**.

It is important to note that the binary diagram for the transition temperatures determined by calorimetry, as shown in Figure 6.44, are broadly in agreement with the phase diagram obtained by POM. In addition, the temperatures of the peak maximums show little hysteresis with respect to heating and cooling cycles and it means that there is little phase separation in the phase diagram. Furthermore, there are effectively no enthalpies of the transition peaks at the point of 5 mol% of compound **21**.

If we examine the values of the enthalpies of the phase transitions as a function of concentration, as shown in Figure 6.45, it can be seen that a number of the

enthalpies for the N-I phase transition are missing and the enthalpies for the Col<sub>h</sub>-I phase transition showed a big depression as the concentration of compound **21** decreased. Overall, however, the phase diagram appears to show an accurate representation of the phase behaviour as a function of temperature. Thus it seems strange that the Col<sub>h</sub> to liquid and nematic to liquid phase transition curves appear to join up, indicating that the columnar phase is being inducted into the structure of the discotic nematic phase of compound **64**.

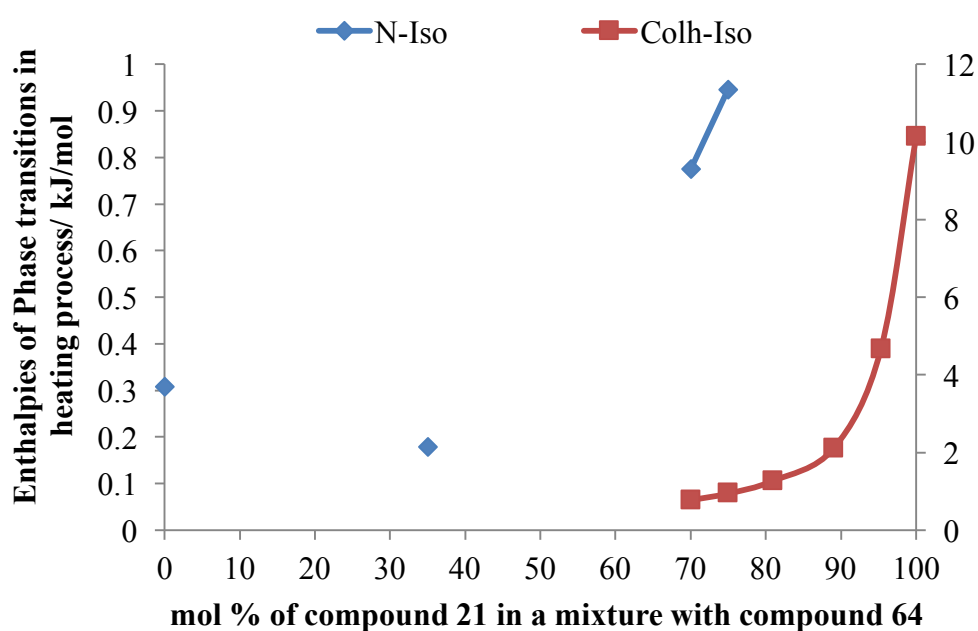
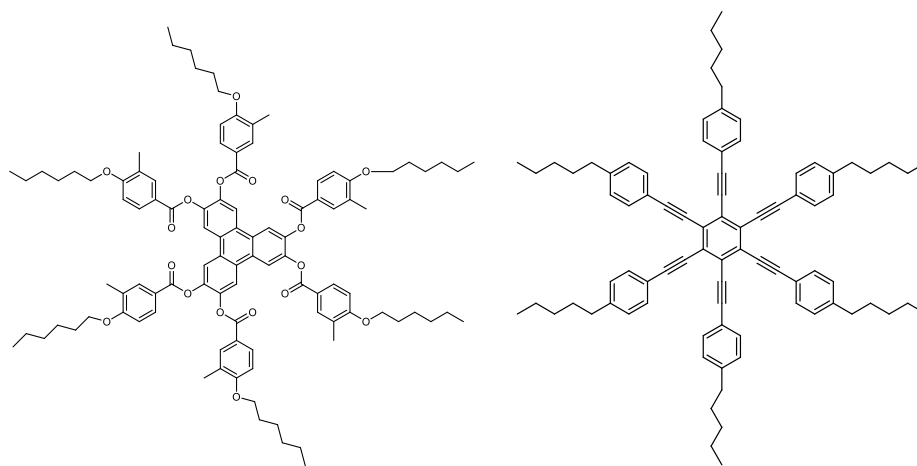


**Figure 6.45** The diagram showing the function of enthalpies (kJ/mol) of phase transitions in heating cycles with the mol concentration of compound **21** in a mixture with compound **64**.

#### 6.4.3.3 Mixture Studies of Compounds **23** and **64**

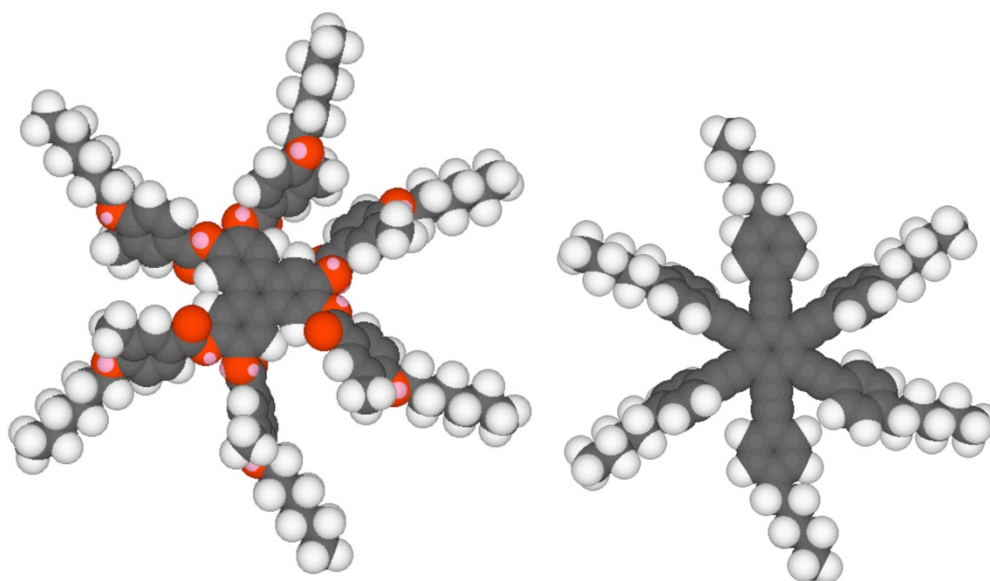
The binary phase diagram between compounds **23** and **64**, shown in Figure 6.49, was selected for investigation because the two previous studies in this section had shown unusual behaviour in their phase diagrams. With longer chains attached to the peripheral rings of the triphenylene esters in the first study complete miscibility of the nematic phase was found, but there were no columnar phases formed in the

phase diagram. In the second study there was a phase separated region where it appeared that the columnar to liquid transitions were running directly into the nematic to liquid transitions. Thus in order to examine this type of behaviour further it was decided again to see if unusual behaviour was observed for a discotic liquid crystal that exhibited nematic and columnar phases when mixed with a purely nematic material. The binary phase diagram between compounds **23** and **64** is shown in Figure 6.49, and the structures and phase transition temperatures, the energy minimised space-filling structures using the MM2 force field as implemented in ChemDraw 3D in gas phase at absolute zero, and molecular simulations using DFT theory for compounds **23** and **64** are shown respectively in Figures 6.46 to 6.48.



**23** K 223.9 (Col<sub>h</sub> 213.8) N 258.9 °C Iso Liq      **64** K 166.0 N 183.8 °C Iso Liq

**Figure 6.46** The chemical structures and phase transitions (°C) for compounds **23** and **64**.

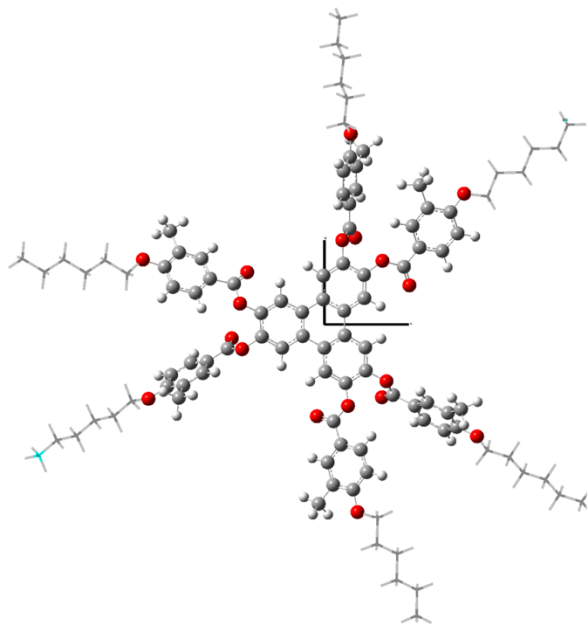


**23**

**64**

**Figure 6.47** The space filling structures of compounds **23** and **64** determined in gas phase at 0 K using the MM2 force field as implemented in ChemDraw 3D.

For the simulation results the calculations by DFT theory for compound **23** using both ONIOM(B3LYP/6-31G(d):PM6) and full B3LYP/6-31G(d) methods showed there wasn't much difference between the two, indicating the method was relatively robust. Compound **64** was found to be planar by the DFT theory but somewhat twisted using ChemDraw 3D. This is because the external phenyl rings have ease of rotation due to the  $sp$  hybridization of the triple bond. Additionally, the diameter of compound **23** as found to be 37.15 Å, whereas the diameter of compound **64** was measured to be 28.05 Å. For compound **23**, three of the peripheral aromatic rings are twisted 90 degrees out of the plane of the central triphenylene core, whereas for compound **64** all of the peripheral rings are in the same plane as the central benzene core according to DFT theory.



23

**Figure 6.48** The energy structure for compounds **23**, at the mixed ONIOM(B3LYP/6-31G(d):PM6) level of theory.

Employing the same methodology as previously, a series of mixtures (**TZ-M029-1-5**) of **23** and **64** were prepared and their phase behaviour was examined POM, and then by DSC. The transition temperatures for the various mixtures determined by POM are given in Table 6.15, whereas those determined from DSC are shown together in Table 6.16. The composition of the eutectic mixture (**TZ-M029-E**) predicted using the Schröder-van Laar equation was found to be 95.8 mol% of compound **23** in a mixture with compound **64**. The phase transition results for the experimental eutectic mixture were determined by POM and DSC, and are shown in the two Tables. The phase diagrams for the results given in the two Tables are shown respectively in Figures 6.49 and 6.50.

**Table 6.15** Compositions (mol%) and transition temperatures (°C) for binary mixtures of compounds **23** and **64** determined by POM.

ID	<b>23</b> /mol%	K	/°C	N	/°C	Col <sub>h</sub>	/°C	Iso
<b>64</b>	0	.	166.0	.	183.8	-	-	.
<b>TZ-M029-5</b>	5	.	165.3	.	188.3	-	-	.
<b>TZ-M029-4</b>	20	.	159.1	.	197.6	-	-	.
<b>TZ-M029-3</b>	50	.	149.2	.	190.9	-	-	.
<b>TZ-M029-2</b>	80	.	146.8	.	180.4	.	169.5	.
<b>TZ-M029-1</b>	90	.	146.2	-	-	.	195.3	.
<b>TZ-M029-E</b>	95.8	.	144.7	-	-	.	192.1	.
<b>23</b>	100	.	223.9	.	258.9	.	(213.8)	.

From the phase diagram (Figure 6.49) and the photomicrographs taken of the mixtures, it was clear that **23** and **64** were not miscible. From 0-80 mol% of compound **23**, the mixtures displayed nematic phase, whereas 80-100 mol% of compound **23**, they exhibited a hexagonal columnar phase. In addition, at the demarcation point of 80 mol% of compound **23**, the mixture displayed a nematic phase on heating, but a hexagonal columnar phase on cooling. The eutectic point was not found as predicted *via* the Schröder-van Laar equation, and no obvious eutectic was observed.

**Table 6.16** Mixture compositions (mol%) and transition temperatures (°C) and enthalpies (J/g) in heating and cooling cycles for binary mixtures of **23** and **64**.

ID	23 /mol%	Col <sub>h</sub> -Iso/ °C		N-Iso/°C	
		Heating	Cooling	Heating	Cooling
<b>64</b>	0	-	-	184.76	192.80
		-	-	$\Delta H = 0.28$	$\Delta H = -0.20$
<b>TZ-M029-5</b>	5	-	-	189.62	-
		-	-	$\Delta H = 0.23$	-
<b>TZ-M029-4</b>	20	-	-	201.32	-
		-	-	$\Delta H = 0.30$	-
<b>TZ-M029-3</b>	50	-	-	-	-
		-	-	-	-
<b>TZ-M029-2</b>	80	-	160.22	188.33	-
		-	$\Delta H = -1.55$	$\Delta H = 0.34$	-
<b>TZ-M029-1</b>	90	203.62	188.2	-	-
		$\Delta H = 1.0$	$\Delta H = -1.44$	-	-
<b>TZ-M029-E</b>	95.8	197.62	178.8	-	-
		$\Delta H = 0.12$	$\Delta H = -0.68$	-	-
<b>23</b>	100	-	212.11	259.61	259.59
		-	$\Delta H = -0.25$	$\Delta H = 0.66$	$\Delta H = -0.75$

In order to investigate the behaviour in the phase diagram further, and to obtain accurate values for the transition temperatures on heating and cooling for the mixtures in the phase diagram calorimetry was performed. The results for each individual mixture are shown in Table 6.16 along with the enthalpies for the transitions.

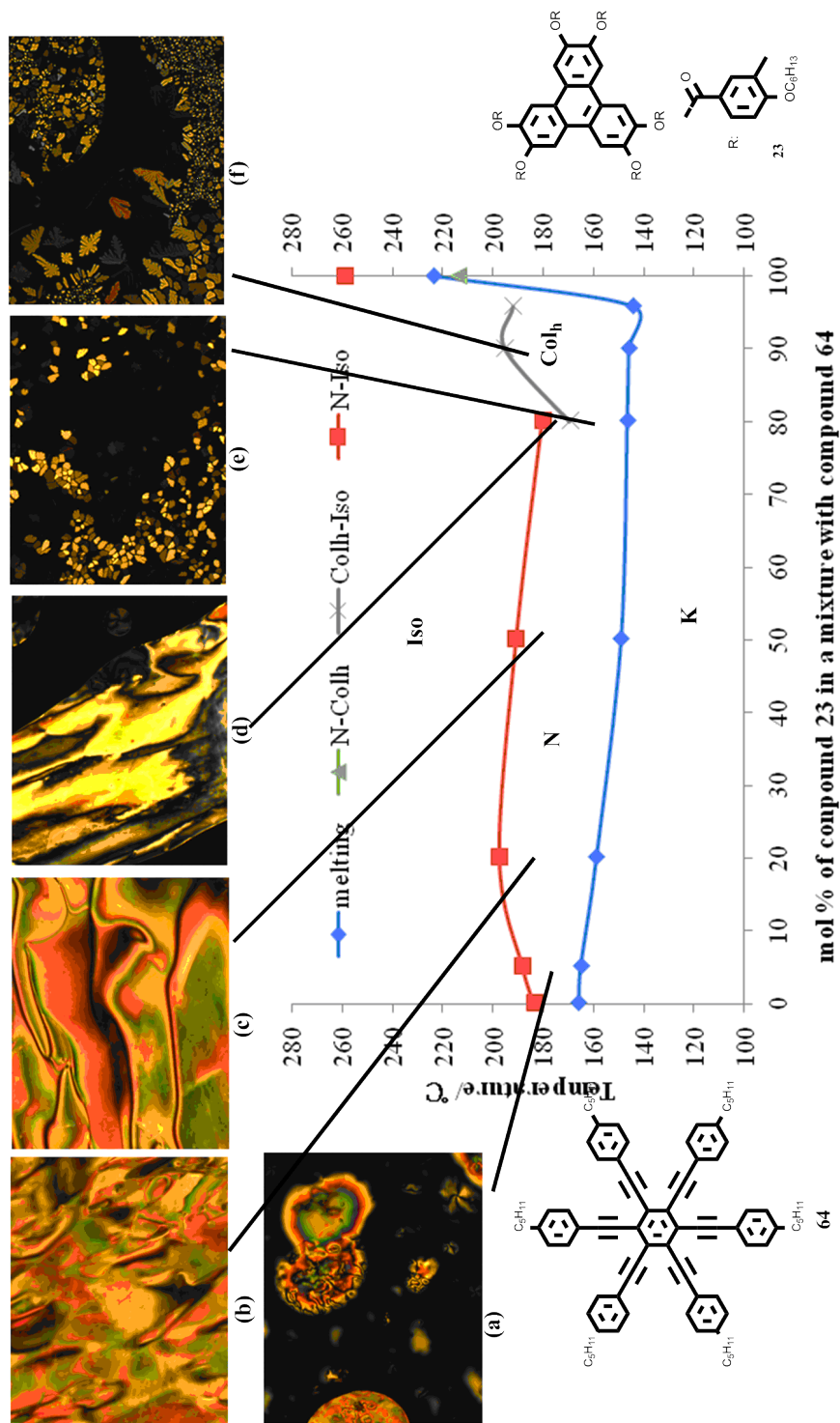


**Figure 6.49** The Gibbs phase diagram for the binary mixture series **TZ-M029**. Photomicrographs (x100 magnification) of the series of mixture **TZ-M029** showing representative optical textures: **(a)** 5.0%, heating, 177.6 °C, N; **(b)** 20.0%, heating, 166.6 °C, N; **(c)** 50.0%, heating, 163.0 °C, N; **(d)** 80.0%, heating, 192.5 °C, N; **(e)** 80.0%, cooling, 145.0 °C, Colh; **(f)** 90.0%, cooling, 187.8 °C, Colh.

The result indicates that the binary diagram for the transition temperatures as determined by calorimetry, in Figure 6.50, are broadly in agreement with the phase diagram obtained by microscopy. The melting points showed an almost linear variation with concentration. For N to I values only up to ~20 mol% of **23** in the mixtures could be observed using DSC, and at higher concentrations the transitions are only observed by microscopy. At high concentrations of **23** it appears that there is some hysteresis as there is the possibility of nematic and columnar phases coexisting. For the demarcation point of 80 mol% of compound **23**, the mixture was noted previously to exhibit a nematic phase on heating, but a hexagonal columnar phase on cooling, this may indicate that the phase transition may also possess kinetic properties in addition to thermodynamic.

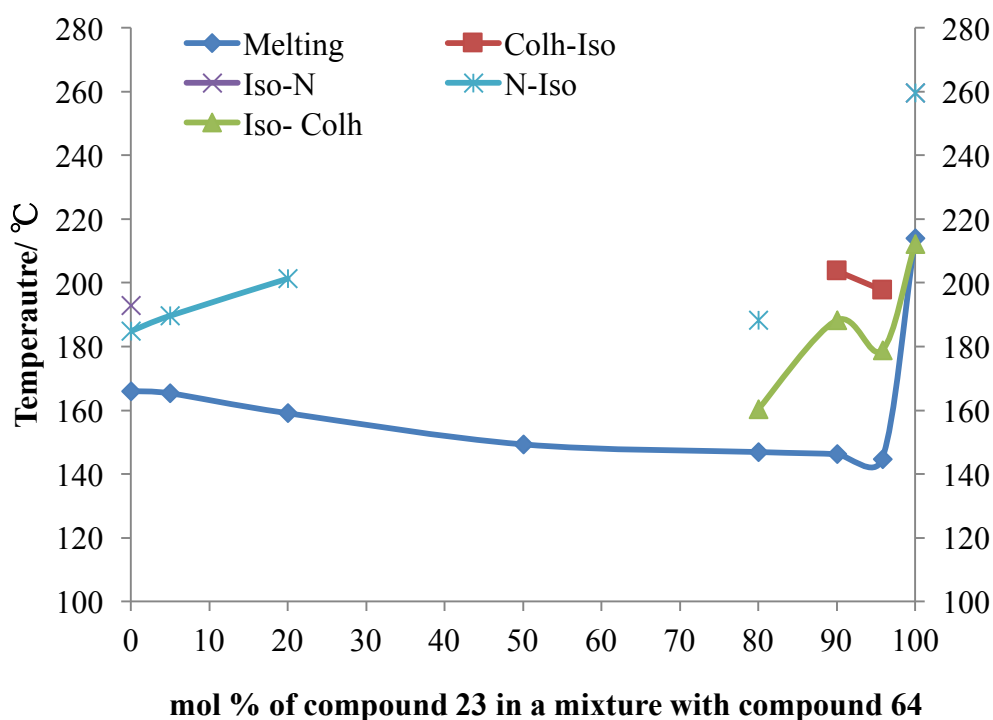


**Figure 6.50** The Gibbs phase diagram showing the biphasic region between heating and cooling for phase transitions (°C) of mixtures (mol%) of **23** and **64**.

If we examine the values of the enthalpies of phase transitions as a function of concentrations, as shown in Figure 6.51, it can be seen that the enthalpies for the

N-I phase transition vary intermittently as low values, but the enthalpies for Col<sub>h</sub>-I phase transition increases with respect to concentrations.

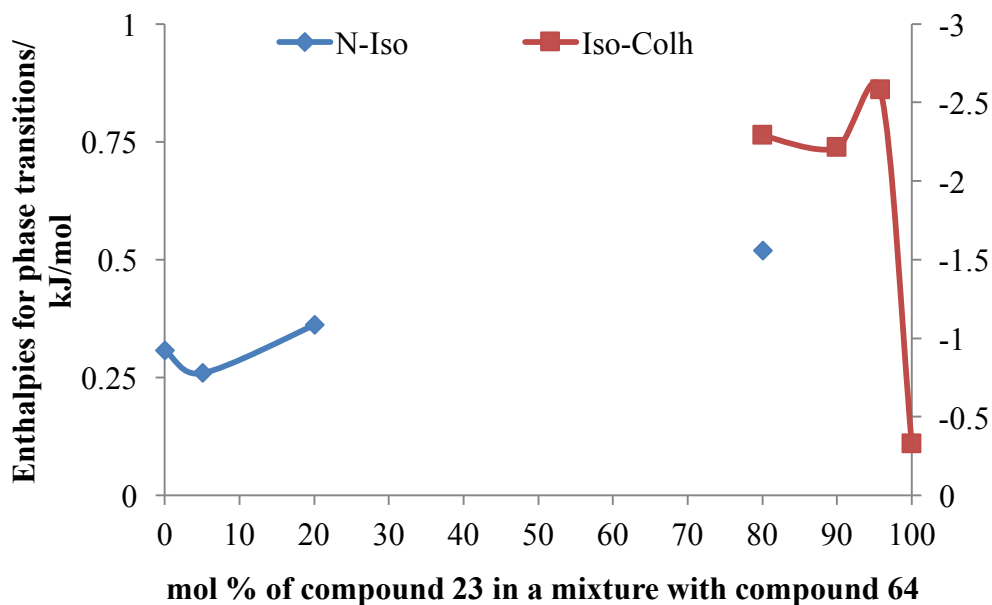


**Figure 6.51** The diagram showing the function of enthalpies (kJ/mol) of each phase transition in heating or cooling session with the mol concentration of compound **23** in a mixture with compound **64**.

## 6.5 Recalculations of the Schröder-van Laar Equation for Mixtures Containing Columnar Mesogens

The Schröder-van Laar equation is normally used to determine the eutectic point for calamitic liquid crystal systems. Although the Schröder van-Laar equation was used to predict the eutectic composition for hexagonal columnar hexa-esters of triphenylene, there was no obvious lowering of the melting point (*i.e.* see Figure 6.5 and 6.13). There was, however, a lowering of the isotropic liquid to hexagonal columnar phase transition (*i.e.* see Figure 6.5). This might indicate that the hexagonal columnar behaves as a soft crystal phase. As a result, the Schröder-van Laar equation was again used to predict a eutectic composition where the isotropic liquid to columnar phase transition and the associated enthalpies were used to

represent the melting point and melting enthalpy. Table 6.17 shows the predicted values for mixture series **TZ-M003** and **TZ-M040** using the melting points for comparison. Table 6.18 shows the values predicted using the Iso-Col<sub>h</sub> phase transition temperatures. However, neither of these predictions account for the behaviour observed in the Gibbs phase diagrams of the mixtures made by columnar mesogens, which might indicate that the columnar phase should not be considered as a 3D soft crystal as it may well be considered as a 2D crystal.

**Table 6.17** Calculation results by Schröder-van Laar equation using melting temperatures and related enthalpies.

Title	<b>21</b> / mol%	Melting Eutectic/ °C	Clearing point/°C
<b>TZ-M040</b>	73.9	14.9	216.8
<b>TZ-M003</b>	79.1	34.9	201

**Table 6.18** Calculation results by Schröder-van Laar equation using Col<sub>h</sub>-Iso temperatures and related enthalpies.

Title	<b>21</b> / mol%	Col <sub>h</sub> Eutectic/ °C	Clearing point/ °C
<b>TZ-M040</b>	40.1	92.4	242.7
<b>TZ-M003</b>	32.7	74.2	209.9

In order for extensive investigations, more re-calculations of results obtained *via* the Schröder-van Laar equation are shown in Table 6.19 and Table 6.20.

**Table 6.19** The eutectic results of the mixture **TZ-M016**. Calculation of results by the Schröder-van Laar equation, using melting temperatures and related enthalpies, is shown in the first line. Calculations of results employing the Schröder-van Laar equation using the Col<sub>h</sub>-Iso transition temperatures and related enthalpies shown in the second line. The experimental results are shown in the third line.

Methods	<b>32/</b> mol%	Eutectic/°C	Clearing point/ °C
Melting point	24.0	98.7	119.3
Col <sub>h</sub> -Iso	71.6	86.1	172.6
Experiment	74.9	93.5	174.2

**Table 6.20** The eutectic results of the mixture **TZ-M018**. Calculation of results by the Schröder-van Laar equation, using melting temperatures and related enthalpies, is shown in the first line. Calculations of results employing the Schröder-van Laar equation using the Col<sub>h</sub>-Iso transition temperatures and related enthalpies shown in the second line. The experimental results are shown in the third line.

Methods	<b>21/</b> mol%	Eutectic/ °C	Clearing point/ °C
Melting point	89.3	78.9	198.4
Col <sub>h</sub> -Iso	42.9	99.4	161.0
Experiment	89.5	94.7	185.4

The results are inconsistent. It can be seen that for Table 6.19 the agreement between experiment and using the Iso Liq to Col phase transition is relatively good which suggests that employing the columnar phase as crystals is reasonable. However, the results obtained in Table 6.20 suggest that the melting behaviour is more in keeping with the experimental studies. This indicates that the columnar phases may have subtly different structures.

## 6.6 Discussion

For these materials investigated in the part of Chapter 6, the aliphatic chains fill in the space between the aromatic cores as shown by the schematic in Figure 6.52. However, the space is extensively filled at the edges of the discs, whereas at the junctions between three discs there is greater space available for the packing of the chains together, as shown in Figure 6.1 (Section 6.2, pp 190) for hexagonal columnar phases.[87]

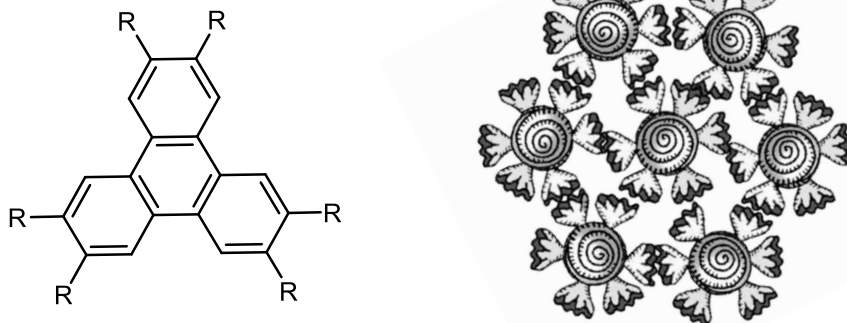


**Figure 6.52** Hexagonal arrangements of triphenylene derivatives that form the basic structure of columnar liquid crystals.

Although disc-like molecular systems are treated as extensions based on the structures and properties of rod-like molecules, unlike rod-like systems, it is too difficult for disc-like molecules to pack together in columns without forming defects between them and subsequently between the columns. Rod-like materials are usually capable of distorting their structures in order to minimise defect formation, however, for disc-like materials in columns defects form in hexagonal arrays. Thus not only do columns pack together in two-dimensional crystalline arrays, but so do the defects thereby creating a lattice. For the disordered columnar phase the lattice is 2D, but when there is the additional ordering of the molecules along the column axis the gross structure is crystalline with a 3D lattice. Herein these phases are soft crystals rather than liquid crystals.

For the three mixture systems above, some do not exhibit conventional binary phase diagrams as found for nematics and normal smectics. This implies that the relationships with crystals are possibly similar in aspects to soft crystals, *i.e.* they are more in keeping with soft crystal smectic phases in their behaviour than true smectics which do not have long range positional ordering. In this case they may not exhibit depressions of the melting points (transition from solid to the liquid and vice versa). Thus they are unlikely to give Gibbs phase diagram based on calamitic systems as shown in Figure 6.7 (Section 6.3.1, pp 199), as shown in the phase diagram in Figure 6.5 (Section 6.3.1, pp 197).

In the following an interesting extension to this argument can be made. Consider a disordered hexagonal columnar phase composed of disc-like molecules with different diameters. Structurally the columns will act as tubes of diameter equal to the diameter of the largest discs. In a mixed system this will be the case because the closest approach to one another of the tubes will be the same as the largest discs. As the columns are disordered there is no need for the centres of the discs to be aligned along the central axes of the tubes, and in fact some of the smaller discs may be off centre with respect to the axes. Thus the centres of mass need not be along the column axes and therefore the hexagonal packing array of the columns need not be exactly periodic (see Figure 6.53). Conversely, the defects between the columns will be in a hexagonal periodic array as determined by the largest molecules in the columns, and therefore the defects (or free space) will possess a lattice-like organization, implying that there will also be related lattice energy.



**Figure 6.53** A disordered hexagonal columnar phase made by molecules differing diameters, which are laterally and vertically disorganised along the column axes. The defects between the columns (thick lines) will possess long range periodic ordering.

## 6.7 Summary

In this chapter, phase behaviour of both binary columnar systems and mixed nematic and columnar systems has been investigated, where mixtures made by discotic triphenylene hexa-esters with each other, and with rod-like tetra-benzoate esters and star sharp phenyl hexa-alkynes are included. The phase behaviour of those materials is quite different with those common phase diagrams of calamitic systems by rod-like molecules and the Col<sub>h</sub>-I phase transition behaviour is much more like melting transition as common Gibbs phase diagram. Thus by the investigation of this chapter, the hexagonal columnar phases formed by the materials presented herein are probably best classified as soft crystal phases.

## **Chapter 7: Mixing Polyaromatics with Conventional Discotic Liquid Crystals**

## **Chapter 7: Mixing Polyaromatics with Conventional Discotic Liquid Crystals**

### **7.1 Introduction**

In the previous chapters (Chapter 5 and Chapter 6) miscibility studies and binary phase diagrams were developed for nematogenic and columnar materials with disc-like molecular structures in order to investigate how well the mesophases mix. In this chapter, the miscibility studies and binary phase diagrams will be examined for the polyaromatics, which have been discussed in Chapter 4, with the conventional discotic liquid crystals (discussed in Chapter 5 and Chapter 6).

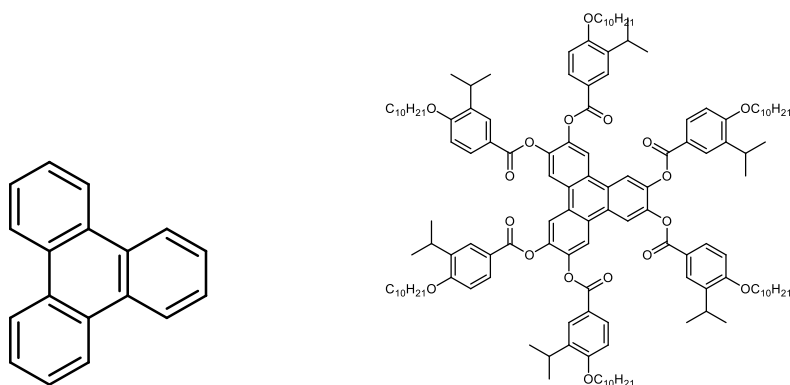
### **7.2 Mixture Studies between Triphenylene and Triphenylene Derivatives**

In the first set of the studies, triphenylene was the primary and essential polyaromatic chosen to investigate because triphenylene itself is a fused tetracyclic, polyaromatic hydrocarbon and exhibits no liquid crystal properties however, when it is substituted with suitably long and aliphatic side-chains, it can exhibit liquid crystalline phases. The triphenylene-based materials discussed in previous chapters are one example of typical discotic liquid crystals. In this section, mixtures based on triphenylene and triphenylene derivatives are prepared and analysed by POM and DSC (here the DSC results are limited), and phase diagrams are constructed and discussed.

#### **7.2.1 Mixture Studies of Triphenylene and Compound 14**

Triphenylene and compound **14** were selected for investigation because compound **14** only exhibits a nematic phase, and therefore it was expected that there would be only one mesophase to track in the binary phase diagram. The transition temperatures (°C), the space filling minimised structures determined using the

MM2 force field as implemented in ChemDraw 3D in gas phase at absolute zero for compound **14**, the 3D structure for triphenylene and simulations based on DFT theory to show the stereochemical structures for compound **14** are shown together in Figures 7.1 to 7.3 respectively. The binary phase diagram for triphenylene and compound **14** is shown in Figure 7.4.



Triphenylene K 197.4 °C Iso Liq      **14** K 160.7 N 202.5 °C Iso Liq

**Figure 7.1** The chemical structures and phase transitions (°C) for triphenylene and compound **14**.

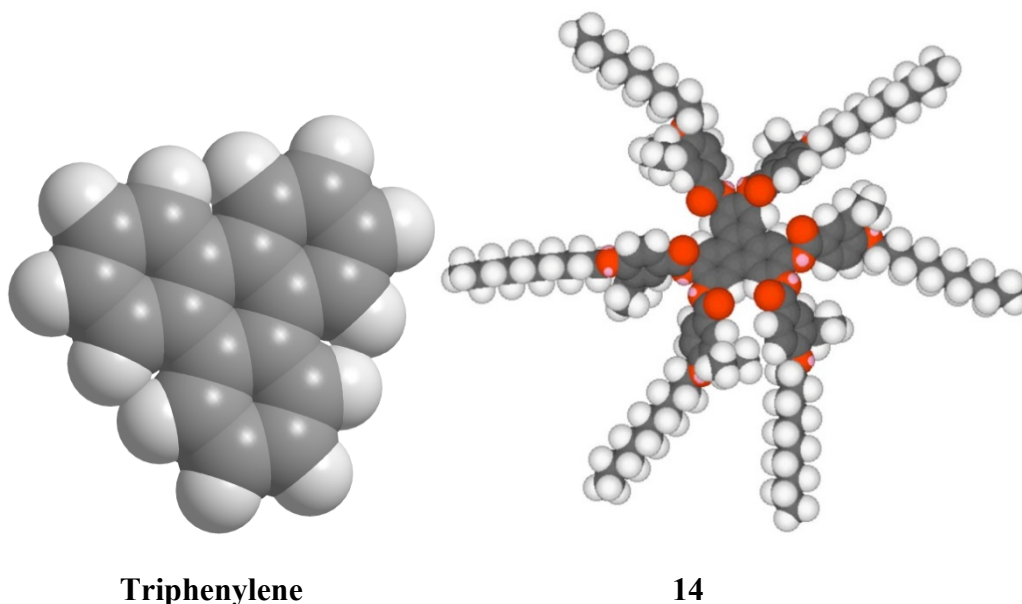
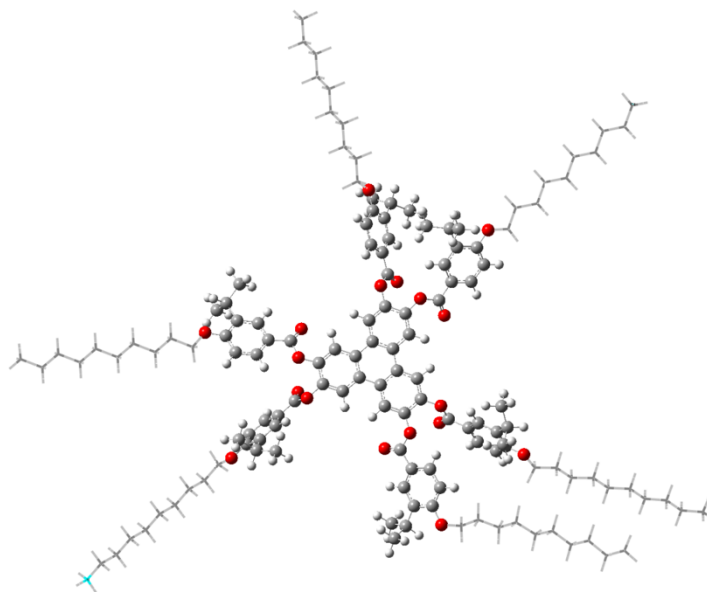


**Figure 7.2** The space filling structures of triphenylene, and compound **14** determined in gas phase at 0 K using the MM2 force field as implemented in ChemDraw 3D.



14

**Figure 7.3** The energy structure for compound **14**, at the mixed ONIOM(B3LYP/6-31G(d):PM6) level of theory.

A series of mixtures (**TZ-M046-1-6**) of triphenylene and compound **14** were prepared, and their phase behaviour was examined using POM and then by DSC. The transition temperatures for the mixtures are shown in Table 7.1. The binary phase diagram for the results given in Table 7.1 is shown diagrammatically in Figure 7.4. In addition, photomicrographs of the defect textures at various concentrations are incorporated into the phase diagram.

In the phase diagram (shown in Figure 7.4), the melting point curve did not have an obvious eutectic point. Instead, for the concentration range between 50 mol % and 80 mol % of triphenylene, the melting temperatures were similar and the curve bottomed-out indicating that a eutectic point may occur in this region. Conversely, for the nematic to isotropic liquid transition temperature curve, as the concentration of triphenylene was increased, the lower N to I phase transition became. In addition, at concentrations of 90 mol % or more of triphenylene in the mixtures no mesophases were observed. However, extrapolation of the N-I curve

to 100 mol % of triphenylene, shows that triphenylene possesses a virtual N-I point at approximately 135 °C.

This is reasonable evidence that non-amphiphilic disc-like molecular systems, *i.e.* those with rigid structures but without flexible peripheral groups, can potentially exhibit thermotropic mesophases. For rod-like systems, this occurs for the linear five ring system quinquephenyl, which has a melting point of 386 °C, and a clearing point of 415 °C, whereas the temperature is much lower for triphenylene. Nevertheless, the result infers that Onsager theory of hard particles could be applied to particles with disc-like topologies as well as to those that are rod-shaped.

**Table 7.1** Mixture compositions (mol %) and transition temperatures (°C) for binary mixtures of triphenylene and compound **14**.

ID	Tri/ mol %	K	/°C	N	/°C	Iso Liq
<b>14</b>	0	.	160.7	.	202.5	.
<b>TZ-M046-1</b>	10	.	156.6	.	199.8	.
<b>TZ-M046-2</b>	30	.	139.5	.	189.0	.
<b>TZ-M046-3</b>	50	.	123.3	.	176.8	.
<b>TZ-M046-4</b>	70	.	123.2	.	156.9	.
<b>TZ-M046-6</b>	80	.	127.4	.	152.2	.
<b>TZ-M046-5</b>	90	.	158.7	-	-	.
<b>Triphenylene</b>	100	.	197.4	-	-	.

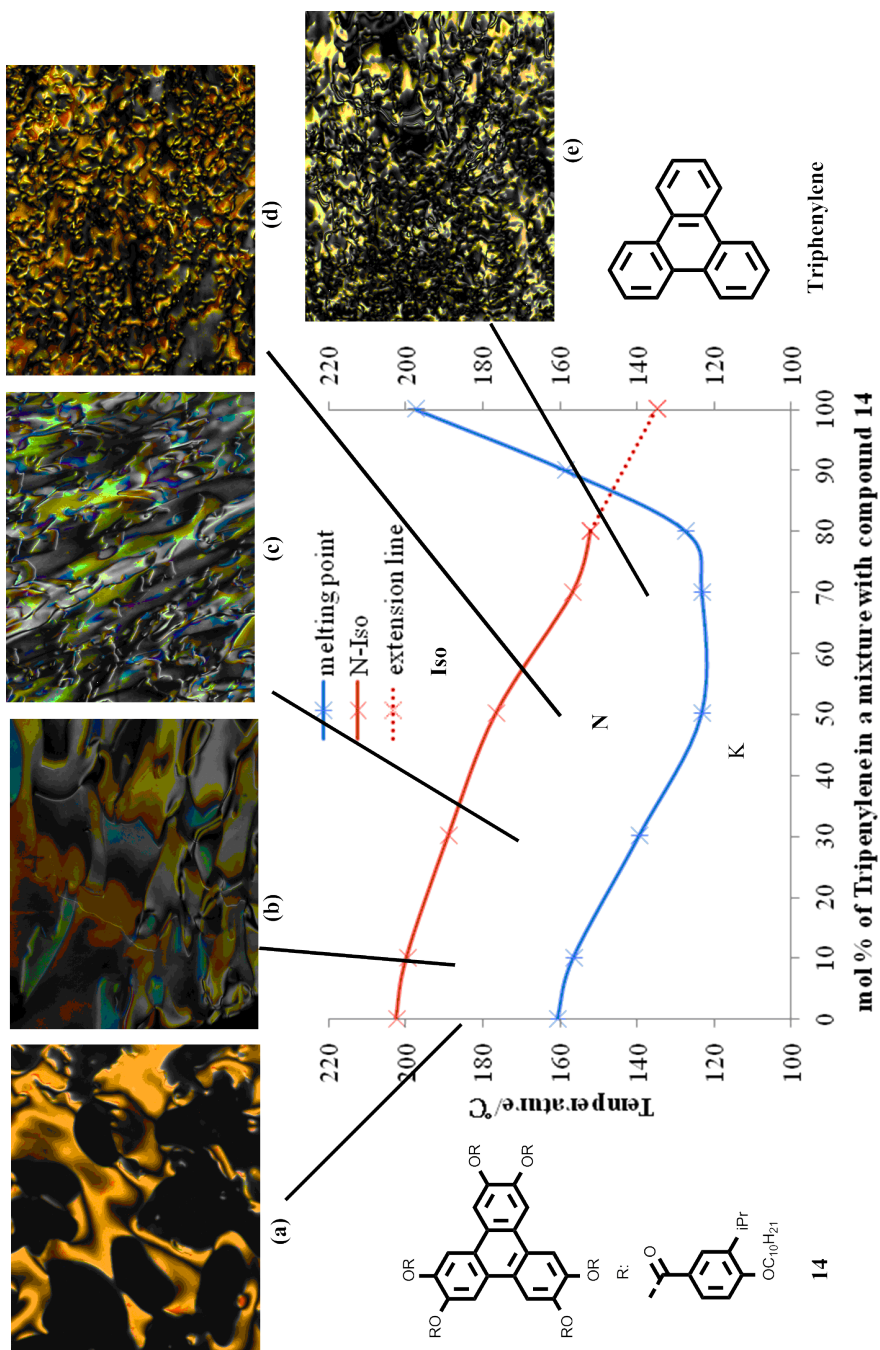
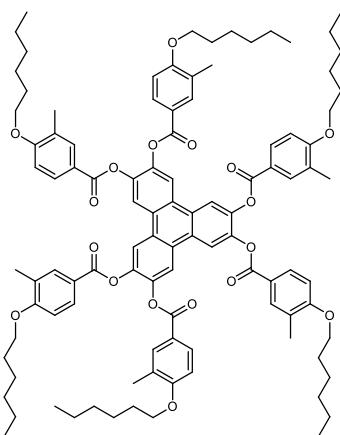


**Figure 7.4** The phase diagram for the binary mixture series **TZ-M046** of **Triphenylene** and **14**. Photomicrographs (x 100 magnification) showing representative optical textures for **TZ-M046**: **(a)** **14**, cooling, 183.5 °C, N; **(b)** 10.0%, heating, 178.8 °C, N; **(c)** 30.0 %, cooling, 175.5 °C, N; **(d)** 50.0%, cooling, 171.0 °C, N; **(e)** 70%, cooling, 158.0 °C, N.

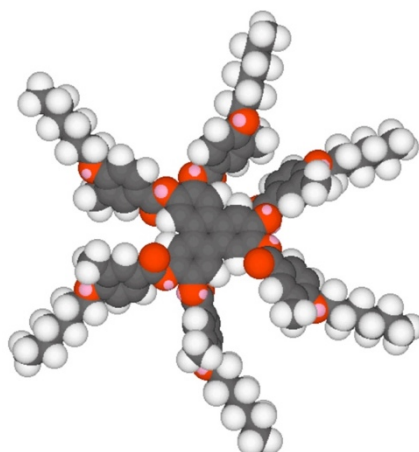
### 7.2.2 Mixture Studies of Triphenylene and Compound 23

Triphenylene and compound **23** were selected for investigation because compound **23** exhibits a hexagonal columnar phase as well as a nematic phase. The phase diagram for mixtures between the two materials is shown in Figure 7.4. The transition temperatures ( $^{\circ}\text{C}$ ), the space filling minimised structures determined using the MM2 force field as implemented in ChemDraw 3D in gas phase at absolute zero, and simulations based on DFT theory to show the stereochemical structures for compound **23** are shown in Figures 7.5 to 7.7 respectively, while those for triphenylene is shown in Figure 7.1 and 7.2 (Section 7.2.1, pp 268).



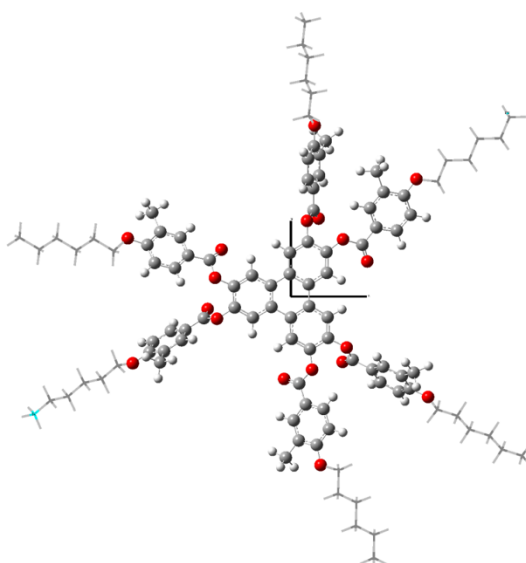
**23** K 223.9 (Col<sub>h</sub> 213.8) N 258.9  $^{\circ}\text{C}$  Iso Liq

**Figure 7.5** The chemical structure and phase transition temperatures for compound **23**.



**23**

**Figure 7.6** The space filling structures of triphenylene, and compound **23** determined in gas phase at 0 K using the MM2 force field as implemented in ChemDraw 3D.



**23**

**Figure 7.7** The energy structure for compound **23**, at the mixed ONIOM(B3LYP/6-31G(d):PM6) level of theory.

Employing the same methodology as previously used in section 7.2.1, a series of mixtures (TZ-M047-1-5) of **23** and triphenylene were prepared, and their phase behaviour was examined by POM and by DSC. The transition temperatures for the

various mixtures are given in Table 7.2, and the related phase diagram shown in Figure 7.8 which includes representative optical textures.

**Table 7.2** Mixture compositions (mol %) and transition temperatures (°C) for binary mixtures of triphenylene and compound **23**.

ID	Tri/ mol %	K		Col <sub>h</sub>		N		I		
		/°C	/°C	/°C	/°C	/°C	/°C			
<b>23</b>	0	.	214.1	-	-	.	167	.	224.4	.
<b>TZ-M046-1</b>	10	.	210.4	-	-	.	218.1	.	249.4	.
<b>TZ-M046-2</b>	30	.	197.4	-	-	.	203.3	.	238.7	.
<b>TZ-M046-3</b>	50	.	162.0	-	-	.	182.8	.	221.8	.
<b>TZ-M046-4</b>	70	.	130.0	-	-	.	122.0	.	173.9	.
<b>TZ-M046-5</b>	90	.	134.4	.	172.9	.-	-	-	-	.
<b>Triphenylene</b>	100	.	197.4	-	-	-	-	-	-	.

In Figure 7.8, it indicates that both the nematic phase and hexagonal columnar phase were exhibited in mixtures containing less than 70 mol % of triphenylene. Additionally, the temperatures of the N-I and the N-Col<sub>h</sub> phase transition curves fall as the concentration of triphenylene is increased. Moreover, no mesophases were observed above 70 mol % of triphenylene in the mixtures. The phase diagram also shows a potential eutectic point between 70 and 80 mol % of triphenylene in the mixtures. The extrapolated N-I phase transition curve to 100 mol% of triphenylene gives a virtual N-I phase transition of approximately 135 °C, whereas the N-Col<sub>h</sub> curve could not be extrapolated to 100 mol% of triphenylene, indicating that triphenylene does not have any latent columnar phase properties.

These results are similar to those of rod-like systems where only nematic phases are observed for the smaller aromatic systems. However, as the aspect ratios for the rod-like molecules are increased by increasing the number of phenyl units, the introduction of smectic phases results. Thus, it might be expected that as the diameters of the disc-like materials are increased, columnar phases will result.

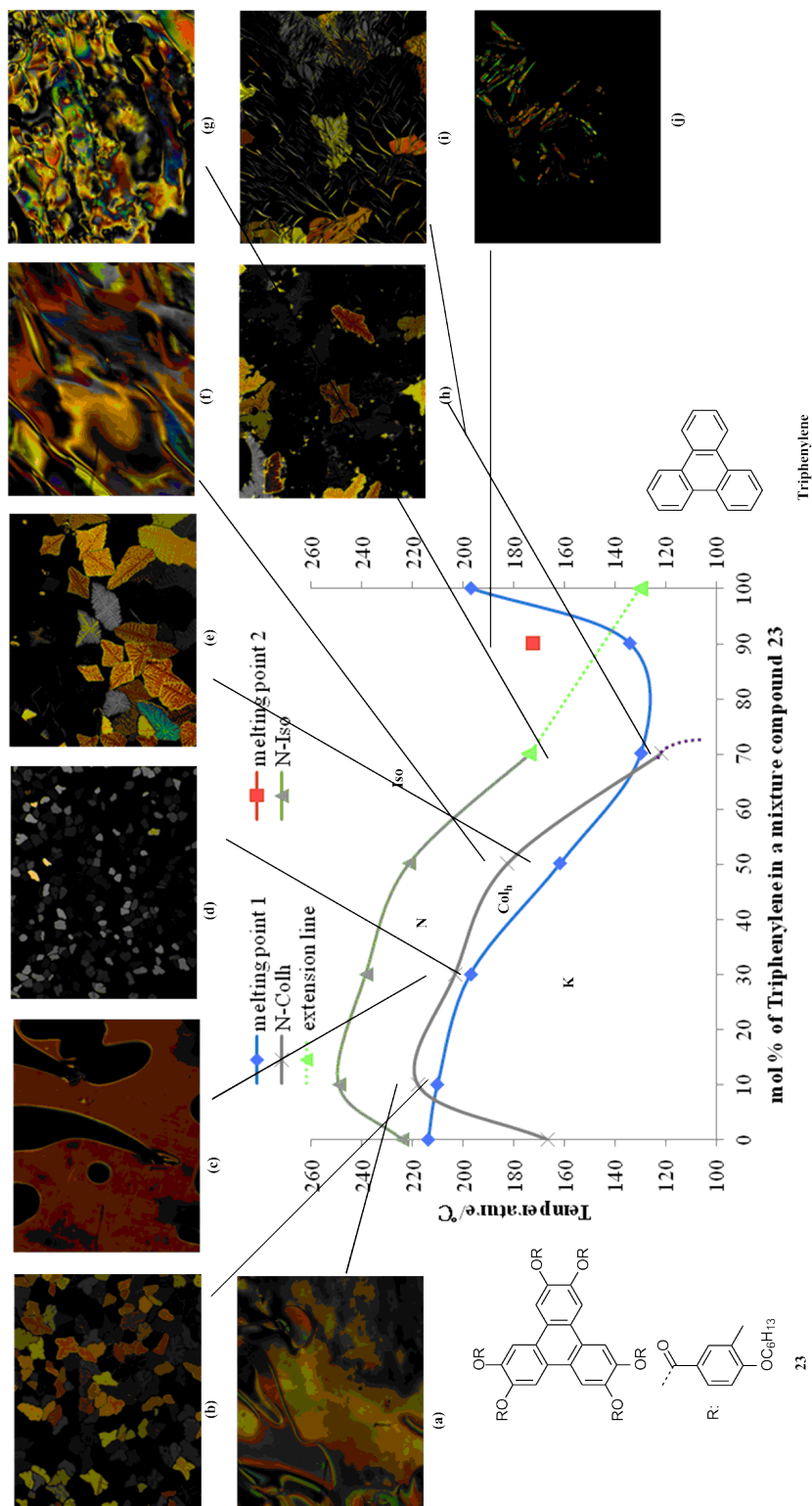


**Figure 7.8** The phase diagram for the binary mixture series **TZ-M047** of **Triphenylene** and **23**. Photomicrographs (x 100 magnification) showing representative optical textures for **TZ-M047**: **(a)** 10 %, heating, 220 °C, N; **(b)** 10.0%, cooling, 215.0 °C, Col<sub>h</sub>; **(c)** 30.0 %, heating, 224.0 °C, N; **(d)** 30.0%, cooling, 210.0 °C, N; **(e)** 50%, cooling, 187.1.0 °C, Col<sub>h</sub>; **(f)** 50%, heating, 187.1.0 °C, Col<sub>h</sub>; **(g)** 50%, heating, 216.3.0 °C, ; **(h)** 70%, cooling, 120.0 °C, Col<sub>h</sub> and partly recrystallization; **(i)** 90%, cooling, 190.0 °C, N.

### 7.2.3 Discussion

From the phase diagrams described in Section 7.2.1 and 7.2.2, the virtual N-I phase transition temperature for triphenylene can be approximated (which was mentioned in Section 4.3, Chapter 4, pp 64) because both Figure 7.4 and 7.8 give similar temperatures *via* extrapolation (shown in Figure 7.9).

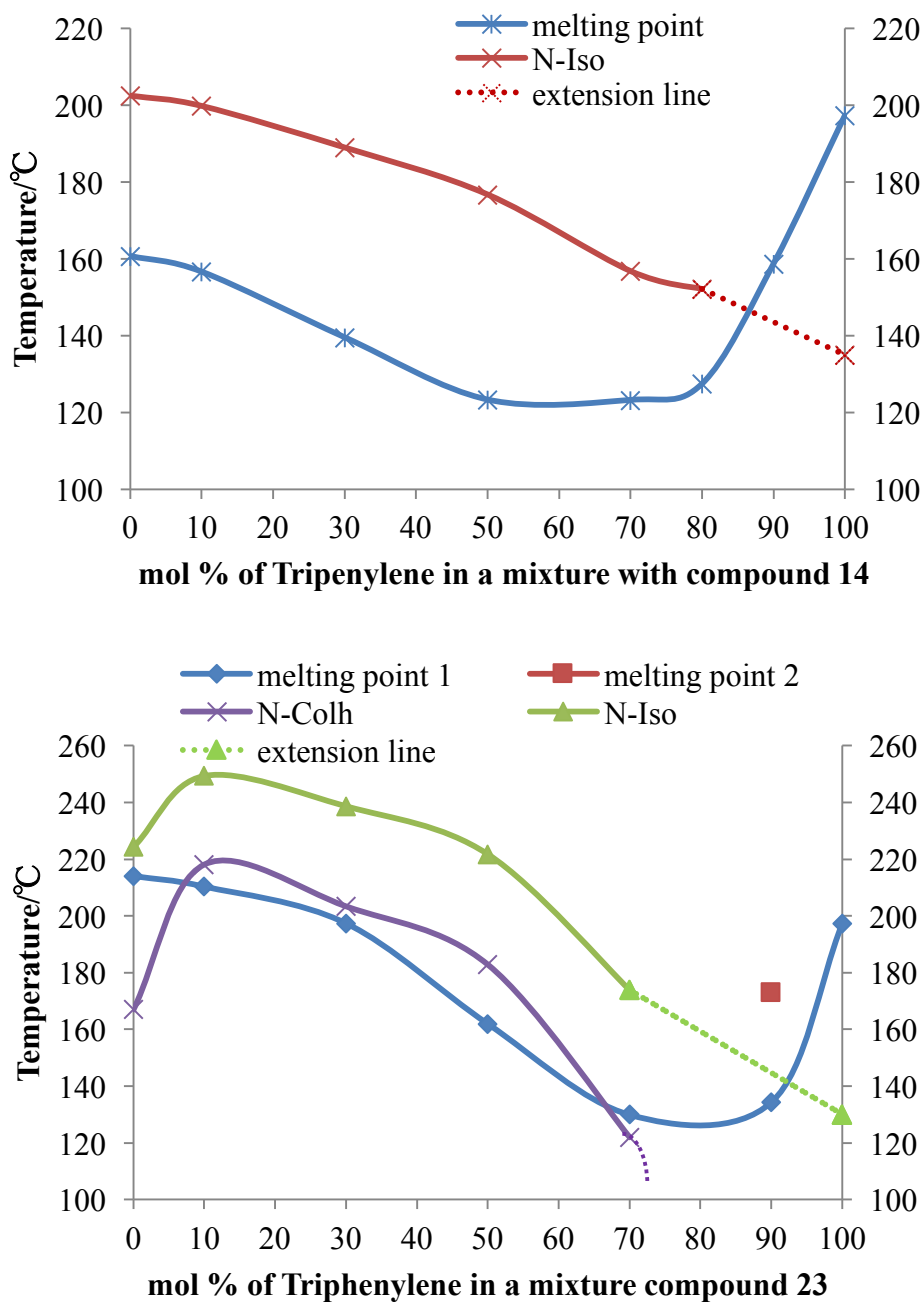


**Figure 7.9** Comparison of the phase diagrams and the determination of the virtual N-I transition temperature (°C) for triphenylene.

Considering both phase diagrams, the virtual N-I temperature for triphenylene was found to be about 135 °C. Conversely, Béguin *et al*[88] attempted to determine the discotic phase potentialities for triphenylene and pyrene in 1979, and they found that the discotic phase transition for triphenylene was 55 °C and for pyrene was 80 °C. In these studies, they used the hexa triphenylene ethers series (n = 5, 7) to mix with triphenylene and pyrene. However, the series of material are known to exhibit columnar phases but not nematic phases, and this might be the reason why the result of the N to I is lower than the value determined through this work in the chapter where a bonafide discotic nematogen was used as the standard material for the miscibility studies.

### **7.3 Miscibility Results of Other Polyaromatics with Triphenylene Derivatives**

For the family of polyaromatics based on triphenylene derivatives, only substantial mixing was found for triphenylene. For the other polyaromatics, such as pyrene and perylene, mixing was found not to occur with a range of triphenylene derivatives (compounds **14**, **16** and **18**). Separation was observed by optical microscopy in melting cycles and odd shapes were obtained for DSC thermograms. Thus generally the phase diagrams were not formed and so could not be discussed. The mixtures that were investigated are shown in Table 7.3.

**Table 7.3** The miscibility results for the mixtures obtained by different polyaromatics with different nematic and columnar triphenylene derivatives.

Component A	Component B / Nematic	Miscibility
<b>Triphenylene</b>	<b>14</b>	Section 7.2.1
<b>Truxene</b>	<b>14</b>	None
<b>Pyrene</b>	<b>18</b>	None
<b>Perylene</b>	<b>16</b>	None
<b>Coronene</b>	<b>16</b>	None

Component A	Component B / Columnar	Miscibility
<b>Triphenylene</b>	<b>23</b>	Section 7.2.2
<b>Truxene</b>	<b>24</b>	None
<b>Pyrene</b>	<b>21</b>	None
<b>Perylene</b>	<b>24</b>	None
<b>Coronene</b>	<b>24</b>	None

## 7.4 Summary

In this chapter, all the attempts made were to investigate the co-miscibility of polyaromatics with different triphenylene hexa-esters that exhibited nematic or columnar phases, and thereby to determine the virtual phase transition temperature for the polyaromatics. There was only one success, that of triphenylene, where a virtual N-I temperature was found to be 135 °C, but for the other polyaromatics the experiments failed to yield any results.

## **Chapter 8: Conclusion**

## Chapter 8: Conclusion

As there are few studies on the phase behaviour of disc-like systems in comparison with the calamitic systems made up of rod-like materials, this thesis sought novel investigations of the thermodynamic behaviour and miscibilities for discotic liquid crystals. A number of significant results were obtained as follows:

- A novel new phase was discovered in the isotropic liquid of four-component mixtures of polyaromatic materials, suggesting the possibility of the theoretically predicted cubatic nematic phase being present.
- The nematic phases of structurally compatible discotic materials were found to be miscible and therefore such phases could be classified as liquid crystals.
- The nematic phases of materials that possessed X- or disc-shaped molecular structures were found to be immiscible, indicating that rod and disc systems are immiscible and that there is no evidence for the formation of biaxial mesophases.
- Columnar mesophases of disc-like systems appeared to be generally immiscible indicating show that these phases are soft crystal phases.

In the sections below specific conclusions are made for the various points raised above.

### 8.1 Conclusion for Polyaromatics and Cubatic Phases

Onsager theory suggests that for calamitic phases made up of rod-like molecules the molecular aspect ratio (molecular length to breadth) is important, however, for hard disc-like systems very few investigations have been made into their mesomorphic properties and studies of mixed systems. Most of the materials found in the mixtures of the heavy ends of oil were found to be polyaromatics, and nematic phases have been found to be exhibited by the heavy ends of oil when they are heated to high temperatures. The investigation for the melting behaviour of selected polyaromatics such as triphenylene, pyrene, perylene, coronene, and truxene, and the comparison with *p*-sexiphenyl suggest that hard discs may be less likely to form mesophases, and that the  $\pi$ - $\pi$  face-to-face intermolecular

interactions are more important than for rod-like systems. It also indicates that intermolecular twisting of adjacent phenyl rings in rod-like materials such as *p*-sexiphenyl prevents to some degree  $\pi$ - $\pi$  interactions, thereby allowing mesophases to form, whereas for disc-like molecules, the intermolecular interactions are expected to be strong, and as such polyaromatics could effectively hide in the local structure by packing between the molecules of the amphiphilic discotic liquid crystal material.

In the studies performed, mixtures of polyaromatics (hard discs) and discotic liquid crystals (soft discs) were prepared, and the binary phase diagrams were used to determine the virtual N-I phase transition temperatures by extrapolations for binary phase diagrams. As a result, the virtual N-I temperature for triphenylene was found to be approximately 135 °C. However, for the family of polyaromatics studied, for miscibility studies based on triphenylene derivatives (soft discs) as the standard sources of nematic discotic mesophases, only substantial mixing was found for triphenylene. Conversely, for all of the other polyaromatics, such as pyrene and perylene, mixing was found not to occur with a range of standard materials, even for standard materials exhibiting nematic and columnar mesophases. This result indicates that the polyaromatic materials, other than triphenylene, had an extremely low tendency to exhibit liquid crystal phases. As a consequence, the phase diagrams for other polyaromatics were not developed and were therefore not discussed. However, it should be noted that triphenylene being the smallest hard disc material fitted best with the packing of the standard triphenylene soft disc-materials, and also of the polyaromatics studied it had the smallest delocalisation of the electrons and hence the weakest intermolecular interactions. Thus, as the planar disc size was increased across the family of materials there was potentially a lowering of the mesomorphic susceptibility simply because the intermolecular interactions increased, which preferentially stabilised the solid state, *e.g.* compare the melting point of triphenylene (197 °C) with that of coronene (432 °C). Figure 8.1 shows the comparison between the structures of triphenylene and coronene on the same scale at 0K as determined by ChemDraw, and an impression of the local staggered organization.

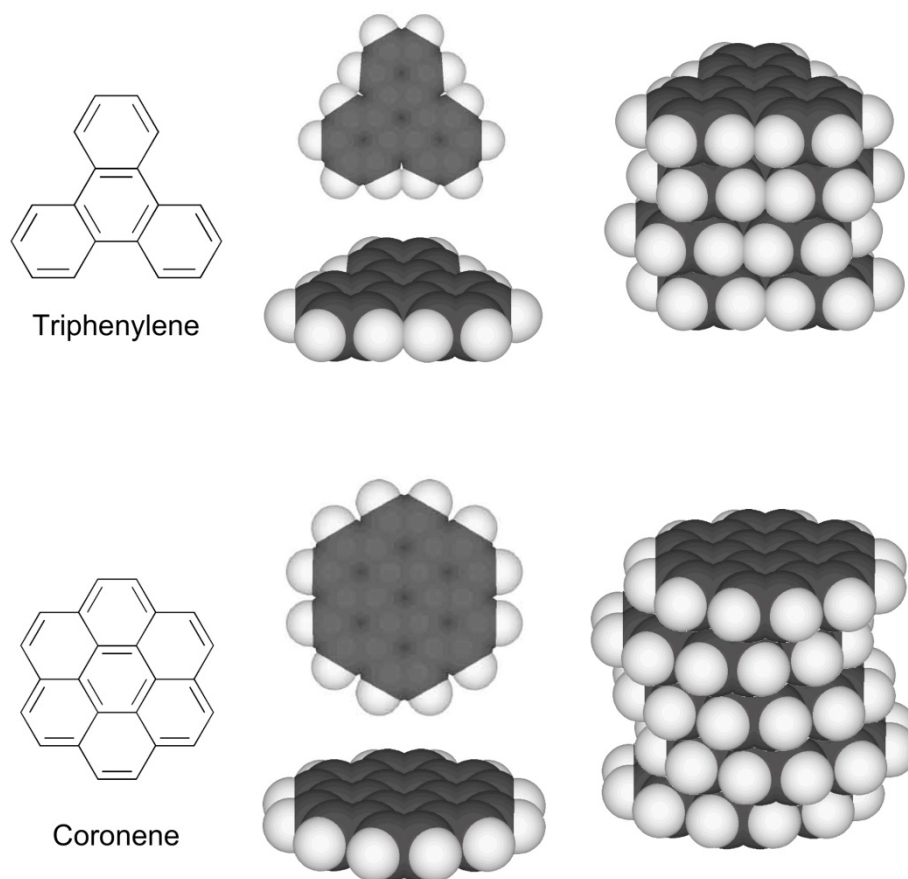


**Figure 8.1** An impression of the shapes of the polyaromatic materials triphenylene and coronene in gas phase at 0 K as determined by modelling using the MM2 force field as implemented in ChemDraw 3D, and their local self-organizations.

Basing research on the studies of carbonaceous mesophases,[49-50, 53] mixture studies were performed on a variety of polyaromatics that had hard discoidal structures. Using the Schröder-van Laar equation to simulate combinations of eutectic mixtures for the study of the self-organization of hard disc systems a number of mixtures possessing no aliphatic chains were prepared. As a result, a novel mesophase for the mixture **TZ-4M** (eutectic for triphenylene, perylene, truxene and coronene) was discovered, and was shown to exhibit and a dark (almost optically extinct) texture by POM at approximately 200 °C between solid state and liquid state. The almost extinct texture indicates that it is close to being optically isotropic and is probably amorphous in nature or it might be a cubic phase, which at 200 °C is the most likely candidate to be formed. The only theoretical model that predicts similar properties is that of the cubatic nematic phase. Why

this may occur is probably related to the incorporation of truxene in the mixture. Truxene has a twisted structure, see Figure 8.2, which means that it is a disruptor for the face-to-face packing of the flat discs of the other molecules in the mixture. This will reduce the molecular correlation length, thereby favouring the formation of short molecular stacks, which are favoured for the formation of the cubatic phase. Further and extensive studies on this unique system are required in order to confirm or not the presence of this novel phase.

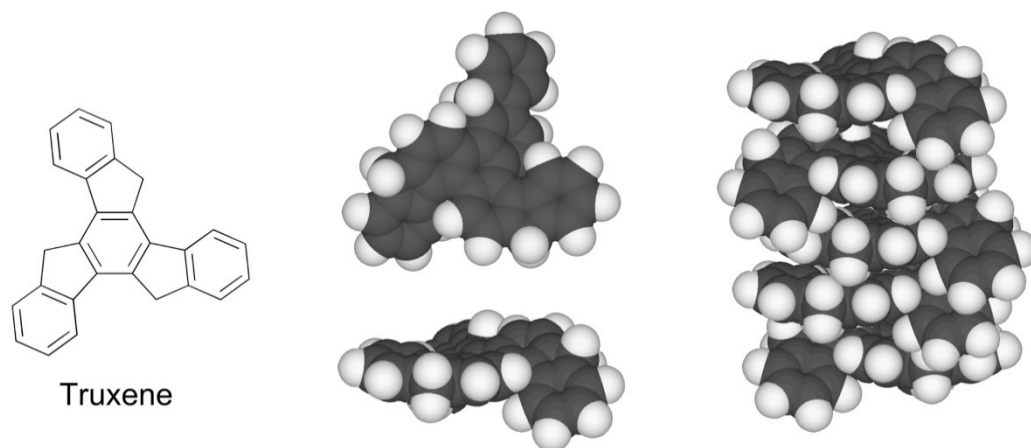


**Figure 8.2** An impression of the twisted shape of truxene in gas phase at 0 K as determined by modelling using the MM2 force field as implemented in ChemDraw 3D, and its local self-organization.

## 8.2 Conclusion for Miscibility Investigation for Discotic Liquid Crystals

As disc-like molecular systems are sometimes treated as complementary to calamitic systems that have structures and properties based on rod-like molecules, and where miscibility and eutectic mixtures using Gibbs phase diagrams is commonplace, it was decided to see if similar behaviour and applications were possible for disc-like analogues. Thus, miscibility investigations for the discotic materials were based on the construction of Gibbs phase diagrams and their relative thermodynamic behaviour or stability. Mixtures were prepared using simulations of the Schröder-van Laar equation to determine eutectic points, and computer modelling was employed to identify the molecular structural features

that might support co-miscibility, and analysis was made by polarized optical microscopy and differential scanning calorimetry. As a result, it appeared that for materials exhibiting nematic discotic phases, disc-like materials with rigid central regions and flexible external chains formed mixtures relatively easily, whereas mesogens possessing more rigid disc-like structures or x-shaped molecular architectures did not form phases easily. However, the co-miscibility indicates that the nematic phase of discoidal materials could be considered to be a true liquid crystal. Conversely, columnar phases often appeared to be immiscible, and therefore they have a closer relationship with crystals even though they do not necessarily have long range positional ordering.

### **8.2.1 Co-miscibility of Nematic of Disc-like Mesogens**

Miscibility studies and binary phase diagrams for disc-like nematogenic materials were made in order to examine their mixing as a function of molecular architecture, and to investigate how well the fluid-like mesophases integrated with one another. In addition, as the nematic phases of discoidal materials have similar properties to those of the nematic phase formed by rod-like molecules, materials with intermediary structures between rods and discs were selected for study in mixtures. In this part of research programme, the co-miscibilities of nematogens of disc-like triphenylene derivatives with each other, and with rod-like tetra-benzoate molecules and disc-like phenyl hexa-alkynes were investigated, the mixture series and results are as shown in Table 8.1-8.3.

**Table 8.1** The mixture series and results for the binary mixtures of triphenylene hexa-esters with each other.

Series ID	Component A	Component B	Miscibility	Actual eutectic
<b>TZ-M001</b>	<b>4</b>	<b>11</b>	Similar behaviors as rod-like systems	Similar as Schröder-van Laar equation prediction

**Table 8.2** The mixture series and results for the binary mixtures of triphenylene hexa-esters and rod-like tetra-benzoate molecules.

Series ID	<b>TZ-M012</b>	<b>TZ-M019</b>	<b>TZ-M021</b>
Component A	<b>4</b>	<b>11</b>	<b>27</b>
Component B	<b>38</b>	<b>51</b>	<b>56</b>
Miscibility	Poor co-miscibility		
Actual eutectic	Experimental value not as Schröder-van Laar equation prediction		

**Table 8.3** The mixture series and results for the binary mixtures of triphenylene hexa-esters and star-shaped phenyl hexa-alkynes.

Series ID	Component <b>A</b>	Component <b>B</b>	Miscibility	Actual eutectic
<b>TZ-M022</b>	<b>16</b>	<b>64</b>	Similar behaviors as rod-like systems	Similar as Schröder-van Laar equation prediction
<b>TZ-M023</b>	<b>26</b>			
<b>TZ-M024</b>	<b>18</b>		No good miscibility	No obvious eutectic
<b>TZ-M030</b>	<b>27</b>		Dissimilar behaviors to rod-like systems	No obvious eutectic
<b>TZ-M031</b>	<b>22</b>			
<b>TZ-M032</b>	<b>14</b>			
<b>TZ-M033</b>	<b>19</b>			
<b>TZ-M034</b>	<b>20</b>			
<b>TZ-M035</b>	<b>13</b>			
<b>TZ-M036</b>	<b>15</b>			
<b>TZ-M037</b>	<b>17</b>			

The results of these studies show that for the nematic discotic triphenylene derivatives, they show similar behaviour as found for rod-like systems. However, when the smaller molecules such as rod-like tetra-benzoate molecules were added into the discotic triphenylene derivatives, they exhibited behaviour more in keeping with that of rod-like systems, *i.e.* they were immiscible even though the tetra-esters had deformable shapes and could have formed board-like structures. Conversely the small rigid disc-like alkyne showed continuous miscibility of the nematic phase with the triphenylenes. This indicates that the disc-like materials formed mixtures relatively easily, whereas mesogens possessing x-shaped molecular architectures did not. When nematogens having different sizes were mixed together, for the smaller molecules such as compound **64** being in larger concentration, the larger molecules for example compound **20** and **13**, still exhibited lateral effects, which occurred through correlations between adjacent

molecular clustering; thus the binary phase diagram would be composed of two, but unsymmetrical halves.

### 8.2.2 Phase Behaviour of Columnar Discotic Mesogens

The mixing of materials that exhibited columnar phases was examined in order to investigate how such systems, which potentially have 2D crystal structures, might mix or alternatively phase segregate. This type of study ultimately gave insights into the nature of crystallinity versus true liquid-crystallinity. Here the mixing of columnar phases of disc-like triphenylene derivatives with each other or with rod-like tetra-benzoate molecules or star-shaped phenyl hexa-alkynes was investigated and discussed. The series of mixtures are listed as shown in Table 8.4 and 8.5.

**Table 8.4** The series of mixtures and results for the columnar phases of triphenylene hexa-esters with each other.

Series ID	<b>TZ-M003</b>
Component <b>A</b>	<b>21</b>
Component <b>B</b>	<b>32</b>
Miscibility	Unlikely to give a Gibbs phase diagram

**Table 8.5** The mixture series and results for mixing of materials exhibiting columnar and possibly nematic phases.

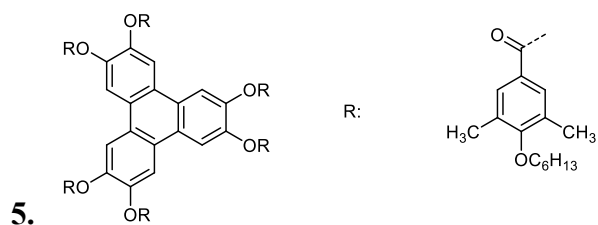
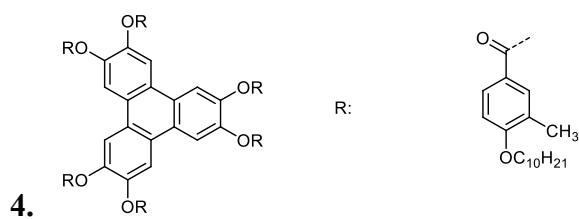
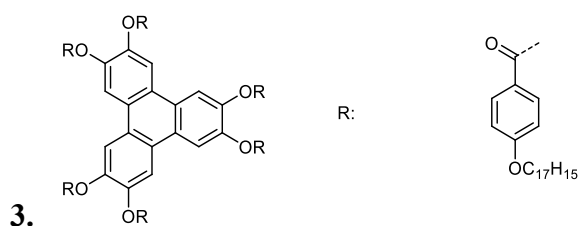
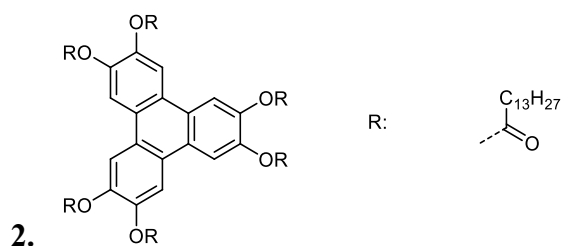
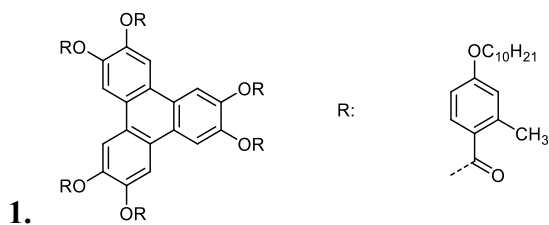
Series ID	Component A	Component B	Miscibility
<b>TZ-M040</b>	<b>21</b>	<b>24</b>	Phase separation found.
<b>TZ-M016</b>	<b>32</b>	<b>52</b>	Co-miscibility of the nematic phase not observed.
<b>TZ-M018</b>	<b>21</b>	<b>40</b>	Immiscible
<b>TZ-M020</b>	<b>29</b>	<b>41</b>	Full co-miscibility was not achieved.
<b>TZ-M027</b>	<b>24</b>	<b>64</b>	Continuous miscibility of the nematic phase found with no mixtures exhibiting a columnar phase.
<b>TZ-M028</b>	<b>21</b>		Phase separation found.
<b>TZ-M029</b>	<b>23</b>		Not miscible.

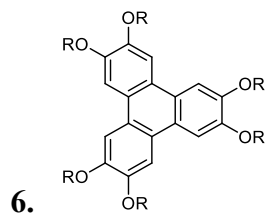
The Schröder van-Laar equation was used to predict the eutectic composition for hexagonal columnar hexa-esters of triphenylene, but in the binary phase diagrams, there was no obvious lowering of the melting point, or a lowering of the isotropic liquid to hexagonal columnar phase transition. This result might indicate that the hexagonal columnar behaves as a soft crystal phase rather than a liquid crystal. The Schröder-van Laar equation was again used to predict a eutectic composition where the isotropic liquid to columnar phase transition and the associated enthalpies were used to predict the melting point and melting enthalpy. As a result, the inconsistent results indicate that the columnar phases may have subtly different structures.

It can be seen that the phase behaviour of the columnar discotic materials is quite different in comparison with those commonly seen in the phase diagrams of calamitic smectic systems formed by rod-like molecules. The Col<sub>h</sub>-I phase transition behaviour is much more like a melting transition found in the common Gibbs phase diagrams. However, the phase behaviour of columnar phases is

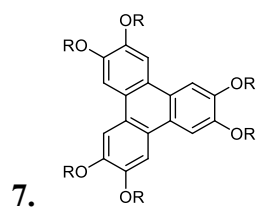
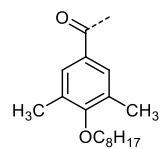
similar to that seen for the smectic soft-crystal phases, indicating that the hexagonal columnar phase could also be a soft crystal phase. Thus, through this research, the hexagonal columnar phases formed by the discoidal materials presented in the thesis herein are probably better classified as soft crystal phases.

## Appendix 1: The Chemical Structures of the Compounds for Misibility Studies in the Thesis

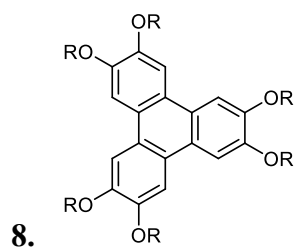
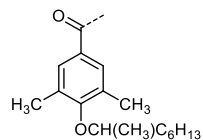




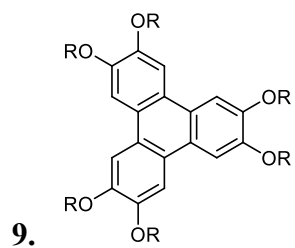
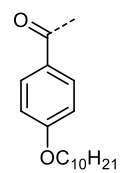
R:



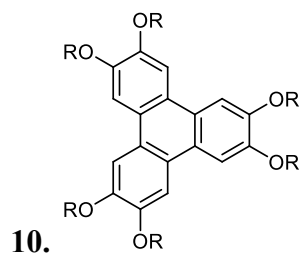
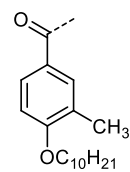
R:



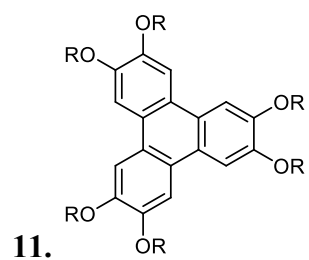
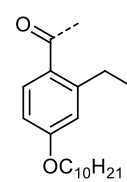
R:



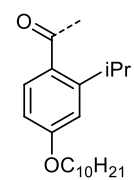
R:

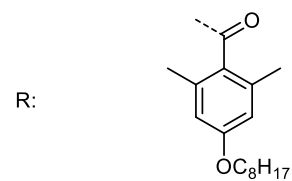
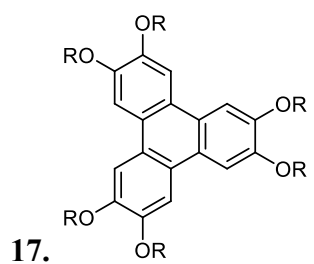
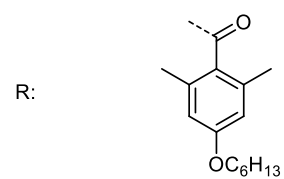
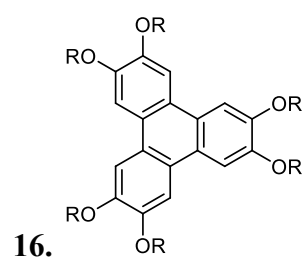
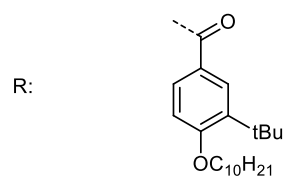
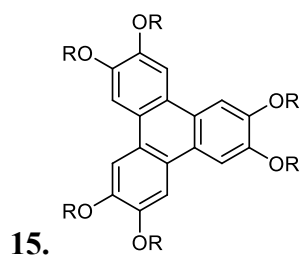
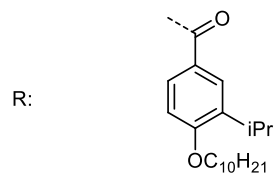
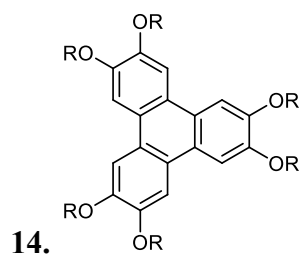
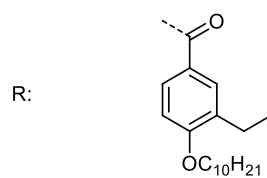
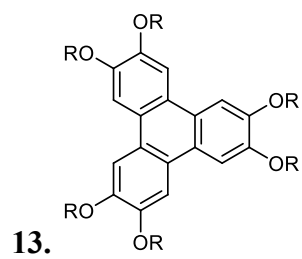
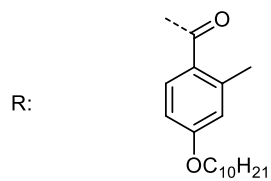
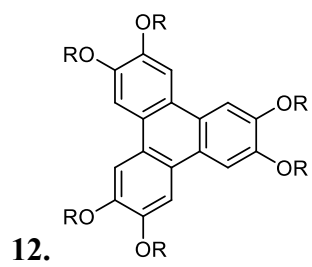


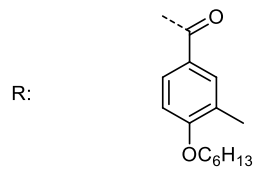
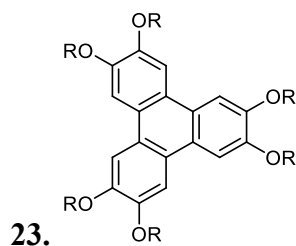
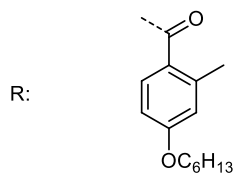
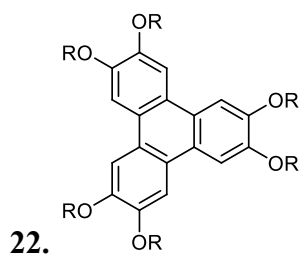
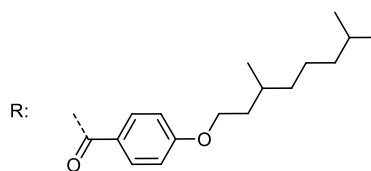
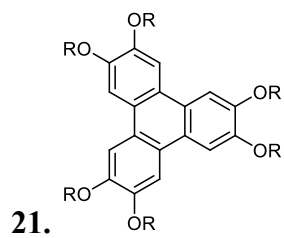
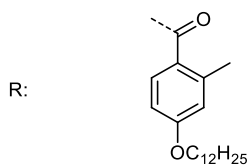
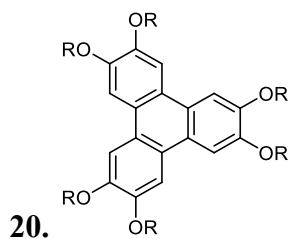
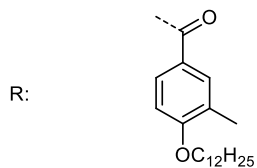
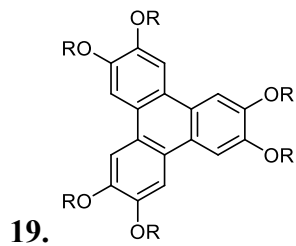
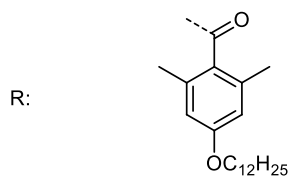
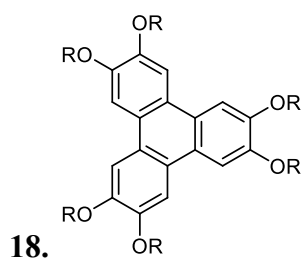
R:

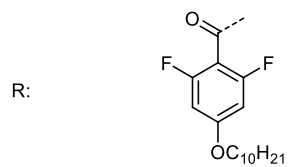
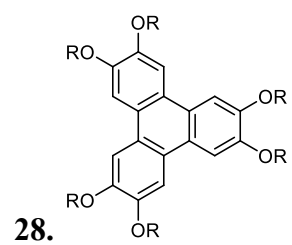
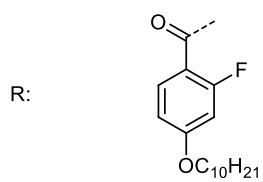
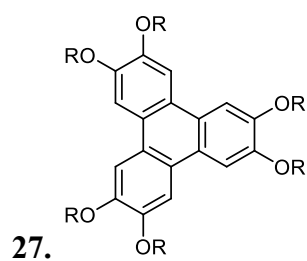
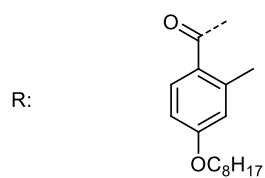
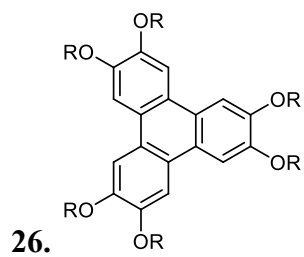
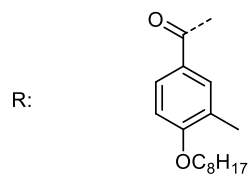
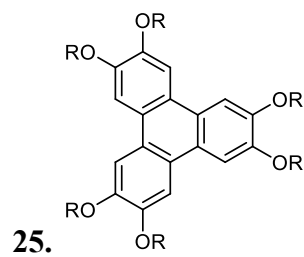
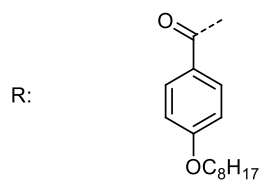
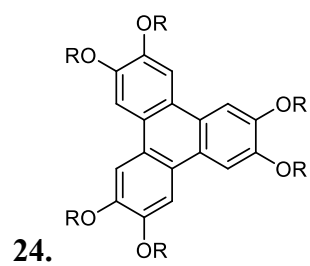


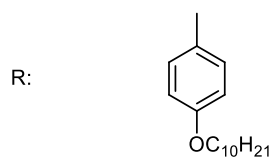
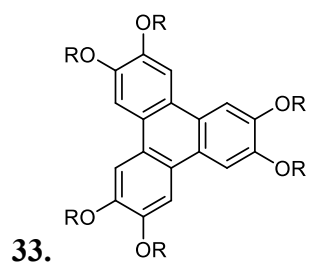
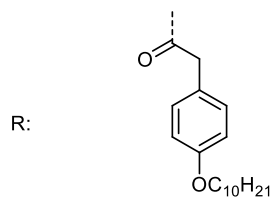
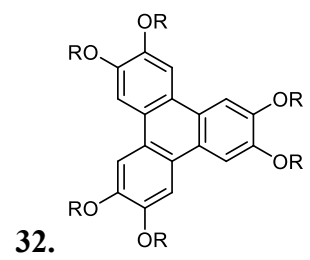
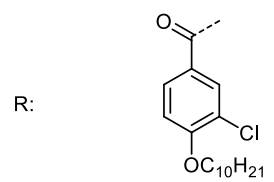
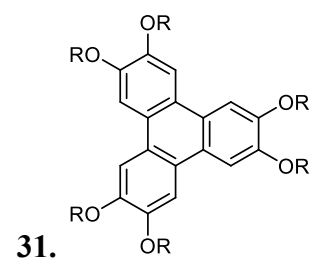
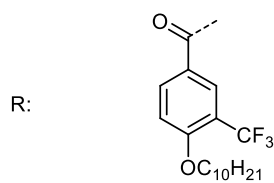
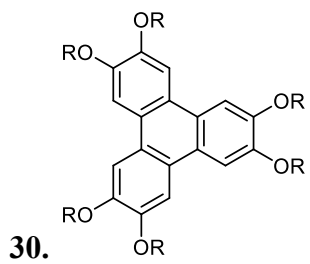
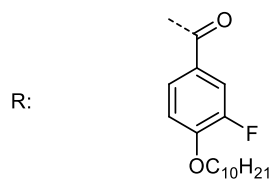
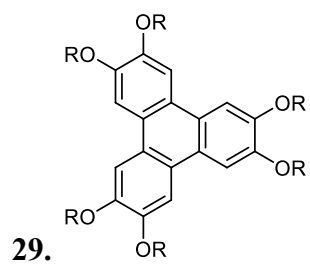
R:

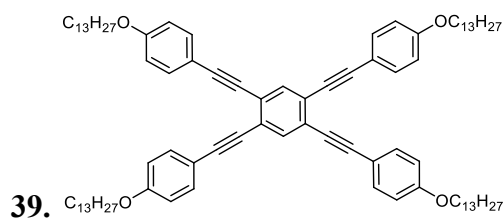
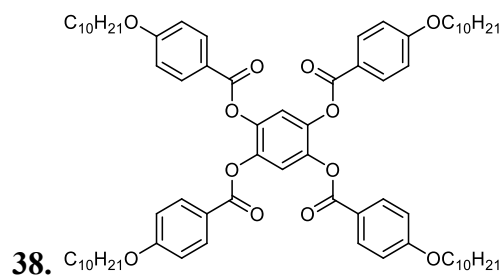
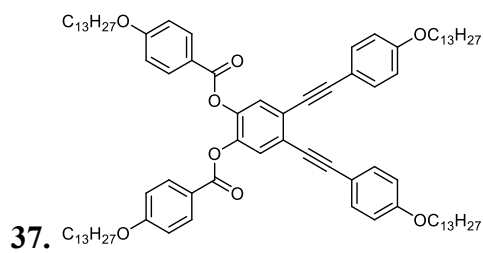
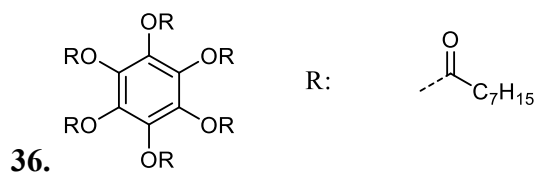
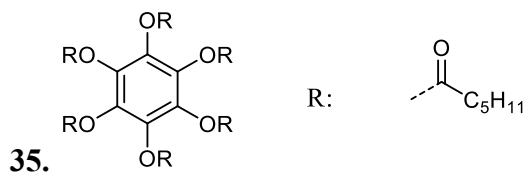
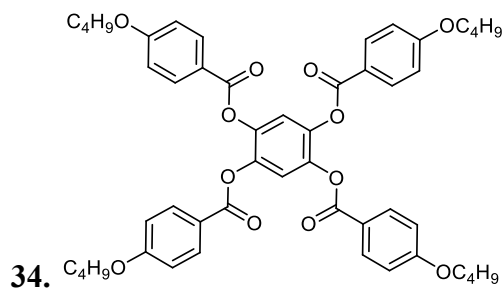


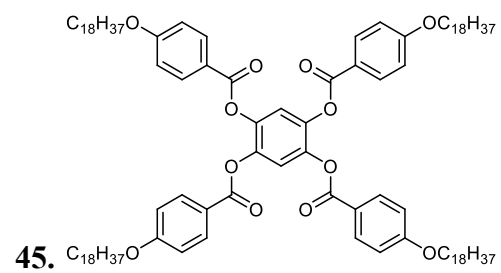
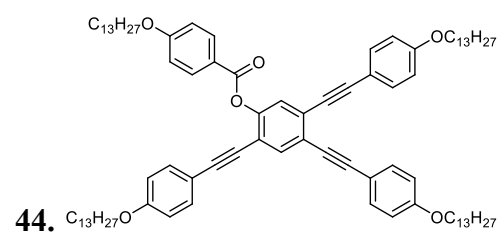
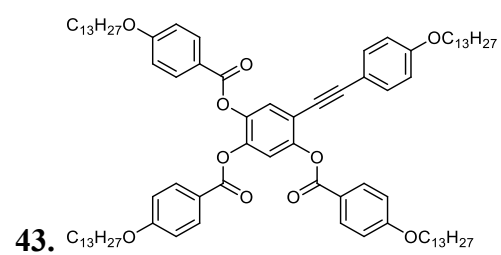
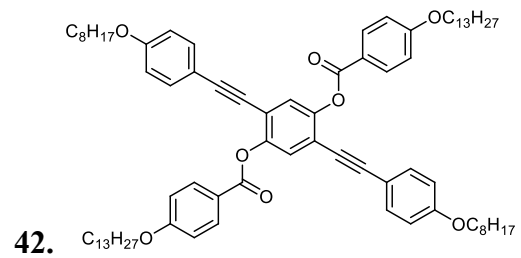
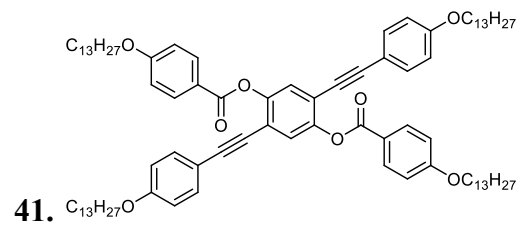
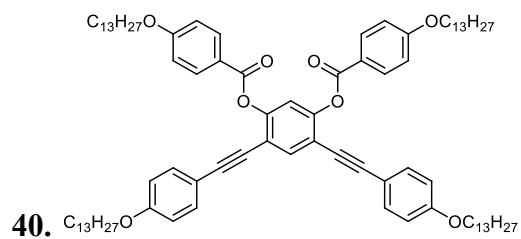


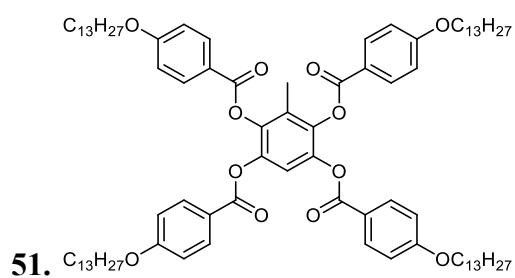
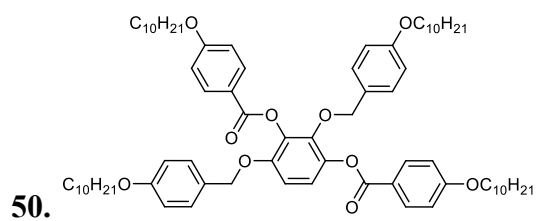
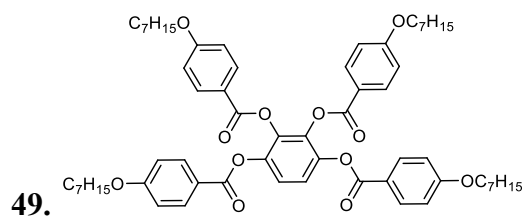
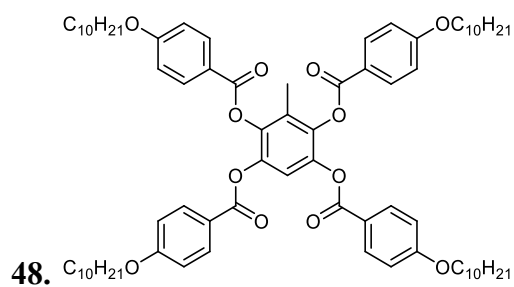
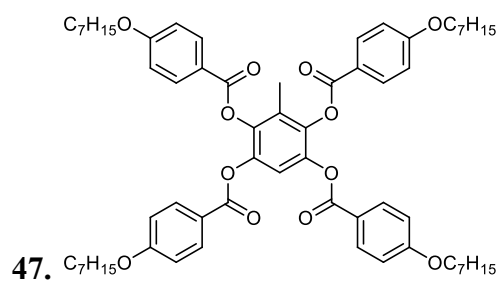
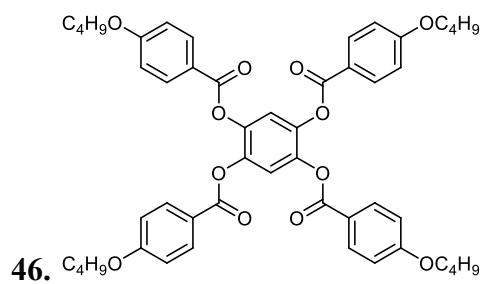


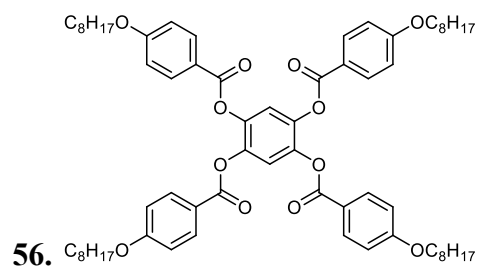
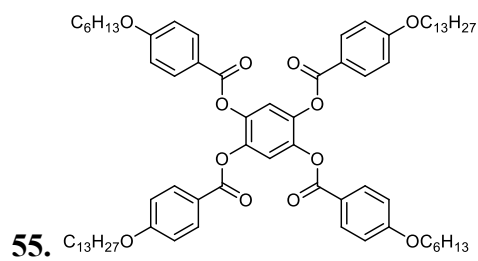
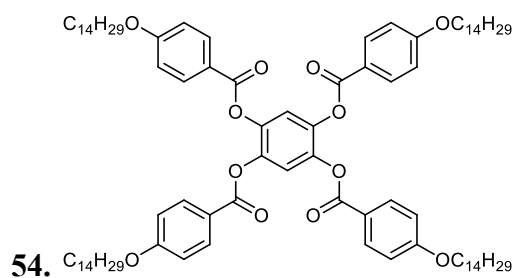
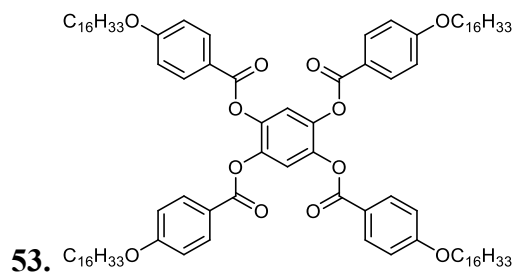
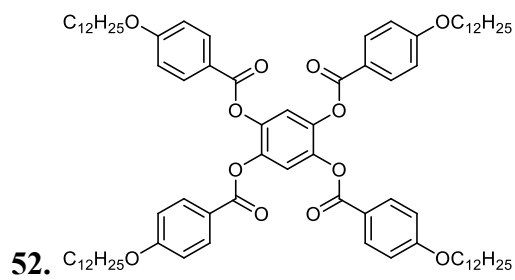


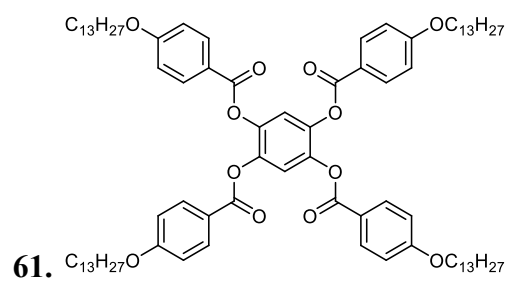
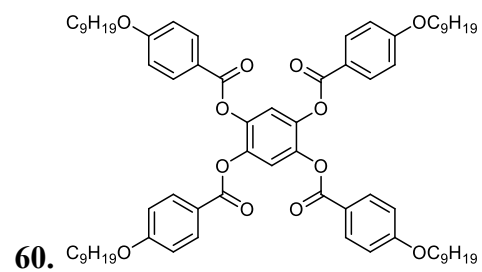
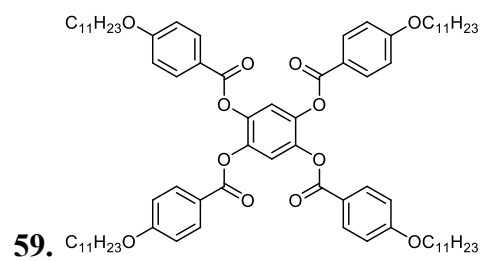
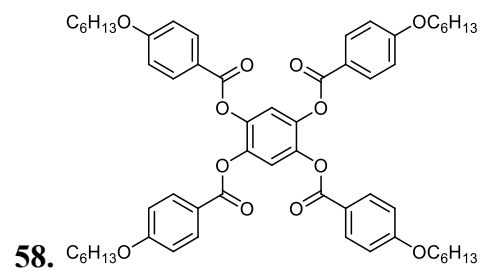
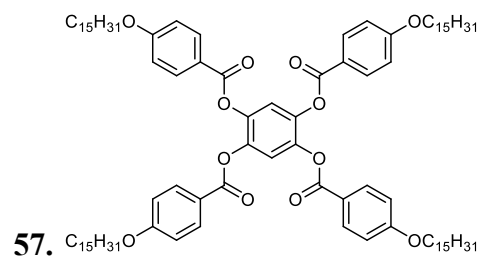


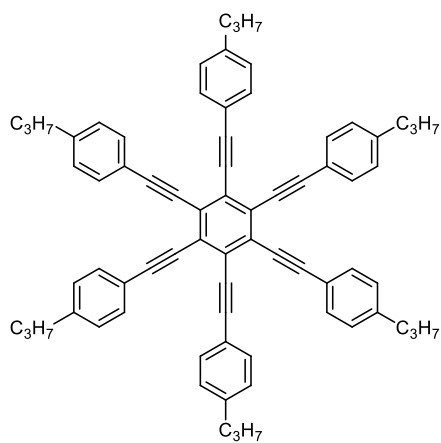




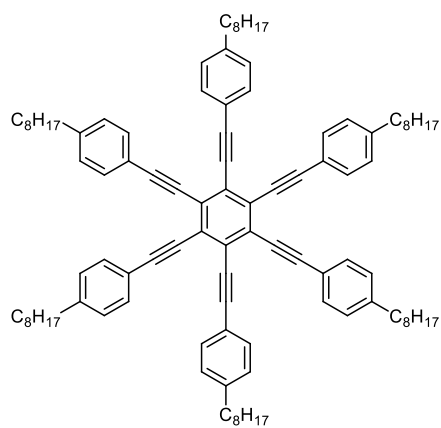




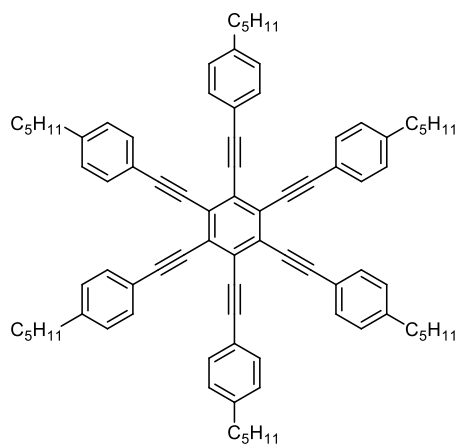




62.



63.



64.

## References

1. J.W. Goodby, D. Demus, G.W. Gray, H.W. Spiess and V. Vill, *Handbook of liquid crystals*, Wiley-VCH, Weinheim, 1998.
2. G.W. Gray, *Thermotropic liquid crystals*, John Wiley & Sons Inc, 1987.
3. W. S. Maier, A. Z. *Naturforsch*, 1958, **13a**, 564-570.
4. W. S. Maier, A. Z. *Naturforsch*, 1959, **14a**, 882-890.
5. W. S. Maier, A. Z. *Naturforsch*, 1960, **15a**, 287-292.
6. R.J. Mandle, E. Bevis, J.W. Goodby in *Handbook of Liquid Crystals, Vol. 3: Nematic and Chiral Nematic Liquid Crystals*, Ed. J.W. Goodby, P.J. Collings, T. Kato, C. Tschierske, H.F. Gleeson and P. Raynes, Wiley-VCH, Weinheim 2014.
7. L. Onsager, *Ann. NY Acad. Sci*, 1949, **51**, 286-287.
8. P.J. Wojtowicz, P. Sheng and E. Priestley, *Introduction to liquid crystals*, Springer, 1975.
9. X. Xiao and P. Sheng, *Phys. Rev. E*, 2013, **88**, 062501.
10. H. Schubert, R. Dehne and V. Uhlig, *Z. Chem.*, 1972, **12**, 219-220.
11. G.W. Gray, K.J. Harrison and J. Nash, *Electron. Lett.*, 1973, **9**, 130-131.
12. S. Chandrasekhar, B.K. Sadashiva, K.A. Suresh, *Pramana*, 1977, **9**, 10.
13. H. Hakemi, E. Jagodzinski and D. Dupré, *Mol. cryst. liq. cryst.*, 1983, **91**, 129-136.
14. E.J. Davis, *PhD Thesis*, University of York, 2012.
15. S. Kumar and S.K. Gupta, *Tetrahedron Lett.*, 2011, **52**, 5363-5367.
16. S.K. Pal, S. Setia, B. Avinash and S. Kumar, *Liq. Cryst.*, 2013, **40**, 1769-1816.
17. D.R. Beattie, P. Hindmarsh, J.W. Goodby, S.D. Haslam and R.M. Richardson, *J. Mater. Chem.*, 1992, **2**, 1261-1266.
18. J.W. Goodby, M. Hird, K.J. Toyne and T. Watson, *J. Chem. Soc., Chem. Commun.*, 1994, 1701-1702.

19. S. Cross, J. Goodby, A. Hall, M. Hird, S. Kelly, K. Toyne and C. Wu, *Liq. Cryst.*, 1998, **25**, 1-11.
20. P. Hindmarsh, M.J. Watson, M. Hird and J.W. Goodby, *J. Mater. Chem.*, 1995, **5**, 2111-2123.
21. R. Zniber, R. Achour, M.Z. Cherkaoui, B. Donnio, L. Gehringer and D. Guillon, *J. Mater. Chem.*, 2002, **12**, 2208-2213.
22. V. Bhalla, H. Singh and M. Kumar, *Org. Lett.*, 2009, **12**, 628-631.
23. A. Kotlewski, W.F. Jager, E. Mendes and S.J. Picken, *Liq. Cryst.*, 2010, **37**, 579-586.
24. A. Alavi and D. Frenkel, *Phys. Rev. A*, 1992, **45**, R5355.
25. M.D. Luca, M. Neal and C. Care, *Liq. Cryst.*, 1994, **16**, 257-266.
26. S. Kumar, *Chemistry of discotic liquid crystals: from monomers to polymers*, CRC Press, Boca Raton, 2010.
27. J. Kirkpatrick, V. Marcon, K. Kremer, J. Nelson and D. Andrienko, *J. Chem. Phys.*, 2008, **129**, 094506.
28. V. Marcon, T. Vehoff, J. Kirkpatrick, C. Jeong, D.Y. Yoon, K. Kremer and D. Andrienko, *J. Chem. Phys.*, 2008, **129**, 094505.
29. H.K. Bisoyi and S. Kumar, *Liq. Cryst.*, 2011, **38**, 1427-1449.
30. J. Veerman and D. Frenkel, *Phys. Rev. A*, 1992, **45**, 5632.
31. P.D. Duncan, M. Dennison, A.J. Masters and M.R. Wilson, *Phys. Rev. E*, 2009, **79**, 031702.
32. M. Marechal, P. A. Patti and M. Dijkstra, <http://arxiv.org/abs/1112.1209>, 2012
33. E.J. Davis, J.W. Goodby, in *Handbook of Liquid Crystals, Vol. 1: Fundamentals of Liquid Crystals*, Ed. J.W. Goodby, P.J. Collings, T. Kato, C. Tschierske, H.F. Gleeson and P. Raynes, Wiley-VCH, Weinheim 2014.
34. L.M. Blinov, *Structure and Properties of Liquid Crystals*, Springer Science & Business Media, 2010.

35. H. Takezoe, K. Kishikawa and E. Gorecka, *J. Mater. Chem.*, 2006, **16**, 2412-2416.
36. R.J. Bushby and K. Kawata, *Liq. Cryst.*, 2011, **38**, 1415-1426.
37. W. Pisula, A. Menon, M. Stepputat, I. Lieberwirth, U. Kolb, A. Tracz, H. Sirringhaus, T. Pakula and K. Mullen, *Adv. Mater.*, 2005, **17**, 684-689.
38. G. Lüssem and J. Wendorff, *Polym. Adv. Tech.*, 1998, **9**, 443-460.
39. T. Hassheider, S.A. Benning, H.S. Kitzerow, M.F. Achard and H. Bock, *Angew. Chem. Int. Edit.*, 2001, **40**, 2060-2063.
40. M. Oukachmih, P. Destruel, I. Seguy, G. Ablart, P. Jolinat, S. Archambeau, M. Mabiala, S. Fouet and H. Bock, *Sol. Energ. Mater. Sol. C.*, 2005, **85**, 535-543.
41. L. Li, S.W. Kang, J. Harden, Q. Sun, X. Zhou, L. Dai, A. Jakli, S. Kumar and Q. Li, *Liq. Cryst.*, 2008, **35**, 233-239.
42. J.P. Schmidtke, R.H. Friend, M. Kastler and K. Müllen, *J. Chem. Phys.*, 2006, **124**, 174704.
43. J. Clements, N. Boden, T. Gibson, R. Chandler, J. Hulbert and E. Ruck-Keene, *Sensor. Actuat. B-Chem.*, 1998, **47**, 37-42.
44. S. Sergeev, W. Pisula and Y.H. Geerts, *Chem. Soc. Rev.*, 2007, **36**, 1902-1929.
45. K. Kawata, *Chem. Rec.*, 2002, **2**, 59-80.
46. P. Hindmarsh, M. Hird, P. Styring and J.W. Goodby, *J. mater. Chem.*, 1993, **3**, 1117-1128.
47. H. Mori, Y. Itoh, Y. Nishiura, T. Nakamura and Y. Shinagawa, *Jpn. Jind. Appl. phys.*, 1997, **36**, 143.
48. Y. Ito, R. Matsubara, R. Nakamura, M. Nagai, S. Nakamura, H. Mori, K. Mihayashi, , *FujiFilm Res. & Dev.*, 2006, **51**, 147-150.
49. J. White, G. Guthrie and J. Gardner, *Carbon*, 1967, **5**, 517-518.
50. J. Brooks and G. Taylor, *Carbon*, 1965, **3**, 185-193.
51. J. Kipling and P. Shooter, *Carbon*, 1966, **4**, 1-4.

52. M. Ihnatowicz, P. Chiche, J. Deduit, S. Pregermain and R. Tournant, *Carbon*, 1966, **4**, 41-50.
53. H. Honda, H. Kimura and Y. Sanada, *Carbon*, 1971, **9**, 695-697.
54. Phase diagrams, <http://nptel.ac.in/courses/113106032/>.
55. ASM Handbook, Volume 3: Alloy phase diagrams, *ASM international*, 1992.
56. P. Raynes, in *Handbook of Liquid Crystals, Vol. 1: Fundamentals of Liquid Crystals*, Ed. J.W. Goodby, P.J. Collings, T. Kato, C. Tschierske, H.F. Gleeson and P. Raynes, Wiley-VCH, Weinheim 2014.
57. I.Z. Schröder, *phys. Chem*, 1893, **11**, 449-465.
58. J.J. van Laar, *Arch. Neerl II*, 1903, **8**, 264-284.
59. V. Meltzer and E. Pincu, *Analele Universitatii din Bucuresti–Chimie*, 2008, **1**, 15-18.
60. C. Safinya, E. Sirota and R. Plano, *Phys. Rev. Lett.*, 1991, **66**, 1986.
61. I. Hamley, V. Castelletto and P. Parras, *Phys. Rev. E*, 2006, **74**, 020701.
62. V. Castelletto, A. Squires, I. Hamley, J. Stasiak and G. Moggridge, *Liq. Cryst.*, 2009, **36**, 435-442.
63. P. Panizza, P. Archambault and D. Roux, *J. de Phys. II*, 1995, **5**, 303-311.
64. D.S. Hulme, E.P. Raynes and K.J. Harrison, *J. Chem. Soc., Chem. Comm.*, 1974, 98-99.
65. Y. Takanishi, G.J. Shin, J.C. Jung, S.-W. Choi, K. Ishikawa, J. Watanabe, H. Takezoe and P. Toledano, *J. Mater. Chem.*, 2005, **15**, 4020-4024.
66. L. Bedjaoui, N. Gogibus, B. Ewen, T. Pakula, X. Coqueret, M. Benmouna and U. Maschke, *Polymer*, 2004, **45**, 6555-6560.
67. P. Nolan, M. Tillin and D. Coates, *Mol. Cryst. Liq. Cryst. Lett.*, 1992, **8**, 129-135.
68. D.A. Higgins, *Adv. Mater.*, 2000, **12**, 251-264.
69. M. Mucha, *Pro. Polym. Sci.*, 2003, **28**, 837-873.

70. B. Bahadur and M. Tilton, *Liquid crystals: applications and uses*, World Scientific, 1992.
71. H.-W. Chiu and T. Kyu, *J. Chem. Phys.*, 1998, **108**, 3249-3255.
72. D. Frenkel, *J. Phys-Condens. Matter*, 1994, **6**, A71.
73. J. Billard and B.K. Sadashiva, *Pramana*, 1979, **13**, 309-318.
74. R. Berardi and C. Zannoni, *Soft Matter*, 2012, **8**, 2017-2025.
75. A. Galindo, A. Haslam, S. Varga, G. Jackson, A. Vanakaras, D. Photinos and D. Dunmur, *J. Chem. Phys.*, 2003, **119**, 5216-5225.
76. L. Henriques and S. Salinas, *Eur. Phys. J. E*, 2012, **35**, 1-9.
77. Y. Bouligand, *J. de Phys.*, 1980, **41**, 1307-1315.
78. S. Singh, *Phys. Rep.*, 2000, **324**, 2-4, 107-269.
79. D.M. Agra-Kooijman, S. Kumar, in *Handbook of Liquid Crystals, Vol. 1: Fundamentals of Liquid Crystals*, Ed. J.W. Goodby, P.J. Collings, T. Kato, C. Tschierske, H.F. Gleeson and P. Raynes, Wiley-VCH, Weinheim 2014.
80. A.D. Vries, *J. Chem. Phys.*, 1979, **71**, 25-31.
81. A.D. Vries, *Mol. Cryst. Liq. Cryst.*, 1970, **11**, 361-383.
82. A.D. Vries, *Mol. Cryst. Liq. Cryst.*, 1985, **131**, 125-145.
83. A.D. Vries, *Mol. Cryst. Liq. Cryst.*, 1970, **10**, 219-236.
84. D. Demus, in *Handbook of Liquid Crystals: Fundamentals, Volume 1*, Ed. J.M. Seddon, D. Demus, J.W. Goodby, G. Gray, H.W. Spiess and V. Vill, 1998, 635-679.
85. A. Bradley, C. Hardacre, J. Holbrey, S. Johnston, S. McMath and M. Nieuwenhuyzen, *Chem. Mater.*, 2002, **14**, 629-635.
86. O.V. Kruglova, *Discotic liquid crystals: from dynamics to conductivity*, IOS Press, 2007.
87. J.W. Goodby, R.J. Mandle, E.J. Davis, Tingjun Zhong and S.J. Cowling, *Liq. Cryst.*, 2015, **42**, 593-622.

88. A. Beguin, J. Billard, J. Dubois, N.H. Tinh and A. Zann, *Le Journal de Physique Colloques*, 1979, **40**, C3-15-C13-16.
89. M.J. Watson. P. Hindmarsh, M. Hird and J.W. Goodby, *J. Mater. Chem.*, 1995, **5**(12), 2111-2123.
90. N. H. Tinh, H. Gasparoux and C. Destrade, *Mol. Cryst. Liq. Cryst.*, 1981, **68**, 101.
91. P. Hindmarsh, M. Hird, P. Styring and J.W. Goodby, *J. Mater. Chem.*, 1993, **3**(11), 1117-1128.
92. A.W. D. J. Norbert, J.W. Goodby, M. Hird, K.J. Toyne, J.C. Jones and J.S. Patel, *Mol. Cryst. Liq. Cryst.*, 1995, **260**, 339-350.
93. A.W. D. J. Norbert, J.W. Goodby, M. Hird, K.J. Toyne, *Liq. Cryst.* 1997, **22**(5), 631-642.
94. S. Kumar, S.K. Varshney and D. Chauhan, *Mol. Cryst. Liq. Cryst.*, 2003, **396**, 241-250.
95. R.C. Weast and M. Astle, *CRC handbook of Physics and Chemistry*, CRC Press, Boca Raton, FL (1988 1989), 1982.
- 96 T. Campbell and R. MaDonal, *J. Org. Chem.*, 1959, **24**(5), 730-730.
97. I. Lewis and C. Kovac, *Mol. Cryst. Liq. Cryst.*, 1979, **51**, 173-178.98. N.A. Zafiroopoulos, E-J. Choi, T. Dingemans, W. Lin, and E.T. Samulski, *Chem. Mater.*, 2008, **20**, 3821-3831.
99. S. Kumar and S.K. Varshney, *Angew. Chem. Int. Edit.*, 2000, **39**, 3140-3142.
100. S. Chandrasekhar, B. Sadashiva and K. Suresh, *Pramana*, 1977, **9**, 471-480.
101. S. Laschat, A. Baro, N. Steinke, F. Giesselmann, C. Haegele, G. Scalia, R. Judele, E. Kapatsina, S. Sauer and A. Schreivogel, *Angew. Chem. Inter. Edit.*, 2007, **46**, 4832-4887.
102. H.L. Ong, Presented in part of Conference Asia Pacific Symposium on Optoelectronics' 98, *International Society for Optics and Photonics*, 1998.
103. M. Hird and K.J. Toyne, *Mol. Cryst. Liq. Cryst.*, 1998, **323**, 1-67.